

7-12-2021

In-Vitro and In-Silico Investigations of Alternative Surgical Techniques for Single Ventricular Disease

Arka Das

Follow this and additional works at: <https://commons.erau.edu/edt>



Part of the [Mechanical Engineering Commons](#)

This Dissertation - Open Access is brought to you for free and open access by Scholarly Commons. It has been accepted for inclusion in PhD Dissertations and Master's Theses by an authorized administrator of Scholarly Commons. For more information, please contact commons@erau.edu.

IN-VITRO INVESTIGATIONS OF ALTERNATIVE SURGICAL TECHNIQUES FOR
SINGLE VENTRICULAR DISEASE

by

Arka Das

A Dissertation Submitted to the College of Engineering Department of Mechanical
Engineering in Partial Fulfillment of the Requirements for the Degree of
Doctor of Philosophy in Mechanical Engineering

Embry-Riddle Aeronautical University
Daytona Beach, Florida
July 12, 2021

IN-VITRO AND IN-SILICO INVESTIGATIONS OF ALTERNATIVE SURGICAL
TECHNIQUES FOR SINGLE VENTRICULAR DISEASE

by

Arka Das

This dissertation was prepared under the direction of the candidate's Dissertation Committee Chair, Dr. Eduardo Divo, Professor, Daytona Beach Campus, and has been approved by the Dissertation Committee. It was submitted to the Department of Mechanical Engineering in partial fulfillment of the requirements for the degree of Doctor of Philosophy in Mechanical Engineering

Dissertation Review Committee:

Eduardo Divo

Eduardo Divo, Ph.D.
Committee Chair

Fardin Khalili

Dr. Fardin Khalili
Committee Member

Alain Kassab

Dr. Alain Kassab
Committee Member

Eric Coyle

Eric Coyle, Ph.D.
Ph.D. Program Chair,
Mechanical Engineering

Maj Dean Mirmirani

Maj Mirmirani, Ph.D.
Dean, College of Engineering

Birce Dikici

Dr. Birce Dikici
Committee Member

William M. DeCampi

Dr. William DeCampi
Committee Member

Eduardo Divo

Eduardo Divo, Ph.D.
Department Chair,
Mechanical Engineering

Lon Moeller

Lon Moeller, J.D.
Senior Vice President for Academic
Affairs and Provost

Acknowledgements

I would like to express my deepest appreciation to my advisor, **Dr. Eduardo Divo**, for his guidance, encouragement, and patience rendered throughout my years of study at the Embry-Riddle Aeronautical University (ERAU). I'm highly indebted to his advice, suggestions and support; he continually and convincingly conveyed a spirit of adventure regarding fundamental research and its application in various levels. Without his guidance and continuous support, this dissertation would not have been possible. I would also like to thank my Ph.D. committee members, **Dr. Fardin Khalili**, **Dr. Birce Dikici**, **Dr. Alain Kassab**, and **Dr. William DeCampi**, for their advice and cooperation in preparing this dissertation document. I am extending my thanks for **Dr. Ray Prather** for his never-ending helpful advice and efforts to make this dissertation more intuitive. Furthermore, I would like to express my appreciation to my friends in the lab for their limitless help and support. Last but not least, I am grateful for this opportunity to acknowledge all of my family members – especially my parents and grandparents – for their encouragement, prayers, and unwavering support.

Abstract

Researcher: Arka Das

Title: IN-VITRO INVESTIGATIONS OF ALTERNATIVE SURGICAL
TECHNIQUES FOR SINGLE VENTRICULAR DISEASE

Institution: Embry-Riddle Aeronautical University

Degree: Doctor of Philosophy in Mechanical Engineering

Year: 2021

Single ventricle (SV) anomalies account for one-fourth of all cases of congenital Heart disease. The conventional second and third stage i.e. Comprehensive stage II and Fontan procedure of the existing three-staged surgical approach serving as a palliative treatment for this anomaly, entails multiple complications and achieves a survival rate of 50%. Hence, to reduce the morbidity and mortality rate associated with the second and third stages of the existing palliative procedure, the novel alternative techniques called “Hybrid Comprehensive Stage II” (HCSII), and a “Self-powered Fontan circulation” have been proposed. The goal of this research is to conduct in-vitro investigations to validate computational and clinical findings on these proposed novel surgical techniques. The research involves the development of a benchtop study of HCSII and self-powered Fontan circulation.

Table of Contents

	Page
Thesis Review Committee	ii
Acknowledgements	iii
Abstract	iv
List of Tables	viii
List of Figures	ix
 1. Introduction.....	 21
1.1. Blood Flow.....	23
1.2. Blood Pressure	24
1.3. Frank-Starling Law	26
1.4. Single ventricular disease	26
1.4.1. Hypoplastic left heart syndrome	27
1.4.2. Three-stage palliative procedure	28
1.5. Significance of Study	30
1.6. Problem Statement – 1	30
1.7. Problem Statement -2.....	31
1.8. Limitations and Assumptions	33
1.9. Definition of terms	33
1.10. List of Acronyms	36
 2. Review of the Relevant Literature	 38
2.1.1. Stage 1: Norwood Surgical Procedure	38
2.1.2. Stage 2: Bi-direction Glenn and Comprehensive Stage II Surgical Procedure	
41	
2.1.2.1. Morbidity and Mortality	45
2.1.2.2. In-vitro and in-silico approach.....	46

2.1.3.	Stage 3: Fontan	64
2.1.3.1.	Extra cardiac and intra cardiac Fontan.....	66
2.1.3.2.	Fenestration and PVR	70
2.1.3.3.	Morbidity and Mortality	72
2.1.3.4.	In-vitro and in-silico approach.....	73
2.1.4.	Passive and Active techniques to improve Fontan	74
2.1.4.1.	Ejectors and Nozzles.....	75
2.2.	Mock Flow Loop.....	75
2.2.1.	Resistance	84
2.2.2.	Inductor	87
2.2.3.	Compliance	90
2.3.	Summary	97
3.	Methodology	99
3.1.	Anatomical model.....	99
3.1.1.	HCSII	99
3.1.1.1.	Initial Design.....	103
3.1.1.2.	Design Iteration 1.....	105
3.1.1.3.	Design Iteration 2.....	106
3.1.1.4.	Final Design	106
3.1.2.	Fontan IJS	108
3.1.2.1.	Fontan model version 1.....	110
3.1.2.2.	Fontan model version 2.....	111
3.2.	Lumped Parameter Model.....	116
3.2.1.	Lumped Parameter Model for HCSII	122
3.2.2.	Lumped Parameter for Fontan	124
3.3.	PVR.....	127
3.3.1.	Pulmonary Vascular Resistance Calibration.....	129
3.4.	PVR and entrainment quantification.....	130

3.5.	Blood Analog	133
3.5.1.	Newtonian and Non-Newtonian Fluid	133
3.6.	Oxygenation model	137
3.6.1.	Oxygenation model for HCSII	137
3.6.2.	Oxygenation model for Fontan	140
3.7.	Stent and baffle characterization.....	142
3.8.	Fatigue Analysis.....	147
3.9.	Otoscope	151
3.10.	Uncertainty.....	154
3.10.1.	Type B Estimates	154
3.11.	Statistical Analysis.....	156
3.11.1.	Hypothesis.....	156
3.11.2.	Statistical testing	156
3.11.3.	p-value.....	157
3.11.4.	Z-test	157
4.	Results.....	159
4.1.	Experimental Set-Up.....	159
4.1.1.	Experimentation of HCSII	160
4.1.1.1.	In-Situ Stent Deformation.....	170
4.1.1.2.	Particle Residence Time	171
4.1.2.	Experimentation of Fontan	173
4.1.3.	PVR and entrainment study	191
4.2.	Experimental Results	192
4.2.1.	HCSII	192
4.2.1.1.	Hemodynamic	192
4.2.1.2.	Statistical analysis (z score).....	198
4.2.1.3.	Oxygen transport.....	198
4.2.1.4.	Stented-Baffle tracking	199

4.2.1.5. Fatigue Study	201
4.2.1.6. Particle Residence Time	207
4.2.2. Fontan with IJS	209
4.2.2.1. Comparative study of IJS nozzles: 2mm, 3mm, and 4mm	209
4.2.2.2. Comparative study of angles : 5,45 and 90 degree	214
4.2.2.3. Comparative study of PVR drop by 10 and 30 percent	218
4.2.2.4. Oxygen transport.....	222
4.2.3. PVR entrainment Study	224
4.2.3.1. Hemodynamics for PVR protocol.....	224
4.2.3.2. Entrainment Quantification.....	241
4.3. Uncertainty Analysis.....	244
5. Conclusion	247
6. Recommendations and Future Work	250
7. References.....	251
Appendix A.....	288

List of Tables

Table 1 MFL parameters chosen by Rosenborg et al. [177]	78
Table 2 Compliance values for MFL	123
Table 3 Vascular compliance of sections.....	125
Table 4: Compliance values used for MFL.....	126
Table 5 Injection protocols provided by clinicians at Arnold Palmer Hospital.....	130
Table 6 Mechanical properties of Nitinol (annealed)	145
Table 7 Geometric parameters of PG 2510B stent	146
Table 8 Hemodynamic flowrate results obtained using Catheter data and MFL for patients 1 and 2	193
Table 9 Hemodynamic pressure results obtained using Catheter data and MFL for patient 1 and 2.....	193
Table 10 Displacement of stent at various sites for patient 1 and patient 2.....	201
Table 11 Conclusion summary of fatigue study on the stent for patient 1 and patient 2 data	207
Table 12 Pressure and flow measurement for baseline and various IJS diameters	210
Table 13 Pressure and flow measurement for active 3mm IJS with varying angle	215
Table 14 Pressure and flow measurements for active IJS and decreasing PVR.....	219
Table 15 Short multiple injections at 5cc/s A. Flowrate values B. Pressure values	225
Table 16 Short multiple injection at 10cc/s A. Flowrate values B. Pressure values.....	227
Table 17 Short multiple injection at 15cc/s A. Flowrate values B. Pressure values.....	229
Table 18 Short multiple injection at 20cc/s A. Flowrate values B. Pressure values.....	231
Table 19: Long single injection at 5cc/s A. Flowrate values B. Pressure values	233

Table 20 Long single injection at 10cc/s A. Flowrate values B. Pressure values.....	235
Table 21 Long single injection at 15cc/s A. Flowrate values B. Pressure values.....	237
Table 22 Long single injection at 20cc/s A. Flowrate values B. Pressure values.....	239
Table 23 Jet relaxation time [s] for various injection rates Q_{inj} and injection volumes V_{inj} for (A) continuous and (B) pulsed injections. Green values $t_{rel} > 0$ and red values $t_{rel} < 0$	242
Table 24 Jet relaxation time [s] for various injection rates Q_{inj} and injection volumes V_{inj} for (A) continuous and (B) pulsed injections . Green values $t_{rel} > 0$ and red values $t_{rel} < 0$	244
Table 25 Error parameters for Pressure sensor	244

List of Figures

Figure 1 Human Circulatory System [1].....	22
Figure 2 Wiggers Diagram for Cardiac Cycle [2]	24
Figure 3 Mean blood pressures and percent volumes in major vessels in the cardiovascular system [5]	25
Figure 4 Frank-Starling mechanism showing Left Ventricular: volume vs pressure [5] .	26
Figure 5 Anatomy of Normal heart (L) and HLHS heart (R) (The Children's Hospital of Philadelphia, n.d)	28
Figure 6. HLHS circulation before three staged procedure (L) and rectified circulation after three staged procedure (R).....	29
Figure 7 Proposed Fontan surgery with proposed injection jet shunt (IJS).....	32
Figure 8 Norwood with mBT shunt	38
Figure 9 Normal circulation (L) and stage 1 reconstructed (R) parallel pulmonary and systemic circulation. LV= left ventricle, RV= right ventricle, SC= systemic circulation, PC= pulmonary circulation, SPAS= systemic to pulmonary artery shunt.....	39
Figure 10 Bidirectional Glenn Surgical Procedure	41
Figure 11 Comprehensive Stage II procedure [25]	42
Figure 12 Hybrid Comprehensive Stage II procedure conducted by DeCampi et al. [113]	61
Figure 13 Stage 3 Fontan	64
Figure 14 MFL by Liu et al. [188]	83
Figure 15 Resistance mechanism used by Donovan et al. . [166]	85
Figure 16 Resistance segment used by Scotten et al. [176].....	87

Figure 17 Three and four element Windkessel model by Stergiopulos et al. [195]	88
Figure 18 Comparison of measured aortic pressure trace vs three and four element windkessel simulations [195].....	90
Figure 19 Effect of ventricular compliance [5].....	91
Figure 20 Compact spring compliance chamber by Woodruff et al. [200]	92
Figure 21 Spring compliance chamber by Arabia et al. . [201]	93
Figure 22 Compliance element used by Haft et al. [206]	95
Figure 23 Angiogram data of three de-identified patients provided by Arnold Palmer Children’s Hospital	100
Figure 24 Angiogram data representing the aortic root and their dimensions.....	100
Figure 25 Development of 3D CAD model of HCSII centerpiece from angiogram A. Diameter of RCA, RSA, LCA and LSA B. Diameter of MPA root C. 3D CAD model on CATIAv.5 D. Diameters of the aortic arch and descending aorta E. Diameter of ascending aorta F. Diameter of MPA	102
Figure 26 3D CAD printed with the conduits	102
Figure 27 Design 1 of the top half of the centerpiece A. Ascending aorta is stenosed B. HCS II centerpiece within the rectangular block C. Interior view of the centerpiece with rails D. Side view of the top half	104
Figure 28 Design 1 of the bottom half of the centerpiece A. Bottom half of centerpiece with stent stopper and slots for laser C. Slots to place the camera	104
Figure 29 Design iteration 1 for top and bottom half of the centerpiece A. Changes made to the machined part with a slot for otoscope B. View of the centerpiece. C. Clamp designed to hold the baffle D. Interior view of the top half of the centerpiece	105

Figure 30 Design iteration 2 for top and bottom half of the centerpiece A. Interior view of the top half and B. Front view of the top half C. Back view with the square slot	106
Figure 31 Final design of centerpiece A. Gasket B. Front view of <i>the</i> top half of centerpiece C. Interior view of top half D. Side view of the backplate E. Stent	107
Figure 32 3D printed and machined centerpiece A. HSCII centerpiece B. The top half of centerpiece with baffle C. Bottom half of centerpiece with stent and gasket D. machined backplate	108
Figure 33 2D drawing of 2mm, 3mm, and 4mm IJS (L), 3D printed IJS prototype	110
Figure 34 2mm IJS shunt A. elliptical profile B. Side view of the IJS shunt C. Diamond profile D. Circular profile	111
Figure 35 A Side view representing lip section and IJS dimension B. TCPC front view C. Interior view of the bottom block with two circular profiles of the IJS nozzle	113
Figure 36 A. Side view of the TCPC B. TCPC front view with the length of the conduits C. Interior view of the bottom block with two elliptical profiles of the IJS nozzle.....	114
Figure 37 A. Interior view of the bottom block with one circular profile of the IJS nozzle B. Front view TCPC with the diameter of conduits.....	114
Figure 38 A Side view of TCPC with IJS at fenestration site B. Front view of TCPC with adapters C. Interior view of the bottom block with one elliptical profile of the IJS nozzle	115
Figure 39 Lumped Arterial and Venous bed coupled for LPM development	117
Figure 40: Needle valve to replicate vascular resistnace in MFL.....	118
Figure 41 Design of annular compliance chamber replicating the vascular compliances.	120

Figure 42 LPM representation of HCSII	122
Figure 43 LPM representation of Fontan.....	124
Figure 44 Correlation for percent PVR change too percent pulmonary flow change	128
Figure 45 A. Resistance calibration loop and B calibration curves for pulmonary resistances for 3 flow rates (1.45 L/min, 1.75 L/min and 2 L/min).	129
Figure 46 Fontan region of interest flow rate Q^* sampling schematic.....	132
Figure 47 Viscometer used during the study	135
Figure 48 Viscosity vs shear rate for non-Newtonian blood model	136
Figure 49 viscosity of non-Newtonian fluid vs theoretical value	137
Figure 50 Oxygenation model for HCSII	138
Figure 51 Oxygenation model for Fontan.....	141
Figure 52 Palmaz Genesis (PG) 2510B stent characteristic features obtained under SEM	144
Figure 53 Palmaz Genesis (PG) 2510B stent characteristic features obtained under SEM	145
Figure 54 Gore Preclude Pericardial Membrane	146
Figure 55 Relation between cyclic stress intensity and crack growth rate	150
Figure 56 A. Otoscope angle and dittance B. Slot for otoscope C. Side view of Otoscope and stent D. The Firefly Digital Video Otoscope	154
Figure 57 Compliance chambers used for HCSII.....	161
Figure 58 Flowmeters to capture the flow at upper, lower, LPA and RPA	162
Figure 59 Upper, Lower, MPA, Asc. aorta and RPA Resistors.....	162
Figure 60 Pressure sensors placed on the MFL	163

Figure 61 Pressure sensors and resistors connected to the 3D printed Phantom	164
Figure 62 Direction of flow on the HCSII based MFL.....	165
Figure 63 Magnitude and Phase response of A. Patient 1 B. Patient 2.....	166
Figure 64 Pole-Zero Plot A. Patient 1 B. Patient 2	166
Figure 65 flowrate FFT of Patient 1	167
Figure 66 flowrate FFT of Patient 2	168
Figure 67 Pressure FFT of Patient 1	168
Figure 68 Pressure FFT of Patient 2	169
Figure 69 Orginal and filtered Pressure waveforms of Patient 2.....	170
Figure 70 Stent and baffle tracking.....	171
Figure 71 PRT: original	172
Figure 72 Particle tracking study using Kalman tracker during systole and diastole a. in-situ particle tracking in the MPA b. Trained Kalman tracker c. In-situ tracked particles in the MPA conduit using trained Kalman tracker	173
Figure 73 Mock Flow Loop set up for Fontan circulation with IJS in PAs.....	174
Figure 74 Mock Flow Loop set up with DAQ and compliance chambers	175
Figure 75 Magnitude and phase response of flowrate at A. Upper B. Lower C. Left D. Right for 3 mm IJS.....	175
Figure 76 Pole-zero plot of flowrate at A. Upper B. Lower C. Left D. Right for 3 mm IJS	176
Figure 77 Magnitude and phase response of flowrate at A. Upper B. Lower C. Left D. Right for 3 mm IJS at 5 degree	177

Figure 78 Pole-zero plot of flowrate at A. Upper B. Lower C. Left D. Right for 3 mm IJS at 5 degree	177
Figure 79 Magnitude and phase response of flowrate at A. Upper B. Lower C. Left D. PVR 30.....	178
Figure 80 Pole-zero plot of flowrate at A. Upper B. Lower C. Left D. Right for PVR 30	178
Figure 81 A. Magnitude and phase response B. Pole-Zero plot of IVC pressure for 3mm IJS	179
Figure 82 A. Magnitude and phase response B. Pole-Zero plot of IVC pressure for 3mm IJS at 5 degree	179
Figure 83 A. Magnitude and phase response B. Pole-Zero plot of IVC pressure for PVR 30.....	180
Figure 84 flowrate FFT 3mm IJS.....	180
Figure 85 flowrate FFT of 3mm IJS at 5 degree.....	181
Figure 86 flowrate FFT PVR30	181
Figure 87 Unfiltered flowrate for 3mm IJS	182
Figure 88 Unfiltered flowrate for 3mm IJS at 5 degree.....	182
Figure 89 Unfiltered flowrate for PVR30.....	183
Figure 90 Filtered and Unfiltered flowrate for 3mm IJS	184
Figure 91 Filtered and unfiltered flowrate for 3mm IJS at 5 degree	184
Figure 92 Filtered and unfiltered flowrate for PVR30.....	185
Figure 93 Pressure FFT 3mm IJS	186
Figure 94 Pressure FFT of 3mm IJS at 5 degree	186

Figure 95 Pressure FFT PVR30.....	187
Figure 96 Unfiltered Pressure for 3mm IJS	188
Figure 97 Unfiltered Pressure for 3mm IJS at 5 degree.....	188
Figure 98 Unfiltered Pressure for PVR30.....	189
Figure 99 Filtered and unfiltered pressure for 3mm IJS	189
Figure 100 Filtered and unfiltered pressure for 3mm IJS at 5 degree	190
Figure 101 Filtered and unfiltered pressure for PVR30.....	190
Figure 102 MFL setup for PVR study	191
Figure 103 Pressure plots obtained from catheter data for patient 1	194
Figure 104 Pressure plots obtained from catheter data for patient 1	195
Figure 105 Pressure plots obtained from catheter data for patient 2	195
Figure 106 Filtered flowrate of patient 1	196
Figure 107 Filtered flowrate of patient 2	196
Figure 108 Filtered pressure of patient 1	197
Figure 109 Filtered pressure of patient 2	197
Figure 110 Systemic Oxygen saturation level between patient 1 and patient 2	199
Figure 111 Stent and baffle tracking.....	200
Figure 112 Critical locations for crack propagation	204
Figure 113	208
Figure 114 PRT Result plots.....	209
Figure 115 IJS proximal anastomosis angle.	210
Figure 116 Filtered flowrate 2mm IJS	211
Figure 117 Filtered flowrate 3mm IJS	212

Figure 118 Filtered flowrate 4mm IJS	212
Figure 119 Filtered pressure 2mm IJS	213
Figure 120 Filtered pressure 3mm IJS	213
Figure 121 Filtered pressure 4mm IJS	214
Figure 122 Filtered flowrate of 3mm IJS at 5 degree	216
Figure 123 Filtered flowrate of 3mm IJS at 45 degree	216
Figure 124 Filtered flowrate of 3mm IJS at 90 degree	217
Figure 125 Filtered pressure of 3mm IJS at 5 degree	217
Figure 126 Filtered pressure of 3mm IJS at 45 degree	218
Figure 127 Filtered pressure of 3mm IJS at 90 degree	218
Figure 128 Filtered flowrate PVR10.....	220
Figure 129 Filtered flowrate PVR30.....	221
Figure 130 Filtered Pressure PVR10	221
Figure 131 Filtered Pressure PVR30	222
Figure 132 - Systemic arterial (A) and venous (B) oxygen saturations for various pulmonary venous saturations (SpvO ₂) in all the models explored.	224
Figure 133 Filtered flowrate for 5cc/s with 20cc volume for one shot.....	226
Figure 134 Filtered pressure for 5cc/s with 20cc volume for one shot.....	227
Figure 135 Filtered flowrate for 10cc/s with 20cc volume for one shot.....	228
Figure 136 Filtered pressure for 10cc/s with 20cc volume for one shot.....	229
Figure 137 Filtered flowrate for 15cc/s with 20cc volume for one shot.....	230
Figure 138 Filtered pressure for 15cc/s with 20cc volume for one shot.....	231
Figure 139 Filtered flowrate for 20cc/s with 20cc volume for one shot.....	232

Figure 140 Filtered pressure for 20cc/s with 20cc volume for one shot.....	233
Figure 141 Filtered flow rate for 5cc/s with 100cc volume for one long shot.....	234
Figure 142 Filtered pressure for 5cc/s with 100cc volume for one long shot.....	235
Figure 143 Filtered flow rate for 10cc/s with 100cc volume for one long shot.....	236
Figure 144 Filtered pressure for 10cc/s with 100cc volume for one long shot.....	237
Figure 145 Filtered flow rate for 15cc/s with 100cc volume for one long shot.....	238
Figure 146 Filtered pressure for 15cc/s with 100cc volume for one long shot.....	239
Figure 147 Filtered flowrate for 20cc/s with 100cc volume for one long shot.....	240
Figure 148 Filtered pressure for 20cc/s with 100cc volume for one long shot.....	241
Figure 149 IVC mean pressure value with the error band	246
Figure 150 DAQ instrumentation schematic	288
Figure 151 Filtered and unfiltered flowrate (U) and pressure (L) for IJS with 2mm diameter.....	289
Figure 152 Filtered and unfiltered flowrate (U) and pressure (L) for IJS with 4mm diameter.....	290
Figure 153 Filtered and unfiltered flowrate (U) and pressure (L) for 3mm IJS at 45 degree	291
Figure 154 Filtered and unfiltered flowrate (U) and pressure (L) for 3mm IJS at 90 degree	292
Figure 155 Filtered and unfiltered flowrate (U) and pressure (L) for PVR10.....	293
Figure 156 Filtered flowrate (U) and pressure (L) for 5cc/s with 15cc volume for one short shot.....	294

Figure 157 Filtered flowrate (U) and pressure (L) for 5cc/s with 10cc volume for one short shot.....	295
Figure 158 Filtered flowrate (U) and pressure (L) for 5cc/s with 5cc volume for one short shot.....	296
Figure 159 Filtered flowrate (U) and pressure (L) for 10cc/s with 15cc volume for one short shot.....	297
Figure 160 Filtered flowrate (U) and pressure (L) for 10cc/s with 10cc volume for one short shot.....	298
Figure 161 Filtered flowrate (U) and pressure (L) for 10cc/s with 5cc volume for one short shot.....	299
Figure 162 Filtered flowrate (U) and pressure (L) for 15cc/s with 15cc volume for one short shot.....	300
Figure 163 Filtered flowrate (U) and pressure (L) for 15cc/s with 10cc volume for one short shot.....	301
Figure 164 Filtered flowrate (U) and pressure (L) for 15cc/s with 5cc volume for one short shot.....	302
Figure 165 Filtered flowrate (U) and pressure (L) for 20cc/s with 15cc volume for one short shot.....	303
Figure 166 Filtered flowrate (U) and pressure (L) for 20cc/s with 10cc volume for one short shot.....	304
Figure 167 Filtered flowrate (U) and pressure (L) for 20cc/s with 5cc volume for one short shot.....	305

Figure 168 Filtered flowrate (U) and pressure (L) for 5cc/s with 50cc volume for one long shot.....	306
Figure 169 Filtered flowrate (U) and pressure (L) for 5cc/s with 150cc volume for one long shot.....	307
Figure 170 Filtered flowrate (U) and pressure (L) for 10cc/s with 50cc volume for one long shot.....	308
Figure 171 Filtered flowrate (U) and pressure (L) for 10cc/s with 150cc volume for one long shot.....	309
Figure 172 Filtered flowrate (U) and pressure (L) for 15cc/s with 50cc volume for one long shot.....	310
Figure 173 Filtered flowrate (U) and pressure (L) for 15cc/s with 150cc volume for one long shot.....	311
Figure 174 Filtered flowrate (U) and pressure (L) for 20cc/s with 50cc volume for one long shot.....	312
Figure 175 Filtered flowrate (U) and pressure (L) for 20cc/s with 150cc volume for one long shot.....	313

1. Introduction

In human anatomy, the cardiovascular system comprises the heart and the system of vessels that include the arteries, veins, and capillaries. The heart plays a vital role in the circulatory system. The heart's main function is to pump the continuous flow of blood throughout the body's circulatory system. The circulatory system consists of systemic and pulmonary circulations. In the systemic circulation, the heart pumps oxygenated blood to the body through arteries, and the deoxygenated blood gets transported back to the heart through veins. In the pulmonary circulation, blood is transported between the heart and lungs to exchange carbon dioxide with oxygen during the respiration process. The heart comprises four chambers. The two lower chambers are ventricles, and the two upper chambers are atria. Two ventricles (left and right) are separated by a wall called the interventricular septum. Two atria (left and right) are separated by a wall called the interatrial septum. The deoxygenated blood from the systemic circulation returns to the heart's right atrium through two large veins. The blood from the lower systemic circulation returns through the inferior vena cava (IVC), and the upper systemic circulation returns through the superior vena cava (SVC). The deoxygenated blood from the myocardium returns to the right atrium through the coronary sinus.

The deoxygenated blood flows through the tricuspid valve from the atrium to the ventricle during atrial contraction in the right heart. When the right ventricle contracts, the tricuspid valve closes, and the blood flows through the pulmonary valve into the pulmonary trunk. The pulmonary trunk is bifurcated into left and right pulmonary arteries to flow the blood to the right and left lung through the arterioles and into the capillaries present in the lungs.

The oxygenated blood returns from the lungs to the left atrium through pulmonary veins in the left heart. Then the blood is pumped from the left atrium to the left ventricle through the mitral valve and finally into the aorta through the aortic valve for systemic circulation.

Figure 1 depicts the human circulatory system.

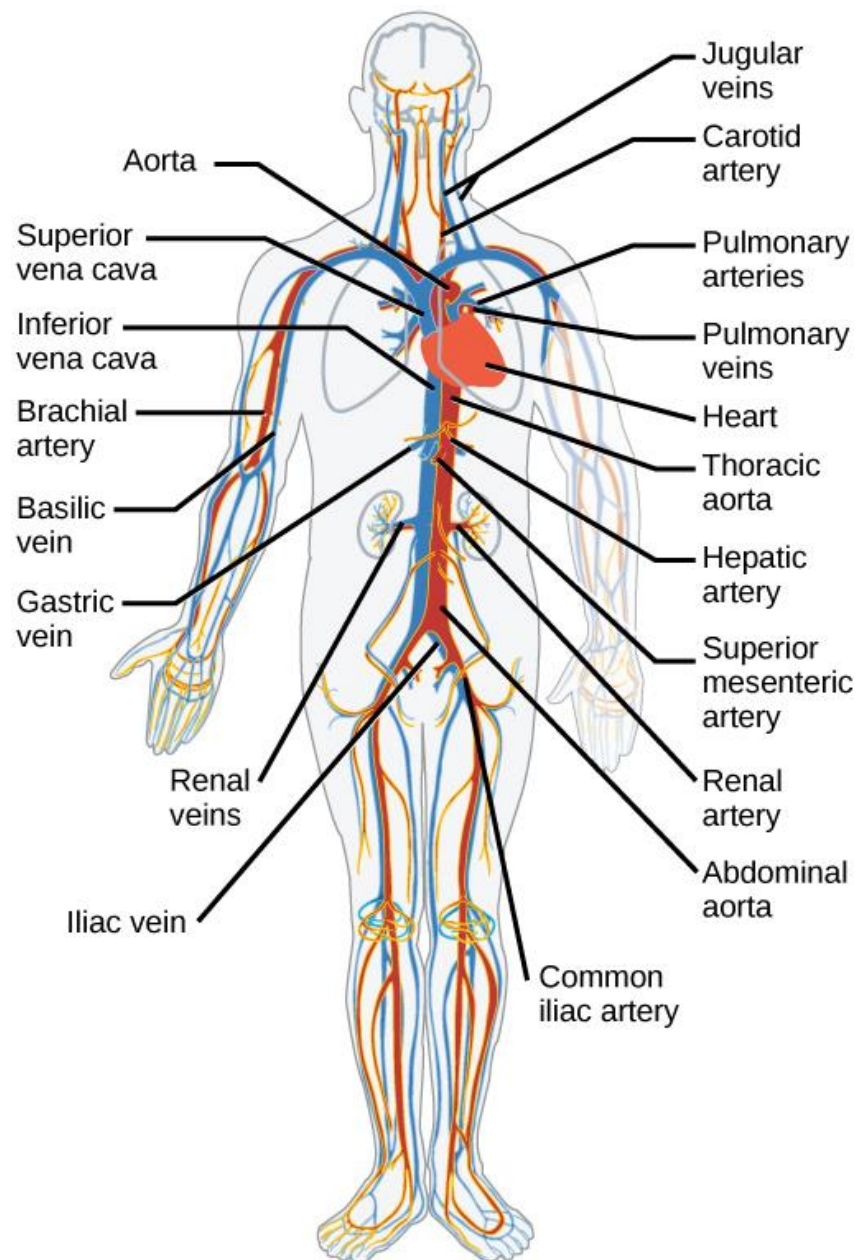


Figure 1 Human Circulatory System [1]

The human heart functions in a cardiac cycle. The cardiac cycle consists of four major stages :

1. Isovolumic relaxation
2. Inflow,
3. Isovolumic contraction
4. Ejection

The Wiggers diagram shows these four significant stages during a cardiac cycle [2], as shown in Figure 2. Stages of “Isovolumic relaxation” and “Inflow” comprise the atrial “Systole” and the ventricular "Diastole" period. In this period, blood returns into the relaxed ventricle of the heart by flowing through the atria. Notably, towards the end of the "Diastole," the atria contract and pump blood into the ventricles. This pressurized blood flow from atria to ventricles during the ventricular diastole period is called the atrial systole (“atrial kick”). Stages of “Isovolumic contraction” and “Ejection” comprise the ventricular “Systole” period. In this period, simultaneous pumping of both ventricles occurs to push blood to the pulmonary trunk and aorta.

1.1. Blood Flow

In the circulatory system, the blood flow is primarily considered as laminar in major conduits and turbulent in specific regions. Typically, a healthy adult's average cardiac output (CO) is around 5-6 L/min at a resting condition [3]. In a vessel, the blood flow is related to the difference in pressure and the resistance (R) in that vessel. Blood flow occurs from higher pressure (P1) to lower pressure (P2). This is represented in Equation (1)

$$Q = \frac{P_1 - P_2}{R} \quad (1)$$

CO is defined as the amount of blood pumped out by the left ventricle per minute. This is a product of heart rate and stroke volume.

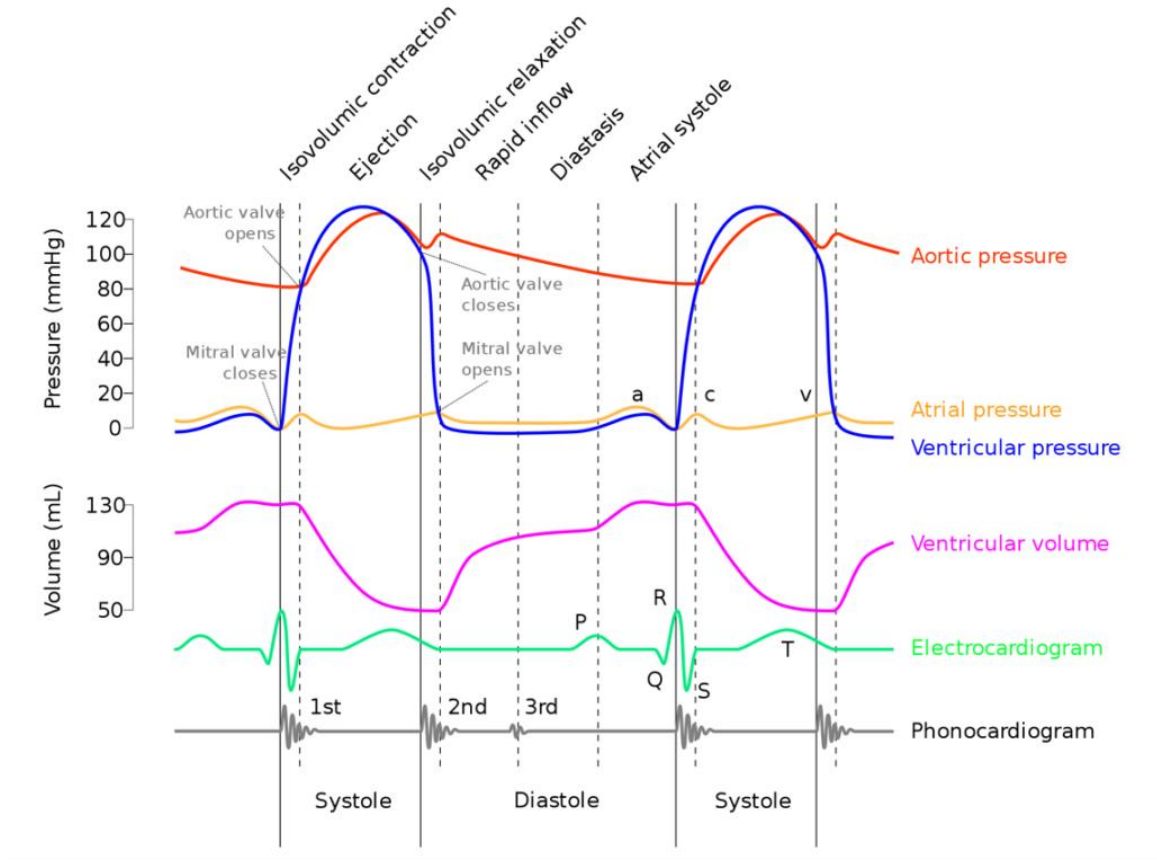


Figure 2 Wiggers Diagram for Cardiac Cycle [2]

1.2 Blood Pressure

Blood pressure is an essential hemodynamic parameter in the cardiovascular system. Typically for normal physiology, the peak systolic and diastolic aortic pressures are 120 *mmHg* and 80 *mmHg* [4]. The difference between systolic and diastolic is known as

“pulse pressure”. The compliance level and stroke volume dictate the pulse pressure. The pulse pressure increases based on the increase in the stroke volume and decrease in vascular compliance. The pressure decreases if the stroke volume decreases and vascular compliance increases.

Mean Arterial Pressure (MAP) is defined as the average aortic pressure over one cardiac cycle. This pressure is lower than the average systolic (30% of the cardiac cycle) and diastolic (70% of the cardiac cycle) pressures. MAP can be computed by multiplying the CO and systemic vascular resistance and summing with central venous pressure. Figure 3 shows the mean pressure and the percentage of total CO present in major vessels of the cardiovascular system.

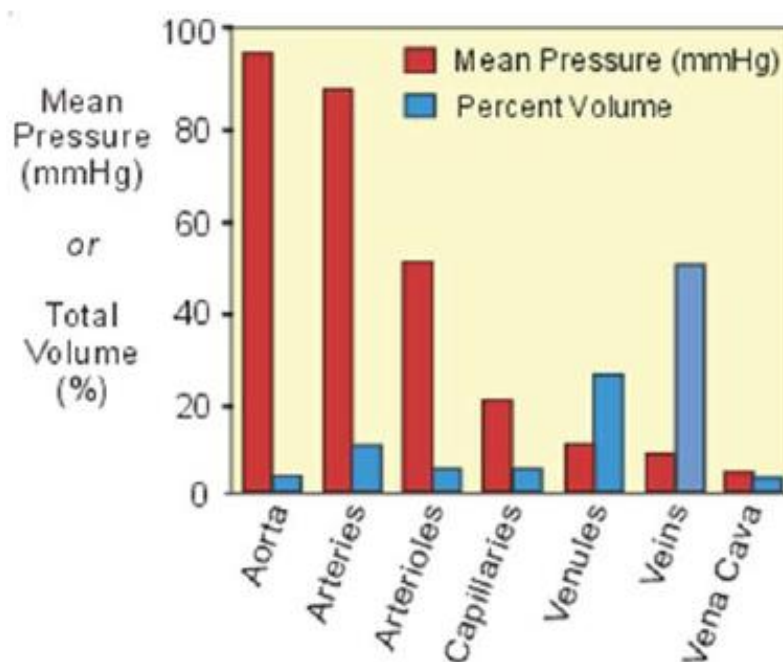


Figure 3 Mean blood pressures and percent volumes in major vessels [5]

1.3. Frank-Starling Law

This law states that the heart has an intrinsic capability of increasing its contraction force and the corresponding stroke volume due to an increase in the end-diastolic volume (EDV) [5]. Deconstructing the law, the heart works harder to increase CO to synchronize with the venous return. To satisfy the law of conservation of mass in the circulatory system, what goes into each ventricle must come out. Due to this mechanism, as a larger blood volume flows into the ventricle, the cardiac muscle gets stretched and increases in contraction force. Figure 4 shows that the EDV increases as more blood is pumped into the ventricle. This increases the force of contraction and increases stroke volume to maintain a constant end-systolic volume (ESV).

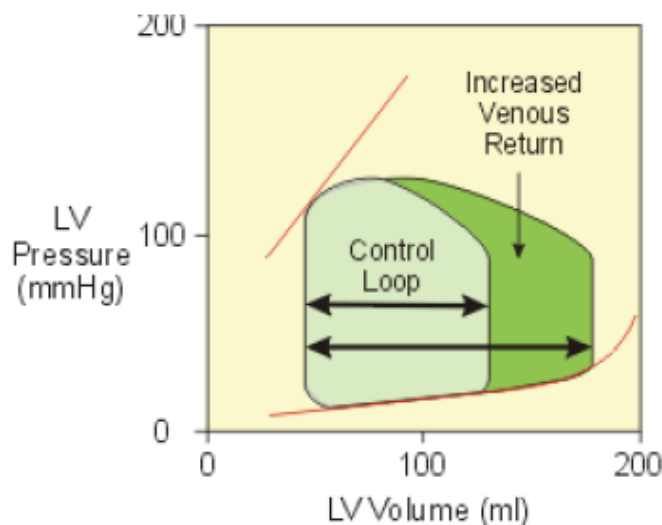


Figure 4 Frank-Starling mechanism [5]

1.4. Single ventricular disease

Congenital Heart Diseases or defects (CHD) are the problems with the heart's structure that are present at birth. There are various types of CHD [6]. Single ventricle (SV) anomalies account for one-fourth of all cases of CHD. Generally, the most complex form of CHDs

falls under the category of SV anomalies. Untreated, the anomaly is uniformly fatal. Despite surgical and pharmaceutical advances for the treatment of SV anomaly, this anomaly remains the significant cause of morbidity and mortality in the pediatric CHD population.

A single ventricle is a defect in the heart where one ventricle of the heart is malformed. As a result, the heart has one pumping chamber. This causes the oxygenated blood to mix with the deoxygenated blood, thereby reducing the amount of oxygenated blood getting to the systemic circulation. As a result of this abnormal circulation, various symptoms like cyanosis (blue or purple tint to the skin), difficulty in breathing and feeding, and lethargy can be seen in this subset of patients.

Single ventricle defects are classified into

- Hypoplastic left heart syndrome (HLHS)
- Pulmonary atresia
- Tricuspid Atresia
- Univentricular heart

1.4.1. Hypoplastic left heart syndrome

Hypoplastic left heart syndrome (HLHS) is a congenital heart condition where the left ventricle, mitral and aortic valves, and aorta are underdeveloped and unable to function. Lev initially coined this in 1952 as hypoplasia of the aortic tract complex [7]. Figure 5 shows the comparison between normal heart anatomy and HLHS heart anatomy. In HLHS, the remaining ventricle becomes the pump for both the pulmonary and systemic circulation.

Two options exist to treat HLHS: a series of staged palliations using a single ventricle strategy [8], [9] or primary cardiac transplantation. The transplantation procedure is limited due to the availability of infant organs, the limited lifespan of the organ, and the need for continued anti-rejection therapy. The surgical technique depends on the patient's physiological condition and the institution's surgical planning. The mortality rate remains high even after treatment. A three-stage palliative procedure was developed to improve the survival rate.

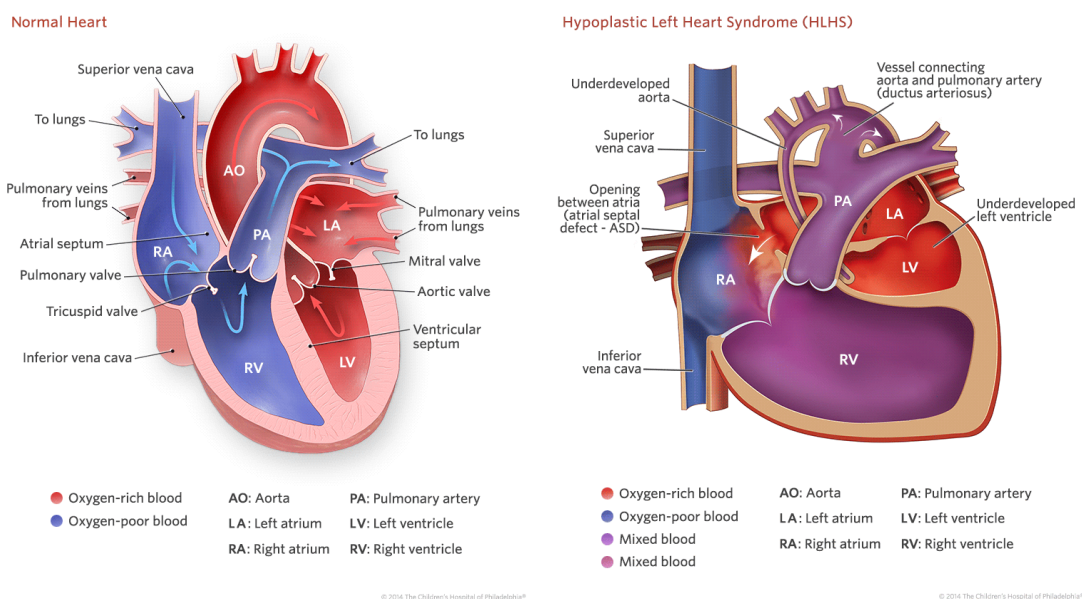


Figure 5 Anatomy of Normal heart (L) and HLHS heart (R) (The Children's Hospital of Philadelphia, n.d)

1.4.2. Three-stage palliative procedure

In the last few decades, different strategies were implemented to treat HLHS. The three-staged palliative procedure was developed to convert the parallel circulation to series circulation with one ventricle and bypass the underdeveloped chamber. Deoxygenated venous blood is not mixed with the oxygenated blood, as shown in Figure 6.

- Stage 1: Norwood Procedure

In this stage, atrial septectomy is performed. Then hypoplastic aorta is reconstructed and connected to the right ventricle in place of the pulmonary root. A Blalock Taussig (BT) shunt is implanted between the innominate artery and the pulmonary arteries to create a parallel path between the systemic circulation and the pulmonary circulation. The Norwood procedure is performed very shortly after birth [10], [11].

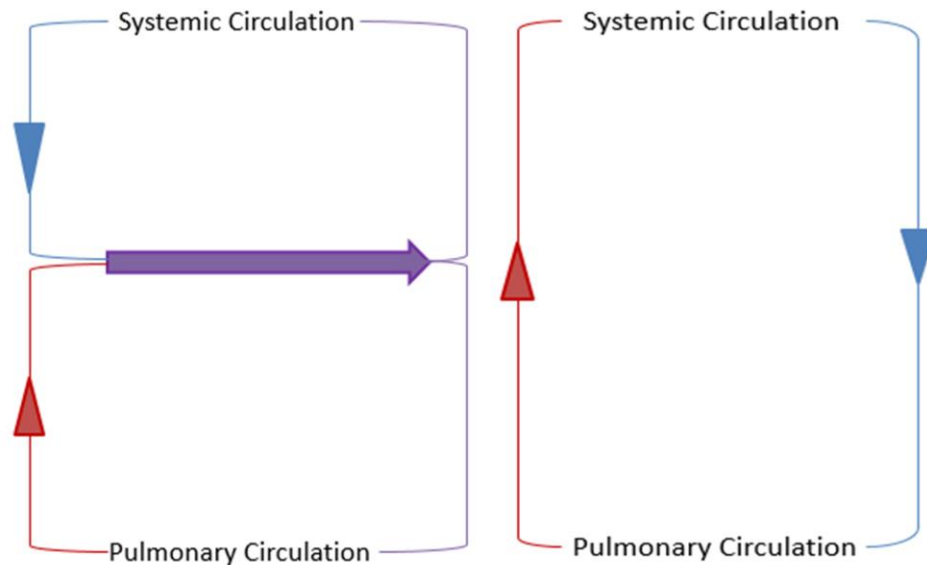


Figure 6. HLHS circulation before three staged procedure (L) and rectified circulation after three staged procedure (R)

- Stage 2: Glenn Procedure

In this stage, SVC is disconnected from the right atrium and connected directly to the right pulmonary artery, and the BT shunt is disconnected. The primary purpose of this surgery is to send the deoxygenated blood flow from the upper systemic circulation to the pulmonary circulation. The Glenn procedure is performed between three and six months after the first stage [12].

- Stage 3: Fontan Procedure

IVC is disconnected from the right atrium in this stage and connected directly to the pulmonary arteries for a Total Cavopulmonary Connection (TCPC). This surgery results in total passive drainage of the caval blood flow to the pulmonary circulation, relieving the single ventricle from pumping blood to the pulmonary circulation. The atrial septal defect is closed. The Fontan procedure is performed around six months to a year after the second stage.

1.5. Significance of Study

Though the three-staged palliative procedure is established as the most viable option to treat this HLHS anomaly but this three-staged procedure is still flawed. The research topic is at the interface of the engineering and pediatric congenital heart disease domain. It combines in-vitro modeling techniques to analyze the hemodynamics of two novel alternative palliative procedures for single ventricular disease.

This study will elucidate the various in-vitro modeling techniques used to investigate the hemodynamics and efficacy of the following alternative surgical techniques:

- In-vitro validation of Hybrid Comprehensive stage II (HCSII) circulation
- In-vitro validation of self-powered Fontan circulation

The outcome of these studies can significantly contribute to the positive outcome of patient care and provide additional insight into the hemodynamics of these palliative procedures.

1.6. Problem Statement – 1

The existing three staged palliative procedure for the single ventricular anomaly entails multiple complications and achieves a survival rate of 50%. To reduce the trauma associated with the second stage of the existing procedure, a novel alternative surgical procedure, i.e., hybrid comprehensive stage 2 (HCSII), has been developed by the clinical

collaborators in Arnold Palmer children's hospital. This palliative procedure can be an alternative for a select subset of SV patients with the adequate antegrade aortic flow. The procedure reduces surgical trauma in patients by introducing a stented intrapulmonary baffle to avoid dissection of the pulmonary arteries and reconstruction of the aortic arch while obviating the dissection of the distal arch and ductal continuation.

The goal of this study is to validate in-silico results relative to stented baffle deformation and particle tracking. This in-vitro model is tuned to match the catheter data and then used to verify whether pulmonary arteries are obstructed due to systemic pressure loads and track particles to identify the potential pathological flow fields and the possibility of thrombus formation.

1.7. Problem Statement -2

Although the Fontan circulation has been successfully established as the final stage in the palliative procedure for treating HLHS but can lead to failures. The major reason for failures comprise

- High pressure in IVC
- High Pulmonary vascular resistance (PVR)
- Ventricular dysfunction

These reasons can lead to a multitude of diseases. Many techniques to improve the failing Fontan circulation have been proposed over decades. These techniques involve improving geometrical parameters of total cavopulmonary connection (TCPC) and active powering of Fontan circulation. But most of the proposed ideas involved issues. These issues include pulmonary embolism, driveline infections, and various types of pathological flow conditions.

A novel, innovative, rapidly testable alternative is proposed to achieve the same endpoints as a synthetic pump in the Fontan circulation. Through this procedure, the reserve mechanical energy of the heart itself is tapped to “assist” the Fontan circulation by creating a novel bifurcation graft, henceforth called the Injection Jet Shunt (IJS), seen in Figure 7. A new, technically straightforward surgical operation is proposed in which this graft, originating from either the ventricle or aorta, bifurcates with each tapered distal limb sutured into the pulmonary arteries (PA) in such a way that flow is directed parallel to each PA and the energy and momentum of this flow is efficiently transferred. The hypothesis is as follows: The inclusion of an IJS of suitable geometry into the “failing Fontan” circulation can (1) decrease IVC pressure and (2) increase systemic oxygen delivery while limiting the obligatory left-to-right shunt through the graft to a clinically acceptable value. The approach challenges the existing paradigm that a synthetic pump is required to assist the Fontan circulation. It addresses the critical barriers to progress in this field by offering an alternative, effective palliation for the failing Fontan while delaying or circumventing the need for heart transplantation and implantation of synthetic pumps with their well-known complications.

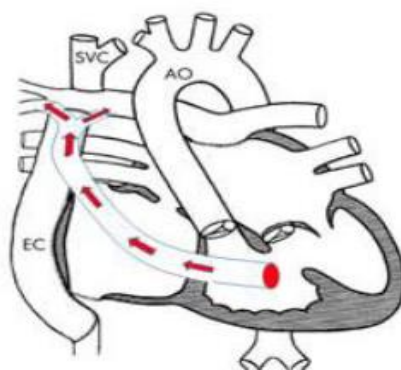


Figure 7 Proposed Fontan surgery with proposed injection jet shunt (IJS)

This study aims to validate the Computational Fluid Dynamics (CFD) results and characterize the jet flow field in the Fontan circulation. Increased inferior vena cava pressure has been identified as a clinically significant parameter for Fontan failure. The in-vitro model helps to elucidate the relevant hemodynamics that can lead to optimal implementation of an injection jet to reduce the pressure in the inferior cava.

1.8. Limitations and Assumptions

In-vitro efforts have seen the implementation of lumped parameter models of the peripheral circulation as well as the region of interest. To simplify the modeling, the lumped parameter has been reduced to four compartments, i.e., upper and lower systemic circulations and left and right pulmonary circulations. In the lumped parameter model, the inertance effect is not replicated. Moreover, the region of interest in Mock Flow Loop (MFL) has been assumed to be rigid. The blood model used in MFL studies is assumed to be Newtonian.

1.9. Definition of terms

A	Area of the conduit
\bar{V}	Average velocity of the fluid
C	Compliance
$\pm L$	Containment limit
p	Containment probability
a_c	Critical crack growth
ΔK	Cyclic stress intensity factor
ρ	Density of blood

t_{fall}	Fall time
\dot{Q}_{ent}	Flow entrainment rate
Q	Flowrate
g	Gravitational constant
Δh	Head loss in fluid
σ_{hoop}	Hoop stress
L_i	Inertance
μ_{∞}	Infinite-shear viscosity
a_i	Initial crack growth
Q_{IJS}	Injection jet shunt flow
ϕ^{-1}	Inverse normal distribution
t_{rel}	Jet relaxation time
L	Length of the conduit/Inductance
K	Loss coefficient
Q_{IVC}	Lower body blood flowrate
C_{lower}	Lower compliance
μ	Mean
N	Number of cycles to failure
P	Pressure
ΔP	Pressure drop in fluid

σ_1	Principal stress
Q_p	Pulmonary flow
r	radius of conduit
$\frac{da}{dN}$	Rate of crack growth
λ	Relaxation time constant
R	Resistance
t_{rise}	Rise time
γ	Shear rate
σ	Standard deviation
ε_x	Strain in x-direction
ε_y	Strain in y-direction
σ_x	Stress in x-direction
σ_y	Stress in y-direction
Q_s	Systemic flow
Ca_{o_2}	Systemic oxygen concentration
$C_{SVC O_2}$	Systemic venous concentration
Q_{SVC}	Upper body flowrate
η	Viscosity
σ_v	Von-mises stress
σ_{yp}	Yield stress

E	Young's modulus
μ_0	Zero-shear viscosity

1.10. List of Acronyms

ABS	Acrylonitrile butadiene styrene
ABG	Assisted bi-directional Glenn
APC	Atriopulmonary connection
BDG	Bidirectional Glenn
BSA	Body surface area
CO	Cardiac output
CPB	Cardiopulmonary bypass
CVP	Central venous pressure
CFD	Computational Fluid Dynamics
CAD	Computer Aided Design
CHD	Congenital Heart Diseases
DHCA	Deep hypothermic circulatory arrest
EDV	End-diastolic volume
ESV	End-systolic volume
HCSII	Hybrid comprehensive stage II
ICPC	Inferior cavopulmonary connection
IVC	Inferior vena cava
IJS	Injection jet shunt
LCA	Left carotid artery
LPA	Left pulmonary artery

LSA	Left subclavian artery
LPM	Lumped parameter model
MRI	Magnetic resonance imaging
MPA	Main pulmonary pressure
MAP	Mean arterial pressure
MFL	Mock flow loop
PRT	Particle residence time
PTFE	Polytetrafluoroethylene
PA	Pulmonary arteries
PVR	Pulmonary vascular resistance
RCA	Right carotid artery
RPA	Right pulmonary artery
RSA	Right subclavian artery
RV	Right ventricle
SV	Single ventricle
SVC	Superior vena cava
SVR	Systemic vascular resistance
TCPC	Total cavopulmonary connection
VVC	Veno-venous collateral vessel
VAD	Ventricular assist device
WSS	Wall shear stress

2. Review of the Relevant Literature

2.1.1. Stage 1: Norwood Surgical Procedure

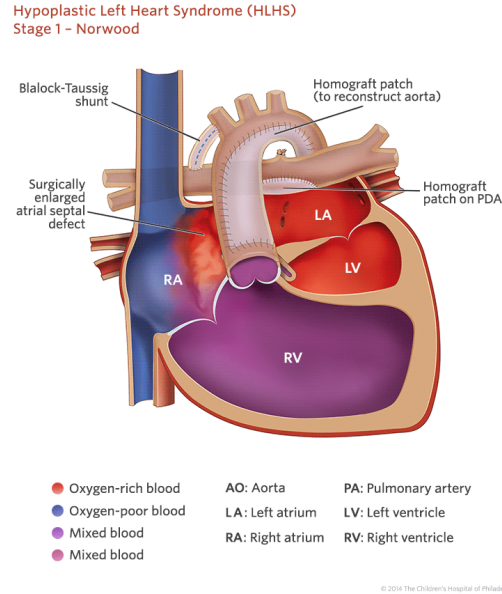


Figure 8 Norwood with mBT shunt

Figure 8 represents the stage I Norwood surgery. The primary aim of this surgical procedure is to provide an unrestrictive systemic blood flow while balancing the pulmonary flow, i.e., the Q_p / Q_s ratio. To achieve this physiology, a neo-aorta is constructed using the autologous aorta and pulmonary artery, followed by placing a shunt in the pulmonary artery. Depending on the patient's condition, an alternative procedure is to band the pulmonary artery and stent the descending aorta. The mixing of oxygenated and deoxygenated blood occurs due to the doubling of volumetric load on the single ventricle. The diameter of the shunt is designed to provide a balanced pulmonary flow with the systemic flow. Figure 9 highlights the outcome of creating parallel pulmonary and systemic circulation. Pulmonary Vascular Resistance (PVR) and Systemic Vascular Resistance (SVR) must be controlled for a balanced circulation with adequate systemic oxygen. The

relative resistance from the PVR and SVR determines the distribution of blood to the systemic and pulmonary as the single ventricle supplies the blood.

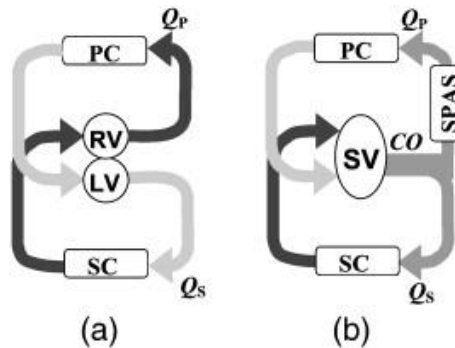


Figure 9 Normal circulation (L) and stage 1 reconstructed (R) parallel pulmonary and systemic circulation. LV= left ventricle, RV= right ventricle, SC= systemic circulation, PC= pulmonary circulation, SPAS= systemic to pulmonary artery shunt

In 1945 Blalock and Taussig [13] [13] developed a shunt to treat tetralogy of Fallot. The original procedure proposed was to connect the cut end of the subclavian artery or carotid artery to the pulmonary artery. The main disadvantage of BT shunt includes phrenic nerve injury and operative dissection time. In addition, some of the blood supply to the upper body is interrupted due to the occluded artery [14].[14]. To overcome the disadvantage of BT shunt, a modified BT shunt (mBT shunt) was developed, which involves the introduction of polytetrafluoroethylene (PTFE) as a biomaterial. The mBT shunt is placed in between the pulmonary artery and subclavian or carotid artery. Diastolic runoff and high pulse pressure are characteristics of mBT shunt physiology. As a result, diastolic coronary circulation is reduced, thereby giving rise to myocardial ischemia and circulatory instability, leading to the patient's death [15][15].

In 1961 central shunt or Waterson shunt (WS) was reported to treat the tetralogy of Fallot. A conduit is installed between the pulmonary artery and ascending aorta, giving a balanced flow between two pulmonary arteries. The Waterson shunt is considered as an alternative

for neonates having a small subclavian artery. The Sano shunt or right ventricle shunt is a variation where a conduit is inserted between the pulmonary artery and the right ventricle [16]. As the Sano shunt is larger in diameter, less diastolic pressure runoff is possible due to a more pulsatile pulmonary blood flow and less pulsatile systemic flow.

Bilateral Pulmonary Artery banding (bPAB) is an alternative option for the Stage I procedure. The aim of bPAB is to reduce the excess pulmonary blood flow and pulmonary artery pressure. A band is installed around one or both sides of the pulmonary artery, thereby reducing the blood flow in the lungs, which prevents the pulmonary over circulation that regulates the Q_p / Q_s . Resistance at the banded location is sensitive to the band's tightness; it is difficult to achieve the optimal tightness followed by the desired balance of pressure and flows, making it bPaB's limitation. This technique is useful when the ductus arteriosus is kept patent or there is a sufficient section of the native aorta is present to provide systemic circulation.

In Sano et al. [16][16] study, improvement was seen in short and long-term RVS patient survival compared to mBT patients. RVS eliminated the diastolic runoff, and hence the diastolic pressure was restored, ventricular work reduced, and systolic hypertension was relieved. Sano et al.'s [16]Sano et al.'s [16] study were successful as hemodynamic instabilities did not occur in patients, and it was successful with low-weight patients. There was an increase in the transconduit pressure, and diastolic reverse flow decreased months after the procedure. Keeping a transplant-free 12 months as a criterion, a clinical study was conducted at 15 centers across the USA; based on a sample of RVS and mBT shunts, patients with RVS shunts were healthier compared to the patients with mBT shunt. A study was conducted to compare the interventions after the Norwood procedure using Sano and

mBT shunt. A sample size showed that more interventions were required with Sano shunt as complications included cerebral embolic, cardiopulmonary resuscitation, and femoral or subclavian veins closure.

Different shunts have been developed to overcome the drawbacks associated with the BT and mBT shunts. Changes to physiological conditions make Norwood's procedure difficult. As the lungs of a neonate develop, the PVR decreases significantly, which results in increased pulmonary flow rate and decreases systemic flow rate, thereby causing an unbalanced Q_p / Q_s . Placement of shunt and surgical anastomosis design influences the final surgical results. In addition, a variety of native aortic arch morphologies and coarctations exist. They range from tubular, dilated, and typical for native arch and localized for coarctation.

2.1.2. Stage 2: Bi-direction Glenn and Comprehensive Stage II Surgical Procedure

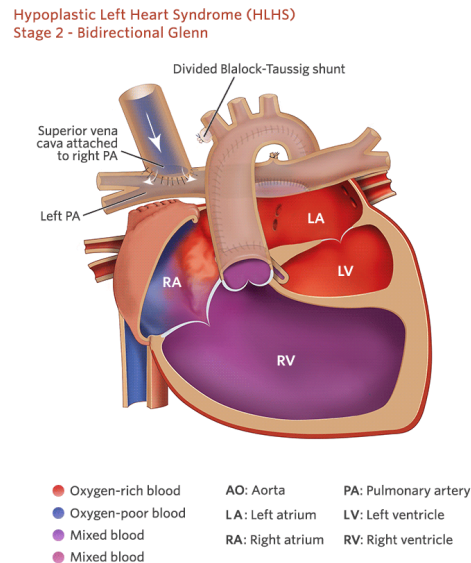


Figure 10 Bidirectional Glenn Surgical Procedure

Two different processes usually perform the stage II surgical procedure. Figure 10 represents the Bidirectional Glenn (BDG) surgical procedure. This procedure is performed during six to eight months of age. The surgical procedure aims to lower the load on the right ventricle and provide a low-pressure pulmonary flow. The BDG procedure involves removing mBT shunt and dissection of SVC from the right atrium and anastomosed to Right Pulmonary Artery (RPA). The deoxygenated blood from the upper body returns to the lungs. The Norwood procedure has been the option to achieve the stage I palliation aim for the past twenty years [17], [18]. [17], [18]. Early mortality remains as high as 20-30% after the palliation despite significant improvement in survival [19], [20] [21], [22], [23]. [19], [20], [21], [22], [23]. This procedure avoids cardiopulmonary bypass (CPB), deep hypothermic circulatory arrest (DHCA), and cardiac arrest. The potential disadvantages of the hybrid procedure include malperfusion, which arises due to the retrograde aortic arch obstruction and mechanical distortion of the branch PAs. Due to the learning curve of the new technology, high morbidity and mortality were reported [21], [22], [24]. [21], [22], [24]. This places a greater surgical requirement on the comprehensive stage II palliation.

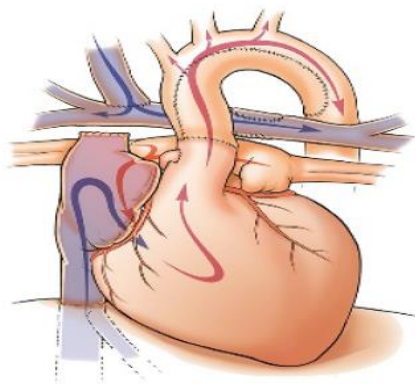


Figure 11 Comprehensive Stage II procedure [25]

Akintuerk et al. [23] [23] reported success in the comprehensive stage II procedure, an alternative surgical procedure to BDG. The surgical technique is considered complex and is conducted during 4-6 months of age. As shown in Figure 11, the comprehensive stage II involves the patent ductus arteriosus stent removal followed by the bands on pulmonary arteries. Following this, the aortic arch reconstruction occurs, followed by atrial septectomy and bidirectional cavopulmonary anastomosis creation. This procedure also involves the creation of the Damus-Kaye Stansel connection. Same physiology is established between comprehensive stage II and Bi-directional Glenn procedure.

Gibbs et al. [26] [26] proposed and reported various results when comparing the hybrid procedure to Norwood. The combined surgical and interventional technique is an alternate to stage I palliation. Ruiz et al. [27] [27] reported a patient undergoing a heart transplant after ductal stenting. Mitchell et al. [28] [28] reported the PA banding as a bridge to transplantation to prevent irreversible pulmonary vascular disease. Galantowicz et al. [22] [29] [22], [29] pioneered and popularized the hybrid approach and intended to use this approach on neonates with HLHS conditions. No difference in PA pressure existed between Norwood and hybrid during the pre-stage II hemodynamics. No difference between arterial saturation Q_p / Q_s . Both groups had equivalent parameters during the pre-stage II evaluation.

The crucial cause of failure in staged palliation for HLHS is progressive systemic ventricular dysfunction. The mechanism of failure for the right ventricular may be related to the myocardial damage during the Norwood procedure with cardiac arrest DHCA, high afterload on the right ventricle, and volume overload, which occurs due to the systemic-pulmonary shunt being controlled inadequately. The progressive systemic ventricular

dysfunction is one of the primary indicators for a heart transplant. Patients who completed the pre-stage II palliation, a patient, had atrioventricular valve insufficiency. The atrioventricular valve was corrected by valve repair during stage II palliation. Norwood group had patients with mild ventricular dysfunction and patients with a severe condition requiring transplantation. Patients had more than a moderate level of atrioventricular valve insufficiency, and patients underwent valve repair.

Progressive ventricular dysfunction was identified during the interim stage on patients that underwent hybrid stage I. A Patient required heart transplantation after stage II palliation. Another patient had aortic arch perfusion diminished, aortic isthmus obstruction, myocardial dysfunction, and minor narrowing of the reverse BT shunt.

Cardiopulmonary bypass (CPB) is initiated with the arterial cannula placed in the main pulmonary artery; this is done after the re-sternotomy procedure. For deep hypothermic circulatory arrest (DHCA), the patient is cooled, the branch pulmonary artery bands are removed. Atrial septectomy is performed when cardioplegic cardiac arrest is achieved. Using a homograft patch, the aortic arch is reconstructed under DHCA condition along with regional cerebral perfusion. With the standard technique, a proximal Damus-Kaye-Stansel anastomosis is achieved. In most patients, an autologous pericardial patch from hilum to hilum is used to enlarge the branch PA. The bidirectional cavopulmonary shunt is placed with the standard technique while kept on-pump beating state. The final procedure involves the closure of the sternum in most patients.

To facilitate aortic arch reconstruction, retained stented duct tissue is used in origin [30]. Upon DHCA, the main PA and the branch PA were transected and resected. The area opposition between the stented ductus and ascending aorta is divided up to the orifice of

the aortic isthmus. The patch for the aortic arch reconstruction is obtained from the remains of the stented ductus. The reconstruction is achieved by sewing the divided native aortic arch to the lateral edges of the divided ductus.

Advantages of using this modification are as follows, the stented material in place as in natural transverse aortic arch, the risk of bleeding and recurrent laryngeal nerve injury is significantly reduced as there is a continuity between the ductal material and the descending aorta. Immunologic sensitization can be avoided as homograft material is not used, thereby improving the potentiality of transplantation. Potential disadvantages include the development of aneurysmal and recurrent obstruction at the aortic isthmus.

Honjo and Caldarone [31] concluded the study by mentioning that a conclusion cannot be reached on the impact on the ventricular function and type of palliation based on preliminary analysis. Hybrid patients appear to have a better ventricular function at the pre-stage II evaluation.

2.1.2.1. Morbidity and Mortality

Recent studies show that there is 80-97% survival after stage I hybrid palliation; during such studies, extreme high-risk patients were excluded [23], [29], [32]. [23], [29], [32]. Between 2004-2007, a study was conducted on neonates with HLHS and its variants that have undergone Norwood and hybrid. No difference in survival was seen between patients with or without reverse BT shunts. Neonates died, and additional neonates underwent heart transplantation after stage I palliation. Neonates were in the interim death stage after the hybrid palliation.

Clinical and investigations have reported the adoption of systemically derived accessory pulmonary flow in bi-directional Glenn (BDG) [33], [34], [35], [36].) [33], [34], [35],

[36]. Van de Wal et al. [33].[\[33\]](#) studied patients with an average age of 5.6 years, reported no influence on survival rate. McElhinney et al. [34] [34] studied patients with an average age of 7.8 months, reported higher but statistically insignificant mortality. Mainwaring et al. [35] [35] studied patients with an average age of 10 months reported higher mortality.

2.1.2.2. In-vitro and in-silico approach

Many researchers have conducted both in-vitro and in-silico simulations to address problems that arise postoperatively. Pulmonary artery stenosis is one problem that is seen in patient's post-operative. The venovenous collateral vessel is the second problem seen in 31-33% of patients who undergo the BDG procedure. To improve the efficacy of the procedure, the use of ABG is discussed. Results obtained by researchers show the advantages of ABG and how it could potentially reduce the three-stage palliative procedure to a two-stage palliative procedure. An in-depth analysis is done of the literature to understand the need to improve this surgical technique. To overcome the surgical trauma associated with BDG, a novel surgical technique is discussed at the end of the section that mentions the procedure and its advantages compared with BDG and comprehensive stage II.

Liancai et al. [37] [37] conducted a study that focused on patients with HLHS and unilateral pulmonary artery stenosis after the Glenn procedure. Four three-dimensional Glenn models with different left pulmonary artery stenosis rate by diameter were generated (0%,25%,50%,75%). The extreme condition was considered to understand the effect of stenosis on the flow field, which is the acute artery blockage by 75%.

A multiscale model was developed along with the lumped parameter model (LPM). Global parameters that include average flow and total pressure at the pulmonary vein, the

ascending aorta, the descending aorta, and the SVC can be computed [38]. [38]. The LPM consisted of six blocks that included the single ventricle heart, left and right lung, the ascending aorta, and lower and upper limb vein. The vessels' viscous, compliance, and inertia were represented using the Windkessel models that consist of resistors, capacitors, and inductors. To simulate the cardiac valves, diodes were used in the circuit. For each compartment, the mass and momentum conservation laws were expressed using $Q_{in}(t)$, $P_{in}(t)$, $Q_{out}(t)$, and $P_{out}(t)$, which represent the instantaneous volumetric flow rate and pressure at the inlet and outlet of compartments [39]. [39].

The rhythmic contraction $E(t)$ [40], [41], [42] [40], [41], [42] of a single ventricle was represented as a function of pressure and volume. $E(t)$ is the elastance function that changes with time is represented as mmHg/ml. The elastance is expressed using $S_v V(t)$, representing the ventricle volume and pressure, and V_0 refers to reference volume.

Boundary conditions were applied to the coupled 0D and the 3D model. Initial conditions were imposed on the 3D model, the output obtained at each step was imposed on the 0D model. The limitation in this study includes rigid boundary conditions on the walls of the 3D model, and fluid-structure interaction models were not taken into account. To guarantee a convergent solution, five cardiac cycles were simulated. Parameters such as Wall shear stress (WSS), total pressure, and flow were recorded every 10-time steps. For this model, the boundary conditions set on the 3D model were the pressure on the pulmonary artery distal branch and flow rate through the superior vena cava.

Further to the simulation result, models 2,3 and 4 showed imbalanced pulmonary perfusion compared to model 1. Relation between blood flow to the localization of atherosclerosis [43] [43] and the plaque rupture [44], [45] [44], [45] was proposed by the wall shear stress

(WSS mechanism). There was a decrease $R_{LPA/SVC}$ when stenosis was above 75%; this results in abrupt pressure differences between distal and proximal stenosis. The development of the PA tree may be complicated due to the unbalanced lung perfusion [46]. [46]. Liancai et al. concluded the study by mentioning that if the stenosis rate above 75% may lead to power loss and severely unbalanced blood perfusion into each lung. For the patient's development, this condition must be treated before Glenn.

Chiara et al. [47] [47] study focused on an eight-month-old patient who underwent bi-directional Glenn and was diagnosed with a venovenous collateral (VVC) vessel. Clinical studies reported 31-33% of patients undergoing the BDG procedure have the venous collateral vessel associated with several alterations of the physiological hemodynamics [48], [49]. [48], [49]. The aim of the study was threefold (i) how to build a patient-specific model and describe the hemodynamics with VVC presence (ii) quantitative hemodynamics prediction by performing virtual VVC (iii) compare the prediction with measurements obtained from post-operation. Four months after undergoing the BDG procedure, the stage two patient was diagnosed with VVC. To improve the O₂ saturations, closure of VVC is performed. Closure of such collateral can have unintended consequences such as alteration in systemic blood flow or elevation of pulmonary artery pressure.

The LPM layout for this study was similar to the one presented in Kung et al. [50] ... [50]. In addition, the VVC resistance was placed between the single atrium and the SVC, and the aortopulmonary collateral vessels resistances connecting the aorta to each PA branch. A multi-domain model of the four-month-old patient's circulation was developed by following the methodologies described by Corsini et al. [51] .[51]. To account for the increase in body surface area (BSA) due to the growth and the different vessel growth in

lungs, scaling factors were applied to the RLC circuit using the allometric equations [52], [53], [54] [52], [53], [54]. PVR and SVR lower and upper values obtained were compared to the patient-specific models. Differences between the three couples of vascular resistances suggest that growth occurred in the four months after BDG surgery, and hence consideration is needed in the post-operative LPM development. To obtain the eight-month flow and pressure, the patient-specific LPM was tuned with four-month heart parameters. The 3D virtual BDG, coupled with eight-month LPM, runs a pulsatile simulation and then matches with clinical data. Another simulation was conducted by removing the VVC resistance from LPM that is equivalent to the VVC closure.

Based on the growth factor, the PVR and SVR lower and upper values should have dropped by 22, 25, and 13%, respectively. Results showed that this did not correspond to the patient-specific values that indicated a 17% increase in PVR, 37% decrease in SVR lower, and 51% decrease in SVR upper. A recent study showed that PVR increases due to abnormal pulmonary flow that may alter the pulmonary vascular tone [55]. [55]. The PVR vasoconstriction may have occurred due to non-physiological pulmonary flow due to the BDG surgery on this investigated patient. This study's lack of extensive data led to assumptions regarding parameters required to calculate the blood flow. These hypotheses were based on mathematical relationships and reasonable assumptions. Vasodilation in the upper body and vasoconstriction in the pulmonary vasculature in accordance with the SVC and PA hypertension lead to the VVC formation [48]. [48]. Based on the clinical findings of VVC formation after the BDG surgery [48], [49]. [48], [49]. VVC development on the post-stage-2 model could be indicated based on the predicted SVC pressure, pulmonary artery pressure, and trans-pulmonary pressure gradient.

Chiara et al. [47] state that such a study could motivate data collection such as O_2 saturations, systemic blood flow, and critical clinical outcomes. This study highlights only one clinical case, and the developed approach can be applied to other patients if heterogeneous patient-specific data were collected at different intervals. The introduction of patient-specific modeling for growth and adaption with existing clinical data is not feasible. Assumptions made in the allometric equations are high and only applicable to data collected at two large intervals.

The study of Zhou et al. [56] [56] focused on assisted bidirectional Glenn (ABG), an alternative to the mBT procedure; this was initially proposed by Esmaily-Moghadam et al. [57][57]; the proposed procedure remains similar to the BDG but with an accessory shunt that is added between the innominate artery to the SVC. Their study focuses on harvesting the potential energy in the blood within the systemic arteries and increasing the pulmonary flow using an ejector pump concept. The use of ABG has two advantages over Norwood as it improves the systemic and coronary perfusion by reducing the volumetric overload on the single ventricle [57], [58] . [57], [58]. Secondly, this reduces thrombotic risk by providing stable pulmonary flow. Multi-scale in-vitro models were developed to compare with Norwood candidate and previous multi-scale numerical simulation. Local hemodynamics are considered in such multi-scale simulations by providing appropriate boundary conditions to the anastomosis sites, this has been consistent with the clinical measurements [38], [50], [57], [58], [59], [60], [61], [62].Local hemodynamics are considered in such multi-scale simulations by providing appropriate boundary conditions to the anastomosis sites, this has been consistent with the clinical measurements. Local hemodynamics are considered in such multi-scale simulations by providing appropriate

boundary conditions to the anastomosis sites, this has been consistent with the clinical measurements [38], [50], [57], [58], [59], [60], [61], [62].

The MFL used for their study uses the LPM network model coupled with 3D models of the pulmonary artery, anastomosis sites, and aorta. Several resistance and compliance values were scaled during each circulation based on the body surface area or by using clinical values [61], [62]. Vukicevic et al. [62][61], [62]. Vukicevic et al. [62] was followed in modeling the resistance and compliance. PVR has effects on postoperative recovery and hemodynamics of the infant [63], [64]. Cases that included high and low PVR were replicated on the testbed [57] . [57]. In-line elastic tubes and trapped air were used as pulmonary compliance [62], [65]. A 3.5 *mm* diameter shunt was used on the Norwood circulation, and a 2.5 *mm* diameter shunt with a nozzle on the ABG circulation.

Resistance values were set according to the steady flow conditions. Measurement of air volume and volume change with pressure change was used to set the compliance value. To achieve the mean aortic pressure, ventricular assist device (VAD) pressure was adjusted, and the aortic compliance element was adjusted to achieve the required aortic pulse pressure. The numerical simulation uses a multiscale modeling approach, coupling the closed-loop model to the local hemodynamics [60]. [60]. A 3D model along with a 0D LPM was used to represent the heart and closed-loop model.

Using the low and high PVR values on the three circulations, the tests were conducted. Results showed that there was no significant difference in the mean flow rate between numerical and experimental analysis. Pulmonary flow rate and pulmonary pressure for the mBT circulation were the highest. In mBT circulation, as PVR increased, the corresponding SVC flow rate increased, competing with the shunt flow. SVC flow rate

decreased in both ABG and BDG circulations. SVC pressure in ABG showed 2-3.7 *mmHg* higher than BDG. The pulmonary flow rate of ABG provided a 30-38% improvement compared to the BDG. Pulmonary pressure was lowest for BDG circulation. The ABG provided the highest systemic oxygen delivery compared to the other three circulations, irrespective of the PVR. Comparison between the numerical and experimental ABG model showed that RPA and LPA flows and pressures are well produced. SVC flow predicted numerically displayed pulsatility during systole, a possible mismatch in compliance between models [62]. The mean SVC pressure did not show any significant difference.

Zhou et al. [56] stated that the initial aim of their study was to test the physical feasibility of the ABG circulation and validate the results against the numerical model. By comparing the pressure gradient between the PA and SVC relative to the pulmonary blood flow, the effect of the ejector shunt used can be computed. The local flow resistance is reduced at the PA-SVC junction by this ejector-shunt. However, with the current shunt, pulmonary artery pressure and SVC pressure increased about the same value. Using the ABG circulation procedure in place of Norwood would reduce the number of surgeries from three to two. The shunt used in the ABG palliation can be shorter compared to the mBT shunt. The flow through the shunt is drawn from the aorta providing blood at a higher pressure and velocity. This will eventually reduce the risk of thrombosis and cyanosis due to better pulmonary blood flow. The circulation is simplified to the Glenn circulation in the event of mBT shunt occluding. An increase in the pulmonary arterial blood flow increases the pulmonary arterial pressure and improved saturation over the Glenn [66], [67]. McElhinney et al. suggest that pulmonary arterial pressure would improve exercise tolerance and reduced baseline cyanosis.

Ethan et al. [50] study focused on the virtual Hemi-Fontan model along with a multi-scale simulation that predicts the patient's hemodynamic and physiologic condition post-operation. The patients were five and six months old, respectively. The computational model contained a 3D domain of the surgical junction along with a circulatory system that describes the 0D domain. The resting and active conditions of the two patients were considered, and a total of four simulations were performed.

The circulatory system in their study was modeled using 0D lumped-parameter network (LPM). Five main circuit blocks were modeled to represent the heart, right and left pulmonary vasculatures, and the upper and lower body vasculatures. The atrium and ventricle were represented as elastances. Non-linear diodes are used to model the aorta valves along with atrioventricular valves; this allows the unidirectional flow with resistances proportional to the flow rate. The kidney, liver, and intestine were modeled as the lower body and a venous valve in the leg venous block. Based on the outlet of the 3D model, the pulmonary circulation is described using the RCR blocks are arranged parallelly. Coronary circulation, respiratory effects, and gravity are neglected [68]. Pulmonary LPM parameter values were described using a morphometric tree-based impedance approach [69], [70] Systemic LPM parameters were represented using a healthy adult with $BSA = 1.8 \text{ m}^2$ [71], [72], [73] Parameters were scaled by using the allometric equations according to the patient's BSA [54]. The LPM was tuned using the resistance of the upper and lower body to simulate the patient's resting condition. Patient-specific compliance was computed after modifying the resistance of each block while keeping the proportion of impedance [52] [54]. The parameter values of large vessels and the heart were manually tuned to match the mean value and waveforms obtained from

clinical measurements during the resting condition. A set of LPM parameters that is equivalent to active conditions was prescribed. The active state of the infant is compared to the exercise state of an elderly patient. In the active condition, an assumption is considered where the heart rate is generally around 120-160 *bpm* [74].

The entire circulation system was developed computationally by coupling the 3D anatomical model and the 0D LPM model. An implicit coupling algorithm was used to apply the Neumann boundary condition at the inlets and outlets of the 3D model [38]. Wall shear stress (WSS) and particle residence time (PRT) was computed, pressure and flow information was extracted from various points along with the instantaneous pulmonary power loss.

Results showed that the flow from SVC transitioned smoothly into the pulmonary arteries for patient A and swirling was observed for patient B, resulting in high velocities near the circumference. WSS distribution plot in the surgical junction for both patients is uniformly distributed; the band of high WSS characterizes the orientation of swirling flow. The power loss results obtained are similar to previous modeling studies of the HF anatomy [75], [76]. Patient B showed three times higher power loss due to higher flow rates and flow disturbances. There was an increased CO during the active condition, and in the pulmonary blood flow, this increased the SVC pressure in both models. Coupled with the existing SVC baseline pressure of 15.5, patient B had an SVC pressure of 18.8mmHg compared to the SVC pressure, 11.7 *mmHg*. Patient B would exhibit superior venous hypertension or SVC syndrome with headache, face swelling, and orbital edema based on prior clinical experience. For both patients, the area under the pressure-volume loop during an

operational condition is smaller than the loop during the resting condition; this indicates that during each cardiac cycle, less work is performed.

Ethan et al. concluded the study by mentioning that further refinement is required within the HF operation. Improving the surgical junction power loss has minimal impact on the overall post-operative circulation in pressure and flow during the resting and active conditions. PRT and WSS results from computation can assess the relative thrombotic risk; this can be reduced if the PRT values are lower. Platelet activation is possible when the values of WSS are in the range of shear-induced platelet [77]. Considering the junction as a non-linear resistance proportional to the square of the flow rate would be the plausible reason for the increased surgical junction power loss during active conditions [78]. The difference in power loss between the two Hemi-Fontan models could affect systemic parameters during strenuous activity [79].

Schiavazzi et al. [80] study focused on the postoperative hemodynamics of LPA stenosis by using a multiscale computation study on single ventricle patients undergoing stage II superior cavopulmonary connection (SCPC). Postoperative stenting or surgical arterioplasty is often required to relieve LPA hypoplasia or stenosis [81], [82], [83], [84], [85]. This adds complexity and time to the SCPC operation. The treatment of LPA stenosis is still subjective and needs to rely on angiography data and clinical experience. This study aimed to develop quantitative guidelines for the treatment of LPA.

Ninety patients were studied for various configurations in stenosis, in the main pulmonary arteries, or their branches [86]. Data showed that discrete pulmonary artery stenosis was frequent when combined with other anomalies. The local compression induced due to augmentation of the aorta during stage I surgery is the primary reason for distortion in LPA

[82], [83] [87]. This affects the ventricular-arterial coupling [88] that results in increased and eccentric wall shear stresses [89].

Magnetic resonance imaging (MRI) data of each patient before stage II surgery was used to develop the 3D models of the junction between BT shunt and pulmonary arteries. Relevant vasculature was obtained using the combined segmentation and region-growing technique [90]. The LPM model was constructed using a circuit model [72] to simulate the preoperative and postoperative patient's circulatory physiology[50],[51],[52], [91]. The heart, upper and lower systemic, and left and right pulmonary circulations are characterized using five circuit blocks; the remaining modeling technique is followed by the model done by Migliavacca et al. [68] The LPM model was coupled with the 3-D streamline upwind Petrov-Galerkin finite element navier-stokes solver [60], [92].

Results showed that LPA: RPA in patient P1 was weakly affected due to the severity of the stenosis. The ratio in patient P1 was higher than the average compared to the flow split ratio when at 80% stenosis and 35% stenosis. Between Glenn and Hemi-Fontan models, all levels of stenosis showed a maximum relative difference of 4% in patients P1 and P3. For a degree of stenosis at 60% of the diameter, the maximum relative difference in pressure drop across the LPA was higher. A mean pressure drop of greater than 3mmHg across the stenosis is considered clinically significant [84].

There was no change noticed on the pressure-volume loop for severe levels of stenosis. No changes were observed in other clinical parameters such as $\frac{Q_p}{Q_s}$, power losses, systemic and venous oxygen saturation. Pressure and LPA: RPA flow split falls in the range of clinical concern when stenosis is greater than 65%. Pulmonary artery reconstruction is

required in more than 50% of the cases, as pulmonary artery distortion and hypoplasia occur most often in LPA[83], [84]. During stage II surgery, augmentation of central pulmonary arteries is essential, while minimizing pulmonary artery distortion is the primary factor to use the Hemi-Fontan rather than bi-directional Glenn. Treatment of pulmonary stenosis is performed to avoid potential effects on suboptimal growth and exercise tolerance and remodeling caused by reduced flow [93], [94]. Simulations were performed, keeping all other modeling parameters constant. Results show that power loss in the SVC-pulmonary artery junction is a small fraction of the total pulmonary power loss. Parameters of clinical interest remained unchanged.

Schiavazzi et al. [80] concluded the study stating the limitations faced in the study as LPM parameters were identified based on preoperative stage II clinical data. This approach is under the assumption that there are minor physiological changes in the patients. Pulmonary and cardiac dysfunction in the early postoperative period was not considered. The clinical data used for this study came from a patient under sedation. Change in the flow into the pulmonary arteries can influence the result.

Moghadam et al. [57] study focused on a novel surgical approach by using an ejector pump for the flow in BDG to be assisted. The highest mortality was observed [95] in an initial report of the classic Glenn procedure in patients. Inadequate pulmonary blood flow and SVC syndrome were the primary reasons for death. Less formal attempts to use this procedure have led to similar poor outcomes [96] [97] [98].

An ejector pump can be used in the SVC circulation, where the low-energy blood flow in SVC can be assisted by additional energy from flow in the systemic circulation. By assessing the use of ABG and quantify the consequences in hemodynamics due to change

in PVR due to infant physiology. To couple local hemodynamics to a closed-loop model, a multiscale framework is adopted [99]. An LPM network along with a 3D model of large vessels for which Navier-Stokes equations have been solved. The 3D geometric model was constructed based on the former study of the mBT shunt [38]. Three models were created using realistic anatomy and clinically derived geometries. A 3.5 *mm* mBT shunt, the SVC diameter was 4.5 *mm*, a 2.5 *mm* shunt was used in between the innominate artery and the SVC for the ABG approach. The adopted LPM is based on the prior studies of the mBT shunt circulation [100]. Component values for the blocks were obtained from the angiographic data of 28 Norwood patients. A total of six simulations were performed to examine the influence of high PVR during the early postnatal period.

Results showed that for ABG procedure without the distal clipping, at lower PVR, SVC pressure increased, pulmonary flow increased, and oxygen delivery decreased. Once the clipping is done, the upstream pressure from the SVC shunt is lower than the downstream pressure. The energy in the flow is partly transferred to SVC from systemic, thereby making the ejector pump concept feasible. The BDG model lowers the cardiac output, maintains the oxygen delivery, and has higher SVC pressure compared to the mBT shunt. Compared to BDG, the ABG had improved pulmonary blood flow, and the ABG model achieved the highest oxygen delivery and oxygen saturation with the presence of PVR.

Moghadam et al. concluded the study stating that early application of BDG as first stage palliation has been avoided based on outcomes. The ABG provides a different strategy; based on the results obtained, complications from Glenn can be avoided. High SVC pressure at high simulated PVR based on neonatal period remains a concern for ABG application as the first-stage palliation. Use of ejector-pump shunt in the ABG can lead to

early thrombosis due to lower flow residence as the length of the shunt is shorter than the mBT shunt. Mathematical models cannot predict all biological responses, hence the need for an animal model to examine the ABG shunt thrombosis.

Arbia et al. [101] study focused on the use of CFD in cardiovascular research to model hemodynamics changes due to pathology [70], [102] [103] [104], changes due to surgical repair [51], [105] and explore possible different scenarios for treatment [38],[50],[61], [106], plan therapy [107] , design artificial devices or conduits that are subjected to stress and pressure due to the blood flow [108] [109] [110].

To achieve an effective solution, necessary steps are taken to simulate blood flow that includes geometrical mesh generation from image data, the required boundary conditions, and the choice of numerical algorithm to compute flow and pressure. Inaccurate performance in the numerical algorithm can lead to an erroneous result and thereby leading to a misleading conclusion. Governing equations are discretized in space and time to compute the solution close to the exact solution. Finite volume and finite element are two discretization methods in space, within whom many variants existed for Navier-Stokes's equations [111] [112].

Arbia et al. discuss the use of computational fluid dynamics on superior cavopulmonary connection (SCPC). The exact solution for the flow equations cannot be derived analytically due to its complex geometry, compulsory three-dimensionality, and flow characteristics. The SVC anastomosis was reconstructed from MRI data of SVC following the Glenn operation. The geometric complexity with the most straightforward hemodynamic setting is used to see its influence on the solution. Steady flow condition was imposed on the inlet section, reference pressure at the outlet section, and zero flow at

the wall. Using rigid-walled models will yield identical results regardless of the values used for reference. A uniform mesh was generated, and a mesh comparison study was performed. Results showed that mesh had a very minimal impact on the SVC pressure and the flow split between two lungs. The change in the SVC pressure was clinically negligible as they correspond to a small fraction when converted to mmHg.

The above literature discusses the conventional comprehensive stage II procedure with patient-specific data applied on in-vitro and in-silico models and compares the data with clinical generated data.

DeCampli et al. [113] study focused on a hybrid approach to the comprehensive stage II. The “hybrid Norwood” consists of a procedure that is performed without the need for cardiopulmonary bypass. This has a putative advantage in the avoidance of surgical trauma. After using this approach, the outcome from various centers has been laudable, while others report intermediate-term outcome that is not better when compared to the stage I palliation [114], [115], [116] [117]. Deep hypothermia, circulatory arrest, and cardiopulmonary bypass are required for comprehensive stage II palliation. Due to band-induced trauma, bilateral pulmonary artery reconstruction is required and the management of the ductal stent. To reduce the real trauma of the patient, an alternative technique for comprehensive stage II palliation is proposed as shown in Figure 12. This applies to patients who can sustain the upper body perfusion by having sufficient antegrade aortic flow. The creation of the Damus-Kaye-Stansel connection and the need to create the aortic arch reconstruction is avoided.

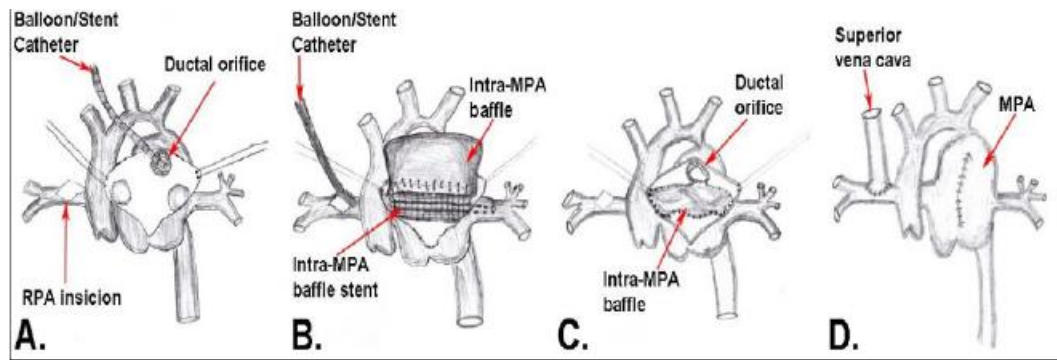


Figure 12 Hybrid Comprehensive Stage II procedure conducted by DeCampi et al. [113]

Two patients were considered for this study. After undergoing hybrid stage I on day four, Patient A had a hypoplastic aortic arch and aortic isthmus along with a sizeable ductal arch with no obstruction to the left ventricle. The palliation procedure begins with the heart, innominate, superior caval veins and great vessels being mobilized and the azygous vein divided. The descending aorta, distal arch, or aortic isthmus are not mobilized. Dual arterial cannulas were placed in the PA trunk and innominate artery. The venous cannulas were placed in the innominate vein and right atrium, followed by the cardiopulmonary bypass. Upon cooling to 18°C degrees, PTFE bands were removed from the branch pulmonary arteries after arresting the heart and clamping the ascending aorta. The arch branches were occluded, followed by PA cannula removal and the procedure for antegrade regional cerebral perfusion. The RPA was opened at the proposed site of the SVC anastomosis. A guide wire was advanced till the left lower lobe artery from the RPA incision. A baffle was sutured partially using a pulmonary homograft material. This was done within the pulmonary bifurcation from the right to the LPA orifices. A stenting procedure was followed to prevent the baffle from being crushed due to the systemic flow; due to the surrounding systemic circulation, a considerable amount of stress is exerted on the stent, thereby requiring a suture fixation.

Upon completion of the surgery procedure, the patient made an unremarkable recovery and became hypoxemic after postoperative day 5. Extensive thrombus condition was noticed in the intra-pulmonary covered stent, LPA, and its lobar branches. The patient succumbed to hypoxia on postoperative day 26.

After undergoing hybrid stage I on day six, Patient B had a double outlet right ventricle and mitral atresia. A left posterior aortic root unobstructed pulmonary outlet and crowding in the subaortic region were seen during the echocardiography. A similar technique was followed, as mentioned above, for patient A. The central PA was opened longitudinally, and the ductal stent was trimmed back to flush along with the PA bifurcation. A homograft baffle was partially sutured between the left and right PA orifices. The same procedure performed on patient A was performed on patient B.

Upon completing the surgery, the patient had a parainfluenza infection due to pulmonary compromise for a prolonged duration. The patient recovered and was discharged on postoperative day 53. The formation of the aneurysm on the intrapulmonary baffle was not revealed during the angiography study. An echocardiography study at the age saw a good RV function, unobstructed flow from the right ventricle, unobstructed flow from the native aortic root, and unobstructed cavopulmonary connection of 15 months.

DeCampi et al. [113] concluded the study stating that this procedure has potential advantages as it limits the baffle construction and arterial incision, shortened duration of regional cerebral perfusion, and hypothermia. The complete avoidance of mobilization and reconstruction of the isthmus, arch, and descending aorta decreases the risk of bleeding, recurrent nerve, and phrenic nerve injury. The procedure has potential disadvantages,

including baffle leak, LPA stenosis, stent migration with LPA occlusion, and recurrent ductal arch stenosis.

The proposed procedure requires 1-2 stents placed; stent management is common with conventional and standard hybrid staged approaches. Dave et al. [118] reported the incidence of branch PA stenting was 17% and 38% for conventional management and hybrid stages I and II. Reinhardt et al. [119] reported that catheter reintervention was required for 37% in the conventional stage approach. Studies have claimed that PA and aortic stents placed during the infant stage can be dilated to a diameter of an adult stent with an average of three interventions [120], [121], [122].

The HCSII procedure is proposed as an alternative technique to the comprehensive stage II procedure to reduce surgical trauma in patients. The HCSII procedure applies to patients with sufficient antegrade aortic flow to sustain the upper body perfusion. The significant advantage of the HCSII procedure avoids the creation of Damus-Kaye Stansel (DKS) connection and aortic arch reconstruction. As discussed in section 1.6, the goal of this research is to validate the efficacy of this surgical procedure by performing in-vitro simulations.

2.1.3. Stage 3: Fontan

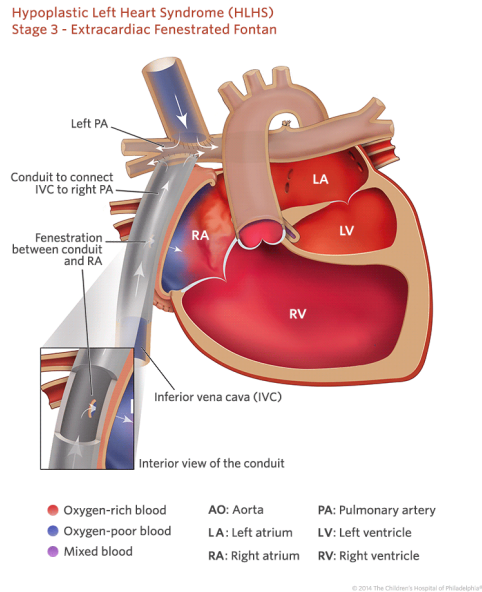


Figure 13 Stage 3 Fontan

Francis et al. [123] performed the third stage operation on patients with tricuspid atresia to route blood from vena cava into the pulmonary circulation, as shown in Figure 13. The right atrium is bypassed and returns the oxygenated blood to the left side of the heart. As a result, the systemic and pulmonary circulations are connected in series. The advantages of the Fontan procedure are decreased load on the ventricle and better oxygen saturation. In addition, flow through the pulmonary circulation is driven by the mechanical energy from the post-capillary action. The downside of the Fontan procedure involves chronic hypertension in the systemic vein [124]. Higher caval pressure is seen in the Fontan patients due to the lack of a pump downstream of the systemic veins. As a result, the cardiac output decreases as the ventricle pumps against the pulmonary and systemic resistance connected in series.

Choussat and Fontan stated that the patient must have good cardiac output and systemic pressure at an acceptable value for the operation to be conducted [124]. In addition, the patient must have good pulmonary arteries such that resistance in the pulmonary circuit is not high. An ideal patient for the Fontan procedure will have a good ventricular function and unobstructed ventricular flow. Fontan operation cannot be performed when the patient is born as the veins are small and their corresponding resistance is high [124]. Hence, a three-stage procedure is followed to allow the body to adjust to different hemodynamics conditions introduced by the third stage.

When the patient attains 1-5 years old, based on the cyanosis at rest and during exercise and the growth of the vascular structures, the stage III procedure is performed on the patient. In the stage III procedure, the IVC is connected to the pulmonary artery. The two methods for connecting to the pulmonary artery are Atriopulmonary connection (APC) and TCPC. The right atrium acts as a valveless contractile chamber between the great systemic vein and the pulmonary artery [125]. The problem associated with the APC connection involves no ventricle to supply power, and the APC connection operates at a higher pressure. In vitro studies have shown a loss of mechanical energy due to turbulence generation when a compliant atrial chamber is placed in between the pulmonary arteries and systemic veins. Superiorventricular arrhythmias and chronic atrial distension are caused due to the APC technique making it an inefficient method within the Fontan procedure [126].

In the TCPC procedure, IVC and SVC are directly connected to the pulmonary artery, making the TCPC procedure superior to the APC procedure. IVC can be connected to the pulmonary artery using two methods. The lateral tunnel method was developed in the

1980s. A channel exists between the IVC and the pulmonary artery via a portion of the lateral atrial wall and a prosthetic baffle in this technique. This method is used on younger patients as the connection grows along with the patient [124]. The lateral tunnel method leads to arrhythmias over a period of time as a small portion of the atrial tissue is exposed to higher pressure. The second method is the extracardiac conduit method developed in 1990 [127] . In this method, a graft tubular in shape is placed in between IVC and pulmonary artery. The right atrium is at low pressure, and the right side of the heart is bypassed. The extracardiac conduit technique is available to patients who have grown large enough such that the graft can be placed for the IVC flow and must have high Pulmonary Vascular Compliance [124], [127]. Pleural effusion and protein-losing enteropathy are associated with this technique if conditions are not met [128].

2.1.3.1. Extra cardiac and intra cardiac Fontan

Alexi- Meskishvili et al. [129] conducted a clinical study to obtain the optimal size for the Gore-Tex conduit for extra cardiac Fontan operation (ECFO). Recommendations to choose the conduit diameter were based on minimizing the risk of thrombosis, and the diameter should not exceed the diameter of IVC by 20%. It was recommended to perform ECFO on patients between 2-4 years old as the distance from IVC to RPA is about 60-80% of an adult.

Itatani et al. [130] conducted a study using CFD analysis to determine the conduit size of the ECFO procedure. Optimum conduit size must be determined to balance the risk associated with energy loss, flow stagnation, and thrombosis. When a smaller conduit is used, there is a lesser chance for flow stagnation, as flow moves faster. In addition, higher resistance and higher energy loss are associated with using a smaller conduit. The conduit

must be large enough to avoid energy loss and flow stagnation as flow stagnation leads to blood clotting, leading to catastrophic consequences for the patient. The variations in flow are driven by respiration, making it non-pulsatile in nature. For different conduit sizes, stagnation volume and energy loss were measured at rest and exercise; it was identified that stagnation occurs during expiration. Stagnation decreased during exercise as the overall flow rate increased. For patients as old as 2-3 years, conduit size lies in between 16-18 *mm* in diameter.

Penny et al. [131] studied the role of the lungs after the Fontan operation, where the sub-pulmonary atrium was connected to the pulmonary circulation. The study examined the right atrium's role in supplying energy related to pulmonary blood flow's energy provided by respiration. At expiration, the contribution of the right atrial to the forward flow was 51.4%, with a standard deviation of 8.8%. During inspiration, the total forward flow was 63% higher than expiration, with a standard deviation of 35%. The contribution of the right atrial to the forward flow was 52% during inspiration, with a standard deviation of 10%.

Hsia et al. [132] conducted a study on the effect of respiration and gravity on the flow in the systemic veins in patients with Fontan and normal biventricular circulation. The Fontan patients studied underwent TCPC and APC operations. The TCPC operation was further divided into lateral tunnel method and extracardiac conduit. Patients who underwent TCPC had significant fluctuations in the flow in the primary vein that returned from the liver and the hepatic vein. Respiration effect was seen lower in APC operation compared to TCPC operation. The average ratio of inspiratory to expiratory flow was 1.6 for APC patients, 3.4 for TCPC patients, and 1.7 for the control group. The inspiratory to expiratory flow ratio in portal vein was 1.1 in APC patients, 1.0 in TCPC patients, and 0.8 for the control group.

The gravity effect did not significantly affect the net forward or retrograded flow for patients with normal circulation. For APC and TCPC patients, gravity reduced the net forward flow and increased the retrograde flow.

Redington et al. [133] conducted a study on pulmonary artery respiration in patients with a total cavopulmonary shunt. Patients have their right heart bypassed, and venous blood from the liver and coronary sinus enters the right atrium. During inspiration and expiration, blood flow increased and decreased in the pulmonary artery. Flow measurements were made using Doppler echocardiography in the pulmonary artery.

Hjortdal et al. [134] conducted a study on the relationship between respiration and blood flow during exercise and rested in Fontan patients with TCPC. Flows in the IVC and SVC were monitored using MRI. SVC flow was not affected by respiration when the patient was at rest. The inspiratory to expiratory flow ratio was 1.0 along with a standard deviation of 0.2; exercise did not significantly affect the ratios. During respiration, the IVC flow was higher. The mean ratio of the patient at rest was 1.9, along with a standard deviation of 0.5. Twice, the amount of flow in IVC during inspiration and exercise was driven by ventricular activity, decreasing the ratio.

Mardsen et al. [135] conducted a study to understand the effects of respiration and exercise on the TCPC using CFD analysis. In this study, realistic hemodynamic data was produced that is close to clinically measured data. The exercise hemodynamics was affected due to the respiration model.

Hsia et al. [136] conducted a study on the effect of diaphragm plication, a surgical procedure done on normal and Fontan patients to relieve symptoms of diaphragm paralysis. Ultrasound doppler evaluated the flow in the portal vein, the hepatic vein, and subhepatic

IVC. Fontan patients under this study had TCPC operations. The normal control group had a hepatic venous flow of 2.4 times higher during inspiration than expiration in the upright position. Patients with diaphragm plication had a ratio of 1.4, showing the effect of respiration diminished. In Fontan patients, the hepatic vein flow ratio was 3.2 in supine for normal diaphragm position; for diaphragm plication condition, the ratio was 2.3. The effects of respiration on systemic venous flow are essential in Fontan patients; for a patient with diaphragm plication, this effect is lost. The phrenic nerve injury should be avoided by all patients who have or will receive the Fontan operation.

Hsia et al. [137], de Level et al. [138], Mardsen et al. [135], and Bove et al. [139] performed studies to modify the surgical procedure that could improve the Fontan hemodynamics. To understand the effect of different design parameters on hemodynamics effect, CFD analysis was performed. Parameters included effects on alternative Hemi-Fontan procedure, inferior cavopulmonary connection (ICPC) diameter, Y-shaped ICPC, and ICPC location. Ovroutski et al. [140] conducted a study on the effect of the Fontan operation on oxygen and exercise capacity. Patients who had TCPC procedures, both adults and children, were studied. Patients were monitored early and late postoperative exercise phase. During the early phase, the mean cardiopulmonary oxygen capacity was higher in children than adults, 27.9 ml/min/kg and 22.9 ml/min/kg . Postoperative tests showed 30.1 ml/min/kg and 16.9 ml/min/kg in children and adults. Cardiopulmonary oxygen capacity in adults and adolescents decreased compared to early and late postoperative. The exercise capacity was better in children compared to adults. The median value for children was 2.2 W/kg and 1.9 W/kg for adults during early and late postoperative. Heart rates of patients were

observed during early and late postoperative. The median rate was 136 bpm and 112 bpm for children and adults.

2.1.3.2. Fenestration and PVR

Gewillig et al. [124], [141] [142] [143] mention the need to address the pulmonary vasculature in sick Fontan patients. Fenestration is a procedure that bypasses pulmonary vasculature by returning IVC blood flow to the right atrium; this reduces IVC flow congestion and improves cardiac output. Due to this process, the oxygen saturation decreases, and identifying the optimum fenestration size has been difficult. A high level of cyanosis can occur due to excess return flow, and smaller fenestration may not efficiently reduce the IVC congestion. Ventricular dysfunction is the other main failure component.

Henain et al. [144] conducted a study on the effect of pulsatility on PVR by implanting cavopulmonary shunt in 30 pigs surgically. Measurement on three control groups revealed that PVR and pulmonary arterial pressure increased due to lack of pulsatility.

Goldstein et al. [145] analyzed the relationship between exercise capacity to diastolic function and PVR. PVR decreased with exercise but remained constant in some patients.

It was found that in Fontan patients, the limitation on exercise was controlled by PVR.

Shachar et al. [146] found that PVR decreases during exercise in four of the five Fontan patients studied. The relationship between the PVR and exercise is still not known.

Reeves et al. [147] conducted a study on the normal human lung distensibility during exercise rather than total PVR. A two percent increase in vessel diameter was seen for every one mmHg pressure in the isolated arterials. The flow pressure increases during exercise cause dilation in the lung vascular bed by 40%. An increased pulmonary flow was seen due to the distensibility of lung arterioles that contributes to the reduction in PVR.

Forton et al. [148] measured the pulmonary arterial pressure (PAP), pulmonary flow, exercise capacity, and PVR of healthy adult volunteers using Doppler echocardiography under different exercise conditions. At peak exercise in all exercise conditions, the PVR reduced by 40%.

Naeije and Chesler [149] stated that PVR is flow-dependent and it decreases curvilinearly as the flow increases. The cardio output decreases as aging increases PVR. Vasodilators such as nitric oxide and prostacyclin are released by pulmonary endothelium during exercise, reducing the PVR. To detect dilation or constriction of pulmonary vessels or changes in the arteriolar vessel caliber, PVR can be used as a good indicator.

Schmitt et al. [150] studied ten Fontan patients' effects on collateral blood flow and PVR before and after administering dobutamine stress. Measurements were taken using MRI catheterization techniques during continuous infusion of 10 ug / kg / min dobutamine and during free breathing. Cardiac output increased due to decreased systemic vascular resistance, and no effect was seen on PVR when administered dobutamine. Due to the increased cardiac output, the PVR decreased.

Rivera et al. [151] studied the relationship between PVR and pulmonary venous blood flow during oxygen inhalation and free breathing. The study was done on 18 patients with CHD with a left to right shunt. Using catheterization and echocardiography, the $\frac{Q_p}{Q_s}$ and PVR was measured. Measurements were taken before and after 100% oxygen inhalation (10 L / min oxygen masks). Pulmonary flow increased, and PVR decreased during oxygen inhalation.

Petrofski et al. [152] conducted a study on lowering PVR using mechanical ventricular support. An adult patient with elevated PVR and heart failure was taken for this study. The PVR decreased from 13.8 to 3.1 *Wu* after 24 hours of mechanical support to the pulmonary and systemic systems.

2.1.3.3. Morbidity and Mortality

The life expectancy of patients undergoing the Fontan procedure will usually be two or three decades of a semi-normal life. The side effects caused due to this procedure lead to congestive heart failure. Level et al. [125] states that reduced cardiac output and elevated systemic venous are the primary reasons for complications. The elevated systemic venous pressure causes plastic bronchitis, liver failure, and protein-losing enteropathy. Increased lymph production is associated with elevated systemic venous pressure, which leads to impairment in lymphatic resorption that leads to protein-losing enteropathy. As a result, the patient experiences reduced exercise tolerance. The lack of ventricle causes flow pulsatility in the pulmonary circulation, and hence the pulmonary compliances gradually reduce over time. Stiffness is increased in the pulmonary circuit due to dilation that arises from a lack of pulsatility. Higher pulmonary vascular resistance is seen due to increased stiffness, which means lower cardiac output due to high systemic venous pressure. Hsia et al. [132] state that gravity reduces the forward venous flow in patients.

Cavalcanti and Silvio [153] studied the failing Fontan operation to determine its factors and correlation with the failing Fontan circulation. The hypothesis stated that the Fontan operation's success or failure depends on the anastomosis site. Patients were categorized into two groups for this study: symptomatic Fontan failure and no symptomatic Fontan failure. There existed no statistical significance between the pulmonary artery and systemic

arterial pressures between the two groups. The failing Fontan group had higher pressure at the end of the pulmonary vein. Pressure in the SVC and IVC was 5.4 *mmHg* and 6.8 *mmHg* higher. The mean cardiac output of the failing Fontan group was 36% lower, pressure loss over the cavopulmonary connections was higher; this was more significant in the IVC connection. The total energy loss was studied across the cavopulmonary connections between the two groups. The failing Fontan group had higher energy loss in the inferior SVC. No statistical significance was seen in the energy loss in the superior SVC. The possibility of reducing these elevated pressure drops depends on minimizing the resistance and energy loss within the TCPC.

2.1.3.4. In-vitro and in-silico approach

Snyder et al. [73] developed a numerical model of the cardiovascular system for NASA. This model included the LPM approach to model characteristics of every branch of the circulatory system. The LPM took into account the effect due to resistance, inductance, and compliance. For this study, a three resistance-compliance element was used to model the pulmonary system based on the average flow and pressure values. This model is split into four sections, the head, thoracic cavity, abdominal cavity, and lungs. Additional pressure generators and grounding relevant compliances to intrathoracic or abdominal pressure were done, including gravity and respiration in this system. In modeling the Fontan circulation, patient data is necessary as the patients have different pulmonary compliance, flow characteristics in the pulmonary circulation, and systemic and venous pressures.

2.1.4. Passive and Active techniques to improve Fontan

To power the pulmonary system, mechanical assist devices have been proposed [154] [155] [156] [157] [158] [159]. These mechanical devices have successfully dropped the IVC pressure back to the normal value of 8 mmHg theoretically. Some current issues include the requirement of two pumps, re-circulation induced by barriers, pumping in one direction, obstruction, and the device cannot be shut off. With fenestration, these issues can lead to pulmonary embolisms, driveline infection, or stroke [154].

Self-powered Fontan is the technique to tap the reserve mechanical energy of the native heart and inject it into the Fontan system. The IJS is placed from the aorta to the Fontan conduit. Assessment of energy losses due to flow mixing and flow jet impingement is critical. Understanding the alternative surgical technique requires a multi-scale 3D and 0D CFD analysis. The full 3D CFD model is tightly coupled to the LPM model, and the 0D model does not model the TCPC. The pulmonary flow is tuned to increase by 50% in this IJS model, directly affecting the PVR. Accurate PVR vs. flow models are not available as other studies include other responses such as exercise, dobutamine stress, and oxygen inhalation [145],[146],[147],[148],[149],[150],[151],[159], [160].

To have a maximum pressure drop at IVC, the IJS configuration was optimized. The nozzle diameter and location were optimized using steady-state study conditions in a CFD model; it was later implemented into three different models. Children's Hospital of Philadelphia gave a patient-specific model through MRI scans [75], [161], and synthetic models were built using patient data average [79],130],.

2.1.4.1. Ejectors and Nozzles

Brahim et al. [162], Kandakure et al. [163], Yadav et al. [164] conducted a study on the effect of liquid to gas mixing using ejectors in a convergent-divergent mixing chamber. Design parameters such as nozzle to throat area ratio, primary to secondary flow ratio, throat to nozzle length, and nozzle diameter were analyzed to optimize mixing, mixing efficiency, and entrainment. Low entrainment rates are observed as the driving pressure decreases due to a decrease in pressure.

Mukherjee et al. [165] conducted a study to analyze liquid to liquid dispersion efficiency using ejectors. Energy loss could be minimized by selecting the optimal primary to secondary flow ratios and the correct throat to nozzle area ratio. A decrease in efficiency is attributed to mixing, flow channel shape, and friction.

The stage III literature mainly focuses on various alternative techniques to improve the efficacy of the procedure. Along with the alternative techniques, the study on PVR, a critical hemodynamic parameter, is conducted. Researchers have studied various factors that affect the PVR, and the goal is to reduce the PVR in Fontan patients as complications arise after the surgical procedure. The usage of injection jet, a passive technique to improve the Stage III procedure, is proposed and discussed in section 2.1.4. As discussed in section 1.7, the goal of this research is to validate the in-silico simulations by performing the in-vitro simulation.

2.2. Mock Flow Loop

The MFL is a mechanical representation of the human cardiovascular system for in vitro testing. The MFL was developed to test artificial heart valves, aortic balloon pumps, and

other cardiovascular devices. The MFL consists of resistance valves that provide constant flow by altering the pressure. Newer MFL includes additional features such as compliance resistance, fluid inertia, pulsatile flow, atrial contraction, pulmonary and systemic circuits.

The first MFL was developed to test the artificial heart valve; the artificial heartbeat was created using pulse duplicators driven by stepper motors [166]. For valve flow visualization, many systems included transparent and flexible ventricles [166], [167] [168] [169] [170] [171] [172] [173]

Cornhill et al. [173] developed an MFL to test prosthetic heart valves. The MFL had a collapsible silicone bag in a pressurized airtight box to mimic the left ventricle. The left ventricle was supplied with pulses of compressed air, controlled by a solenoid valve. The system having characteristic impedance, total arterial capacitance, and peripheral resistance reproduced conditions to test the artificial heart valves. The system failed to simulate the atrial systole, and inertial effects were ignored.

Kolff et al. [174] developed an MFL that consisted of both systemic and pulmonary sides. The ventricles were operated using compressed air. Tall columns of water obtained pressures in the pulmonary artery and aorta. Diastolic pressure could be changed by changing the height of the fluid column. The excessive inertia produced by the water columns had to be overcome to move the fluid up the tube. The inertia was overcome by using a pressurized air chamber that surrounded the bottom half of the tube. For this MFL, resistance valves were not used as resistance increased with increase inflow.

Reul et al. [175] developed an MFL using the flexible tube for the aorta and its branches. The MFL was suspended in a Perspex box filled with water. The loop was connected to a

Windkessel chamber with adjustable air volume for compliance. A tube membrane was used to apply resistance to each branch of the system. The MFL was driven by a cam system that supplied the pulsatile pressure to the mock ventricle. Inertance in this MFL is taken into account by dimensioning the aorta and its branches. The MFL mimicked the systemic circulatory system but did not include a method to connect and test VADs.

Donovan et al. [166] developed an MFL to test new artificial hearts in in-vitro conditions; the cardiovascular device testing capabilities of the rig are limited due to the absence of atria or ventricles. This system was compact and showed positive results in comparison to the calf model.

Scotten et al. [176] developed an MFL to evaluate mitral valve prostheses. A cam created a transparent mock ventricle and was driven to push the fluid in a sealed chamber that includes the ventricle. The ventricle volume was found concerning time by examining the cam position and the cam's cross-sectional area concerning time. The ventricle pumped the fluid into a compliant latex rubber aorta, then to the resistance and the compliance elements. Resistance was simulated by using cellulose fiber water filters. These water filters had a pore size of 5 and 50 μm for characteristics and peripheral resistance, respectively. The resistance values in this MFL could be altered by the cellulose fiber water filters into a plastic tube when the MFL was in operation; the procedure produced discretely variable resistance rather than a continuously variable system. Compliance for this MFL was obtained by the volume of air trapped above the resistance elements. This MFL produced pressure and flow results.

Rosenborg et al. [177] summarized the design and evaluation of the Penn State MFL. The Penn state MFL was designed in 1971 for in-vitro testing of VADs. The MFL included

compliance, resistance, inertance, systemic and pulmonary circulation, VAD connections, and adjustable cardiac conditions. The values selected for the MFL with a cardiac output of 5 L/min , MPAP of 15 mmHg , MAP of 100 mmHg , mean RAP of 2.2 mmHg , and mean LAP of 7.5 mmHg . The resistance and compliance values used for this MFL were based on a healthy male, as mentioned in Table 1. Inertance values were assumed to be equal for systemic and pulmonary circulation, which were incorrectly assumed. This MFL showed satisfactory results representing the human circulatory system and providing a suitable method for in-vitro blood pumps.

Table 1 MFL parameters chosen by Rosenborg et al. [177]

Systemic resistance	Pulmonary resistance	Systemic capacitance	Pulmonary capacitance	Systemic Inertance	Pulmonary Inertance
1.36	0.14	1.33	4.4	0.0158	0.0158
mmHg.s/ml	mmHg.s/ml	mL/mmHg	mL/mmHg	mmHg.s ² /mL	mmHg.s ² /mL

Verdonck et al. [178] created an MFL to test mitral valves, later altered. The MFL could replace the aortic and mitral valves. Fluid enters the MFL from a preloaded reservoir representing the lungs into the two pulmonary veins, which carry the fluid through the mitral valve. The fluid from the left ventricle travels through the aortic valve into the afterload system that consists of a Windkessel chamber for compliance and a hydraulic resistor. A venous reservoir was included to obtain a constant venous pressure of 5 mmHg . The latex atrium and silicone left ventricle were anatomically shaped and mounted in Perspex housing filled with water. An external circuit controlled the pressures in the

Perspex housing. A feedback system determined the pressure delivered to the ventricle. For systole, positive pressures were induced, and for diastole, negative pressures were used. The positive and negative pressure resulted in physiologically inaccurate ventricle filling. This MFL was used by Vandenberg et al. [179] to assess intra-arterial LVADs hydrodynamic performance.

Trittenwein et al [180] designed a neonatal MFL to investigate the effect of extracorporeal membrane oxygenation. The loop was required to produce lower cardiac output with decreased heart rate such that neonatal conditions could be mimicked. The authors concluded by stating that this MFL is valuable in demonstrating conditions in neonates. Due to lack of patient reaction and medication effect, this cannot replace clinical studies. In neonates, biventricular heart failure could not be created as the system lacked pulmonary circulation, resulting in inaccurate simulated ventricle preload.

Sharp et al. [181] conducted a study on the benefits of several Windkessel models from basic two-element to advanced five-element Windkessels. An MFL was developed and compared with existing MFL and natural heart results. A computer simulation was conducted on RC, RLRC, RCLRC, and RC models; R stands for resistance, L for inertance, and C for compliance. Results showed that as each element was added to the design, there was an improvement in results compared to the human data. Four element windkessel model showed slight improvement when compared to the three-element windkessel model. The addition of a fifth element improved the circuit significantly. Due to the difficulty in the construction of the RCLRC model, the RCR model was favored.

Balao et al. [182] studied the elastance-based control of MFL. A new control strategy for the MFL was developed by using the concept of elastance. Elastance is the instantaneous

ventricular pressure vs. the ventricular volume of the ventricle. The maximum value of elastance was taken at the point of end-systole or a measure of ventricular contractility. The authors stated that the design was successful in using elastance-based control to the ventricular chamber's contractility. The inertial effects in the circulation and ventricle were ignored, and only the systemic circulation was simulated.

Fiore et al. [183] designed an MFL to study the mitral valve surgical correction. The study involved developing a flexible mock ventricle and studying the change of shape during the cardiac cycle. This information was used to study the fluid dynamics of ventricular filling. For this MFL, the end-systolic shape of the ventricle was chosen to keep the shape similar when the ventricle fills with the fluid. The ventricle was constructed using the finite element model (FEM) model, the structure was reinforced with five bands, and the model's thickness was 0.21 *mm*. Negative pressure was applied around the mock ventricle to induce ventricular filing. The system's inaccuracy did not exceed 3.5%, and the design behaved naturally like a left ventricle. The mock ventricle represented that of a healthy male. Larger ventricles volumes seen in conditions such as dilated cardiomyopathy could not be replicated in this MFL.

Goodwin et al. [184] developed an infant MFL for education simulation. This study replicated the cardiovascular parameters of the infant.

Pantalos et al. [185] aimed to create an MFL to mimic the Frank-Starling response in normal, failed, and partial recovery situations of the heart. The MFL used a flexible polyurethane atrium and ventricle. The ventricle was placed inside a pressurization chamber with a semi-rigid dome for mounting inflow and outflow valve. The ventricle was not anatomically shaped to produce accurate flow dynamics in the ventricle. The MFL

allowed for aortic outflow cannulation and atrial and ventricular apex inflow. A polyurethane aorta was connected to the ventricles that led to the systemic and coronary vasculature. The inertial effect was taken into consideration through the cross-sectional area and length of the tubing. The pressure-volume loop produced by the MFL represented a natural situation, and the MFL mimicked the Frank-Starling response for all conditions. The MFL also produced accurate hemodynamic waveform magnitudes and morphology for all conditions. Limitations of this study involved a lack of pulmonary vasculature and noise from the aortic pressure waveform. This MFL was later used by Glower et al. and Koenig et al. [186] to evaluate artificial vasculature devices and investigate the hemodynamic and pressure-volume response to continuous and pulsatile VAD.

Koenig et al. developed a systemic MFL to test continuous and pulsatile VAD. The hemodynamic and ventricular pressure-volume response was tested at different levels of assist for pulsatile and continuous flow devices. A mock ventricle was created in a hemi-ellipsoid shape with a semi-rigid dome with the aortic and mitral valves mounts. The pressurized chamber controlled the system to obtain the required pressures and heart rate. A high-fidelity pressure-volume conductance catheter was used to monitor the ventricular pressure and volume. A compliant latex tube in a sealed chamber provided the resistance in the MFL. Pressure from the driveline was supplied to the ventricle and the sealed chamber to produce the required coronary flow. The limitation of the study involved the absence of pulmonary circulation.

Litwak et al. [187] constructed an MFL with coronary vasculature. This MFL aimed to study the aorta outflow graft location with continuous and pulsatile flow VAD. The atrium and ventricle used in this MFL were made of flexible polymer sacs, and the ventricle was

placed in a pressure chamber. The apex of the ventricle achieved ventricular cannulation into the aorta. A coronary and systemic vasculature that includes the carotid artery was included. At the downstream of the MFL, the artificial aorta was connected into the mock vasculature. The accuracy of the cardiovascular simulation is improved by the inclusion of coronary circulation and carotid artery. As the pulmonary circulation did not exist, the venous return was ignored. A latex tube inside a pressure chamber mimicked the phasic coronary resistance. The same pressure pulse that drove the ventricle source was used. As a result, an elevated coronary resistance during the ventricular systole and reduced coronary resistance during diastole was seen. The above phenomenon resulted in a biphasic coronary waveform.

Liu et al. [188] developed an MFL to test continuous-flow LVADs, as seen in Figure 14. Semi ellipsoidal-shaped silicone diaphragms used in pressure chambers mimicked the ventricles. For diastole, negative pressure was applied, and for systole, pulses of compressed air were sent to the chambers. Clear tygon tubing was used to connect all components, VAD was connected via the apex of the mock ventricle and systemic arterial tank. Check valves were used to achieve uni-directional flow. This MFL was sufficient to test LVADs under various conditions. An accurate prediction of LVAD performance could not be provided due to the inability to obey the Frank-Starling law.

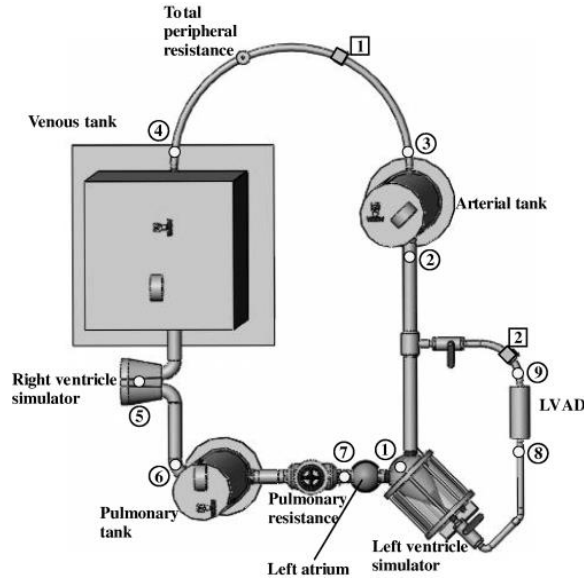


Figure 14 MFL by Liu et al. [188]

Timms et al. [3] developed an MFL to test VADs. The aim was to develop a new MFL that could produce normal and heart failure conditions. The rig adhered to the Frank-Starling law, but the ventricular volume could not be measured. The MFL produced accurate data in terms of pressure and flow for normal and heart failure conditions. Limitations involved the use of heavy brass check valves, restriction of flow in the pulmonary circuit, and lack of measuring ventricular volume.

Kozarski et al. [189] developed a hybrid MFL. This system uses features of present hydraulic and electrical models of the simulation. A flow generator was used to convert the incoming electrical signal into an appropriate flow for the hydraulic. The hydraulic component represented consists of characteristic arterial compliance, resistance, and inertance. They include pulmonary circulation, accurate representation of fluid inertia, and variable compliance.

2.2.1. Resistance

There is a significant effect on the circulatory system due to the resistance to blood flow. The resistance R increases as the radius r of arteries and veins decreases. Resistance is also influenced by the length of the artery L and the viscosity of the blood η . Equation (2) provides the governing equation (2)

$$R \propto \frac{\eta \cdot L}{r^4} \quad (2)$$

A small pressure drop is seen when blood enters and exits the aorta, exhibiting very little resistance. Significant pressure drop on the blood is seen when blood enters the parts of the systemic circulation that includes smaller arteries and the arterioles as they provide higher resistance. By constricting or dilating the arteries, the body can change the resistance to flow. Dilation decreases the resistance causing more blood to flow to the artery, and constriction produces the opposite effect.

SVR is defined as the resistance by the whole systemic circulation to the flow of blood. If the central venous pressure (CVP) is available. The value is usually assumed to be close to zero if CVP is not available. Equation (3) provides the relation between SVR, MAP, CVP and CO

$$SVR = \frac{MAP - CVP}{CO} \quad (3)$$

The value of resistance is obtained by a flexible tube in conjunction with a pinch valve. A variable level of resistance is obtained by lowering an electrical signal to occlude the valve[3],[187], [190] [191] [192] [193].

Donovan et al. [166] provided an innovative technique in obtaining the resistance. Figure 15 shows the mechanism used. Upon rotating the plate about a pivot to occlude the flow tube, the resistance of the pulmonary and systemic system was obtained. The value depended on the angle of rotation which was controlled by a lever arm. The lever arm is connected to bellows placed inside a chamber having water at a specific pressure. The bellows contract due to the pressure difference; this occurs when the aortic/pulmonary arterial chamber pressure increases. Due to this contraction, the valve plate is rotated about the pivot as the bellows are pulled on the lever arm. This makes the valve plate move, making the fluid flow through the flow tube due to a more cross-sectional area. This also lowers the resistance and lowers the arterial pressure. To obtain systemic resistance, an extra spring was used in parallel to the bellows to accommodate for the higher pressure.

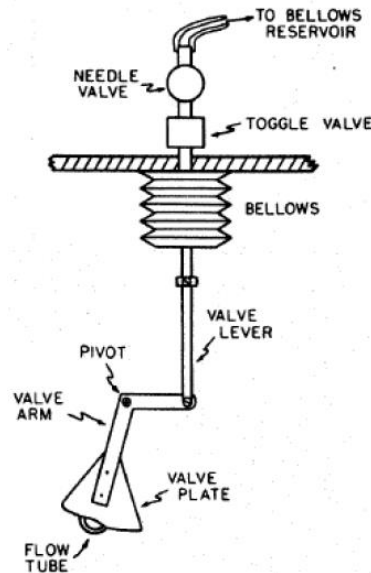


Figure 15 Resistance mechanism used by Donovan et al. [166]

Trittenwein et al.[180] and Liu et al. [188] used sintered aluminum oxide porous blocks to supply resistance. The blocks had the necessary permeability to represent peripheral

resistance and impedance characteristics. The resistance value was adjusted by blocking unblocking the pores on the block; a moving sliding plate was used for this technique.

Scotten et al. [176] used Equation (4) and (5) to represent the pressure drop and resistance

$$\Delta P = R.Q \quad (4)$$

$$R = \frac{8.\mu.L_R.\pi}{A_R^2} \quad (5)$$

R is the resistance, Q is the volumetric flow rate, μ is the fluid viscosity, ΔP is the pressure drop, and L_R A_R are the effective length and area of the resistance tubing. Figure 16 shows the method to apply resistance by compressing small flexible tubes using a flat plate. A higher value of resistance is obtained as the magnitude of compression is increased. Ferrari obtained resistance by a slide that blocked the flow through a pipe when moved up and down. Resistance could be adjusted by choosing a value for the mean arterial pressure or by choosing a value that moved the slide.

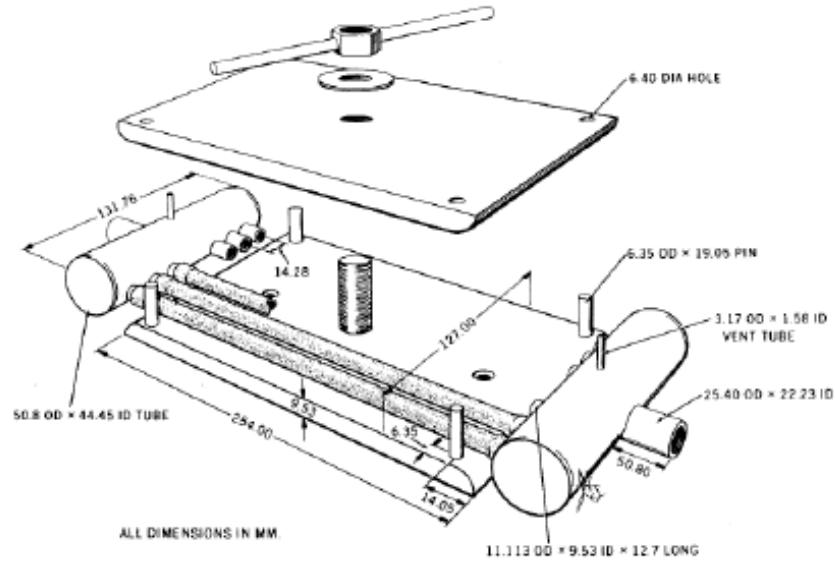


Figure 16 Resistance segment used by Scotten et al. [176]

Patel et al. [194] used a 1.5-inch gate valve to obtain the resistance value. Resistance values for simulation of healthy were 0.85 mmHg.s/ml and for congestive heart failure was $1.2\text{--}1.4 \text{ mmHg.s/ml}$.

Pantalos et al. [185] obtained resistance for peripheral and proximal components by using a chamber that contains open cell foam with different densities. To adjust the value of resistance, the foam can be compressed by a sealed piston.

2.2.2. Inductor

The pulsatile nature of the blood requires constant change in motion when flowing through the circulatory system. On the mock loop, this can be represented by including an inertance component. This component can be achieved with the correct volume of fluid being flown in each section of the circulatory system and representing these values on the mock loop with pipe lengths and diameters.

The Windkessel model models the circulatory system. The system represents features such as resistance, compliance, and inertance in the form of electrical drawings. Many mock loop simulations use arterial compliance C , characteristic resistance R_c , and peripheral resistance R_p for the three-element Windkessel model. A four-element Windkessel model includes an inertial component L . This is shown in Figure 17

Stergiopoulos et al. [195] reported that the inertance (L_i) of a tapered wire can be represented as shown in Equation (6)

$$L_i = \frac{\int_0^{l_s} C_u \cdot \rho \cdot dx}{A} \quad (6)$$

Where l_s is the segmental length, ρ is the blood density; A is the cross-sectional area, and C_u is the coefficient considered for a non-flat velocity profile that equals $4/3$ for low frequencies. Similar to spring constant, inertance in series and parallel are calculated. Inertance in series is the total sum of inertances and in parallel is shown in Equation (7)

$$\frac{1}{L_1 + L_2} = \frac{1}{L_1} + \frac{1}{L_2} \quad (7)$$

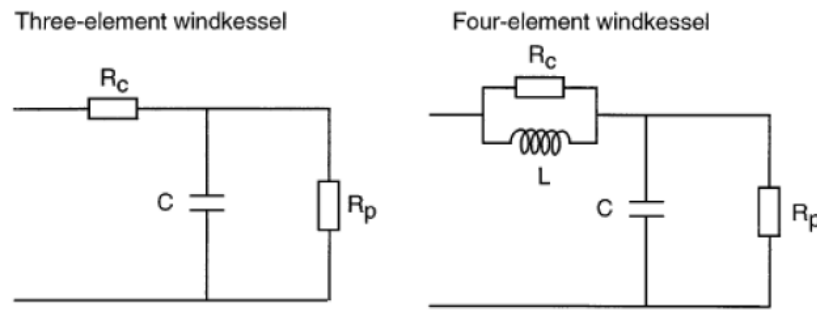


Figure 17 Three and four element Windkessel model by Stergiopoulos et al. [195]

Noble et al. [196] conducted a study in dogs on the contribution of blood momentum to left ventricular ejection. This was conducted by placing a flow probe in the aorta and

pressure transducers in the left ventricle and aorta. Controls noted and showed that the ventricular pressure was higher during the ejection period and an increase in aortic pressure above the ventricular pressure in the last 30-50% of the ejection. By placing an aortic occlusion device around the aorta, that required 20 ms to completely close, a spike in the ventricular pressure trace, and then a distant reduction in pressure. Results showed that blood momentum affects ejection.

Scotten et al. [176] used Equations (8) and (9) to solve inertance when the three-element Windkessel model was used.

$$\Delta P = \phi \cdot \left(\frac{dQ}{dt} \right) \quad (8)$$

$$\phi = \rho \cdot \frac{L_1}{A_1} \quad (9)$$

ΔP is the change in pressure, ϕ is the inertance, Q is the volumetric flow rate, t is time, ρ is the fluid density, L_1 and A_1 represent the length and cross-sectional area of the pipe.

Stegiopulos et al. [195] aimed to find the difference between three and four-element Windkessel models in dogs, humans, and a mock loop. The main aim was to find the difference in pressure and flow measurements in the aortic section. The results obtained can be seen in Figure 18, which shows a significant difference in accuracy between the two models. The four-element Windkessel model presented a greater value of flow measurement aortic pressure compared to the three-element Windkessel model.

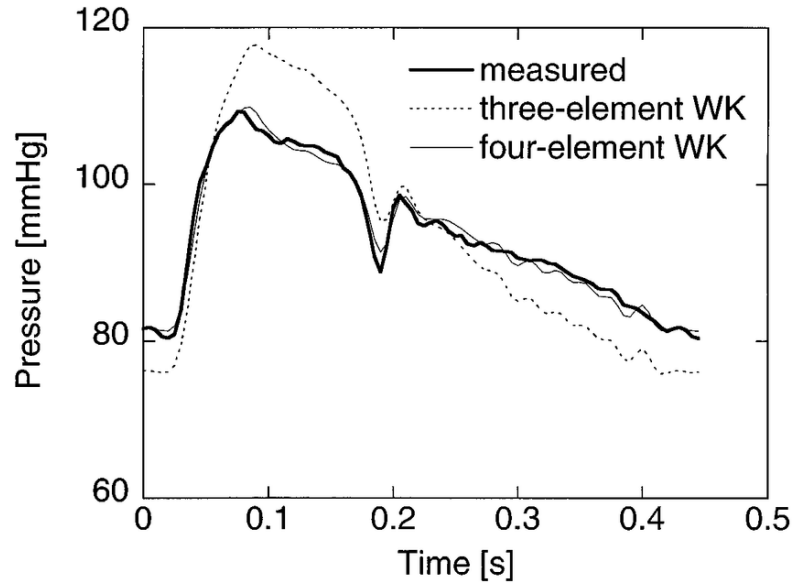


Figure 18 Comparison of measured aortic pressure trace vs three and four element windkessel simulations[195].

Ferreira et al. [197] conducted a study on 26 human patients to estimate arterial compliance using the three and four-element Windkessel model. Improved representation of the arterial compliance was better seen by adding the fourth element.

2.2.3. Compliance

The tendency of the blood vessel volume to increase as blood pressure increases is defined as Compliance [4]. Compliance is inversely related to stiffness, i.e., vessel walls stretch at a higher value of compliance. It can be expressed as shown in Equation (10)

$$\text{Compliance} = \frac{\text{Change in volume (ml)}}{\text{Change in pressure (mmHg)}} \quad (10)$$

Compliance of veins is approximately 24 times greater than that of arteries [4]. Hence veins can hold a large volume of blood when compared to arteries. Ventricle's pressure-volume curve is influenced by ventricular compliance. The end-diastolic pressure for any given

end-diastolic volume increases if the ventricle compliance is decreased. This is represented in Figure 19

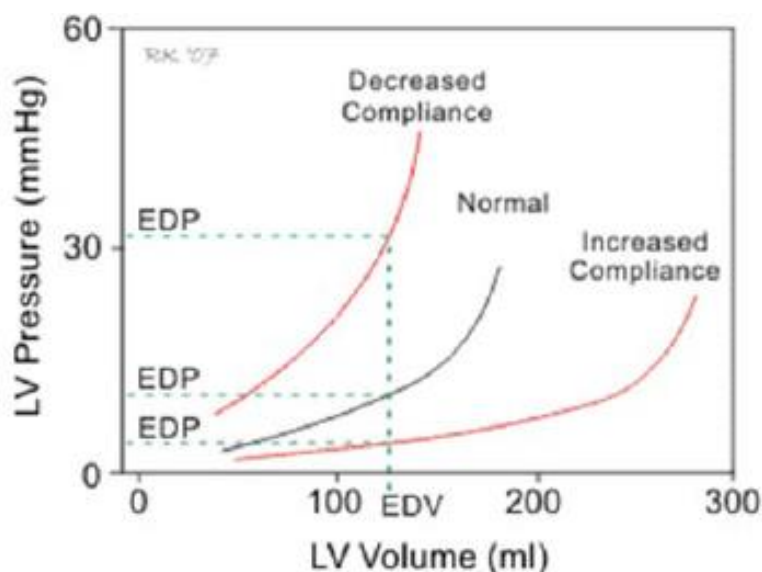


Figure 19 Effect of ventricular compliance [5]

Donovan et al. trapped the air volume in each chamber above the circulatory fluid to obtain compliance.

Garrison et al. [198] designed a mock loop for hemolysis studies associated with VADs. Two 70ml sacs and a sealed chamber were used as the compliance chamber. The chamber designed was large to fit one full and empty sac inside. The chamber limiting volume changes, hence compliance. This feature was used for aortic and venous compliance.

Marcus et al. [199] conducted a study on healthy patients. The aim was to determine the arterial compliance and compare it with the two and three-element Windkessel model. The hemodynamic profile of the population is mentioned.

Woodruff et al. [200] performed studies on cardiac performance in microgravity using a compact mock loop. The Penn State mock loop was chosen as the base, and the weight of the compliance chambers was reduced. In Figure 20, a new spring design was used to

reduce size and weight. To accommodate many different spring diameters and to center the spring, a conical seat is used. Target values for arterial and venous compliance were 1 and 10 $ml/mmHg$. Spring values were chosen at 5, 10, 15 $ml/mmHg$ for venous compliance and 0.5, 1, and 1.5 $ml/mmHg$ for arterial compliance. Limitations in this study included changing springs for each variation in compliance that resulted in inefficient testing procedure, and approximations were made for the desired spring constants and their corresponding compliance values. The weight and volume of the new design were 47% and 64% lower compared to the Penn State design.

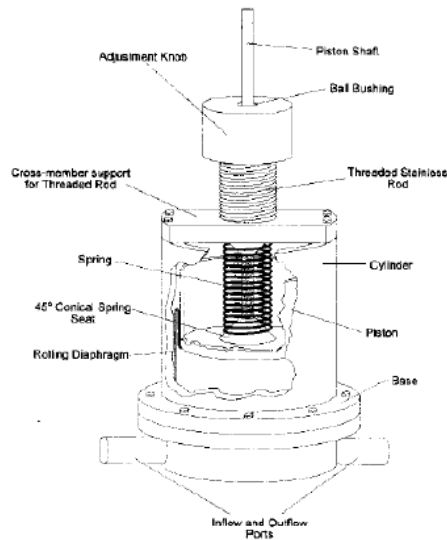


Figure 20 Compact spring compliance chamber by Woodruff et al. [200]

Arabia et al. [201] ,Figure 21, Ferrari et al. [202] used a spring capacitor to obtain compliance. Arabia et al. used 3.6, 4.8, 82.5, and 10 $ml/mmHg$ as compliance values for systemic arterial, pulmonary arterial, systemic venous, and pulmonary venous. Pantalos et

al. [185] used the concept of spring for compliance. The required amount of compliance was obtained by using a spring-loaded piston on a roll sock diaphragm.

Kolh et al. [203] studied the effect of the increase in aortic compliance on ventricular performance. The aim was to investigate the energetic cost of cardiac ejection and left ventricular contractility when aortic compliance applied was increased. The results obtained in this study showed that the effect of increasing aortic compliance had a significant reduction in the energetic cost of the heart, and the effect on the contractile function was minimal.

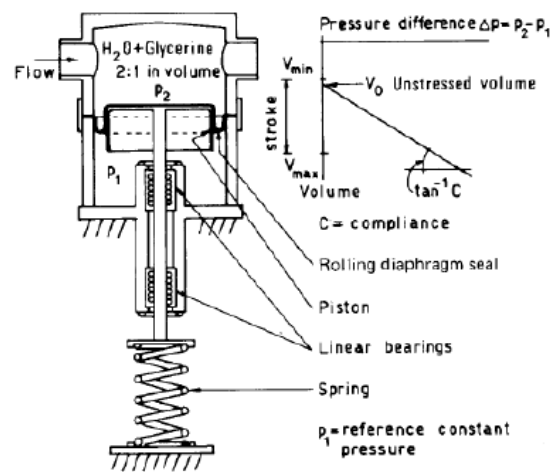


Figure 21 Spring compliance chamber by Arabia et al.[201] .

Lick et al. [204] adjusted the compliance chamber to further a previous study on an artificial lung. Previous in vivo studies of an artificial lung produced a 50% right heart failure immediately causing death. Initial designs were modified by including an inflow compliance chamber, inflow separator, and modified outlet geometry. A solvent cast, polyurethane, was included in the method to obtain the compliance chamber. Pressures would not be generated externally of the chamber using the polyurethane bulging segment

encased in open-faced housing. Significant improvement in results was noted in the new in vivo trials.

Dumont et al. [190] developed a pulsatile bioreactor for the tissue engineering of an aortic valve. The system used variable compliance, where the air pressure above the water inside the chamber was altered. This design would give variable compliance under the assumption that change in volume due to change in pressure is negligible. The mock loop only represented systemic circulation and lacked pulmonary circulation. As the pressure changes in the whole system due to varying compliance, this concept of a compliance chamber is not suitable for full mock circulation. A value of $0.4\text{-}1.2\text{ ml/mmHg}$ was used for compliance.

Papaioannou et al. [205] conducted a study on the effect of arterial compliance on the effectiveness of intra-aortic balloon counterpulsation. Windkessel chamber with a variable air volume was used to simulate the compliance. The isothermic air process assumed by $PV = \text{constant}$, giving rise to the formula for compliance as $C = V / P$. Varying the compliance between $1.05\text{-}2.62\text{ ml/mmHg}$, the heart rate was between 80, 100, 120 *bpm*, and the mean aortic pressure was 55, 75, and 105 *mmHg*. Results showed that arterial compliance is a significant factor that influenced the performance of intra-aortic balloons. Left ventricle stroke volume increased by 6% for systolic dysfunction when the arterial compliance was increased. No change was seen for diastolic dysfunction.

Bustamente et al. [191] created a compliance chamber using a flexible rubber wall. The chamber was primarily clear plastic. A flexible rubber diaphragm was used on one wall to dampen the pulse pressures. The diaphragm was removable to accommodate a new

material having a different stiffness if the compliance needed to be changed. Using the flexible rubber, positive results were recorded.

Haft et al. [206] developed an artificial lung compliance chamber. The mock loop model did not include the inertance and adjustable resistance element but relied on the tubing resistance and pulsatile flow VAD. Constant pressure was delivered into the VAD, which delivered fluid to the compliance chamber; Figure 22 shows the compliance chamber made from a flaccid polyurethane bag in an airtight box that receives compressed air to alter the compliant nature of the bag. External pressure applied to the compliance element maximized the value of compliance and altered its time scale by augmenting diastolic emptying and before systole maximize the capacitance.

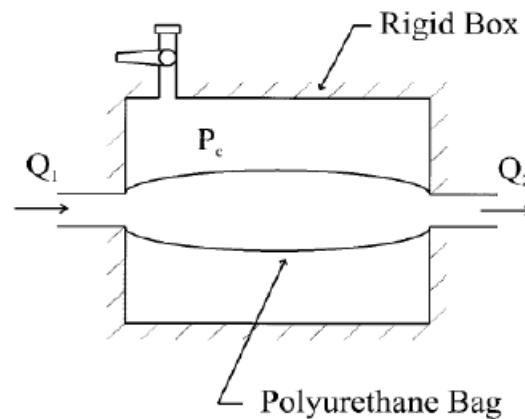


Figure 22 Compliance element used by Haft et al. [206]

Fiore et al.[183] The arterial compliance is used as part of the hydraulic side of the hybrid system. This reduced the effect of mechanical and hydrodynamic disturbances and improved the quality of pressure measurement. The value selected for the compliance was $1.2 \text{ ml} / \text{mmHg}$. Additional arterial compliance was added to the electrical circuit; altering the arterial compliance can obtain a variable compliance value. Loh et al. [214] chose the following values for compliance.

The values for aortic and left ventricular compliance are higher compared to the other literature. Airtight tanks with a trapped volume of air above the fluid were chosen for compliance mechanism.[187],[188],[206], [207] [208] . Variable levels of compliance [209] [210] [211] [212] [213] [214] [215] [216] [217] [218] are produced continuously by these chambers. The mock loop requires a shutdown for each compliance change. Litwak et al. used 43.6, 4.9, and 5.6 L as volumes for systemic venous, systemic arterial, and pulmonary compliances. The volume of air is altered by incorporating an air valve. Equation (11) was used to compute the compliance

$$C = \frac{dV_{fluid}}{dP_{fluid}} = \frac{V_{air}}{P_{air}} = \frac{V_{tank} - A_{tank} \cdot h_{fluid}}{P_{fluid} - \rho \cdot g \cdot h_{fluid}} \quad (11)$$

C corresponds to compliance V_{air} and P_{air} are the volume and pressure (absolute) of air in the tank and the tank's volume and cross-sectional area. P_{fluid} and h_{fluid} are the pressure (absolute) and height of the fluid. ρ is the density of the fluid and g is the acceleration due to gravity.

Hassani et al. [219] developed a mathematical model to study aortic aneurysms. Compliance, inertance, and resistance were included in the model. Equation (12) was used to compute the compliance of an elastic vessel.

$$C = \frac{3 \cdot \pi \cdot R^3 \cdot Z}{2 \cdot E \cdot h} \quad (12)$$

C is the compliance, R is the radius of the vessel, Z is the length of the vessel, h the thickness of the vessel, and e the elastic modulus of the vessel.

Timms et al. a [3]trial compliance was achieved by using an open to air chamber that changes fluid volume in response to venous return. A pressure change is created due to the

height of the fluid and hence changing the level of compliance. Using the fluid-filled chamber with a trapped air method, the aortic, systemic vascular, and pulmonary arterial and pulmonary vascular compliance was used.

Stergiopoulos et al. [220] study was conducted into current methods to estimate the arterial compliance and compared the results with the previously developed mathematical model, including 55 arterial segments modeling the major arteries. Fluid inertia, fluid friction, and nonlinear compliance were considered for this model. Three three-element Windkessel methods were analyzed using various methods, and Four two-element Windkessel was employed, including the area method, two-area method, and the integral method. All methods based on the two-element Windkessel produced less than 10% errors than the three-element Windkessel model. It was concluded that the three-element Windkessel model could be used to represent the arterial system accurately. The two-element Windkessel model represents the systemic arterial tree at low frequencies.

Segers et al. [221] concluded that the pulse pressure method was consistent for estimating total arterial compliance. The in vivo results of the pulse pressure method are compared with stroke volume: pulse pressure ratio and the area method.

2.3. Summary

The three-stage palliative procedure is a series of surgical procedures to treat the HLHS anomaly in neonates. Stage I involves the Norwood procedure, where the surgical procedure aims to provide an unrestrictive systemic blood flow while balancing the pulmonary flow. Stage II involves the Bi-directional Glenn/ comprehensive stage II, and this surgical procedure aims to lower the load on the right ventricle and provide low-

pressure pulmonary flow. The BDG procedure involves removing mBT shunt and dissection of SVC from the right atrium and anastomosed to Right Pulmonary Artery (RPA). The comprehensive stage II is an alternative to BDG. Similar physiology is established between comprehensive stage II and the Glenn procedure. An in-depth literature survey is conducted towards the in-vitro and in-vivo simulations to address complications after the BDG and comprehensive stage II procedure.

Complications involve unilateral pulmonary artery stenosis. An alternate approach is also known as the Assisted Bi-directional Glenn surgical procedure, is also discussed. A novel surgical technique to the comprehensive stage II has been discussed in the literature to reduce surgical trauma in patients. The HCSII procedure reduces the surgical trauma and avoids creating aortic arch reconstruction and Damus-Kyle Stansel (DKS) connection. The HCSII procedure applies to patients with sufficient antegrade aortic flow to sustain upper body perfusion. Stage III involves the Fontan procedure; this procedure aims to connect the systemic and pulmonary circulations in series. An in-depth literature study focuses on extra cardiac Fontan operation and PVR. To improve the efficacy of the stage III procedure, a novel passive surgery technique is discussed using an injection jet.

3. Methodology

3.1. Anatomical model

3.1.1. HCSII

Arnold Palmer Children's Hospital provided the patient-specific angiogram data to develop the phantom for in-vitro simulation. Figure 23 A and B represents the native ascending aorta, right subclavian artery (RSA), right carotid artery (RCA), left subclavian artery (LSA), and left carotid artery (LCA). The diameters of the native ascending aorta, RSA, RCA, LSA, and LCA were 9.96 mm , 4.53 mm , 4.53 mm , 5.75 mm , 4.36 mm . The lengths of the native ascending aorta and LSA and LCA combined length was 29.19 mm , 13.21 mm . Figure 23 C and D represent the Glenn procedure performed. Figure 24 A, B, C, D represents the aortic root and its dimensions. The main pulmonary artery (MPA) root, the aortic arch, and the descending aorta having diameters of 22.67 mm , 8.26 mm (averaged), and 9.88 mm . The lengths of the MPA root, the aortic arch, and the descending aorta were 20.68 mm , 20.59 mm , and 43.06 mm . DeCampi et al. mention that the hybrid comprehensive stage II technique avoids creating Damus-Kyle-Stansel (DKS) connection and aortic arch reconstruction. The HCS II procedure also involves suturing of baffle using a pulmonary homograft material within the pulmonary bifurcation from the right to the LPA orifice. By preserving every eigen feature of the physiology, the phantom was designed to validate the clinical study conducted by performing in-vitro simulations. The information obtained from the angiogram of three de-identified patients was used to design the phantom.

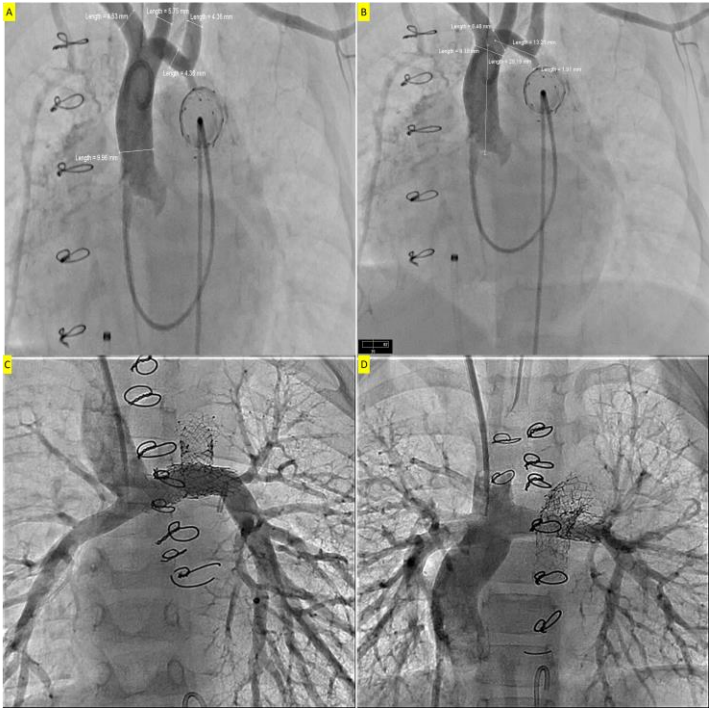


Figure 23 Angiogram data of three de-identified patients provided by Arnold Palmer Children’s Hospital

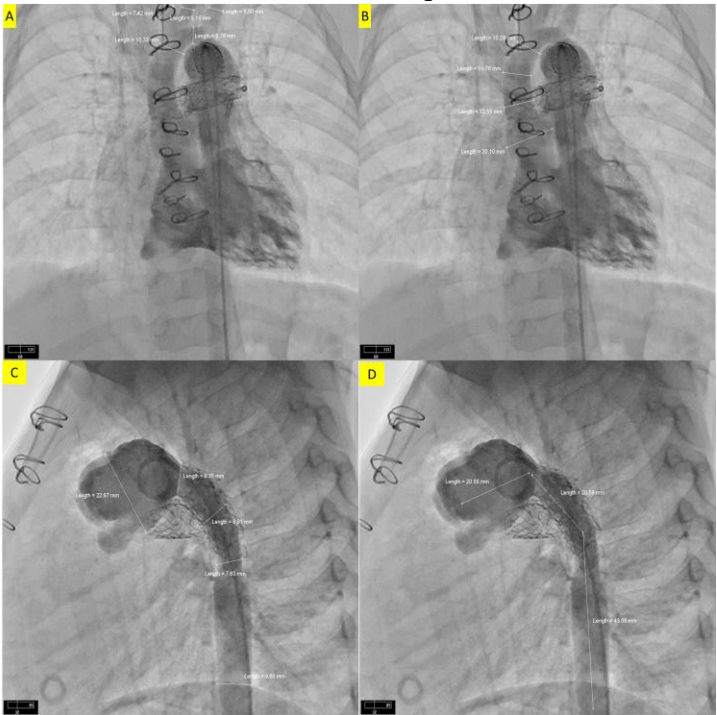


Figure 24 Angiogram data representing the aortic root and their dimensions

The development of the centerpiece is a two-part process; the top half contains all the conduits designed based on the angiogram data. The conduits in the phantom represent the diminutive aorta, MPA, LPA, and RPA. Since the RSA, RCA, LSA, and LCA diameters are lower than other sections, a single conduit was designed to represent the upper circulation. The diameter of this conduit is the summation of RSA, RCA, LSA, and LCA diameters. Following the physiological procedure, the phantom is designed without the patent ductus arteriosus, DKS connection, and the native aortic arch remains natural. The region corresponding to the patent ductus arteriosus is stenosed. The main constrain to be followed during the design stage was no baffle movement and the stent. An elliptical section was designed on the MPA to place the baffle; the stent below the baffle. To integrate the centerpiece with the MFL, barbed conduits are designed at six locations. The pressure sensors are placed over the barbed conduits to obtain the phantom's hemodynamic parameters for each heart cycle during in-vitro simulations. The bottom half of the centerpiece covers the pulmonary arteries once the baffle and the stent are placed in their respective locations. The top and the bottom half of the phantom were designed using CATIAv.5 (Dassault Systèmes). Figure 25 shows the development of a 3D CAD model using angiogram data.

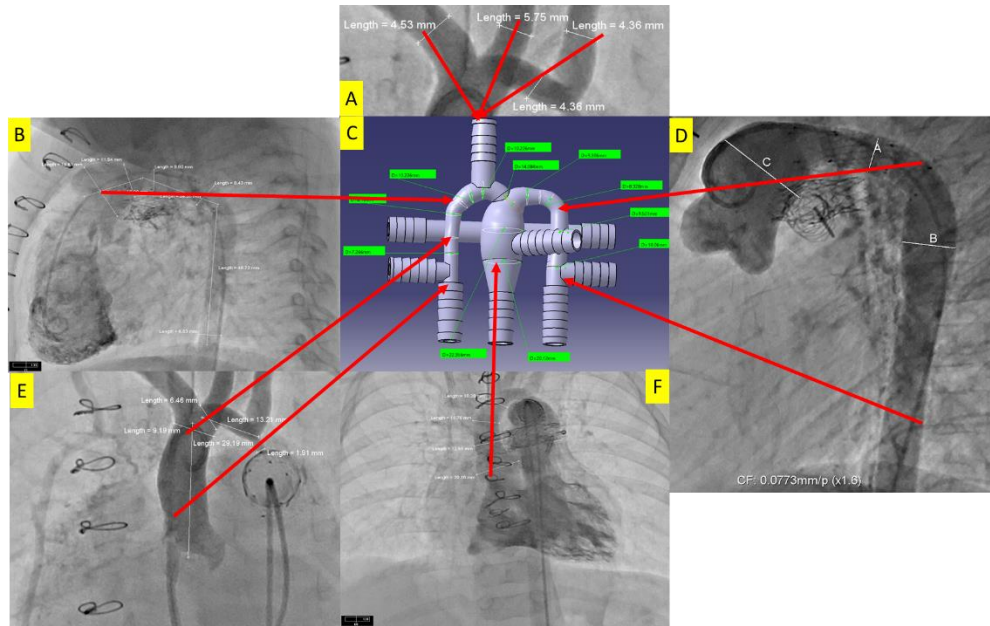


Figure 25 Development of 3D CAD model of HCSII centerpiece from angiogram A. Diameter of RCA, RSA, LCA and LSA B. Diameter of MPA root C. 3D CAD model on CATIA v.5 D. Diameters of the aortic arch and descending aorta E. Diameter of ascending aorta F. Diameter of MPA

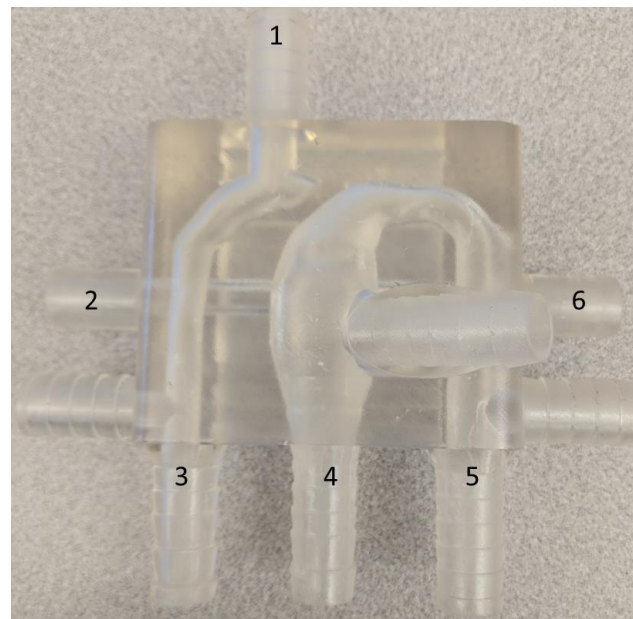


Figure 26 3D phantom printed with the conduits

Figure 26 represents the 3D printed centerpiece with labeled conduits

In Figure 26, section 1 represents the flow towards the upper body. Section 2 and section 6 are connected together to form the PA (pulmonary artery). Section 3 forms ascending aorta, section 4 forms main pulmonary artery and section 5 forms descending aorta in the 3-D phantom.

3.1.1.1. Initial Design

To increase the rigidity of the phantom, a rectangular block was added to the top half. Figure 27 shows the initial design of the centerpiece with the rectangular block. Figure 27 A represents the native aorta being stenosed. Figure 27 B represents the front view of the centerpiece along with the rectangular block. Figure 27 C represents the interior view of the top half with the baffle location. Figure 27 D represents the side view featuring the LPA-RPA conduit.

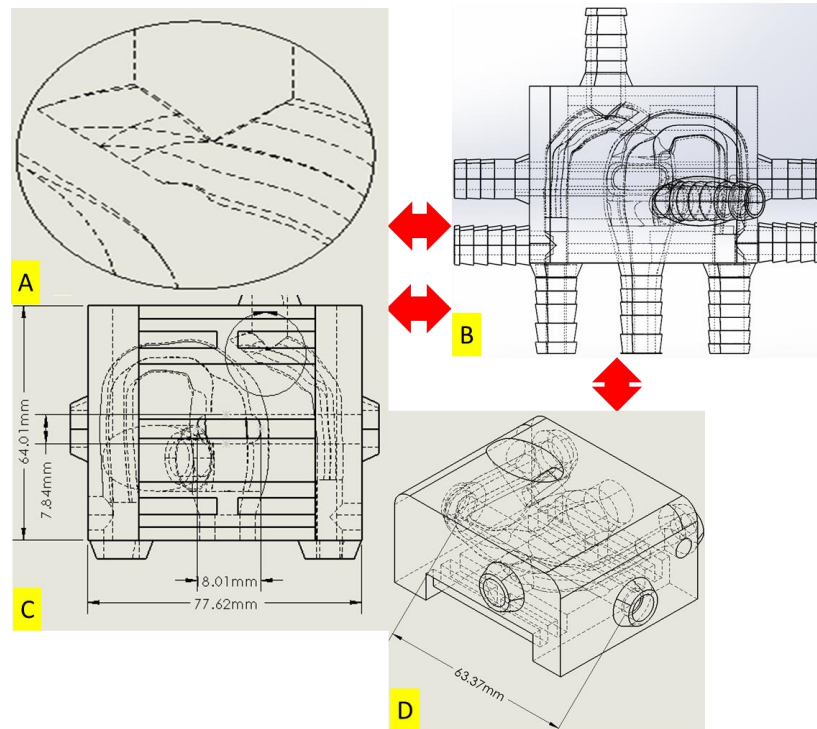


Figure 27 Design 1 of the top half of the centerpiece A. Ascending aorta is stenosed B. HCS II centerpiece within the rectangular block C. Interior view of the centerpiece with rails D. Side view of the top half

The bottom half of the phantom was designed for easy accessibility of baffle and stent. The bottom half was machined using acrylic, as seen in Figure 28 A. Lasers were used to illuminate the characteristic features of the stent. To accommodate the addition of the laser, three slots of equal diameter at an equidistant were extruded. To avoid stent migration during in-vitro simulation, two equal diameter stubs at an equidistant were extruded. The laser slots and stent stopper feature are represented in Figure 28 B. Two slots of equal diameter were created at the opposite ends, and extruded cut was performed at an angle as shown in Figure 28 C to capture the stent and baffle's movement using a camera.

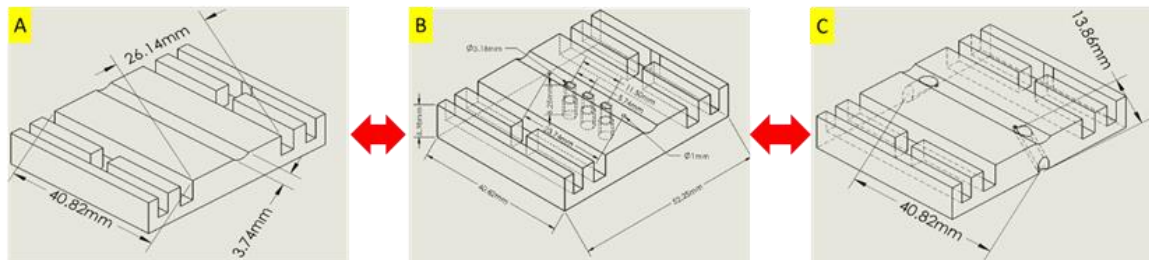


Figure 28 Design 1 of the bottom half of the centerpiece A. Bottom half of centerpiece with stent stopper and slots for laser C. Slots to place the camera

Two sets of rails were designed to reduce the slipping that could occur between the top and bottom half and integrate both halves. The top and bottom half of the phantom went through two iterative design changes. The initial prototype could not maintain the flow separation between the pulmonary trunk and the pulmonary arteries. The barbed ends broke as they could not sustain loads of the connectors used. Leakage was visible during the experimentation due to the improper material selection for the baffle.

3.1.1.2. Design Iteration 1

The first iteration does not involve any changes to the conduits that represent the physiological condition. Figure 29 A shows changes made to the bottom half of the phantom to place an otoscope. To follow the exact procedure mentioned by DeCampi et al. [115] for the baffle, a clip was designed to constrain the baffle movement; the clip is placed onto the top half of the phantom, as seen in Figure 29 C. The railings designed to ease the mating were removed, as seen in Figure 29 D.

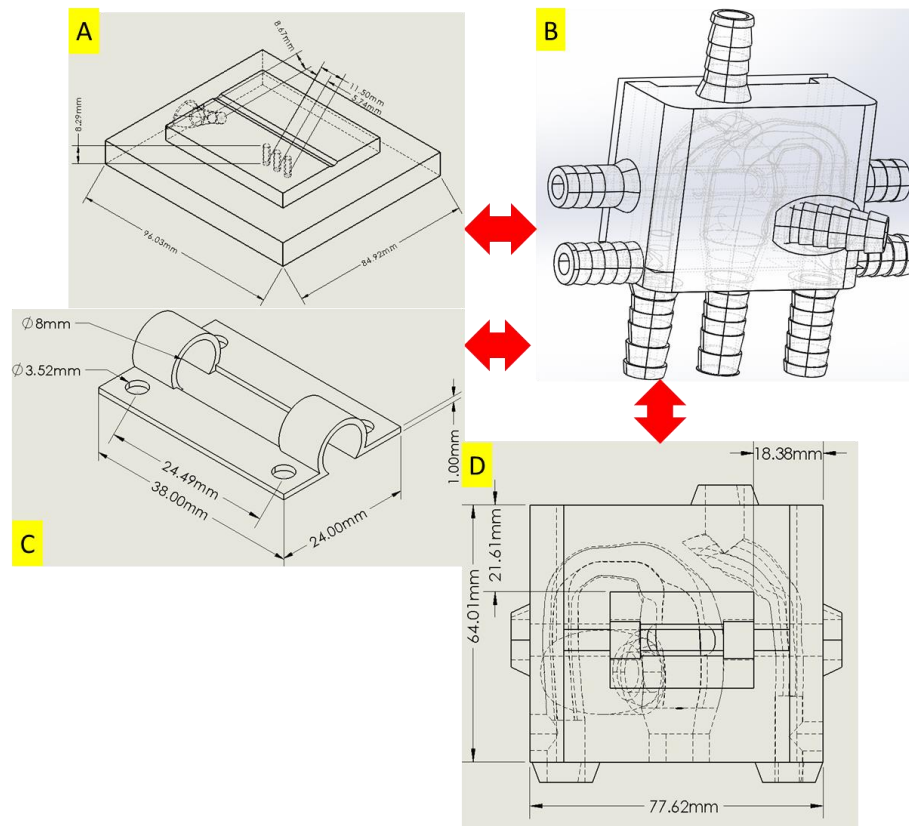


Figure 29 Design iteration 1 for top and bottom half of the centerpiece A. Changes made to the machined part with a slot for otoscope B. View of the centerpiece. C. Clamp designed to hold the baffle D. Interior view of the top half of the centerpiece

3.1.1.3. Design Iteration 2

The second iteration involved considerable changes to the top half of the phantom. In this design, the rectangular block was increased in length and breadth, as seen in Figure 30 A. The barbed connectors protruding outside were removed, as seen in Figure 30 B. A step cut feature was developed on the bottom half of the phantom. Figure 30 C shows the step cut design such that the specula of the camera would touch the bottom to focus on a specific area of the stent.

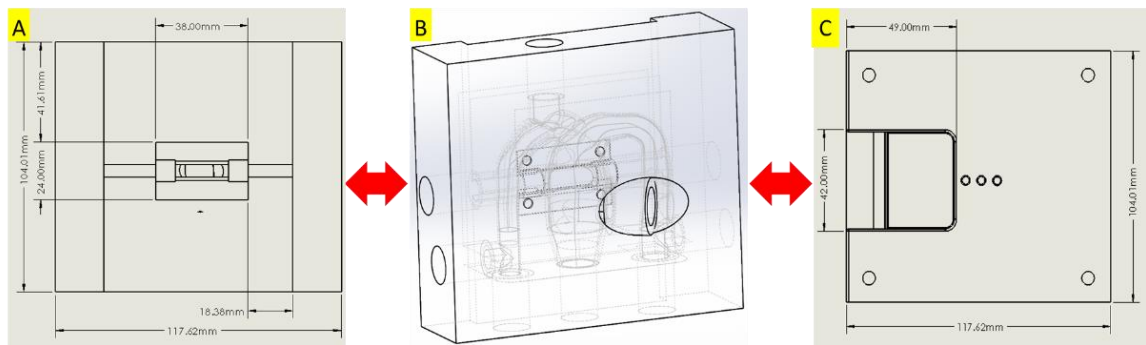


Figure 30 Design iteration 2 for top and bottom half of the centerpiece A. Interior view of the top half and B. Front view of the top half C. Back view with the square slot

3.1.1.4. Final Design

The final design of the phantom involves the modifications that were carried out in the design iteration process 2. Extra layers on the bottom half were removed from the previous design, and a layer of a gasket was added to avoid leaks, as seen in Figure 31 A. A through-hole feature was developed on the top half for the extended length, as seen in Figure 31 C. To accommodate commercially available barb connectors to integrate the phantom with the MFL, threading operations were performed on the remaining circular slots on the centerpiece. Figure 32 A represents the 3D printed centerpiece. Figure 32 B represents the top half of the rectangular block with the baffle placed behind the MPA section. Figure 32

C represents the bottom half of the centerpiece with stent and gasket. Figure 32 D represents the machined backplate with two slots extruded for laser slots.

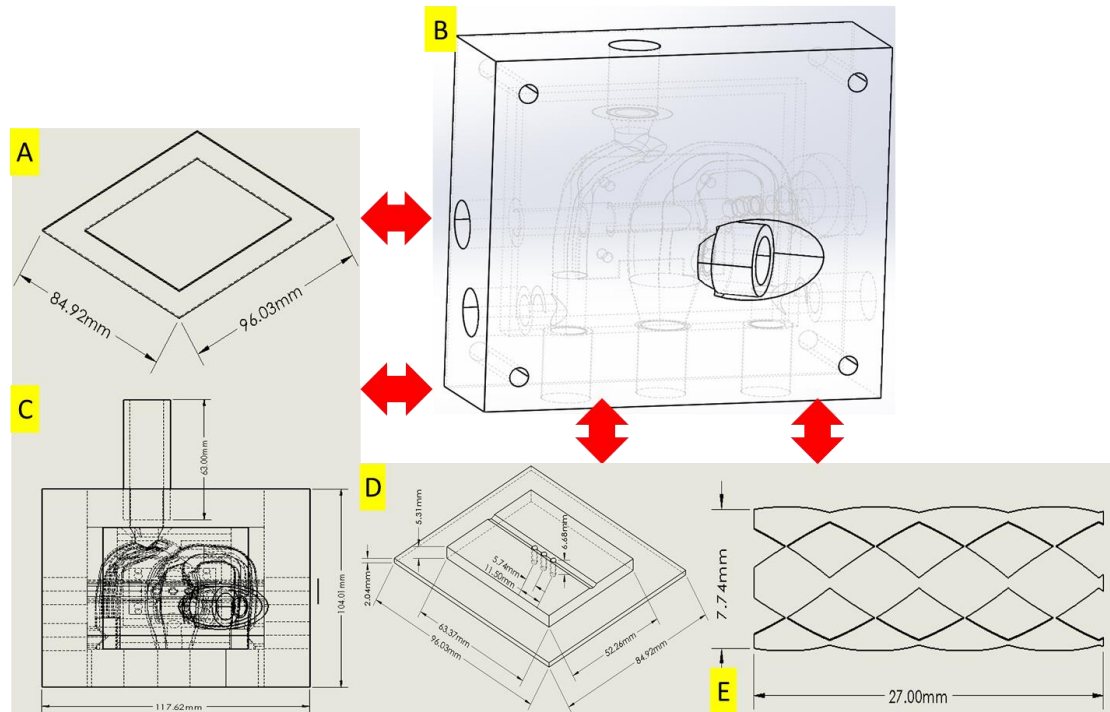


Figure 31 Final design of centerpiece A. Gasket B. Front view of *the* top half of centerpiece C. Interior view of top half D. Side view of the backplate E. Stent

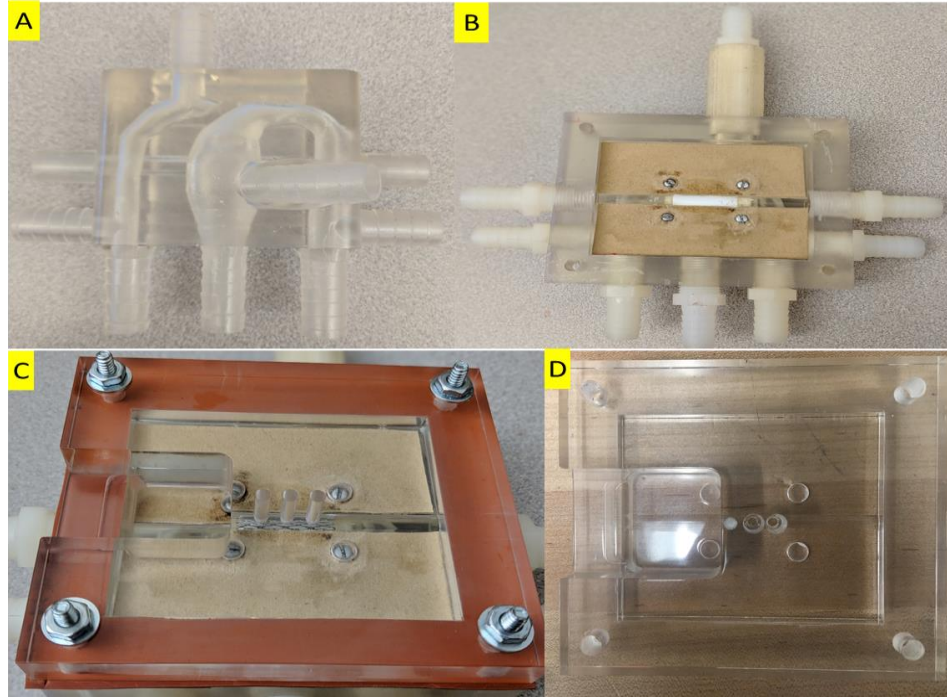


Figure 32 3D printed and machined centerpiece A. HSCII centerpiece B. The top half of centerpiece with baffle C. Bottom half of centerpiece with stent and gasket D. machined backplate

3.1.2. Fontan IJS

The in vitro study was modeled to validate the in-silico simulation of the Fontan patient [222]. modeled the baseline TCPC on SolidWorks (Dassault Systèmes) using an averaged dimensions of 2-4-year-old Fontan patient. Four models' configurations were developed, including the baseline, IJS, NES, and IJS with pulmonary artery radius increase. To accommodate the increase in the pulmonary flow, the cross-sectional flow area of the pulmonary arteries was modeled using the Poiseuille flow $\frac{Q_i}{Q_f} \sim \left(\frac{r_i}{r_f}\right)^4$. Keeping the correlation of the in-silico model, the 3D phantom was developed. The process involved developing the TCPC and the IJS prototype with diameters of 2 mm, 3 mm, and 4 mm.

The TCPC was developed by calculating the diameters of RPA, LPA, SVC, and IVC as 6 *mm*, 9 *mm*, 12 *mm*, and 18 *mm*. Their corresponding lengths of RPA and LPA were 40 *mm* and for SVC and IVC were 23 *mm* and 56 *mm*. A two-part process was carried out to develop the top and the bottom half. The TCPC was developed using Acrylonitrile butadiene styrene (ABS) and manufactured by 3D printing technology. Post manufacturing, the top and bottom half are joined together using a sealant. The ends of the TCPC are clamped when connected to the MFL.

The IJS was developed in three pairs having an internal diameter of 2 *mm*, 3 *mm*, and 4 *mm*. The nozzle is placed on top of a coupler with a total length of 135.7 *mm*. The diameter at the center section is 20 *mm* at the center and 9 *mm* at the ends. The IJS is intruded into the LPA and RPA, and the nozzle orient parallels to the flow direction. The role of IJS is to introduce an entrainment jet that flows concentrically to the pulmonary artery flow. The entrainment jet exchanges momentum with the flow in the pulmonary arteries, decreasing the localized vascular resistance in TCPC and decreasing the IVC pressure. Figure 33 shows the 2D drawing of various IJS developed along with the 3D printed prototypes. To ensure the concentricity of the flow, the diameter of the IJS increases at the entrainment point. The cross-sectional area of the conduits is increased to accommodate the excess flow and reduce the flow momentum effect. The IJS was coated with a sealant to avoid any leaks during the experiment.

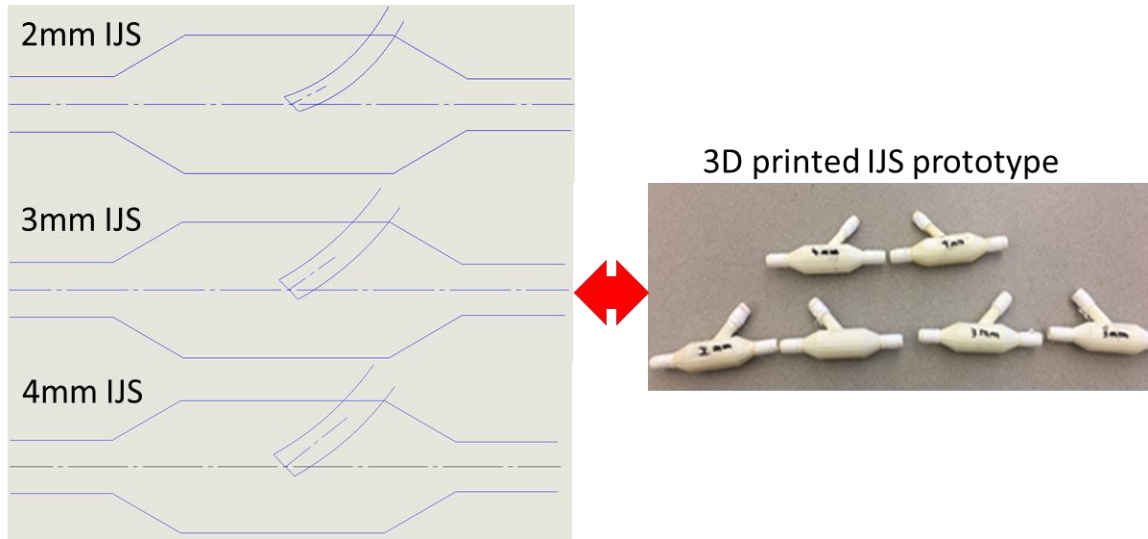


Figure 33 2D drawing of 2mm, 3mm, and 4mm IJS (L), 3D printed IJS prototype

3.1.2.1. Fontan model version 1

The in vitro study was modeled to validate the in-silico simulation of the Fontan patient. The in-silico study involves patients' anatomies within 2-5 years of age, with a BSA of 0.7 m^2 . The traditional Fontan procedure with fenestration is considered as the baseline for the in-vitro study. The fenestrated 2Y graft TCPC connection with the proposed IJS at IVC is another development. The fenestration having a diameter of 4.75 mm and length of 17.5 mm is located at the bifurcation of the Fontan conduit. The fenestration contributes to the IVC pressure drop. In the proposed model, the IJS is designed to be collinear with the fenestration. The excess fluid being injected is captured by the fenestration, thereby enhancing the entrainment. Systemic oxygen saturation remains as part of the IJS flow absorbed in the fenestration. Figure 34 A. represents the elliptical profile. Figure 34 B. represents the IJS shunt. Figure 34 C. represents the diamond profile, and Figure 34 D. represents the circular profile.

The first iteration involves the development of TCPC using acrylic that was machined. A two-part process was performed to carry out the manufacturing process. The TCPC was modeled at a length, width, and thickness of 196 *mm*, 171 *mm*, and 34 *mm*. The diameters of conduits for SVC and LPA were 11 *mm*, 9 *mm* for RPA, and 18 *mm* for IVC. A plane along the LPA-RPA dissects the centerpiece into two parts. To integrate the TCPC centerpiece with the MFL, four aluminum adapters of length 76 *mm*, width 25 *mm*, and 32 *mm* thick were machined.

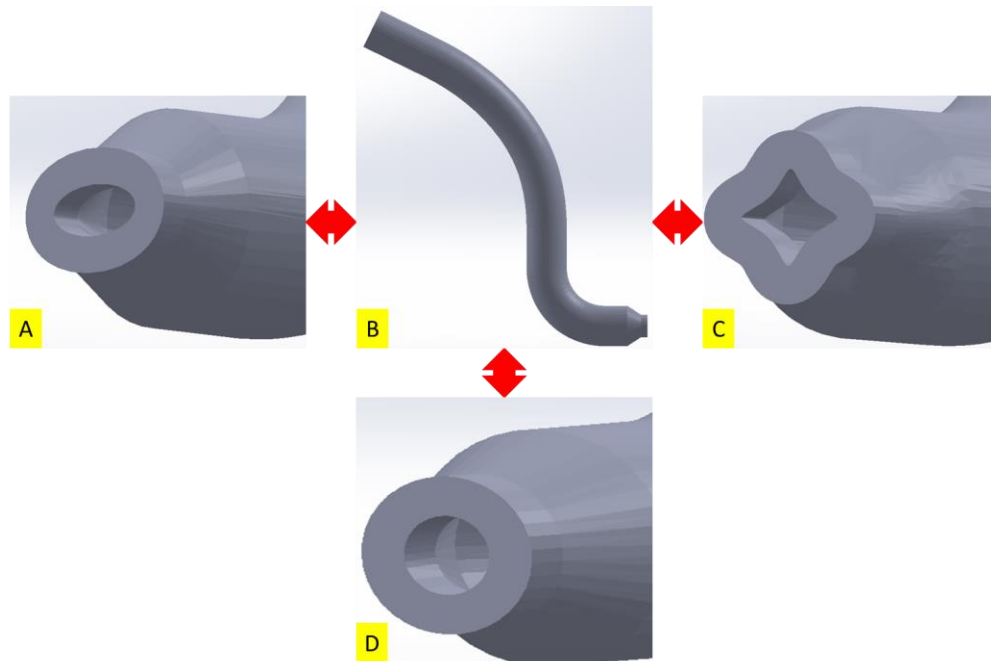


Figure 34 2mm IJS shunt A. elliptical profile B. Side view of the IJS shunt C. Diamond profile D. Circular profile

3.1.2.2. Fontan model version 2

The second version involves the development of TCPC along with the IJS as a two-part process. The fenestrated 2Y graft TCPC Fontan geometry was 3D printed by preserving the physiological parameters of the in-silico model. For the in-vitro simulations, the

conduits that represent the 2Y are simplified to a single conduit. The diameters of SVC, LPA, and RPA are 12.7 *mm*, and IVC diameter is 19.05 *mm*. The TCPC is split into two blocks. The top block contains the conduits representing the SVC, LPA, RPA, and fraction of IVC conduit. The fenestration is developed at the bifurcation of the Fontan conduit.

A parametric study is being conducted on the different IJS types that could yield the optimum pressure drop across the IVC. Four versions of the bottom blocks have currently been developed that house the IJS. The versions are classified based on the shape and number of the nozzles. The IJS nozzles are conically tapered and chamfered at the outlet section and are collinear to the fenestration. Threaded bolts are used on the either side of the IVC to integrate the top and bottom block. A lip with a compression fitting gasket is implemented into the design to provide a tight fit.

Figure 35 shows a 2D model of the 2Y TCPC. Figure 35 A shows the side view representing the lip section's dimensions for compression and the dimension related to the IJS. Figure 35 B represents the front view of the TCPC centerpiece and the dimensions of the top and bottom block. Figure 35 C represents the interior view of the bottom block showing the two circular profiles of the IJS nozzle, each having a diameter of 1.41 *mm*.

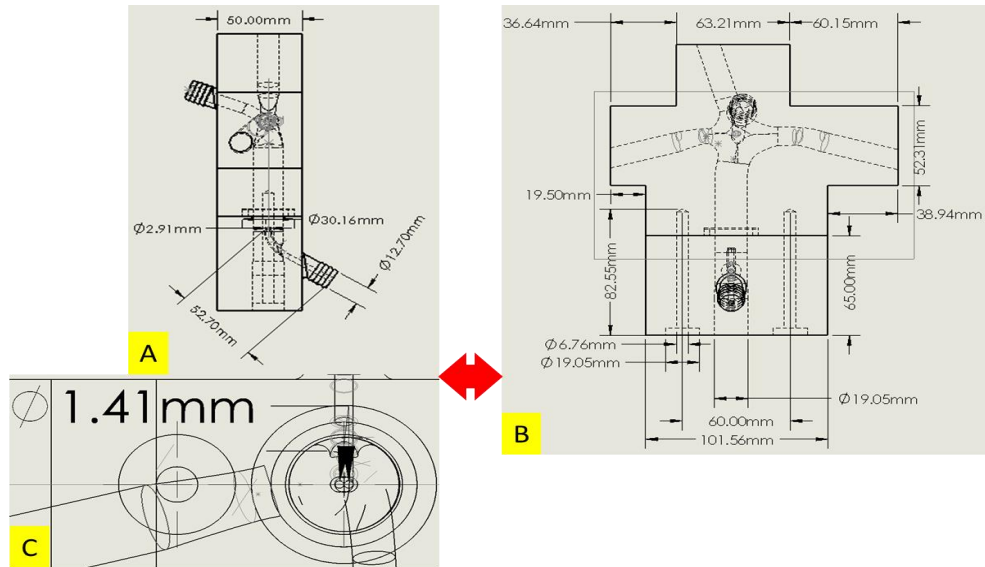


Figure 35 A Side view representing lip section and IJS dimension B. TCPC front view C. Interior view of the bottom block with two circular profiles of the IJS nozzle

Figure 36 A represents the side view of the centerpiece Figure 36 B represents the front view of the TCPC centerpiece and the lengths of SVC, IVC, RPA, and LPA. Figure 36 C represents the interior view of the bottom block showing the two elliptical profiles of the IJS nozzle.

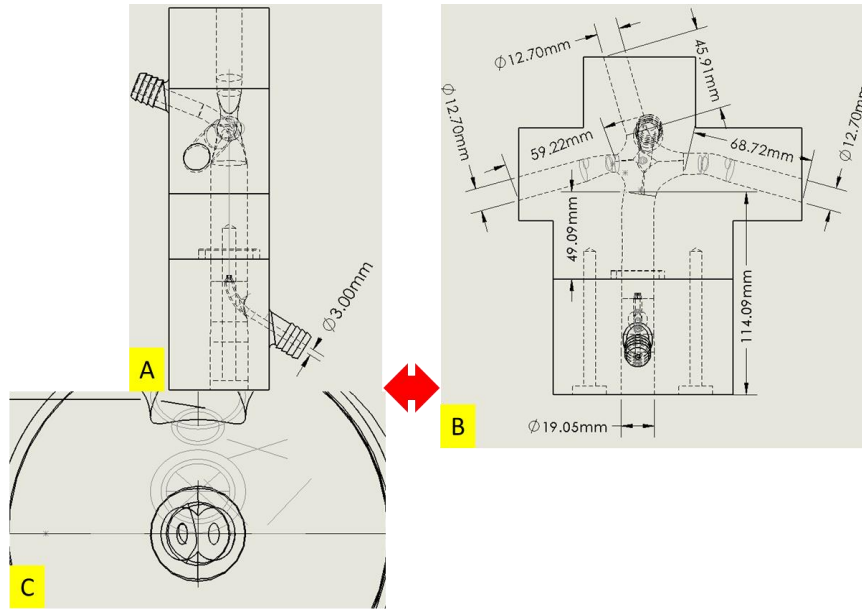


Figure 36 A. Side view of the TCPC B. TCPC front view with the length of the conduits C. Interior view of the bottom block with two elliptical profiles of the IJS nozzle

Figure 37 A represents the interior view of the bottom block showing a single circular profile of the IJS nozzle having a diameter of 2 mm. Figure 37 B shows the front view of the TCPC and the diameters of SVC, IVC, LPA, and RPA.

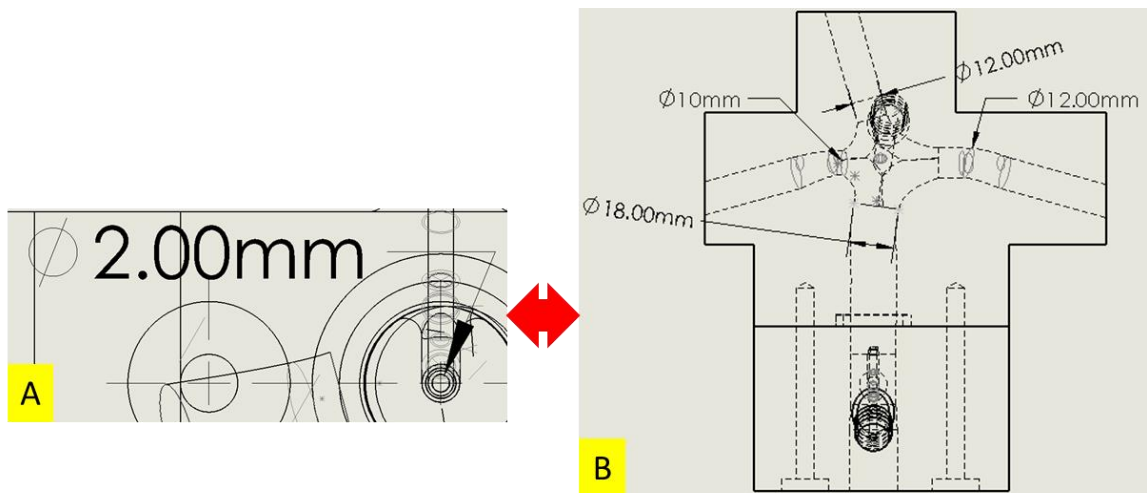


Figure 37 A. Interior view of the bottom block with one circular profile of the IJS nozzle B. Front view TCPC with the diameter of conduits

Figure 38 A represents the side view of the centerpiece and the dimensions of the IJS leading to the fenestration. Figure 38 B represents the front view of the centerpiece and the dimensions of rectangular fittings designed to integrate the centerpiece with the MFL. Figure 38 C represents the bottom block's interior view showing the IJS nozzle's one elliptical profile.

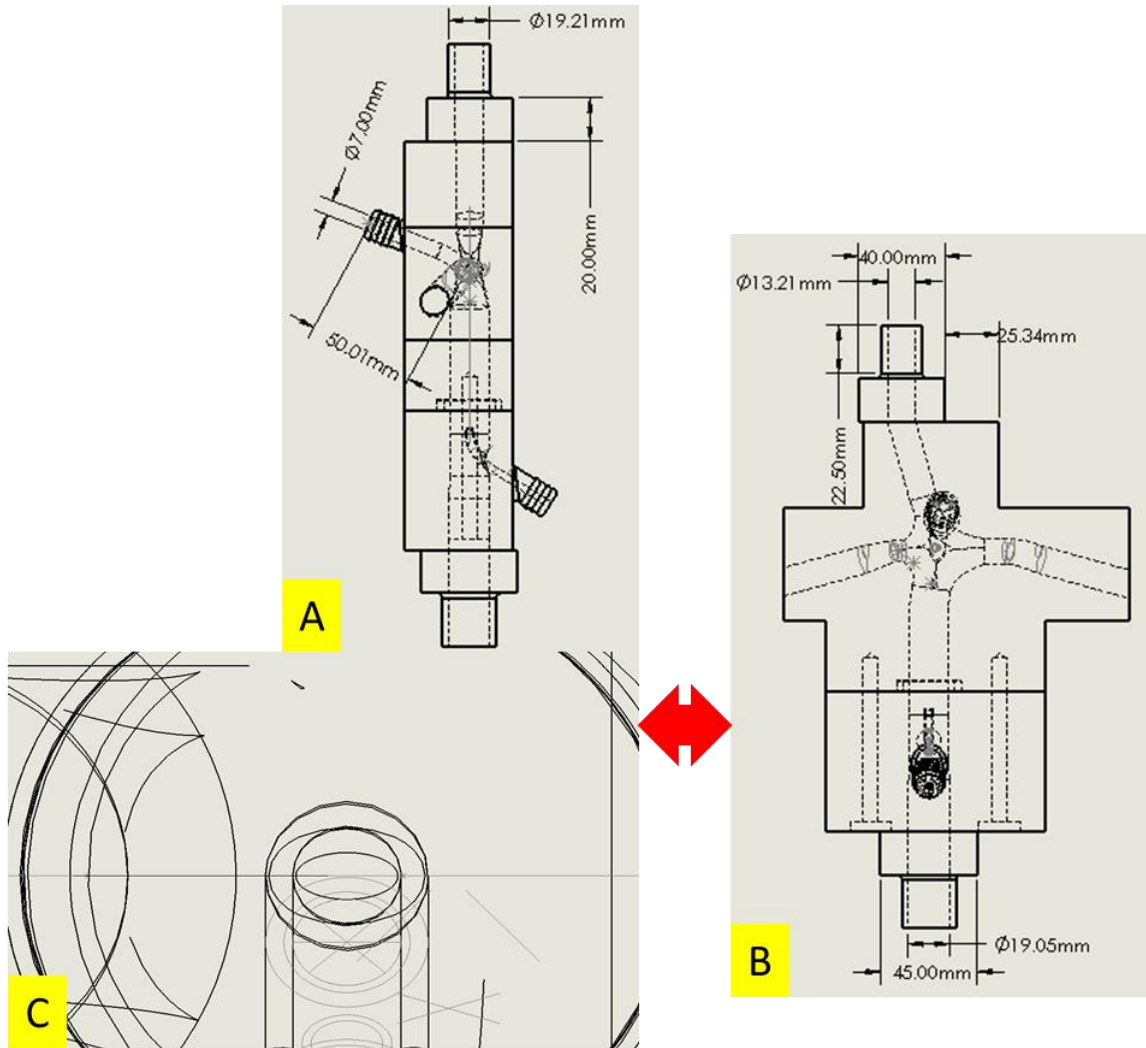


Figure 38 A Side view of TCPC with IJS at fenestration site B. Front view of TCPC with adapters C. Interior view of the bottom block with one elliptical profile of the IJS nozzle

3.2. Lumped Parameter Model

As described in section 2.2, the LPM is an electric analogy used to replicate the circulatory system of human circulation. Using this electric analogy, blood flow through various sections in the cardiovascular system can be lumped and represented as electrical circuits that include resistors, inductors, and capacitors. Each of these elements represents vascular resistance, vascular inertance, and vascular compliance. As discussed in section 2.2, different LPM setups have been modeled to experimentally replicate various reconstructed cardiovascular physiologies in the last few decades. The main goal of the LPM setup is to couple the fluid dynamic behavior within the 3D phantom to the dynamics of the peripheral circulation.

To achieve the research objectives established in each problem statement, a specific LPM has been modeled to replicate the proposed reconstructed physiology. Ideally, a Windkessel compartment in the LPM consists of an arterial bed and venous bed. The arterial bed is developed using an inductor, resistor, and capacitor, while the venous bed is developed using the resistor and capacitor. In our experimental studies, each Windkessel compartment is modeled by lumping the arterial and venous beds together, as shown in Figure 39. Each Windkessel compartment consists of two elements, i.e., a resistor and capacitor.

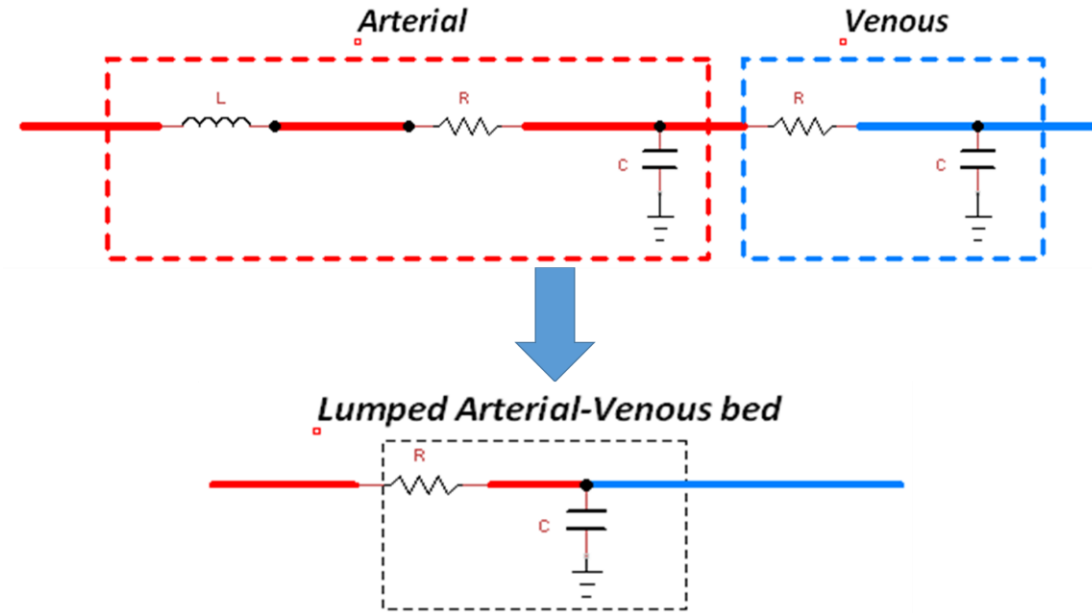


Figure 39 Lumped Arterial and Venous bed coupled for LPM development

In this study, reduced-order LPMs have been modeled to develop both MFL setups.

Hence it is sufficient to control the correct overall resistance and compliance in each branch of the system.

Vascular resistance:

Inlet and outlet pressures are tuned in the MFL. These inlet and outlet pressures generate the pressure differential. This static pressure differential causes the flow to occur in the system. The conduits in the MFL provide a certain amount of resistance, but additional resistance is provided to the system by valves. As discussed in 2.2.1, resistance in a fluid circuit is defined in (4) by Scotten et al. [176]. The pressure drop across each branch is achieved by tuning the resistance in the conduits of MFL. As a result, the blood analog will flow through each conduit across this pressure drop in the MFL setups. In this study, resistance in each conduit of the MFL is achieved by placing a needle valve. Resistances in each compartment of the MFL can be tuned by throttling the respective needle valve.

Head loss across a valve is proportional to the velocity, head of a fluid [223] as shown in Equation (13)

$$\Delta h = K \frac{\bar{V}^2}{g} \quad (13)$$

where Δh is defined head loss, K is the loss coefficient that is dictated by the position of the valve, \bar{V} is the average velocity of the fluid, g is the gravitational constant.

The needle valve resistors are manually actuated and precise. These resistors have a range of seven color bands, and each color band has a setting ranging from 0-9, as shown in Figure 40. The pressure drop produced across the needle valves is linear that majorly contributes to the successful tuning of the MFL rigs.



Figure 40: Needle valve to replicate vascular resistnace in MFL

Vascular Inertance:

Inductors affect only non-steady systems. In fluids, inertance is defined as the pressure gradient to accelerate the flow. It is a parameter that describes how rapidly pressure field changes will affect the flow field in the system. The inertance is defined by Equation (14)

$$L = \frac{2\rho x}{A} \quad (14)$$

In both of the discussed MFL setups, the inertance is captured by the length of the vasculature. A specific length for each vasculature cannot be modeled as the arteries and venous network of a human circulation are extremely long.

Vascular Compliance:

In biofluid mechanics, vascular compliance refers to the change in stored energy in a vessel for a given change in pressure in the time domain. It is entirely analogous to capacitance in electrical circuits. Like an inductor, this parameter does not affect the behavior of a steady system. This parameter is critical in accurately modeling the effects of distensibility of the arterial and venous beds in MFL, as described in Equation (10) from section 2.2.3. Specific annular design-based compliance chambers have been developed to produce the desired compliance (C) in this study. These compliance chambers are capable of matching specific compliance in a Windkessel bed by altering the volume of the chambers for a change in dynamic pressure of the fluid generated across that chamber in the MFL. In this setup, a pair of concentric tubes were used to create the annular inner section of the compliance chamber. The outer tube of the compliance chamber was constructed using the clear schedule 40 and 80 pipes, and the inner wall is constructed by using solid Delrin rods, as shown in Figure 41.

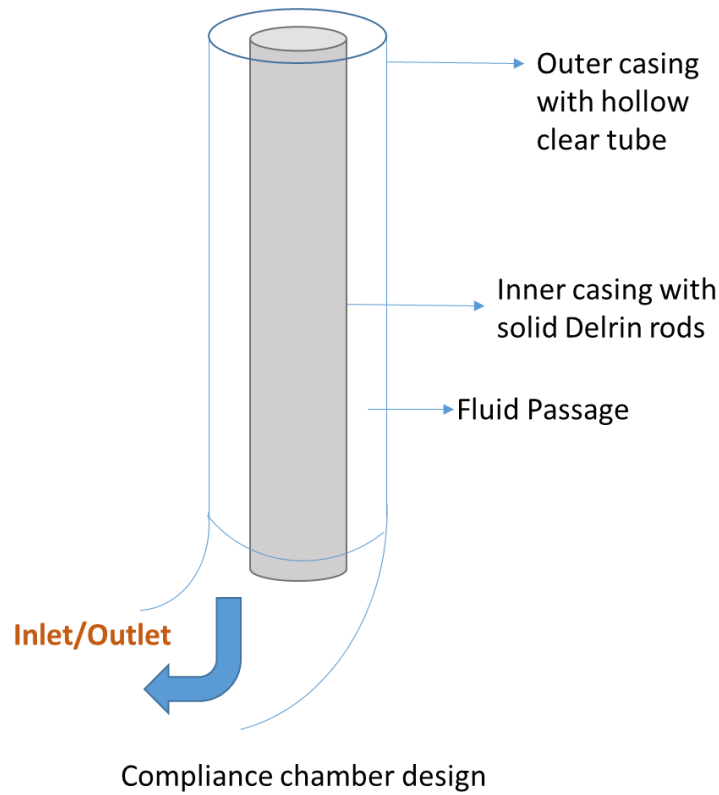


Figure 41 Design of annular compliance chamber replicating the vascular compliances.

To obtain the effective radius, the outer diameter of the compliance chamber was constant while the inner diameter varied for simulating different patient-specific cases. Using this volume-controllable approach, no parameter such as entrapped pressure changes during an MFL run reduces the uncertainty of the analysis. The Equations (15)-(17) show relationships between the pressure and volume of the compliance chamber with the effective radius,

$$Q(t) = \frac{d}{dt} \{C(t)[P(t) - P_g(t)]\} \quad (15)$$

$$\Delta P(t) = \frac{1}{C} \int_{-\infty}^t Q(t).dt \quad (16)$$

$$C(t) = \frac{V(t) - V_o}{\Delta P(t)} \quad (17)$$

To achieve the desired compliance value for the vascular compliance elements, the above equation can be modified to describe the compliance as a function of the compliance element geometry and fluid parameters as seen in Equations (18)-(20)

$$C = \frac{\Delta V}{\Delta P} \quad (18)$$

$$C = \frac{\pi r_e^2 \Delta h}{\rho g h} \quad (19)$$

$$r_e = \sqrt{\frac{\rho g C}{\pi}} \quad (20)$$

Where r_e is the effective radius of the cylindrical compliance chamber.

In the following subsections 3.2.1 and 3.2.2, the construction of LPM for HCSII and Fontan circulations has been discussed.

3.2.1. Lumped Parameter Model for HCSII

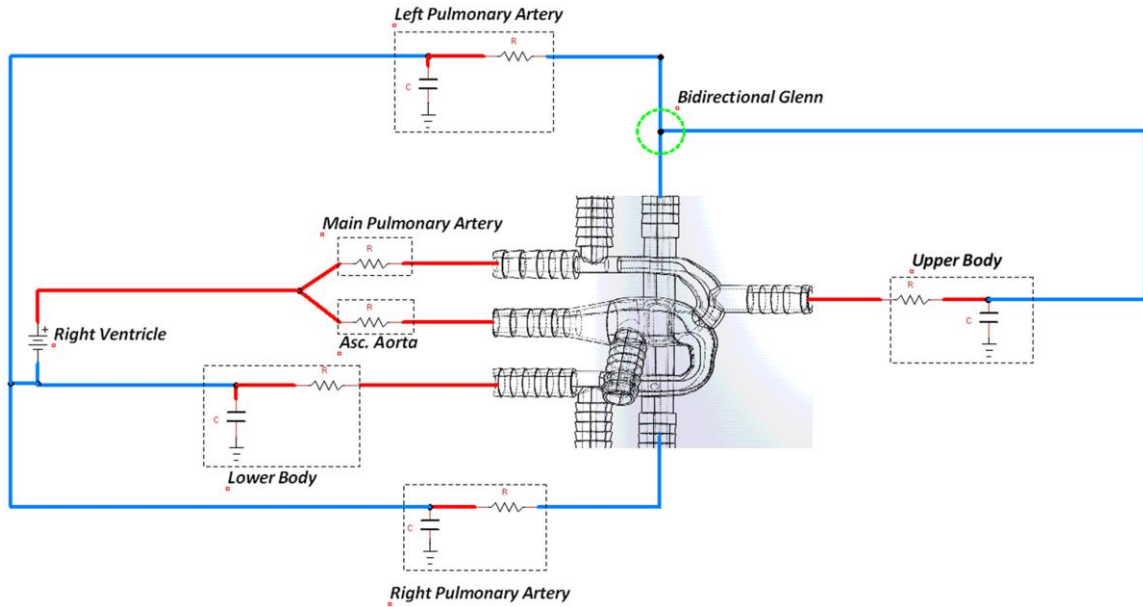


Figure 42 LPM representation of HCSII

As described above in 3.2, a complex circulatory system can be reduced to its equivalent mathematical circuit for analysis using the lumped parameter modeling technique.

The reduced LPM used in this study derived from the full-scale LPM model of Hameed et al. [224] The full-scale LPM is not practically feasible in a laboratory benchtop realization. Tuning such an MFL with a full-scale LPM circuit would be difficult. Furthermore, the number of elements requiring connectors and tubing would create too much inertance. The full-scale LPM is reduced to a branched LPM of equivalent impedance to create a practically feasible system. In-vitro study on HCSII circulation was conducted through a dynamically scaled Mock Flow Loop (MFL) using patient-specific geometry. The MFL was modeled to resemble the physiological anatomy of a patient with 0.34 m^2 BSA. In this MFL setup, the lumped compartments representing the peripheral circulations of the patient are connected to the 3-D phantom of the HCSII geometry. The MFL consists of

four compartments, and each compartment is developed with two elemental (i.e., resistance and compliance) Windkessel models. Four compartments represent upper systemic, lower systemic, right, and left pulmonary circulations, as shown in Figure 42. Each lump represents the arterial and venous vasculature found within the physiological anatomy. The voltage source represents the right ventricle. The ventricular septal defect (VSD) is not modeled in the 3-D phantom but is represented in the LPM circuit. To replicate the VSD, two resistor valves are placed between the bifurcation junction (upstream of the right ventricle) and the inlet of the MPA and Asc. Aorta in the 3-D phantom. This study focuses on the flowfield developed in the HCSII geometry; hence, the BDG section is in the LPM circuit as shown in Figure 42. Every branch in the reduced LPM contains circuit elements that correspond with a device in the MFL that serves as a physical realization of that parameter. Table 2 Compliance values for MFL represent the compliance values considered in each lump while conducting the experimental study.

Table 2 Compliance values for MFL

Compliance sections in MFL	Compliance Value (<i>ml / mmHg</i>)	Effective Diameter (<i>in</i>)
C_upper	0.603	1.304
C_lower	0.735	1.276
C_lpa	0.640	1.295
C_rpa	0.640	1.295

mentioned in section 3.2, every compartment of this model is developed with two elements i.e., resistance and capacitance, as shown in Figure 43. This LPM has two systemic and two pulmonary compartments. Two systemic compartments represent upper and lower systemic circulations, and two pulmonary compartments represent right and left pulmonary circulations, respectively. Each branch in the MFL contains a device that corresponds to a circuit element of the reduced LPM. As mentioned in section 1.2, pulsatility plays a crucial role in the hemodynamic behavior on the arterial side. Also, the arterial network and capillary system of the systemic circulation provide significant vascular resistance and vascular compliance to the flow field. These arterial networks act as low pass filters to the pulsatile flowfield and effectively dampens out most of the pulsatility in the blood flow by the time it reaches the TCPC. Furthermore, the Fontan circulation is especially less pulsatile on the venous side due to the absence of the ventricle. In this study, the remaining pulsatility from the cardiac cycle is not modeled. To accurately replicate the infant anatomy while conducting the Fontan experiment, the values of compliance were determined based on physiological values that correspond to body surface area (BSA) of $1.2 m^2$ defined in [64]

Table 3 shows the values of vascular compliances corresponding to different anatomical sections.

Table 3 Vascular compliance of sections

Upper compliance (C_{upper})	3.12 ± 0.03
TCPC compliance (C_{TCPC})	0
IVC compliance (C_{IVC})	0.055
Liver compliance (C_{liver})	4.41 ± 0.03
Lower compliance (C_{lb})	3.86 ± 0.06
Right compliance (C_{right})	0.066
Left compliance (C_{left})	0.066

Due to the relative similarity between the IJS Fontan Mock Flow Loop used in this experiment and the reduced lumped parameter network model utilized in, all but the lower systemic compliance could be carried over. To calculate the lower systemic compliance, the liver compliance and lower body compliance are combined in Equation (21)

$$C_{\text{lower}} = \left(\frac{1}{C_{\text{lb}}} + \frac{1}{C_{\text{liver}}} \right)^{-1} + C_{\text{ivc}} \quad (21)$$

Therefore, the resulting compliance values used in this experiment are given below in

Table 4

Table 4: Compliance values used for MFL

Vascular Branch	Vascular Compliance	Effective Radius
	($ml/mmHg$)	(in)
C _{upper} , Upper Systemic	3.12	0.3365
C _{lower} , Lower Systemic	3.86	0.3742
C _{left} , Left Pulmonary Artery	2.14	0.2787
C _{right} , Right Pulmonary Artery	2.14	0.2787

3.3. PVR

Pulmonary vascular resistance (PVR) is an essential hemodynamic quantity that is very indicative of Fontan surgeries' outcomes. Abnormal growth of the pulmonary vasculature and significant collateral flow can significantly alter PVR, leading to cardiovascular malfunctions. In particular, elevated PVR can cause pulmonary hypertension, which strongly affects the Fontan patient's wellbeing. Several studies point to the possibility of a strong correlation between pulmonary flow and PVR . The study attempts to quantify changes in PVR between rest and exercise conditions induced by dobutamine administration, which directly affects the heart rate and stroke volume. The data reveals a negative correlation whereby an increase in pulmonary flow induces a drop in PVR.

This observation becomes of particular importance for our study as implementing an IJS significantly enhances pulmonary flow. In the absence of any PVR response, the additional flow would cause an increase in IVC pressure; however, if PVR decrease could be considered, the additional flow would not build up in the Fontan circulation. A PVR drop alone would negate any IVC pressure increase due to fluid build-up as well as potentially

be directly responsible for additional pressure reduction. With the accommodation of the IJS flow, if flow entrainment occurs, the IJS can directly cause a significant pressure drop. Based on the data presented by Schmitt et al. [150] it is possible to derive a curve relating the percent change in PVR with the percent change in pulmonary flow. Out of the ten patients presented in the study, two were considered non-responders as the PVR hardly changed following dobutamine administration although the observed flowrates reacted accordingly. Due to the low population in this study the resulting statistical analysis an accurate trend cannot be extracted, but nonetheless, it can be observed. As shown in Figure 44, for an increasing Q_p the PVR does in fact drop.

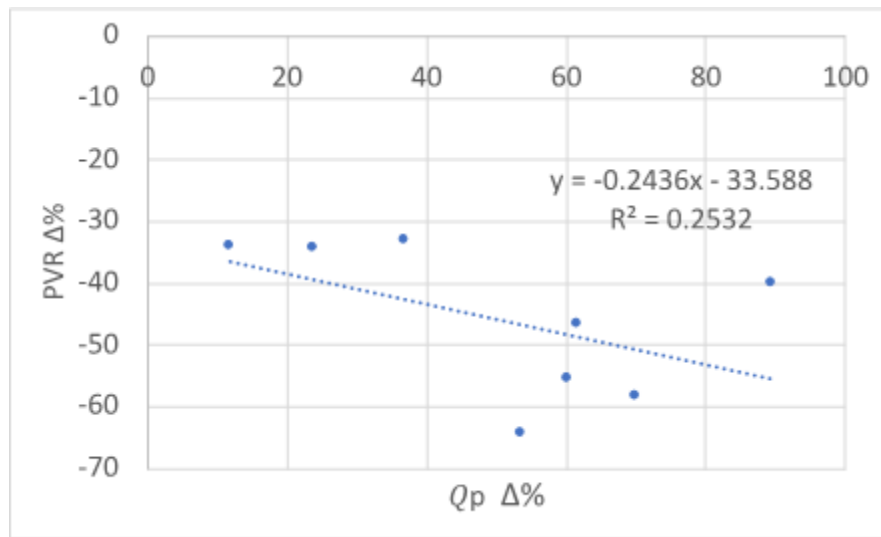


Figure 44 Correlation for percent PVR change too percent pulmonary flow change

The plot suggests that the PVR percent change lies in the region of 30–40% for a maximum. This study will use these results to sequentially drop PVR following IJS activation to observe what happens to the IVC pressure. This study will use these results to sequentially drop PVR following IJS activation to observe what happens to the IVC pressure.

3.3.1. Pulmonary Vascular Resistance Calibration

The relationship between flow rate and needle valve resistance must be determined to implement the PVR drop to increase pulmonary flow. To evaluate the pulmonary resistances, a simple flow loop is set up with a continuous flow pump. The needle valve resistance is calculated by measuring the pressure upstream and downstream of the valve in conjunction with the flow rate Figure 45. Ohm's law relates the scalar valve resistance to the mean pressure gradient ratio to the flow rate. All the valve settings are tested for three flow rates 1.45 L/min , 1.75 L/min , and 2 L/min . The calibration procedure is carried out on the right and left pulmonary resistances. Figure 45 B presents the most significant range of valve settings tested for calibration. The curve shows that for the same valve setting but incremental flow rates, the valve resistance grows. This becomes more evident for more restricting valve settings (green to blue).

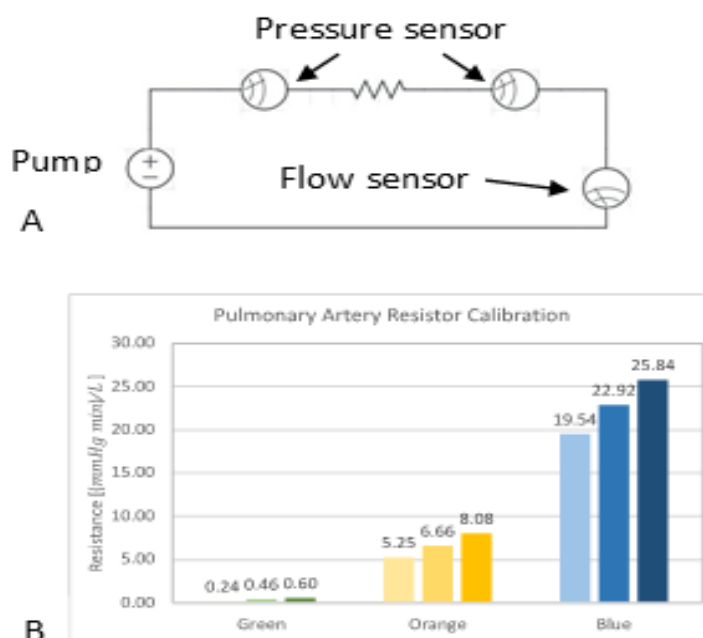


Figure 45 A. Resistance calibration loop and B calibration curves for pulmonary resistances for 3 flow rates (1.45 L/min , 1.75 L/min and 2 L/min).

3.4. PVR and entrainment quantification

The drop in PVR may be considered a concomitant effect as the fluid is injected into the Fontan conduits. There is a scarcity of studies to relate this phenomenon; hence pediatric interventionists from the Arnold Palmer Children Hospital proposed a protocol to quantify this effect in both in-vitro and in-vivo studies. This experiment is independent compared to the IJS in the Fontan study but will support IJS placement in PAs. The efficacy of the experiment, i.e., to study the variation in hemodynamic parameters when injections push the fluid into the PAs, is obtained through this in vivo study. A keen interest is shown towards the coronary effect that could arise during this process.

Table 5 shows the protocol provided by the pediatric interventionist. The protocol was developed based on the instantaneous Q_p/Q_s equal of 1.5 with the injections and the cardiac output of $2.5 L/min$. The protocols are divided based on short multiple injections and single long injections. The short multiple injections were further subdivided into five bursts and ten bursts. The flow rate of the injection fluid was classified into $5 cc/s$, $10 cc/s$, $15 cc/s$, and $20 cc/s$. The total volume of the fluid injected depends on the number of bursts and volume injected during each burst. For this experiment, the volume for each burst was classified into $20 cc$, $15 cc$, $10 cc$, and $5 cc$.

Table 5 Injection protocols provided by clinicians at Arnold Palmer Hospital

Type of injection	Flowrate (cc/s)	Total volume (cc)
Short multiple injection	5	$5 \times 20cc$ injections (100 cc total volume)
		$5 \times 15cc$ injections (75 cc total volume)
		$10 \times 10cc$ injections (100cc total volume)

		10×5cc injections (50cc total volume)
	10	5×20cc injections (100 cc total volume)
		5×15cc injections (75 cc total volume)
		10×10cc injections (100cc total volume)
		10×5cc injections (50cc total volume)
	15	5×20cc injections (100 cc total volume)
		5×15cc injections (75 cc total volume)
		10×10cc injections (100cc total volume)
		10×5cc injections (50cc total volume)
	20	5×20cc injections (100 cc total volume)
		5×15cc injections (75 cc total volume)
		10×10cc injections (100cc total volume)
		10×5cc injections (50cc total volume)
Long single injection	5	1×50cc injection (50cc total volume)
		1×100cc injections (100cc total volume)
		1×150cc injections (150cc total volume)
	10	1×50cc injection (50cc total volume)
		1×100cc injections (100cc total volume)
		1×150cc injections (150cc total volume)
	15	1×50cc injection (50cc total volume)
		1×100cc injections (100cc total volume)
		1×150cc injections (150cc total volume)
	20	1×50cc injection (50cc total volume)
		1×100cc injections (100cc total volume)

$1 \times 150\text{cc}$ injections (150cc total volume)

As shown in Figure 46, the key measurements in this study are the flow rates sampled at each distal PA branch (LPA and RPA), upper body (SVC), and lower body (IVC) circulations. As previously discussed, the pump settings determine the volume injected and the volume flow rate per injection. This allows for a complete outlook of the flow field properties upon injection: before, during, and after.

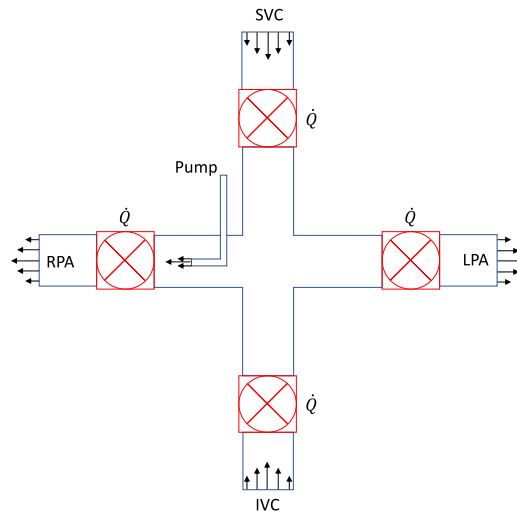


Figure 46 Fontan region of interest flow rate \dot{Q} sampling schematic.

Two flow field properties have been identified to quantify the jet effect: entrainment and jet relaxation time. Given a co-flow configuration with a high-speed jet surrounded by a low-speed background flow, entrainment can be defined as the fluid transport across the fluid-fluid interface caused by shear-induced turbulence resulting in an increased upstream flow. Flow entrainment rate (\dot{Q}_{ent}) has been quantified in Equation (22)

$$\dot{Q}_{ent} = \dot{Q}_{meas,RPA} - (\dot{Q}_{baseline,RPA} + \dot{Q}_{inj}) \quad (22)$$

Where $\dot{Q}_{meas,RPA}$ is the measured flow rate distal of the injection site, $\dot{Q}_{baseline,RPA}$ is the expected flow to RPA based on known \dot{Q}_s (systemic flow) and Pas flow split (set to 50-50) and \dot{Q}_{inj} in the arranged injection rate. Entrainment results in a positive \dot{Q}_{ent} , whereas blockage would entail a negative \dot{Q}_{ent} . Jet relaxation time is defined as the difference between jet rise-time and fall-time. Rise-time can be understood as the time-spanning 10% to 90% of the flow field response to the injection. Conversely, fall-time is the reverse process as the jet winds down. We quantify the jet relaxation time t_{rel} in Equation (23)

$$t_{rel} = t_{rise} - t_{fall} \quad (23)$$

Where t_{rise} is the rise-time and t_{fall} is the fall-time. Positive t_{rel} indicates the low likelihood of downstream fluid buildup as the co-flow takes longer to plateau than to dissipate the jet effect. Negative t_{rel} would suggest a potential fluid buildup. Fluid buildup is an undesirable feature in a Fontan circulation model where PVR is assumed constant. Jet relaxation time is a particularly powerful quantification in the case of pulsed injection (closely resembling actual physiology) as it could highlight a potential fluid buildup that would cascade over many cycles.

3.5. Blood Analog

3.5.1. Newtonian and Non-Newtonian Fluid

Blood is considered to be a non-Newtonian, where the viscosity is inversely proportional to the shear stress. The flow characteristic observed is approximated to a Newtonian fluid

in large arteries [225] The blood carries the non-Newtonian properties at shear rates lower than 100 s^{-1} . For in silico and in vitro simulations, the blood is considered to be a Newtonian. The non-Newtonian behavior can affect the flow separation and the magnitude of WSS. To validate the in-silico experiments using MFL, Newtonian and non-Newtonian fluid were developed. For the HCSII and Fontan project, the Newtonian version of blood was developed using water and glycerin. The non-Newtonian fluid consists of water, glycerin, and nonlinear composition such as surfactant and corn starch compounds. A total of thirteen fluids were developed to obtain the analogous version of blood used for in silico simulation. The fluids were developed based on varying the percentage composition of glycerin, water, and the nonlinear elements. Carreau-Yasuda model was used to develop non-Newtonian blood using Equation (24)

$$\mu(\dot{\gamma}) = \mu_{\infty} + (\mu_0 - \mu_{\infty}) \frac{1}{[1 + (\lambda \dot{\gamma})^2]^{\frac{1}{3}}} \quad (24)$$

μ_0 is the zero-shear viscosity, μ_{∞} is the infinite-shear viscosity, $\dot{\gamma}$ is the shear rate and

λ is the relaxation time constant

The viscosity was measured using The Digital Display Rotary Viscometer NDJ-55, as shown in Figure 47. For the viscosity experiment, the rotational viscometer was chosen. This viscometer has the advantage of operating continuously at a given shear rate, hence preferred during the measurement of absolute viscosity. Viscosity is measured from a rotating cylindrical rotor which varies in shape based on the fluid. Torque produced by the rotor on the fluid depends on the radius of the rotor. The rotational viscometer identifies the torque required to rotate the rotor at a constant speed when immersed in a fluid. The

fluid shear stress is obtained from torque measurements at a given instance, thereby determining the viscosity. The #0 rotor is used for fluids having viscosity values less than 15 mPa.s ; The rotor comes with a fixed sleeve, a test tube with and without a bottom, and a fixed screw for the test tube. The test without the bottom was used to ensure the rotor makes contact with the fluid. The test tube ensures that accurate measurements. A smaller mirror allows the view of the rotor within the bottomless tube. The mirror ensures if the rotor deflects on a specific side. If the rotor deflects, adjustments must be made to move the rotor away from the test tube's inner walls. The rotor should not touch the inner walls of the test tube as it would generate skewed results. Further to the centering of the rotor, water at room temperature is tested to ensure the viscometer measures accurately as the viscosity of water is 1.002 mPa.s at 20°C



Figure 47 Viscometer used during the study

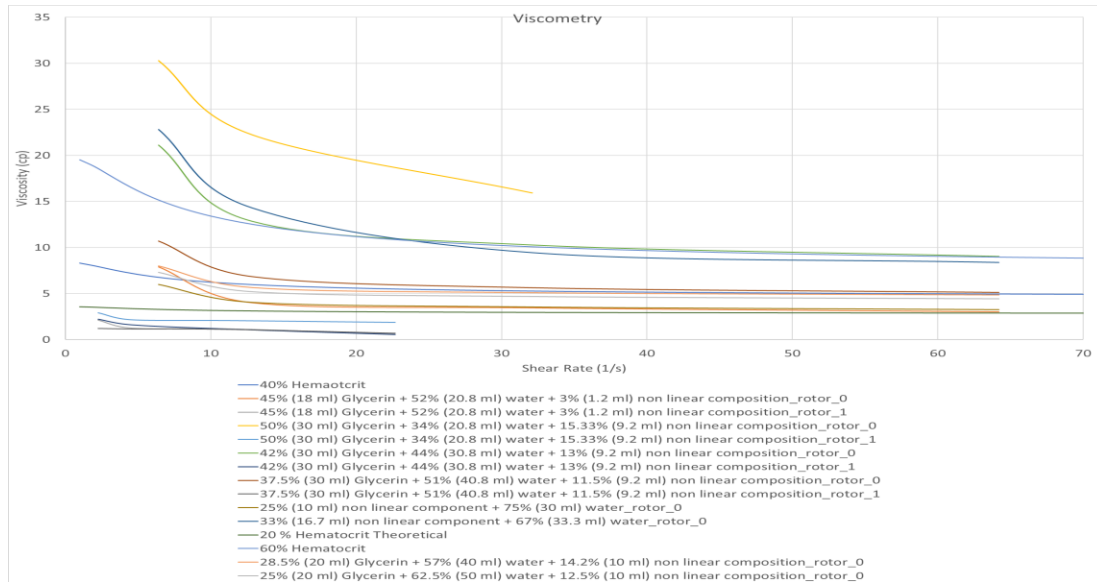


Figure 48 Viscosity vs shear rate for non-Newtonian blood model

Figure 48 represents the plot that corresponds to the viscosity of non-Newtonian fluid vs. theoretical value. Viscosity values that are away from the theoretical values due to large standard deviations were eliminated. Three out of thirteen fluids developed matched closer to the theoretical value having 20%, 40%, and 60 Hematocrit as shown in Figure 49. The fluid with 42% (30ml) Glycerin + 44% (30.8ml) water + 13% (9.2ml) nonlinear composition followed the viscosity profile that was similar to blood having 60% Hematocrit. The fluid with 28.5% (20 ml) Glycerin + 57% (40 ml) water + 14.2% (10 ml) nonlinear composition followed the viscosity profile that was similar to blood having 40% Hematocrit. The fluid with 45% (18 ml) Glycerin + 52% (20.8 ml) water + 3% (1.2 ml) nonlinear composition followed the viscosity profile that was similar to blood having 20% Hematocrit.

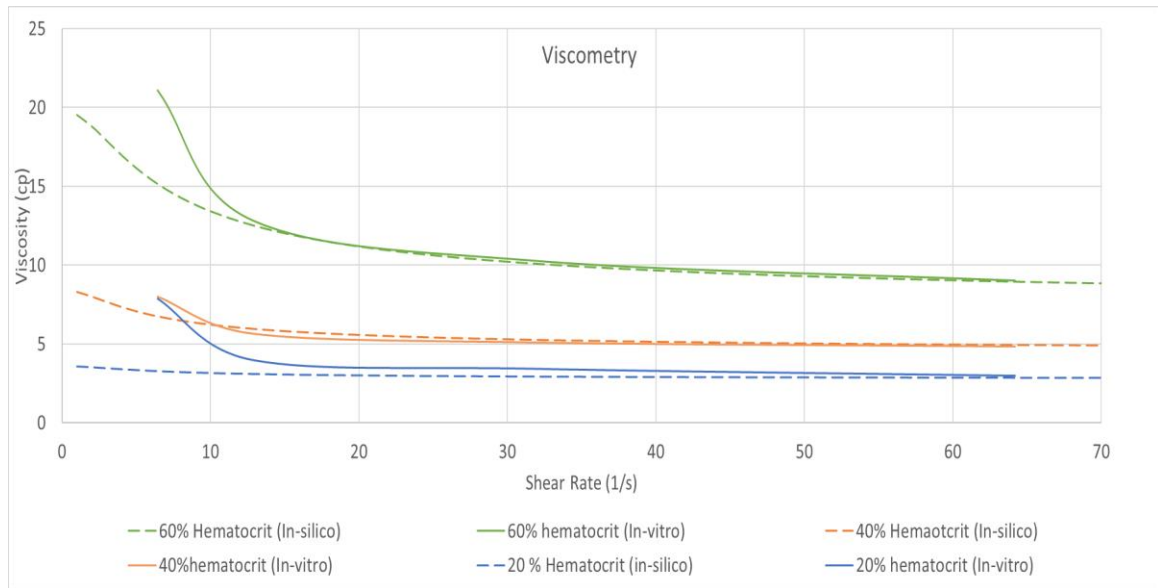


Figure 49 viscosity of non-Newtonian fluid vs theoretical value

3.6. Oxygenation model

3.6.1. Oxygenation model for HCSII

Santamore et al. [226] mentions the lack of natural animal models with HLHS defects. A theoretical analysis was performed to determine the blood flow distribution between the two circulations in terms of systemic oxygen delivery and its effect. A study was also carried out to determine the effect on systemic oxygen delivery and cardiac output due to bidirectional cavopulmonary anastomosis.

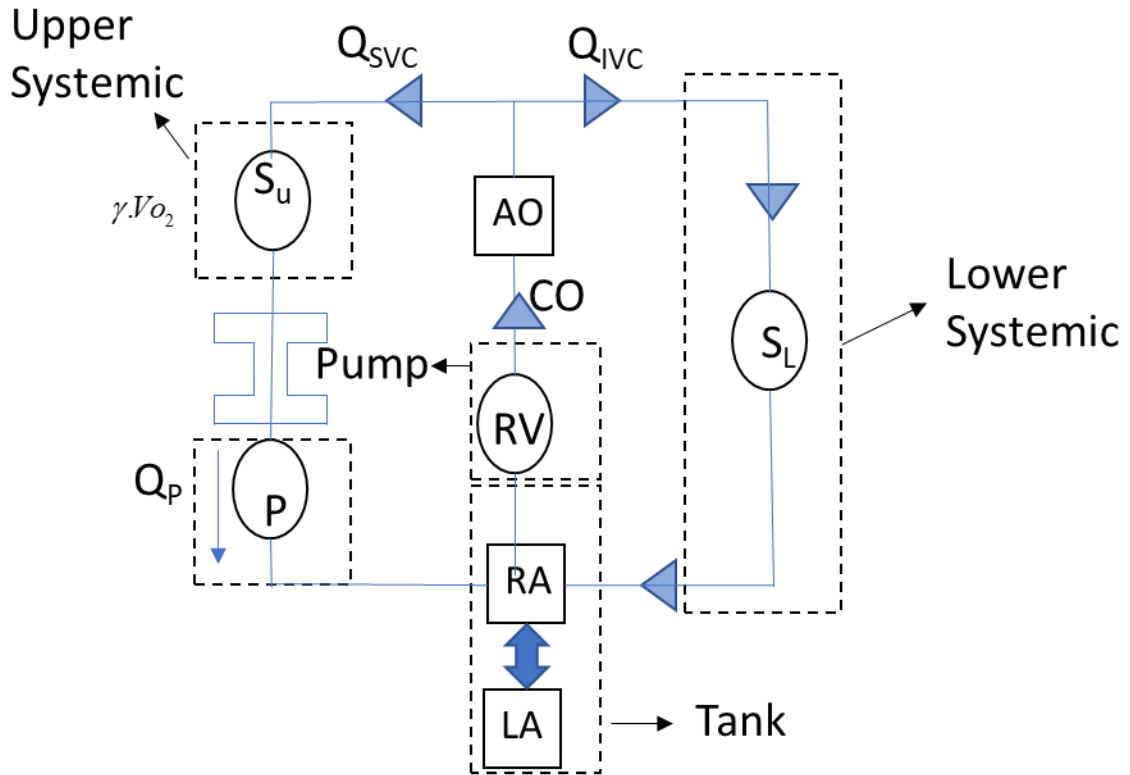


Figure 50 Oxygenation model for HCSII

In the HCSII model, as shown in Figure 50 shows the right ventricle flow is distributed to the upper and lower body circulation. Deoxygenated blood from the upper body flows through the SVC to the PAs, and the blood from lower circulation flows through the IVC to the right atrium. Flow split between the systemic and pulmonary flow is the primary parameter for oxygen content. The oxygen model equations for HCSII are derived from the approach carried out by Santamore et al. [226]. This is based on the oxygen uptake in the pulmonary circulation, O_2 consumption in the systemic circulation, and conservation equation. Equation (25) represents the whole body oxygen consumption divided between the upper body $\gamma.Vo_2$ and lower body $(1-\gamma)Vo_2$

$$Vo_2 = \gamma.Vo_2 + (1-\gamma)Vo_2 \quad (25)$$

Equation (26) represents the oxygen flow rate into the lower system as a product of lower body blood flow Q_{IVC} and arterial blood content Ca_{O_2} . The lower body oxygen consumed reduces the oxygen flow rate into the lower systemic circulation. The reduced oxygen flow rate returns to the right atrium. B_{IVCO_2} represents the oxygen content of the IVC blood.

$$Ca_{O_2} \cdot Q_{IVC} - (1 - \gamma) V_{O_2} = B_{IVCO_2} \cdot Q_{IVC} \quad (26)$$

Equation (27) represents the oxygen flow rate into the upper body system. The reduced oxygen flow rate returns to the PA's via the SVC

$$Ca_{O_2} \cdot Q_{SVC} - \gamma V_{O_2} = C_{SVC O_2} \cdot Q_{SVC} \quad (27)$$

Equation (28) represents the PA's blood flow is equal to the blood flow to the upper systemic circulation. Equation (29) represents the total oxygen flow into the pulmonary circulation and oxygen uptake into the lungs. This gives the oxygen flow rate that returns to the atrium from the pulmonary circulation, C_{PVO_2} representing the SVC blood's oxygen content.

$$Q_P = Q_{SVC} \quad (28)$$

$$C_{SVC O_2} \cdot Q_{SVC} + V_{O_2, L} = C_{PVO_2} \cdot Q_P \quad (29)$$

Equation (30) represents the relation between the total cardiac output to the upper and lower systemic blood

$$CO = Q_{IVC} + Q_{SVC} = Q_{IVC} + Q_P \quad (30)$$

This is based on the assumption of a steady-state condition. Based on the law of mass conservation at the cellular level, oxygen consumption and uptake must be equal represented by Equation (31)

$$V_{O_2}, L = V_{O_2} = \gamma.V_{O_2} + (1 - \gamma)V_{O_2} \quad (31)$$

$C_{svco_2}.Q_{svc}$ from Equation (29) is replaced with Equation (27) and Q_p replaced by Q_{svc} substituted in Equation (31) gives

$$Ca_{O_2}.Q_{svc} + (1 - \gamma).V_{O_2} = C_{pvo_2}.Q_{svc} \quad (32)$$

From Equation (30)

$$Ca_{O_2}.CO = C_{pvo_2}.CO - (1 - \gamma)V_{O_2} + Ca_{O_2}.Q_{IVC} - C_{pvo_2}.Q_{IVC} \quad (33)$$

$$Ca_{O_2}.Q_{IVC} - C_{pvo_2}.Q_{IVC} = (1 - \gamma)V_{O_2}.Q_{IVC} / Q_{svc} \quad (34)$$

Combining the Equation (33) and (34) gives rise to Equation (35)

$$Ca_{O_2}.CO = C_{pvo_2}.CO - \frac{1 + Q_{svc} / Q_{IVC}}{Q_{svc} / Q_{IVC}}.(1 - \gamma).V_{O_2} \quad (35)$$

3.6.2. Oxygenation model for Fontan

A good source of validation for cardiovascular experiments is to track the projected oxygen transport across the model and evaluate the oxygen saturations in systemic and pulmonary circulations.

The Fontan circulation can typically be considered a circuit in series. However, the addition of a graft shunting flow from the aortic arch to the Fontan circuit generates a pseudo-parallel circuit, as shown in Figure 51. The right ventricle (RV) generates a cardiac output (CO) which splits in the systemic flow (Q_s) and the injection jet shunt flow Q_{IJS} . In the systemic circuit, oxygen consumption occurs ($\dot{C}V_{O_2}$), which depletes systemic oxygen concentration (Ca_{O_2}) to the systemic venous concentration (C_{scvO_2}) as described in

equation 1. In the pulmonary circuit, the blood gains oxygen ($S\dot{V}_{O_2}$), increasing the pulmonary arterial blood concentration (C_{PAO_2}) to the pulmonary concentration (C_{PVO_2}), as modeled in Equation (36).

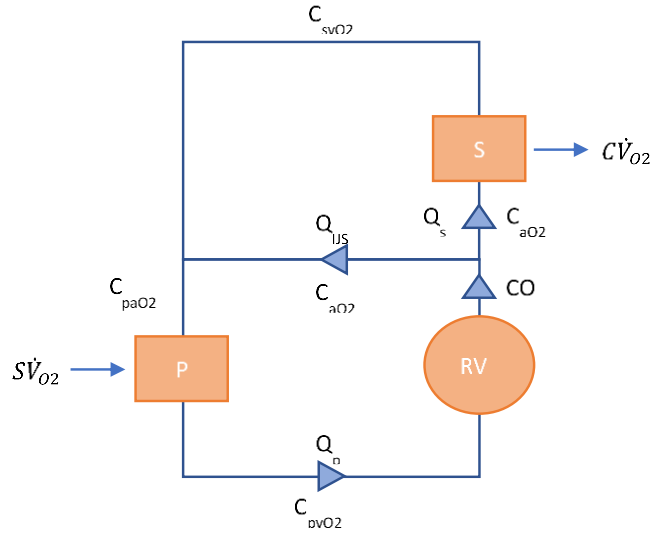


Figure 51 Oxygenation model for Fontan

$$C_{AO_2} \cdot Q_s - C\dot{V}_{O_2} = C_{SVO_2} \cdot Q_s \quad (36)$$

$$C_{PAO_2} \cdot Q_p + S\dot{V}_{O_2} = C_{PVO_2} \cdot Q_p \quad (37)$$

The flow mixing between the systemic venous return and the systemic arterial flow shunted by the IJS can be expressed as in Equation (38)

$$C_{SVO_2} \cdot Q_s + C_{AO_2} \cdot Q_{IJS} = C_{PAO_2} \cdot Q_p \quad (38)$$

Based on the circuit schematic, it can be observed that that $C_{PVO_2} Q_p = C_{AO_2} \cdot CO$ and $CO = Q_p = Q_s + Q_{IJS}$ which suggests that the systemic oxygen saturation matches the pulmonary venous oxygen concentration. The oxygen consumption and assimilation are assumed to occur under “steady” conditions hence $C \dot{V}_{O_2} = S \dot{V}_{O_2}$. Using these observations along with the balance equations derived, the systemic oxygen transport equation can be expressed as in Equation (39) and (40)

$$C_{AO_2} Q_s = C_{PVO_2} CO \frac{1}{1 + \frac{Q_{IJS}}{Q_s}} \quad (39)$$

$$C_{AO_2} Q_s = C_{PVO_2} CO \frac{1}{\frac{Q_p}{Q_s}} \quad (40)$$

These expressions require cycle-average flow rate inputs originating from experimental measurements CO and literature-derived blood oxygen capacity and oxygen consumption data. Pulmonary venous oxygen concentration is calculated from an assumed oxygen saturation (100%, 95%, 90%, 85%, and 80%) depending on patient ventilation and a given oxygen capacity $0.22 \text{ mL O}_2 / \text{mL Blood}$. Oxygen consumption can be determined based on literature derived per-weight oxygen consumption 9 (mL / s) / kg ; hence the user must only know the patient’s weight.

3.7. Stent and baffle characterization

Basic stent design involves successions of connectors and rings. Connectors withhold the rings, thereby contributing to the longitudinal stability. Rings on the stent provide radial support. Stent design and mechanical characteristics are defined based on the strut,

connector, and the number of crowns. Based on the size of the vessel, the number of cells and crowns change.

The stent used for the HCSII procedure and the in vitro simulations follow the Palmez stent design; the Palmez Genesis Transhepatic Biliary Stent 2510B was used. The stent is manufactured by laser-cut operation on a single piece Nitinol tube that follows a closed-cell design. The need for a weldment is avoided by creating slots during the laser cut operation; this manufacturing technique also improves the integrity of the stent. Scanning Electron Microscope (SEM) imaging technique captured the characteristic features of the stent. Figure 52 A and B represent the average length and width of the strut. Figure 52 C and D represent the length and width of the spline feature. Figure 53 E represents the distance between the strut and spline feature Figure 53 F represents the outer diameter of the spline feature. Figure 52 G represents the diameter of the strut feature. Figure 53 H represents the angle of the strut.

DeCampli et al. specifies the placement of the stent during the HCSII surgical procedure. The proposed anastomosis site for RPA and SVC is opened, a longitudinal incision is made into the pulmonary trunk to deploy the stent over a 9-2 Opta Pro balloon catheter. A guide wire is then advanced incision made on RPA into the left lower lobe artery.

Table 6 represents the mechanical property of Nitinol material obtained by the annealing technique. The mentioned mechanical properties will be used to compute the required stresses for fatigue analysis. Table 7 represents the geometric parameter of the stent.

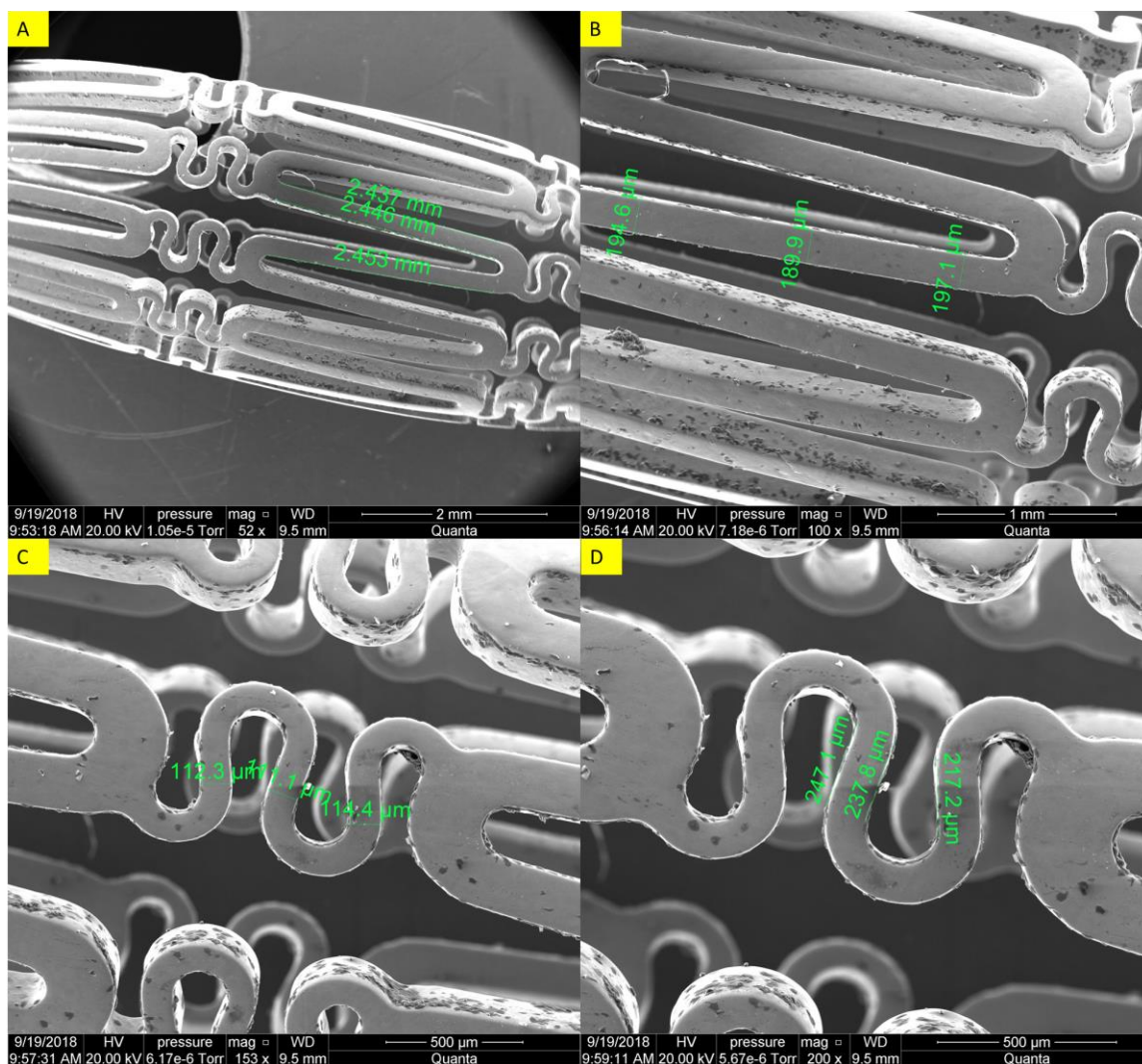


Figure 52 Palmaz Genesis (PG) 2510B stent characteristic features obtained under SEM

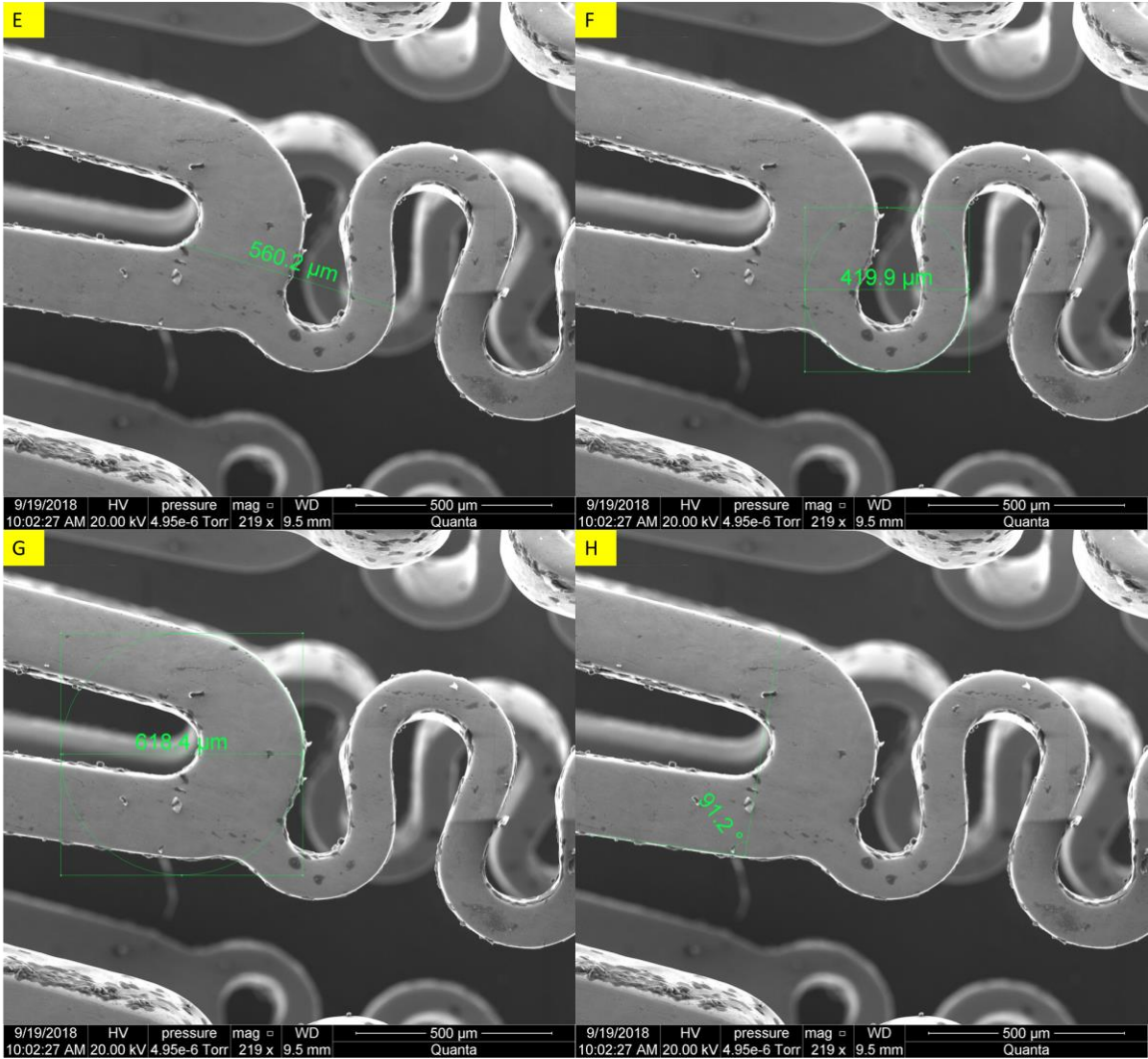


Figure 53 Palmaz Genesis (PG) 2510B stent characteristic features obtained under SEM

Table 6 Mechanical properties of Nitinol (annealed)

Mechanical property	Nitinol (annealed)
Young's Modulus (E)	83 GPa
Yield Strength (σ_{yp})	195 MPa
Ultimate tensile strength	1900 MPa

Table 7 Geometric parameters of PG 2510B stent

Geometrical parameter	PG 2510B
Average length of the strut	2.445mm
Average width of the strut	193.866 μm
Average length of the spline	234.033 μm
Average width of the spline	112.6 μm
Angle between the strut line	91.2°
Diameter of the strut feature	618.4 μm
Inner diameter of the spline	182.8 μm
Outer diameter of the spline	419.9 μm

Alfonso et al. [227] mention that mismatches regarding mechanical/functional properties between the vascular substitute and native vessel cause a higher failure rate in vascular substitute. Commercially available substitutes all low compliance and a reduced distension capacity in physiological pulsations of the native arteries

The expanded polytetrafluoroethylene (ePTFE) grafts have different viscoelastic characteristics compared to the native vessel.



Figure 54 Gore Preclude Pericardial Membrane

Gore preclude pericardial membrane made from ePTFE is the baffle material considered during the HCSII surgical procedure and in-vitro simulations, as shown in Figure 54.

DeCampi et al. specify the placement of the baffle during the HCSII surgical procedure. The baffle material is sutured within the pulmonary bifurcation from the right to the LPA orifice. To preserve this exact technique for the in vitro simulation, the baffle is placed behind the MPA of the centerpiece. A clamp was designed and 3D printed in order to arrest the movement of the baffle. The baffle and the stent complement each other, as the stent protects the baffle from being crushed due to the high pressure from the systemic flow.

3.8. Fatigue Analysis

High stresses observed in the region of calcified plaque are sufficient to fracture the stent. McGarry et al. [228] studied the mechanical performance of stents by modeling stents based on the elasticity and isotropic hardening J_2 flow theory (von Mises flow theory). Considering the size of the stent strut ($< 0.1\text{mm}$), microscale mechanical properties are important. Crystal plasticity theory was used to develop the computational models; the theory incorporated both the microscale deformation mechanism and microstructure. Models having explicit grain representation is necessary as thin polycrystalline stent has a small number of grains across the width. Modeling results showed smooth varying localized stress and strain fields using the J_2 flow theory compared to the crystal plastic theory that predicted non-uniform and localized stress and strain fields. Elementary fatigue analysis was performed by the application of pressure pulse to the stent model. Stresses generated by the pulse were small compared to stresses during deployment and recoil. Fatigue loading is vital for stent and modeling. In the crystal plasticity model, the rough deformed stent surface can predict fatigue crack initiation and growth.

Wei et al. [229] studied the structural and hemodynamic analyses to evaluate the performance of six different stents. This included Palmaz-Schatz shaped, Xience Prime shaped, and Cypher shaped. The other three stents were C-Rlink, C-Rcrown, and C-Astrut. Different materials were assigned to the stents, most of them assigned with 316L stainless steel. During this study, the Dogboning and recoiling phenomena were observed. Dogboning refers to the expansion of the two ends of the stent larger than the center section; this has a more significant effect on thrombosis and hyperplasia. Recoiling is defined as the “spring back” due to the stent's elastic-plastic deformation.

Further to simulation, the maximum plastic strain for the six different shapes showed that larger plastic strain values meant that the stent could sustain the deformation and results in a more significant diameter change. The plastic strain value directly impacted the von Mises stress as the change in diameter induced the stress. Combining structural and hemodynamic properties, the Palmaz-Genesis stent performed better than the Xience Prime and Cypher shaped.

Stents are prone to fail under various axial, circumstantial, radial loading, and other anatomical bending. They also tend to fail due to buckling due to artery wall pressure.

The displacements in the x and y direction obtained are used to compute the strains in the x and y-direction. Since no torque is involved, shear strain and strain in the z-direction are excluded. Equations (41) and (42) are used to compute the ε_x strain in the x-direction and ε_y the strain in the y-direction

$$\varepsilon_x = \frac{\Delta u}{\Delta x} \quad (41)$$

$$\varepsilon_y = \frac{\Delta v}{\Delta y} \quad (42)$$

Using the stress-strain relation, σ_x , the stress in x-direction and σ_y , the stress in y-direction are computed using Equations (43) and (44)

$$\sigma_x = E\varepsilon_x \quad (43)$$

$$\sigma_y = E\varepsilon_y \quad (44)$$

The principal stress $\sigma_{1,2}$ of the stent is calculated using Equation (45). As the stent material is ductile, the liberal failure criterion is used to understand if the stent fails for the given loading conditions. Von-misses criterion, using von misses stress, σ_v along with a factor of safety two is computed as shown in Equation (46)

$$\sigma_{1,2} = \frac{\sigma_x + \sigma_y}{2} \pm \sqrt{\left(\frac{\sigma_x - \sigma_y}{2}\right)^2 + \tau_{xy}^2} \quad (45)$$

$$\sigma_v = \sigma_1^2 - \sigma_1\sigma_2 + \sigma_2^2 = \frac{\sigma_{yp}^2}{2} \quad (46)$$

High cycle fatigue involves elastically applied stress and a large number of cycles to failure. The stress on the component is low, and plastic deformation can occur at any crack tip within the elastic region. Fatigue life is defined as the number of cycles to failure at a specified stress value. The number of cycles to failure increases as the applied stress level decreases. The number of cycles to failure is also determined by the crack growth rate, i.e., the change in the crack length for each cycle. Stress concentrations exist due to the crack presence. Figure 55 shows the relation between the cyclic stress intensity factor and the crack growth rate. Region I represent no crack growth until ΔK reaches the ΔK_{th} (threshold

value). Once the threshold value is attained, the crack growth is at a rapid phase. Region II and III represent the steady-state crack growth and unsteady crack growth.

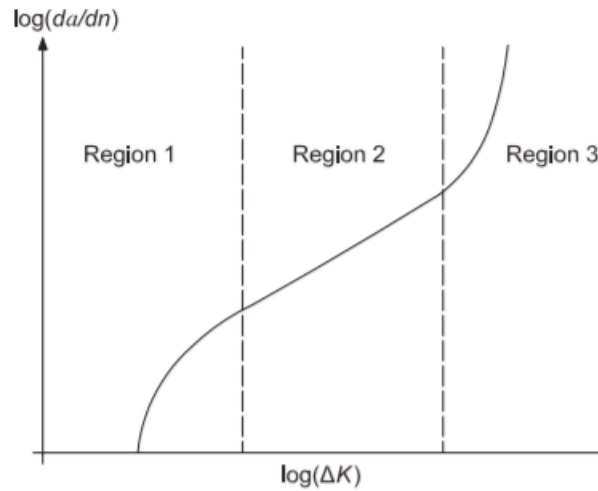


Figure 55 Relation between cyclic stress intensity and crack growth rate

The Paris power law is used to compute the number of cycles to failure, Equation (47).

$\frac{da}{dN}$ is the crack growth rate, ΔK is the difference of maximum and minimum stress intensity factor. C and m are material constants. In this study, two critical locations were considered for the crack to initiate, and based on the critical crack length, the number of cycles to failure change

$$\frac{da}{dN} = C \Delta K^m \quad (47)$$

The analytical approach to compute the number of cycles to failures involves computing the various stresses acting on the stent due to the MPA pressure and baffle. Considering the stent to be a cylindrical element, circumferential stress, axial stress, radial stress, and shear stress are defined using the thin wall cylinder theory. As per the boundary conditions

established, the stent goes through a uniform loading acting on one side of the circumference.

In this experiment, there exists no axial stress due to the absence of axial loading. The method involves computing the hoop stress σ_h of the stent with the given MPA pressure. Equation (48) represents the hoop stress, where p is the pressure acting on the stent, r is the radius and t is the thickness of the stent

$$\sigma_h = \frac{pr}{t} \quad (48)$$

Using Von-misses and criterion and Paris law, the number of cycles to failure can be predicted. The experimental and analytical study can be validated if the stent will sustain the loading condition or fail after the surgical procedure.

3.9. Otoscope

The newly formed Intra-pulmonary junction is 18mm in length and 13mm in width on an 8mm diameter cylindrical surface to measure the normal loading on the baffle surface and shear stress due to the fluid flow over the baffle surface. To measure the stress, different techniques were analyzed. As stress is a measure of a local variable and it changes based on the surface. Hence, strain measurement was considered a global variable, from strain compound stress acting on the baffle, can be identified. Due to the complexity of the patient-specific geometry, various measuring techniques were analyzed. Also, the experiment will be running for 12 days continuously. Hence waterproof and sensor reliability are considered.

Some of the techniques considered during the literature survey are Force (Piezoelectric) Sensors, Strain gauges, Pressure sensors, Micro Electronic Mechanical Systems (MEMS)

based sensors, Non-intrusive optical measurement techniques, and intrusive optical measurement techniques.

Many sensors were ruled out because of the very small dimension and the need for flexibility in the sensing element. Force sensors are not considered because of the measurement of stress instead of strain. Strain gauges and pressure couldn't be used as it excited when to bend to our desired shape. MEMS were considered for best options for this case, but no such off-the-shelf sensors are available; they need to be fabricated as a custom product. The fabrication time usually takes a minimum of 6-8 months with testing and verification, so these sensors were not used. As the entire geometry is complex in shape, rapid prototyping was considered an option for developing a centerpiece. As the region of interest is below the pulmonary artery, a direct view of the baffle is obstructed even when printed using a transparent material. In the end, intrusive optical measurements were considered.

Design limitation in selecting intrusive cameras is that the diameter of the probe should be less than 5mm as the total diameter of the pulmonary arteries is 8mm. The cut section of the pulmonary artery allows the opening of 5.2mm to view the baffle. The camera probe should not block the flow passing through the pulmonary artery. Hence endoscopic camera and borescopes were considered as an option to get the video of the deformation of baffle—another limitation in the fluid that passes through the pulmonary artery. The camera should be able to view the distal end of the pulmonary artery when fluid is passing. The borescope camera lacks clarity, and fixed focus also lacks magnification. In the end, Firefly, Digital Video Otoscope, as shown in Figure 56 A. Otoscope angle and distance B. Slot for otoscope C. Side view of Otoscope and stent D. The Firefly Digital Video Otoscope, is considered

due to its magnification ability similar to the microscope and varying focus but came with a drawback as it's not waterproof. Hence camera should place away from the surface by keeping a transparent material. The specula provided with the camera is 3 and 4 mm in diameter, which suits our requirement.

The Firefly Digital Video Otoscope became the preferred device to capture the stent and baffle movement. For a wider field of area, the 4mm probe is selected. The Digital otoscope has a proper 1.3 Megapixel resolution and a variable magnification up to 150X (digitally) and up to 50X (Optically). Video is captured at a rate of 30 fps. The software comes with a measuring tool and recording tool for easy post-processing of the images for dimensions. Placing the camera at an angle and capturing the whole stent was the constrain as components blocked the lens in the centerpiece. Hand calculations show that the camera should be placed 19.263mm from the proximal end of the stent and 4.84mm in depth at an angle of 24.333° . The values are computed based on the CAD design discussed in section 3.1.1.3. The specula are not interfering with any components of the centerpiece and can view three markers on the stent along the length.

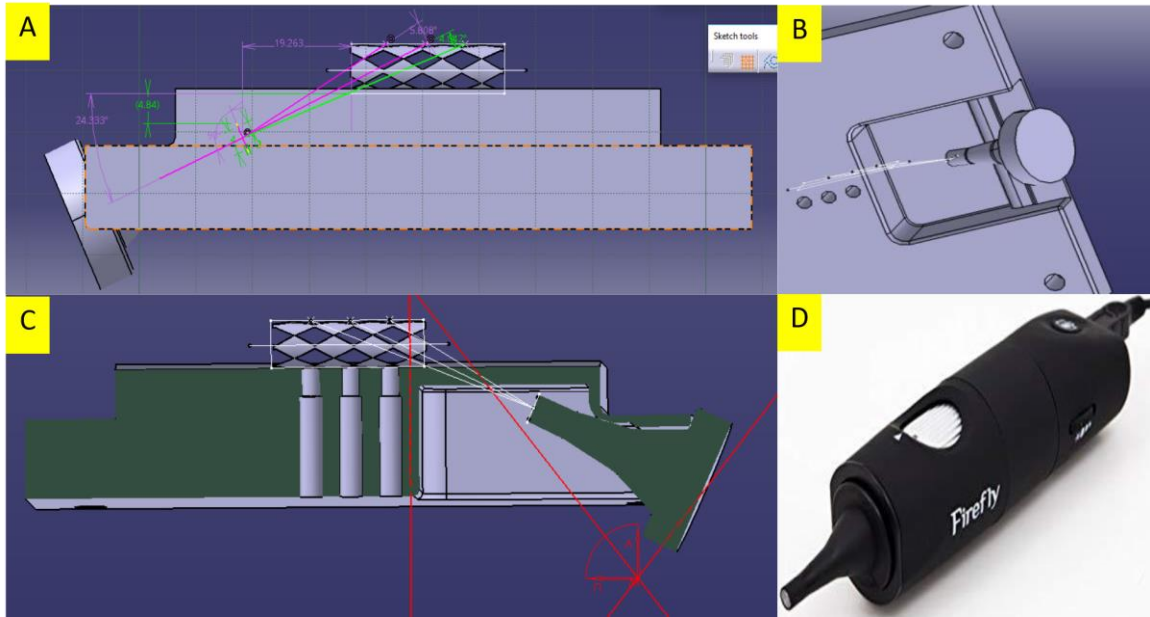


Figure 56 A. Otoscope angle and distance B. Slot for otoscope C. Side view of Otoscope and stent D. The Firefly Digital Video Otoscope

3.10. Uncertainty

Uncertainty quantification is the process in which the uncertainties are characterized quantitatively and reduced in an application. Their likelihood of specific outcomes is determined if some aspects of the system are not known. Uncertainty existence is possible in a mathematical and experimental model, which can be categorized into various sources such as parameter, structural, exponential, interpolation, aleatoric and epistemic.

Experiments mentioned in this report use the sensors to obtain the required output. Uncertainty of sensors can be classified into three types, point, interval, and probabilistic.

3.10.1. Type B Estimates

Type B Estimate is used when the statistics of error distribution is done by knowledge of the error in certain quantities. Uncertainty estimates resulting from reference attribute bias,

display resolution, operator bias, along with computational and environmental factors, are determined using this technique.

Normal Distribution

If the measurement error data is normally distributed, the uncertainty is given by Equation (49)

$$u = \frac{L}{\phi^{-1}\left(\frac{1+p}{2}\right)} \quad (49)$$

$\pm L$ is defined as the containment limit, ϕ^{-1} the inverse normal distribution function, and the containment probability [230] Generally, the containment limits are obtained from manufacturer tolerance limits, calibration records, or statistical process control limits. The containment probability is derived from service data from the past. This study aimed to understand the effect of system-level uncertainty on pressure and flow readings obtained during in-vitro simulations

For the pressure sensors, errors associated with accuracy that combines errors due to linearity, hysteresis, and repeatability are considered. Other errors that are considered include setting zero offset and span error, the total error band that includes errors due to thermal hysteresis, and thermal errors.

Upon establishing the type of error, the corresponding error limits are defined as a number or as a percent of the full-scale reading. The error limits are to be defined by the confidence interval or by a specified level of probability. All the error sources associated with each individual system are assumed to follow a normal distribution. For calculation purposes, the errors are interpreted as a 95% confidence limit if not mentioned by the manufacturer.

Based on the equation, the uncertainty due to each error is computed based on the error limit. This leads to the development of the standardized error model along with the sensitivity coefficients. The model is further simplified as no correlation exists between the individual error sources. The degree of freedom and confidence limit are considered for the final uncertainty.

3.11. Statistical Analysis

3.11.1. Hypothesis

Hypothesis testing is defined as the procedure that involves making decisions based on the nature of the distribution (nonparametric) or the parameter's value (parametric).

Standard parametric hypothesis tests involve the z test and t-test. Nonparametric hypothesis tests involve median test and KS test.

3.11.2. Statistical testing

The null and the alternate hypothesis are formulated along with the significance level (α).

The test statistic $Y(X) = Y(X_1, X_2, X_3, \dots, X_n)$ is constructed, and its distribution has to fall under H_0 . A critical region U is defined for the test statistic Y . The critical region determines whether H_0 is rejected if Y falls inside the region, such that

$$P_{H_0}(Y(X) \in U) \leq \alpha$$

P_{H_0} indicates the inequality is true for all parameters of the population which belong to H_0 .

The value of the critical region is given by $Y(X)$, and the value does not fall under the null hypothesis. $y(x) = Y(x_1, x_2, x_3, \dots, x_n)$ is computed based on the sample data $X_1 = x_1, X_2 = x_2$.

The null hypothesis is rejected, and alternate accepted if $y(x)$ falls inside the critical region.

The null hypothesis is not rejected when $y(x)$ falls outside the critical region. A test is considered statistically significant if and only when the H_0 is rejected.

3.11.3. p-value

The p-value is often used in replacement for the critical region to accept or reject the null hypothesis. The p-value for the given test stat $Y(X)$ is given as by Equation (50)

$$\begin{aligned} \text{two sided: } P_{H_0}(Y \geq y(x)) &= p\text{-value} \\ \text{one sided: } \begin{cases} P_{H_0}(Y \geq y(x)) = p\text{-value} \\ P_{H_0}(Y \leq y(x)) = p\text{-value} \end{cases} \end{aligned} \quad (50)$$

For the null hypothesis to be rejected, the p-value should be smaller than the significance level α . The p-value is a random variable, and it follows a normal distribution under the null hypothesis.

3.11.4. Z-test

Another way of performing a hypothetical test is using the z-test, where the statistic follows a normal distribution curve. The normal distribution is mostly used in real-life scenarios. The central limit theorem states that if the sample size is at least 30 and the sample size remains the same, the distribution of the sample mean is approximated by a normal distribution. A variable X follows a normal distribution if the probability density function (PDF) is given by Equation (51)

$$f(x) = \frac{1}{\sigma\sqrt{2\pi}} e^{-\frac{1}{2}\left(\frac{x-\mu}{\sigma}\right)^2}, -\infty < x < \infty \quad (51)$$

The above equation is usually represented as $X \sim N(\mu, \sigma^2)$ and the parameters of the equation are given by $-\infty < \mu < \infty$ and $\sigma > 0$. The standard normal distribution is defined as

a normal distribution with parameters mean, $\mu=0$ and standard deviation $\sigma=1$ denoted by $Z \sim N(0,1)$. The above (PDF) is given by Equation (52)

$$f(z) = \frac{1}{\sqrt{2\pi}} e^{-\frac{1}{2}z^2}, -\infty < z < \infty \quad (52)$$

The test statistic for the z test is represented as Equation (53), where x is the observed value, μ is the mean and σ is the standard deviation

$$z = \frac{(x - \mu)}{\sigma} \quad (53)$$

The value obtained is compared against the p-value, and the corresponding step involves the acceptance or rejection of the null hypothesis.

Experiments associated with HCSII, and Fontan are conducted with different objectives. Such experiments are conducted multiple times that represent ‘n’ number of heart cycles having the same hemodynamics characters to that of the patient who recently underwent the clinical procedure.

The hypothesis testing for HCSII involves a comparison of in-vitro results obtained with in-vivo results. This comparison is done by conducting a z-score. The null hypothesis for this testing is the studies performed are indifferent with respect to the hemodynamics parameter. The alternate hypothesis is hemodynamic parameters are different.

4. Results

4.1. Experimental Set-Up

As discussed in section 3.2, both MFL setups discussed in this study are based on a reduced LPM. Each R, L, C parameter in the LPM has a specified value derived from clinical measurements. The values for these parameters are physically realized in both MFL setups through respective replicating components as explained in 3.2.1 and 3.2.2. The key to achieving meaningful results in MFL setups highly depends on the accurate tuning of these individual components and data acquisition. Great precision is maintained during the tuning process. Imprecision of one component can lead to an incorrect response of the whole system. As discussed in section 2.2, there are various methods by which MFL setups can be devised for conducting different kinds of experiments. In this study, each MFL is specifically designed to investigate the hemodynamics of the two proposed surgical procedures. Though both MFL setups have been developed to achieve distinctly different research objectives, both MFL setups share the same principal tuning approach.

Both the MFL setups are systematically tuned by following a bottom-up procedure that involves the sequential execution of the following steps:

- I. Set the correct Atrium pressure
- II. Tune the Harvard Apparatus pulsatile blood pump to produce the required CO
- III. Turn ON the NI DAQ 9361, NI 9205, and open the developed LabVIEW project code to start data acquisition
- IV. Tune the systemic and pulmonary resistances to achieve the flow splits by shutting off the compliance chambers.

- V. After attaining the correct flow splits in every compartment, then open compliance chambers to attain the correct pressure waveforms in every compartment of the MFL
- VI. Log the hemodynamic data from the flowmeters and pressure sensors using the LabVIEW code.
- VII. Import the unfiltered logged data using the Matlab post-processing scheme to compute the final filtered results.

In the following subsection, experimentation of both HCSII and Fontan procedure is explained in detail.

4.1.1. Experimentation of HCSII

The experimentation of HCSII was conducted for two patient subsets with different CO.

As mentioned in 3.2.1, the MFL setup majorly consists of four compartments, i.e., Upper systemic, lower systemic, left pulmonary, and right pulmonary circulations. The 3-D printed phantom replicating the reconstructed HCSII physiology, described in 3.1.1.4, has been integrated with the physical components replicating the R, L, and C parameters of the reduced LPM. Figure 57 shows the complete MFL setup of the HCSII circulation.

This research study's prime focus is to investigate the hemodynamics of the proposed HCSII circulation; hence, VSD and the Glenn procedure are modeled in the LPM as a peripheral component to this simulated surgical procedure. Hence to physically represent the VSD feature in the MFL, two resistor valves are used, and the Glenn procedure is replicated using a T junction.

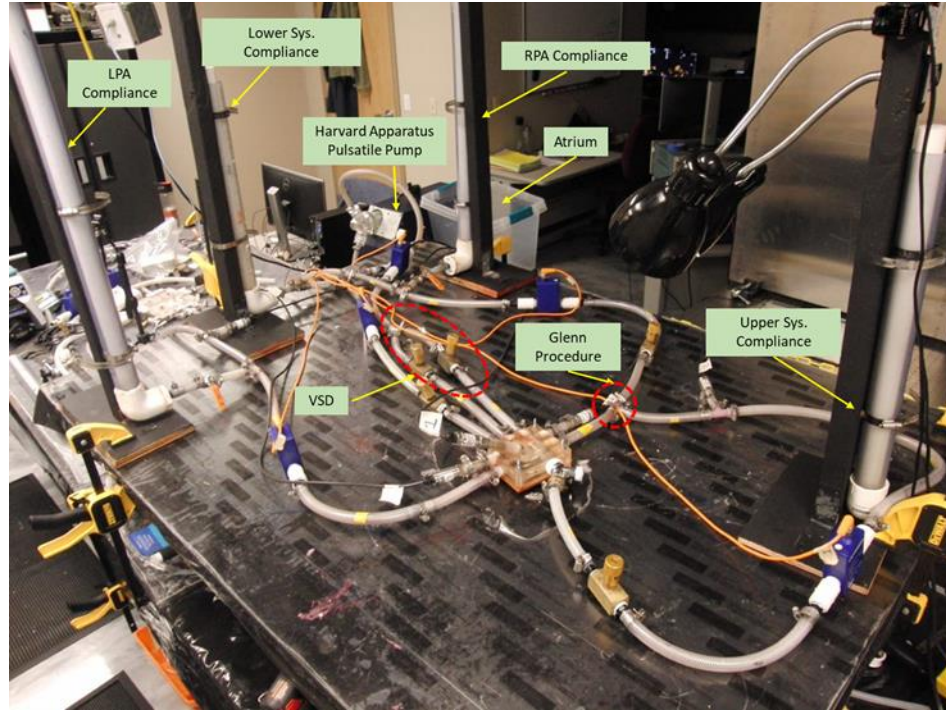


Figure 57 MFL set up of HCSII circulation

Figure 58 shows the location of resistors, flow, and pressure sensors in all four compartments of the MFL. After the Harvard apparatus pump is tuned to produce the required CO, these upper and lower systemic resistors need to be tuned such that the flow split between the upper and lower systemic is maintained. Also, the pulmonary resistances need to be tuned in such a way that the Q_p/Q_s ratio is maintained.

Figure 59 shows the integration of the sensors and the resistors to the 3-D phantom in the MFL. Pressure and flowrate in the MPA, ascending, and descending aorta are maintained by tuning those respective resistances. Pressure from the MPA section over the baffle, ascending, and descending aorta are collected with these integrated pressure sensors.

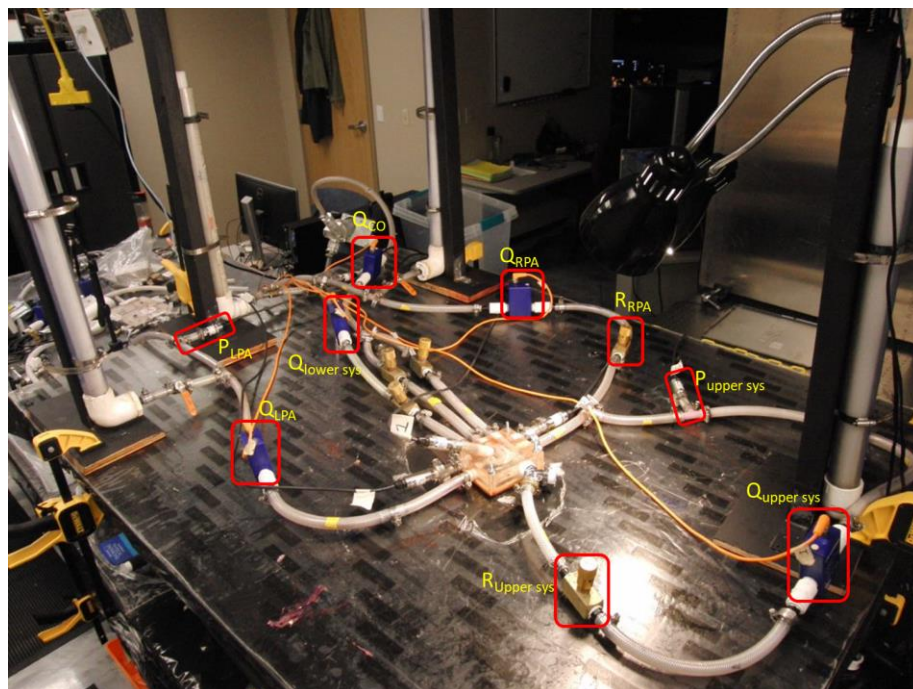


Figure 58 Position of devices in the MFL setup

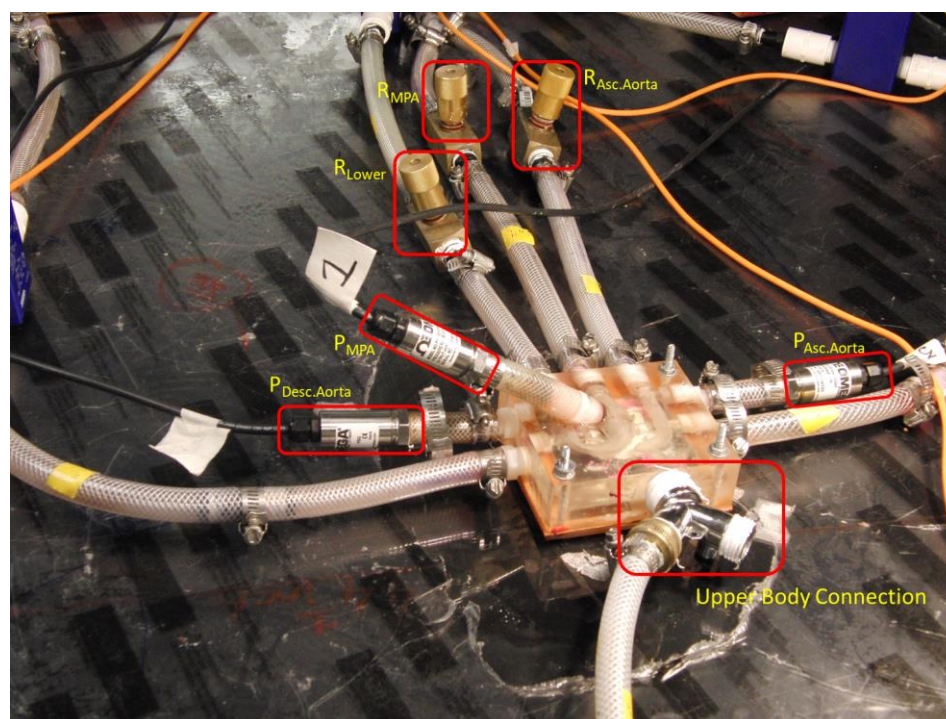


Figure 59 3-D phantom integration with the MFL

Figure 60 shows all the four compartments of the MFL. Once the correct flow splits are achieved by tuning these resistances, then all the compliance chambers are re-engaged. In this way, clinically correct hemodynamic can be achieved in these compartments of the MFL.

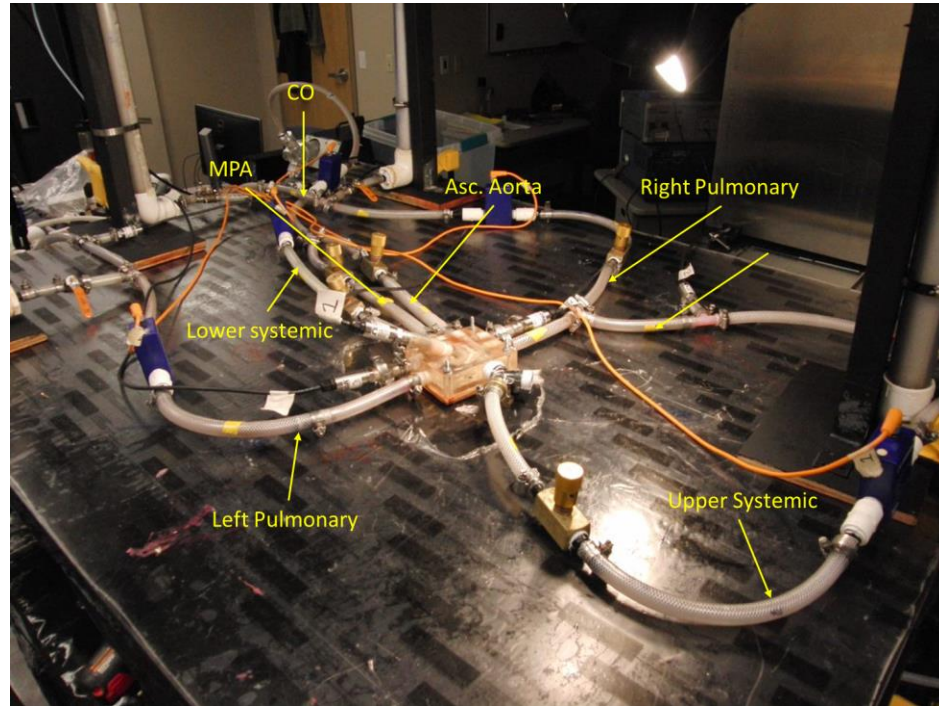


Figure 60 Systemic and Pulmonary circulation in the MFL

To conduct an in-situ PRT experiment a high-speed SONY DSC-RX10 III cybershot camera is installed in the MFL by calculating the hyperfocal distance between the camera lens and the MPA conduit present in the 3-D phantom as shown in Figure 61. Two non rectified light sources have been installed on MFL by focusing on the MPA conduit.

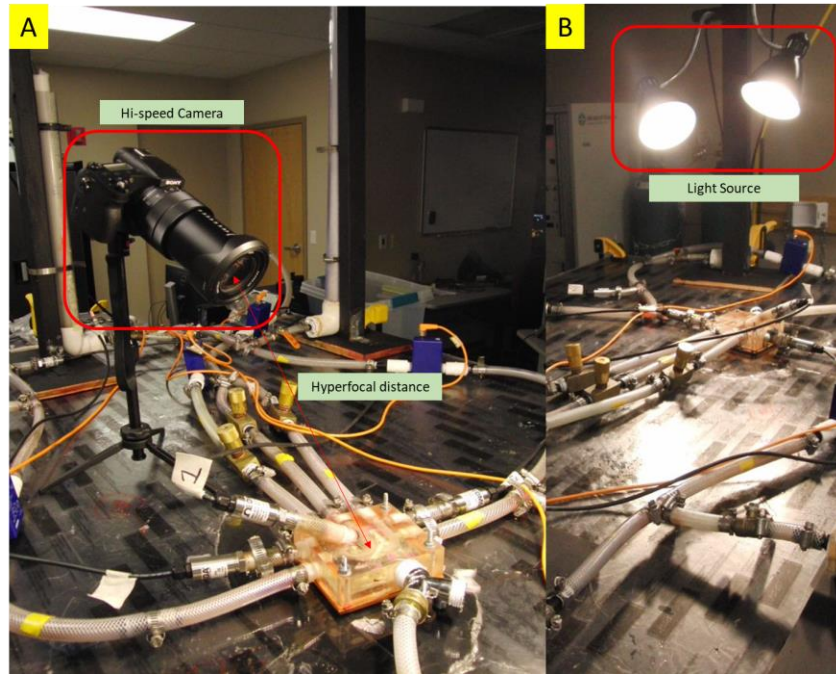


Figure 61 In-situ Image acquisition in the MFL setup

Figure 62 shows the front panel of the LabVIEW code that has been developed to acquire the hemodynamic data from the MFL. All the integrated digital and analog sensors in the MFL are connected to NI DAQ 9205 (analog module) and NI DAQ 9361 (digital module). All live transient and cycle averaged hemodynamic waveforms acquired from each integrated sensor in the MFL are visualized through this panel.

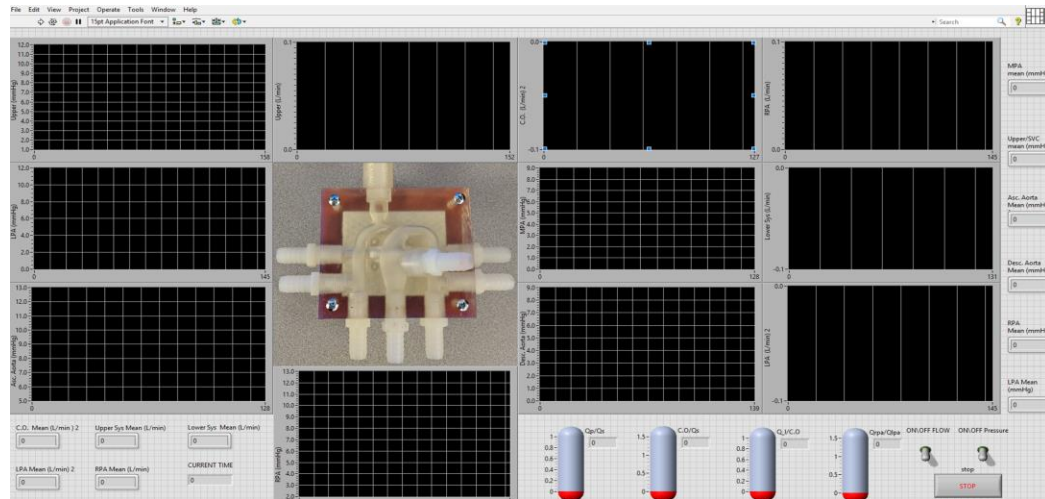


Figure 62 Developed data acquisition and User interface

While acquiring the data during experimentation, noise interference is observed. The trend of noise interference has been consistent for both experimental runs (patient-1 and patient-2). A low-pass Chebyshev type-2 filter is designed to filter the noise. The filter characteristics are shown in Figure 63 and Figure 64.

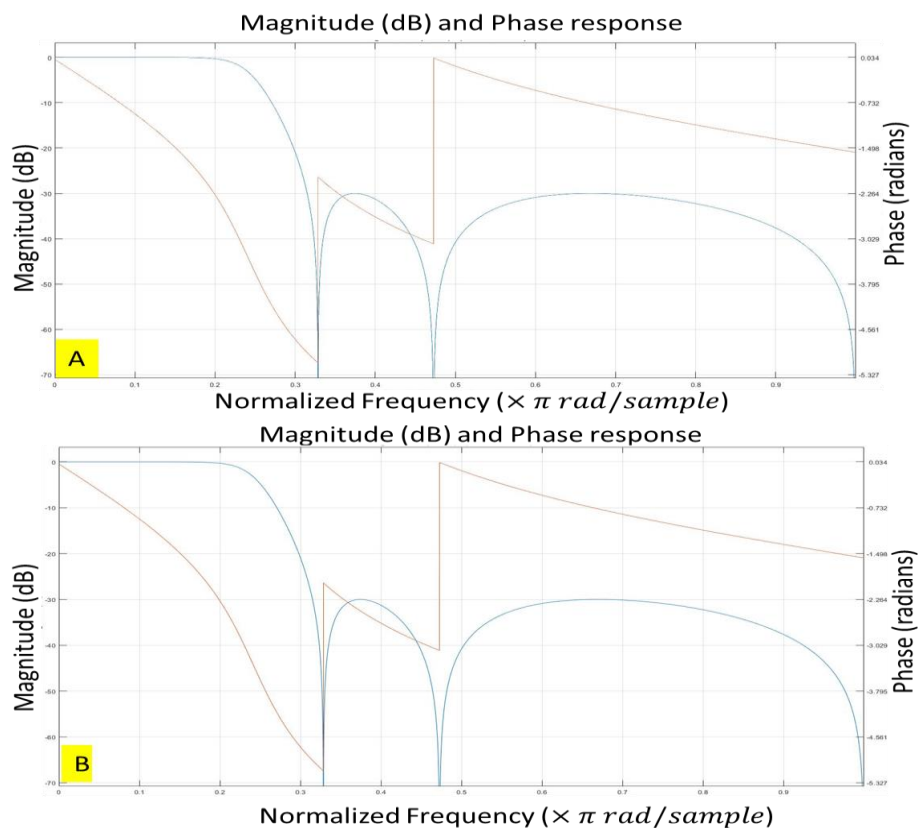


Figure 63 Magnitude and Phase response of filter A. Patient 1 B. Patient 2

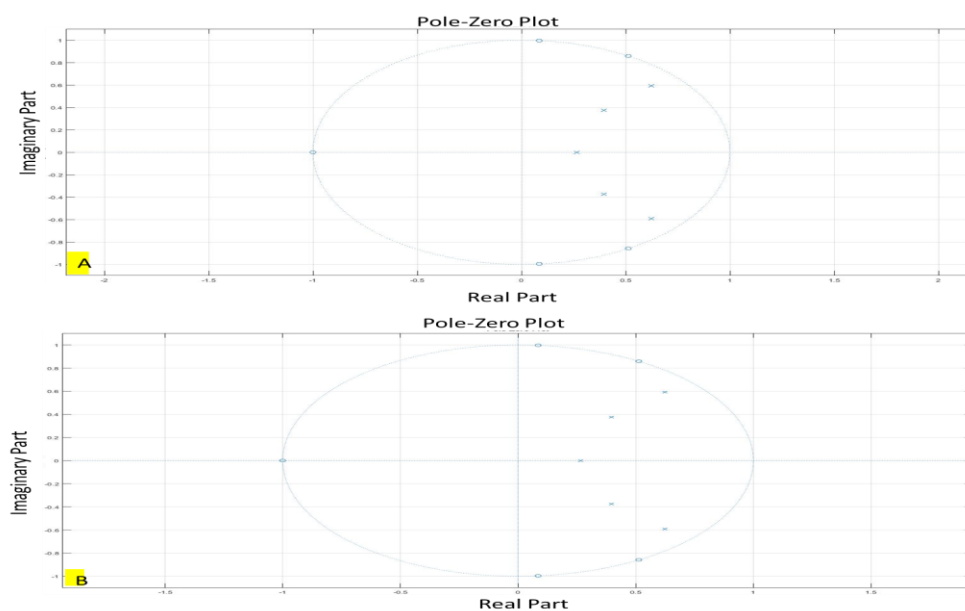


Figure 64 Pole-Zero Plot for filter A. Patient 1 B. Patient 2

Hence after conducting an FFT spectral analysis of the waveform obtained for both patient subsets, a proper cutoff frequency is selected. The spectral analyses of pressure and flowrate waveforms for both patients can be seen in Figure 65-Figure 68.

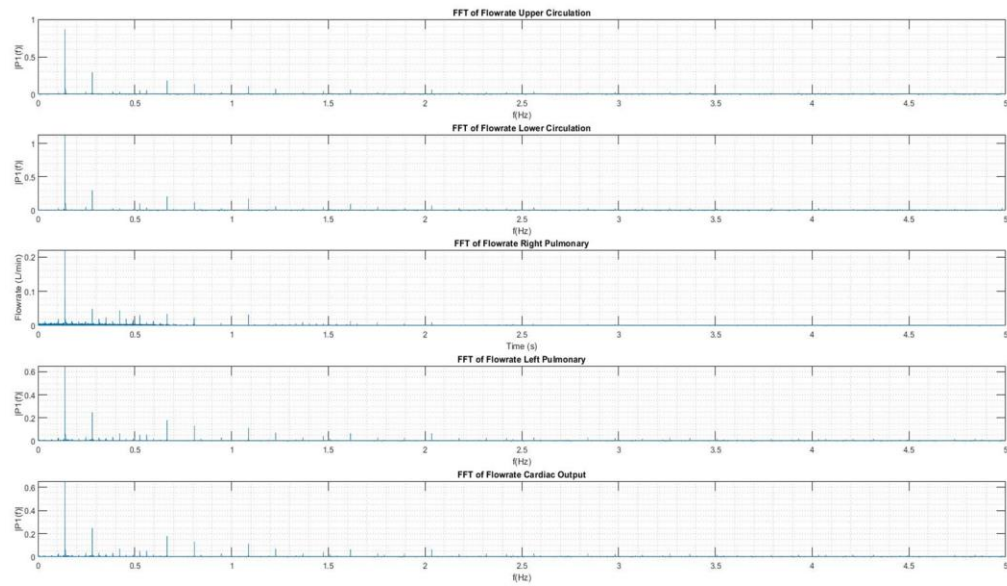


Figure 65 FFT of flowrate waveform for Patient 1

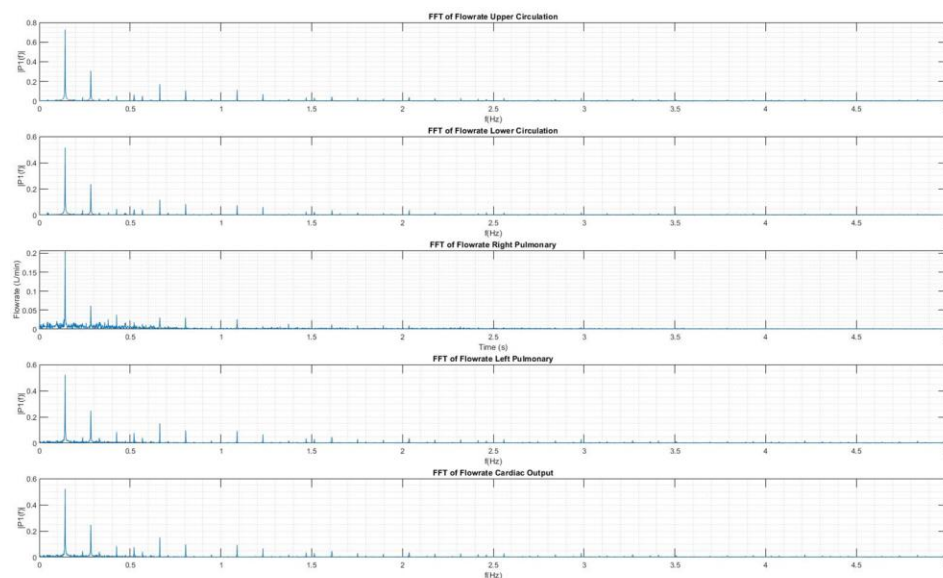


Figure 66 FFT of flowrate waveform for Patient 2

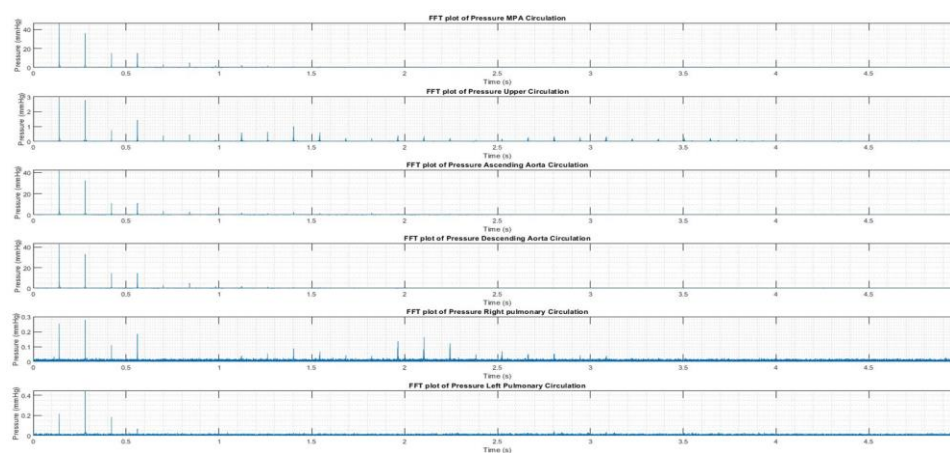


Figure 67 FFT of pressure waveform for Patient 1

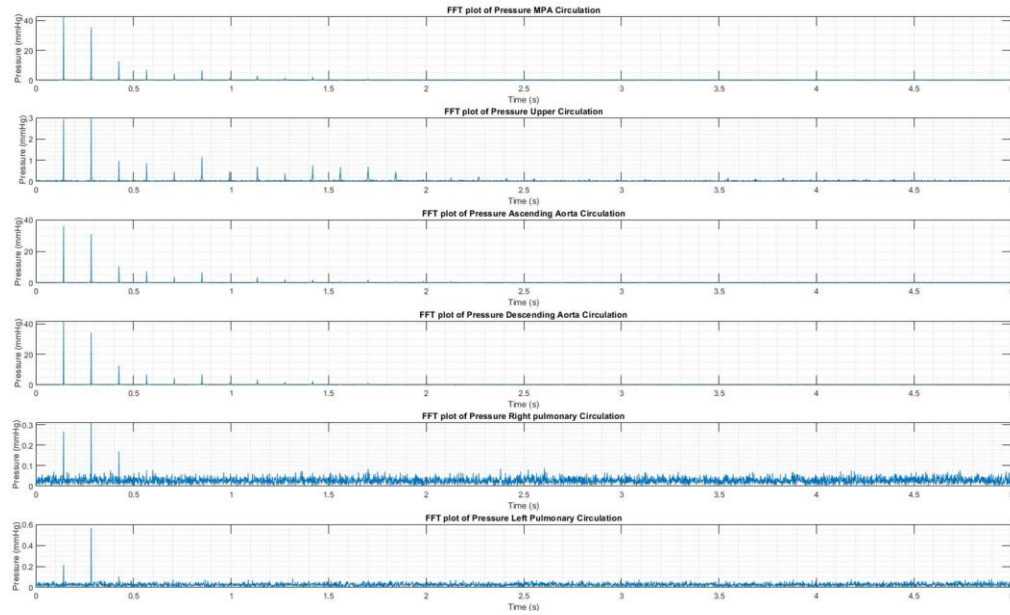


Figure 68 FFT of pressure waveform for Patient 2

Finally, after implementing the chebyshev type-2 filter, another digital filter called savitzky- Golay filter is applied to smoothen out the waveforms. To keep the brevity, the effect of this combined filtering algorithm is shown in Figure 69 for the pressure waveform of patient-2.

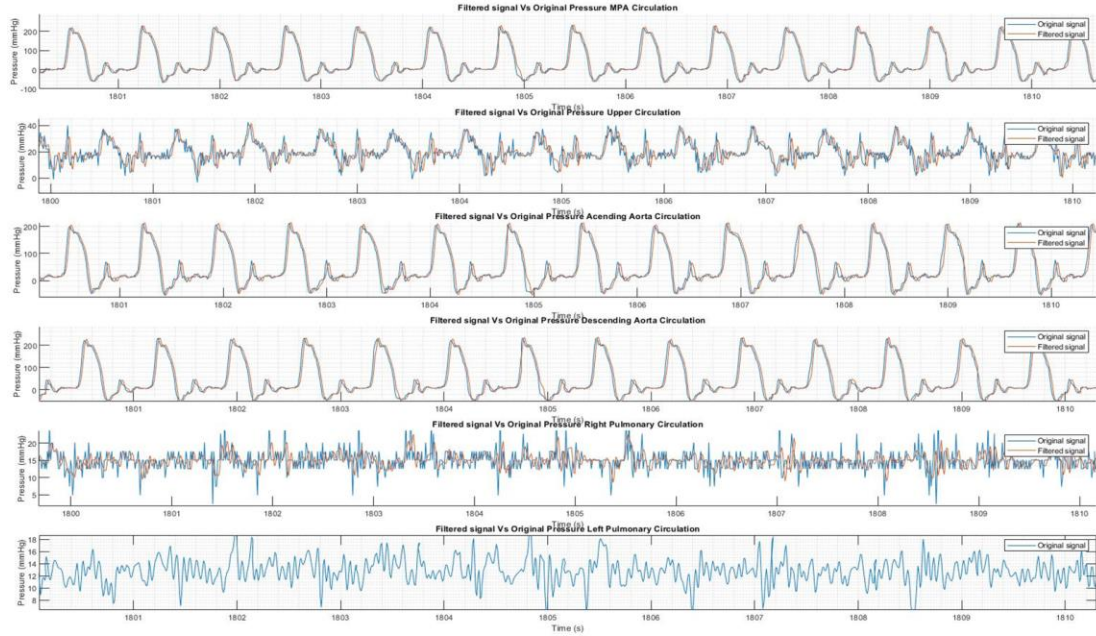


Figure 69 Original and filtered Pressure waveforms of Patient 2

4.1.1.1. In-Situ Stent Deformation

As explained previously in 3.9, an in-situ stented baffle tracking in the PA conduit is one of the key aims of this study. The stented baffle displacement is occurring due to the pulsatile loading of the MPA conduit. Stented baffle tracking is done by developing an in-house computer vision code. This code is developed based on the Lucas Kanade Tracker algorithm. While conducting the MFL experimentation, videos of the stented baffle displacement are acquired by using the otoscope. These videos are acquired under varying lighting conditions and focus. After importing the videos using the computer vision code, a bounding box is created on the region of interest. The tracker algorithm is used to track the Eigen features of the stent during each cardiac cycle as shown in Figure 70. Finally, each tracked location is post-processed and the displacement of each tracker during each cardiac cycle is converted to Euclidean distance.

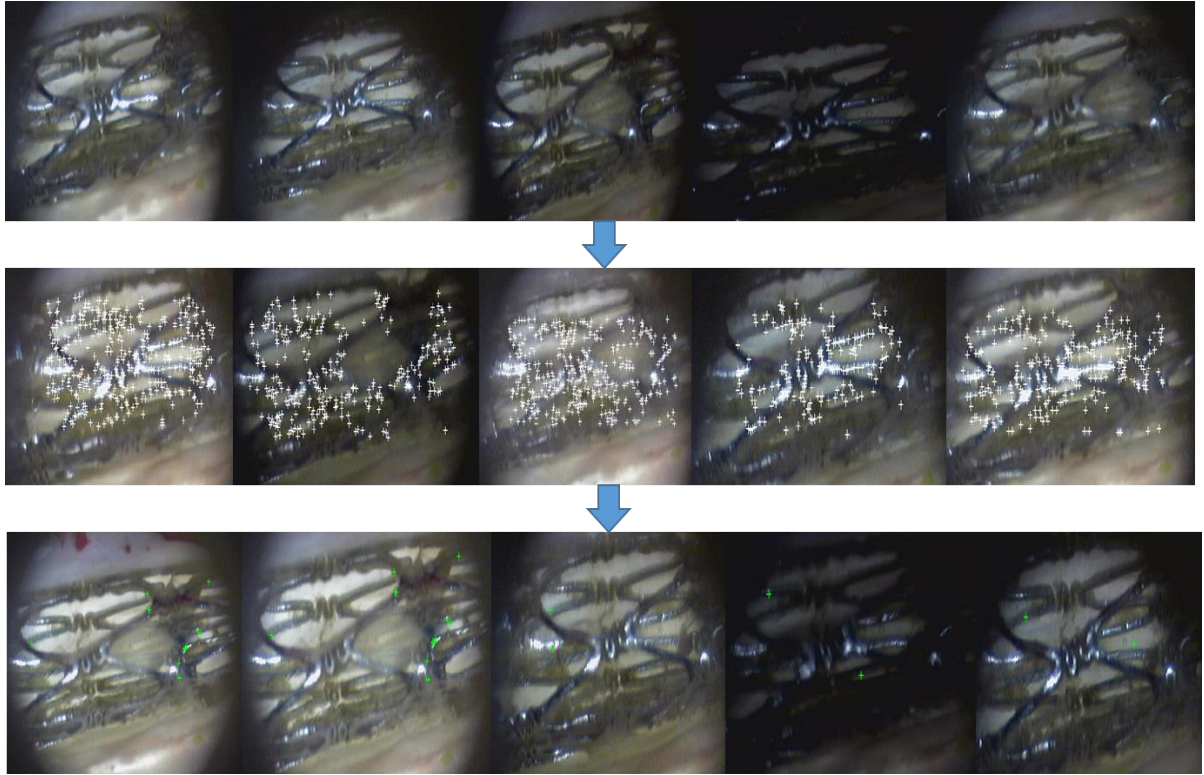


Figure 70 Stent and baffle tracking

4.1.1.2. Particle Residence Time

The particle residence time (PRT) analysis explains the probability of thrombus formation and pathological flows in this reconstructed physiology. To achieve this goal, particles of 2mm diameter in size are injected into the flow stream of MPA. The injected particles closely matched the density of the blood analog that is acting as the working fluid in the MFL setup as shown in Figure 71.

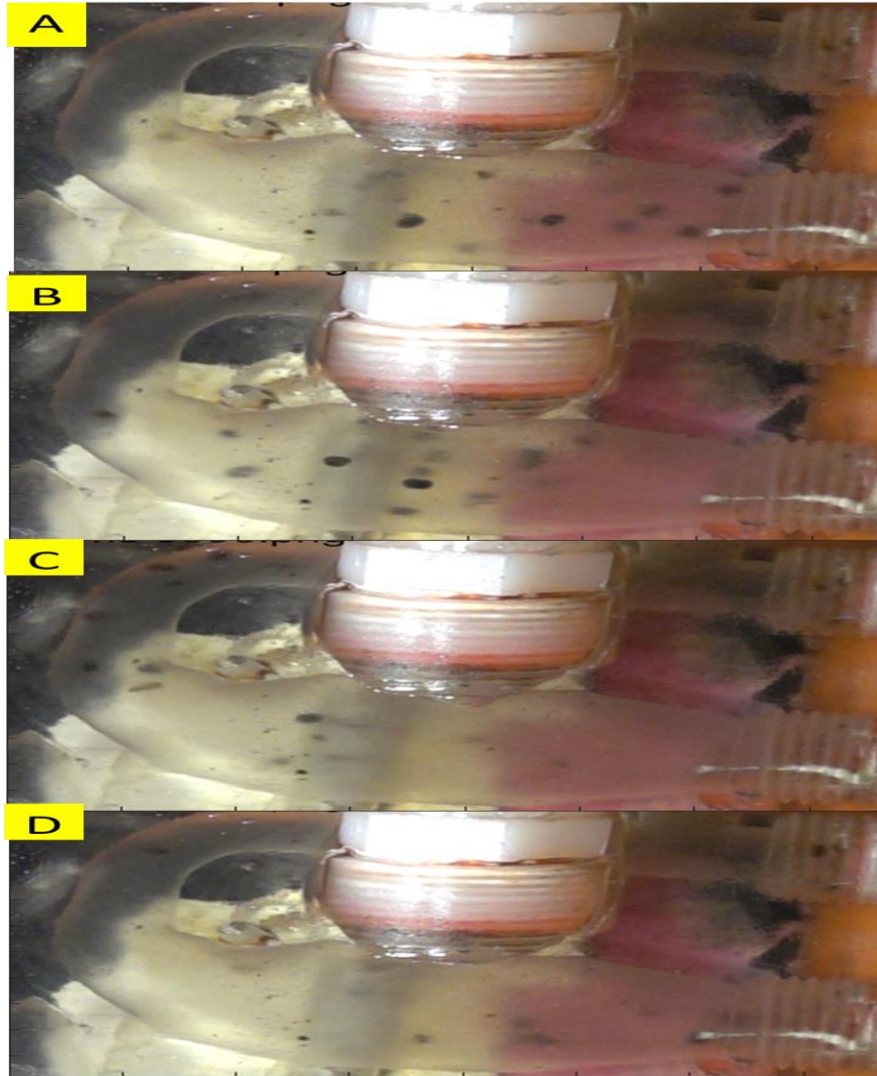


Figure 71 PRT: A: Early systole, B: Peak systole, C: Early Diastole, D: Late Diastole

To track the pathlines of the injected particles, a multi-object Kalman tracker is developed. The main goal of the tracker is to successfully track all the particles once they enter the MPA conduit till those exits out through the DA conduit. The high-resolution video of particle motion was captured with 1000 FPS using the camera. Video has been preprocessed by running a stabilizing scheme to control the blurring and video vibration. Finally, the Kalman tracker for multi-object is launched on the video. The tracker

properties are tuned for detecting the particles during systole and diastole as shown in Figure 72

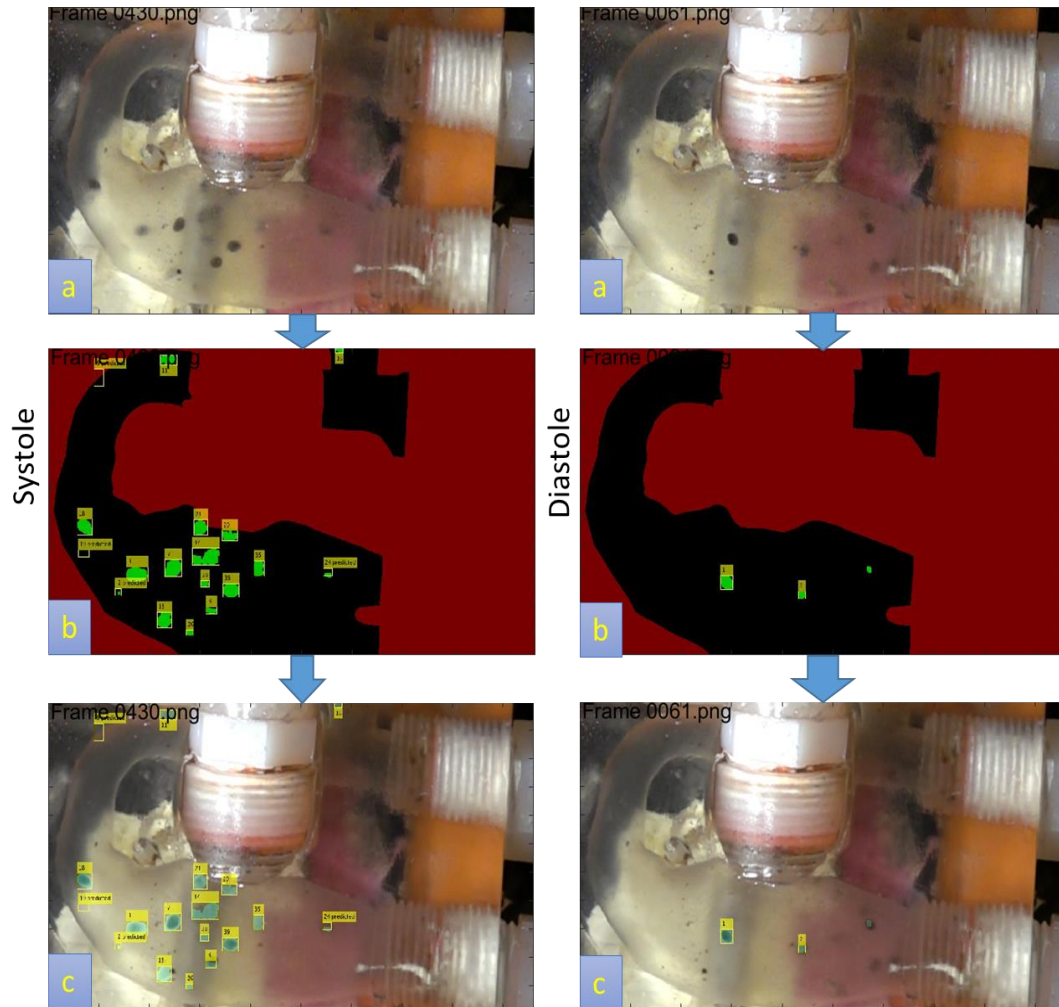


Figure 72 Particle tracking study using Kalman tracker during systole and diastole a original video b. preprocessing c. Kalman tracker

4.1.2. Experimentation of Fontan

The Fontan circulation is modeled in a way the upper systemic circulation receives approximately 30% of the total systemic blood flow while the lower systemic circulation receives approximately 70% of the total systemic blood flow. In the pulmonary circulation, the left and right branches each receive approximately 50% of the pulmonary blood flow.

Thus, the vascular resistances are initially adjusted or tuned to control the ratio of flow within two parallel lumps of the flow loop. Once the flow ratios had been met, the compliance chambers are engaged while maintaining the appropriate flow ratios. Then, IJS graft line is turned on by incorporating the correct IJS graft as mentioned in 3.1.2. In this experiment, various sizes of the IJS nozzle and different angles of anastomosis, and the effect of PVR are simulated, as shown in Figure 73 and Figure 74.

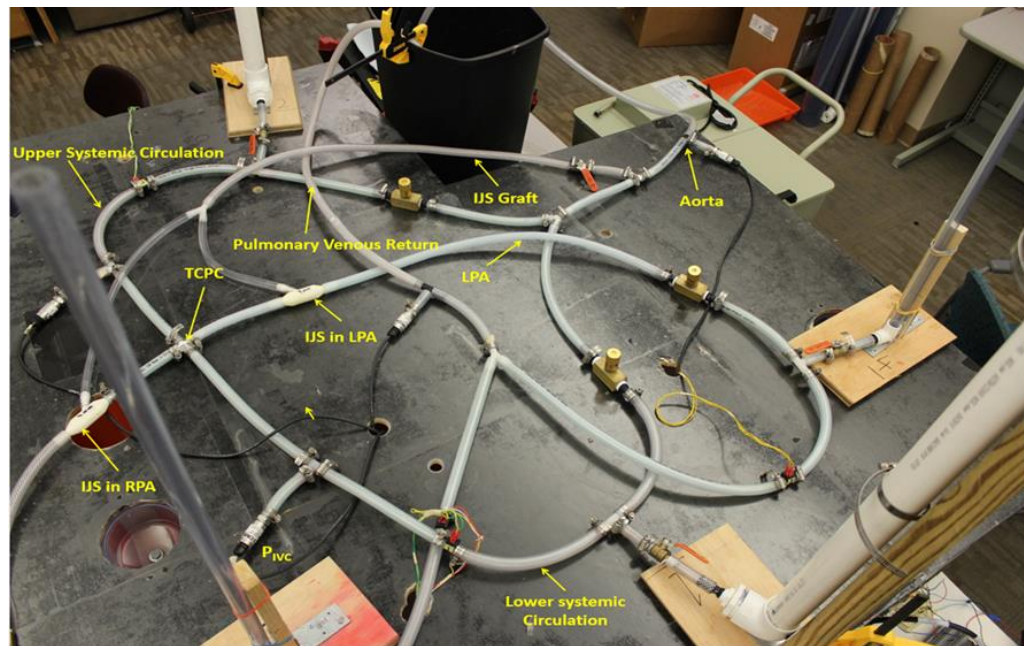


Figure 73 Mock Flow Loop set up for Fontan circulation with IJS in PAs

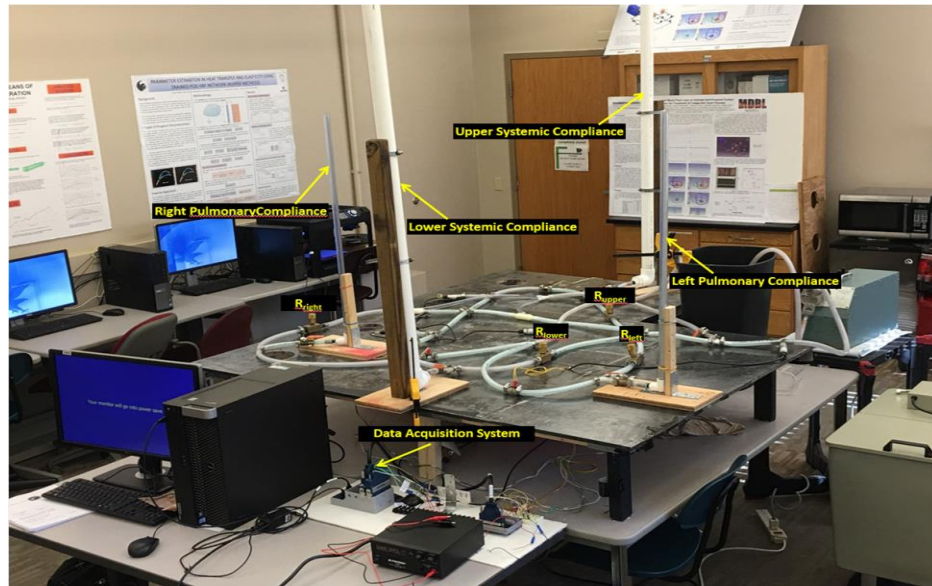


Figure 74 Mock Flow Loop set up with DAQ and compliance chambers

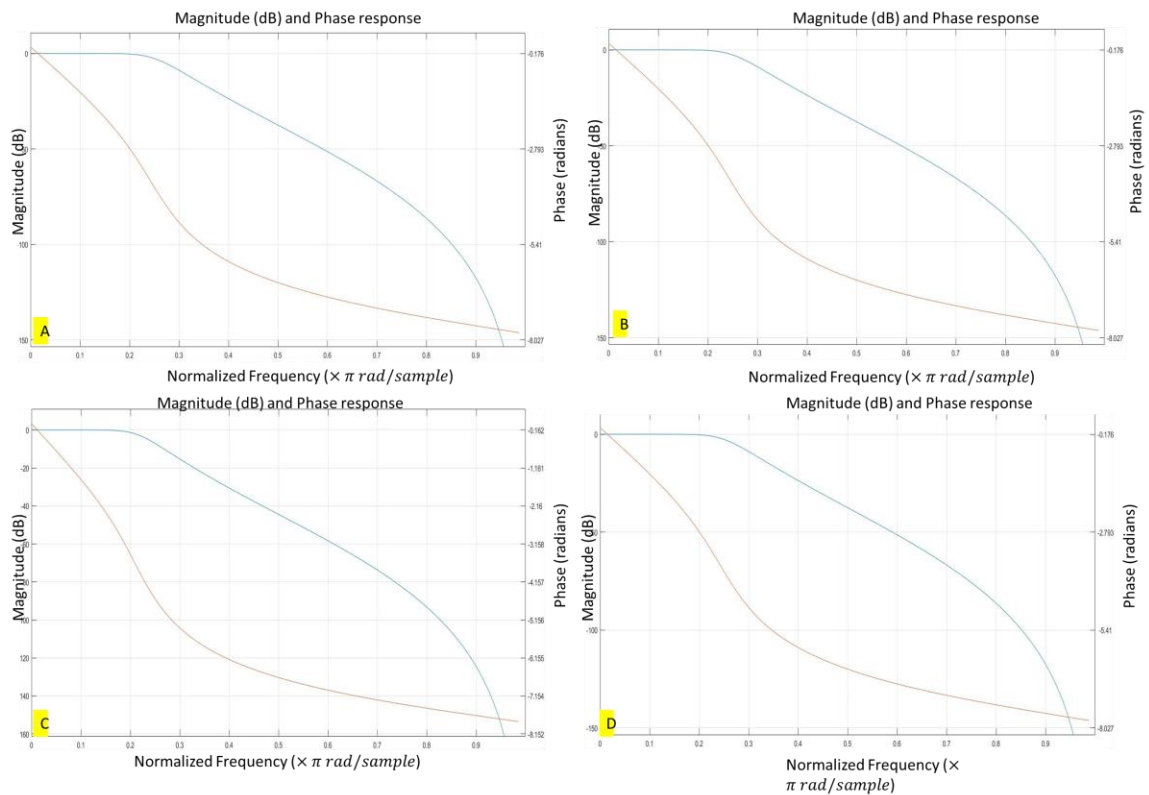


Figure 75 Magnitude and phase response of flowrate at A. Upper B. Lower C. Left D. Right for 3 mm IJS

There is a significant amount of noise interference in the flow and pressure field during experimentation once various parameters are tested out. A butterworth filter and the savitzky-Golay filter are applied to the final post-processed data to filter out these noises. To maintain the brevity in this section, only the performance of the most qualified cases from each of the three parameters (nozzle size, anastomosis angle, PVR %) are discussed here. The filters are applied to the flowrate waveforms for each lump and IVC pressure. Figure 76-Figure 83 shows the filter characteristics for each of the most qualified cases. Pole-zero plots of all these filters show that the designed filter is very stable in performance. Each filter's magnitude and phase response describes a smooth transition from the passband to stopband frequency.

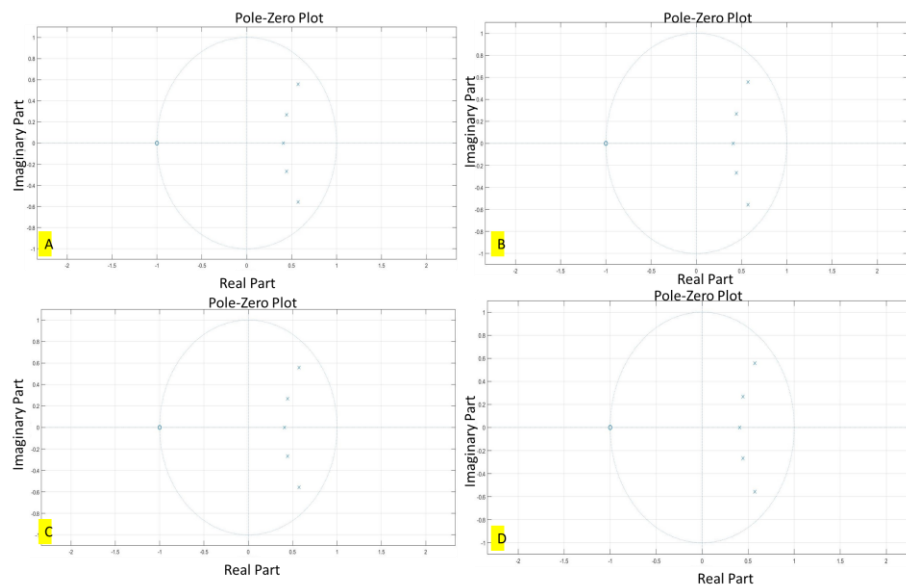


Figure 76 Pole-zero plot of flowrate at A. Upper B. Lower C. Left D. Right for 3 mm IJS

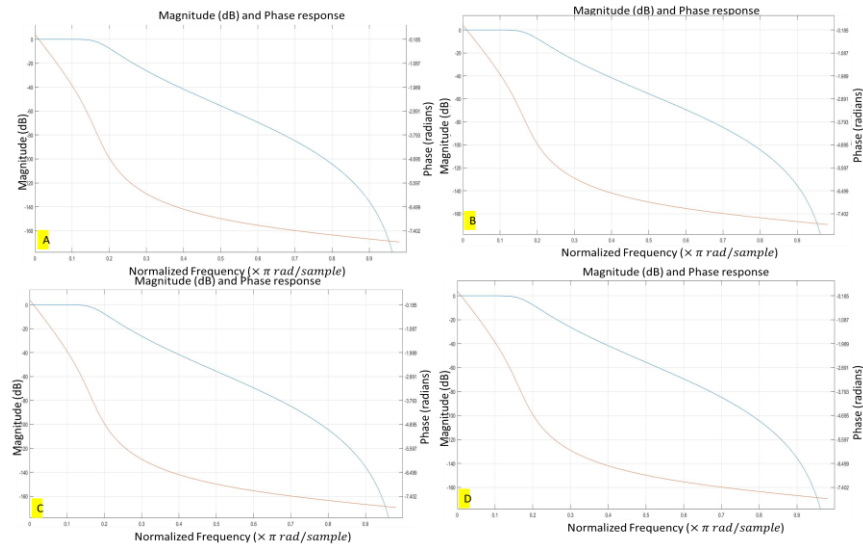


Figure 77 Magnitude and phase response of flowrate at A. Upper B. Lower C. Left D. Right for 3 mm IJS at 5 degree

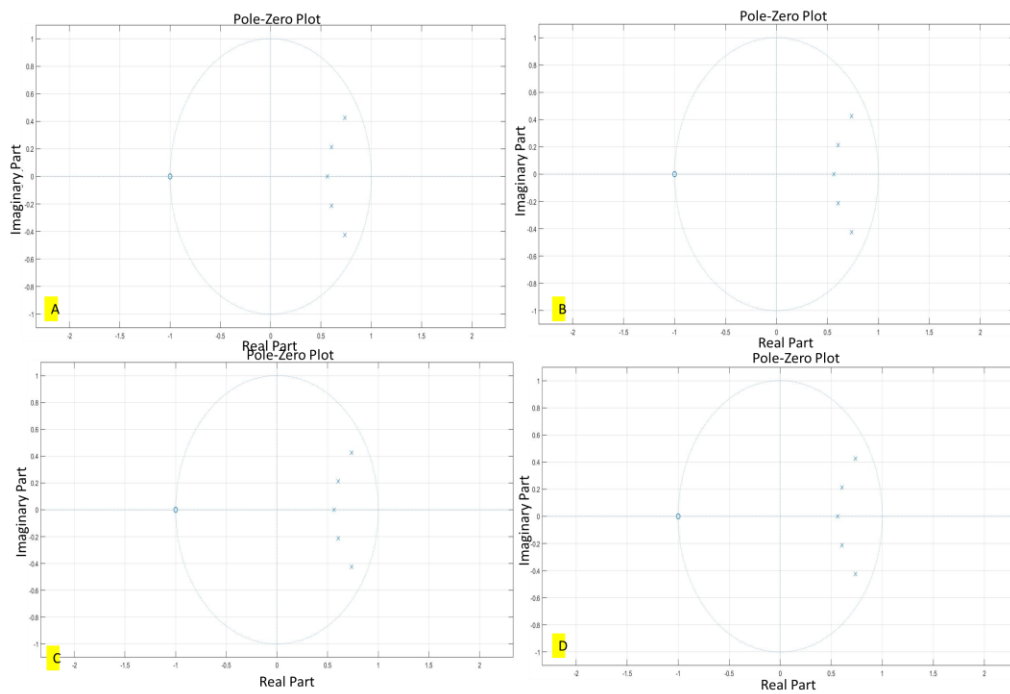


Figure 78 Pole-zero plot of flowrate at A. Upper B. Lower C. Left D. Right for 3 mm IJS at 5 degree

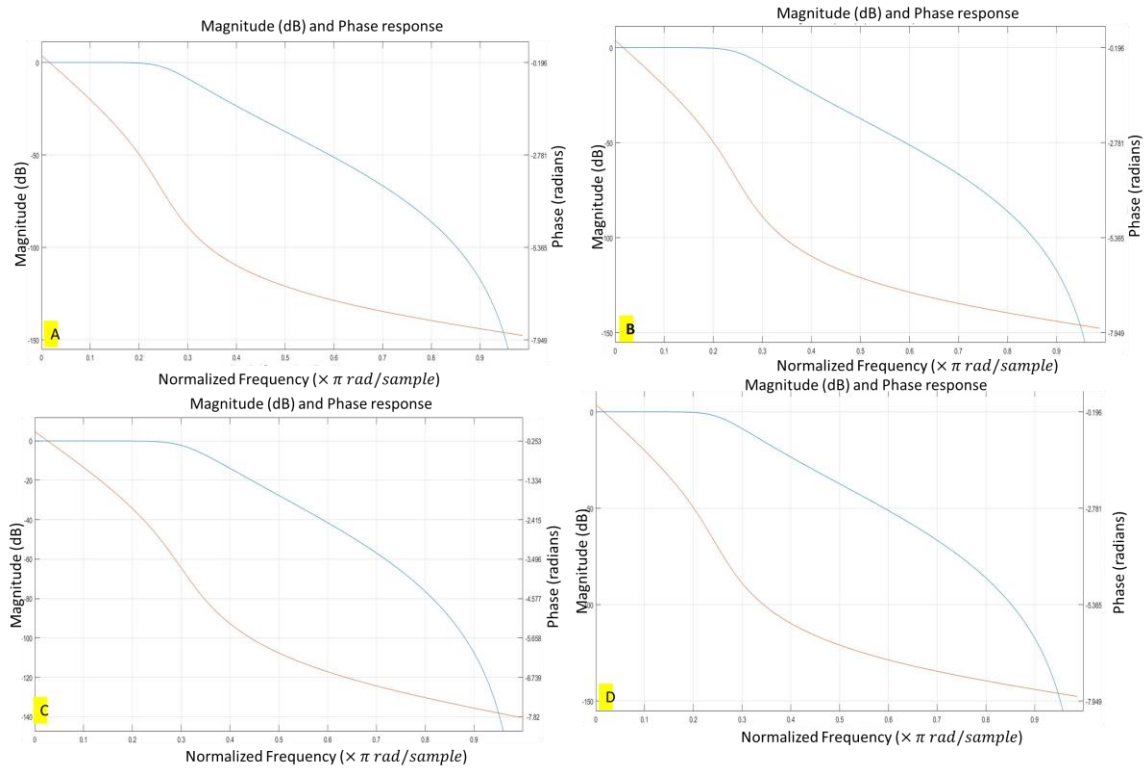


Figure 79 Magnitude and phase response of flowrate at A. Upper B. Lower C. Left D. PVR 30

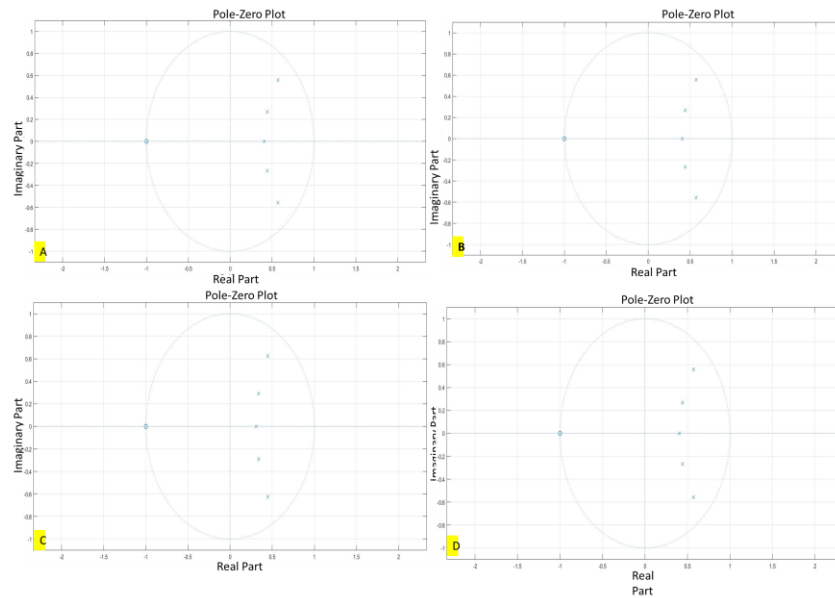


Figure 80 Pole-zero plot of flowrate at A. Upper B. Lower C. Left D. Right for PVR 30

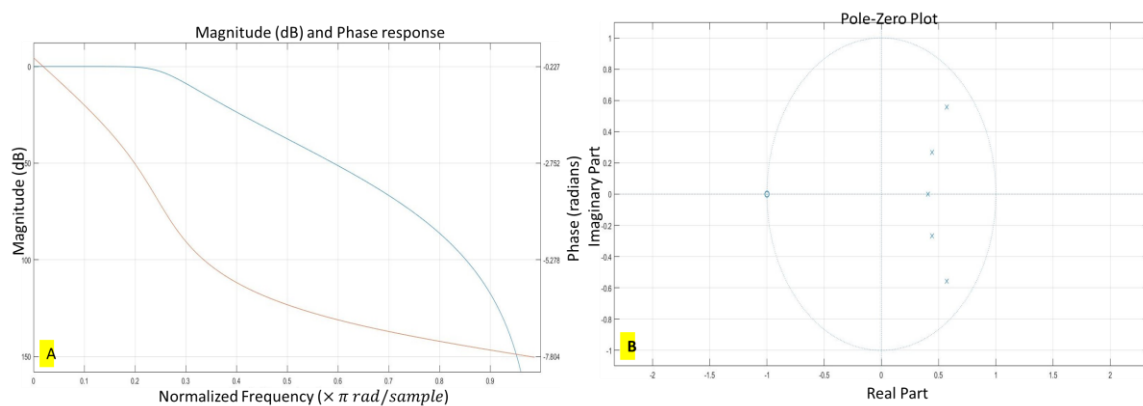


Figure 81 A. Magnitude and phase response B. Pole-Zero plot of IVC pressure for 3mm IJS

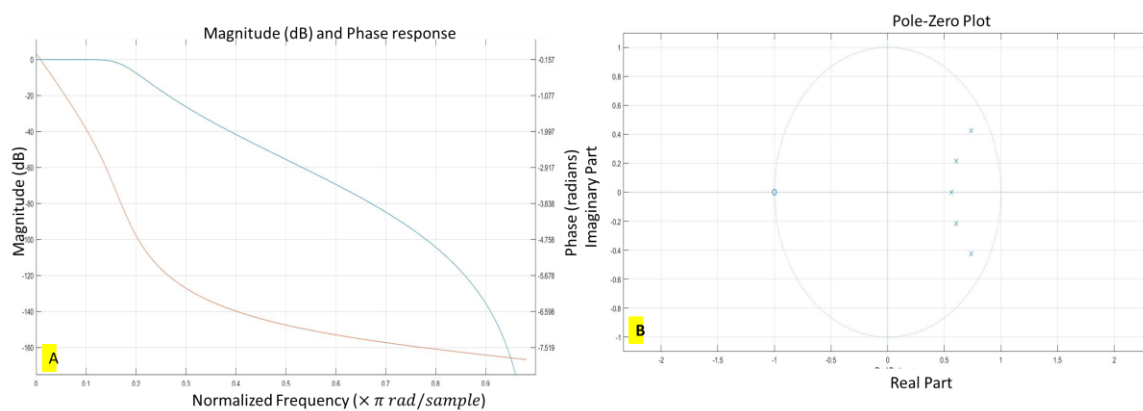


Figure 82 A. Magnitude and phase response B. Pole-Zero plot of IVC pressure for 3mm IJS at 5 degree

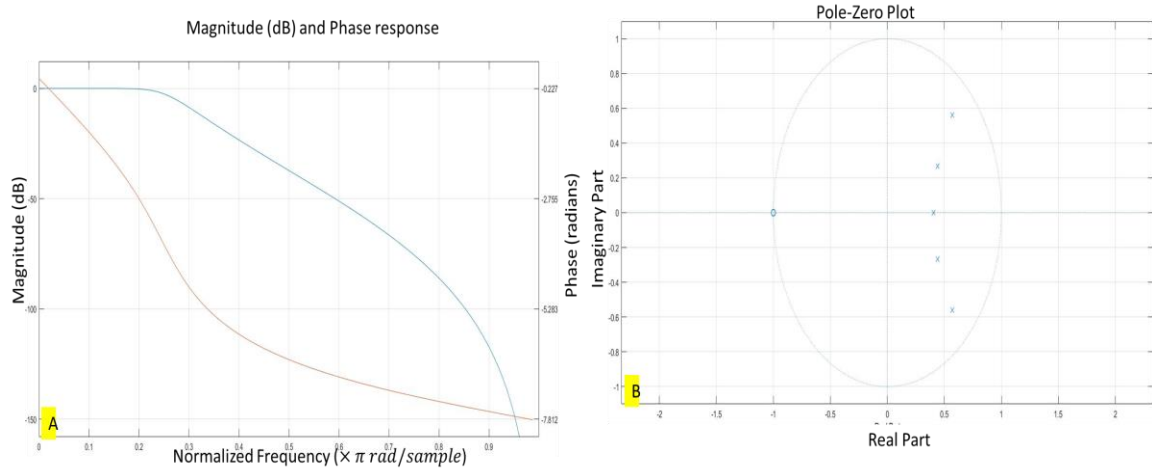


Figure 83 A. Magnitude and phase response B. Pole-Zero plot of IVC pressure for PVR 30

The spectral analysis on all flowrate waveforms for all three parametric studies has been performed to understand the noise interference pattern, as shown in Figure 84 - Figure 86. Depending on the peak frequency, a cutoff frequency has been selected and applied to develop the filters.

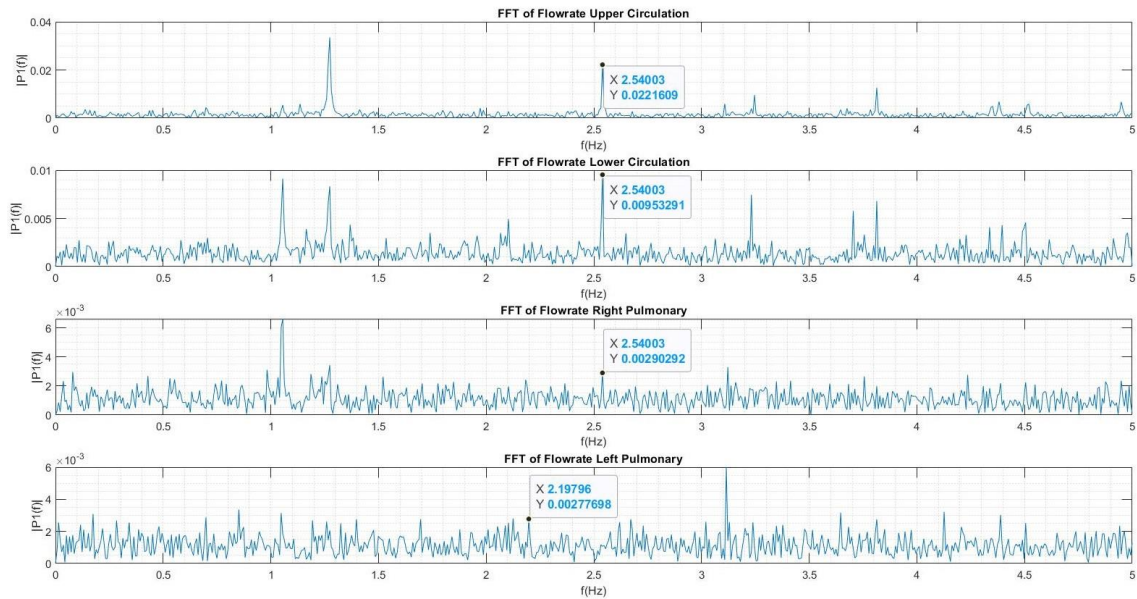


Figure 84 flowrate FFT 3mm IJS

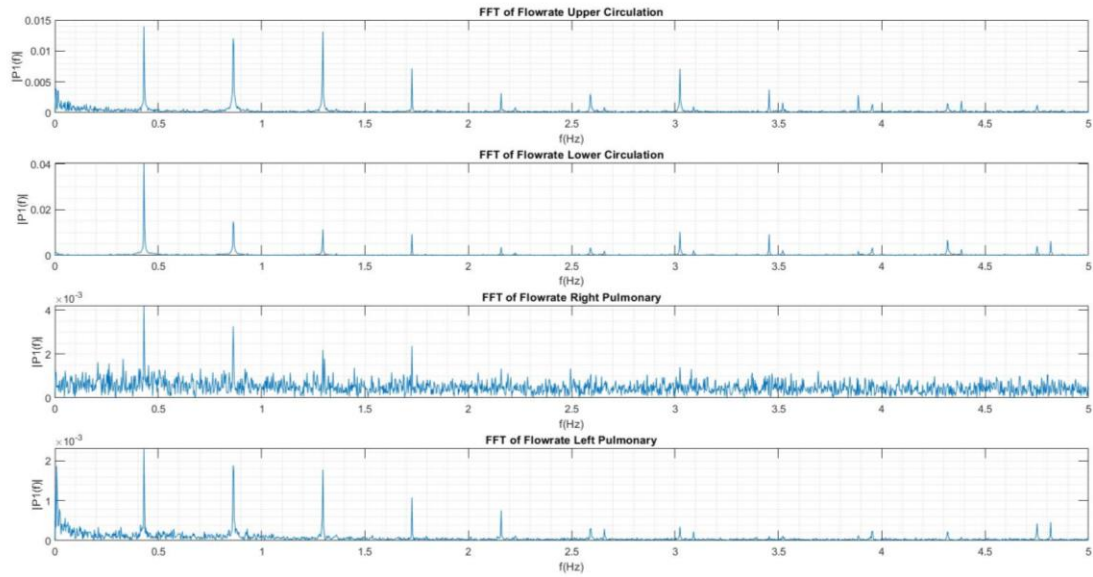


Figure 85 flowrate FFT of 3mm IJS at 5 degree

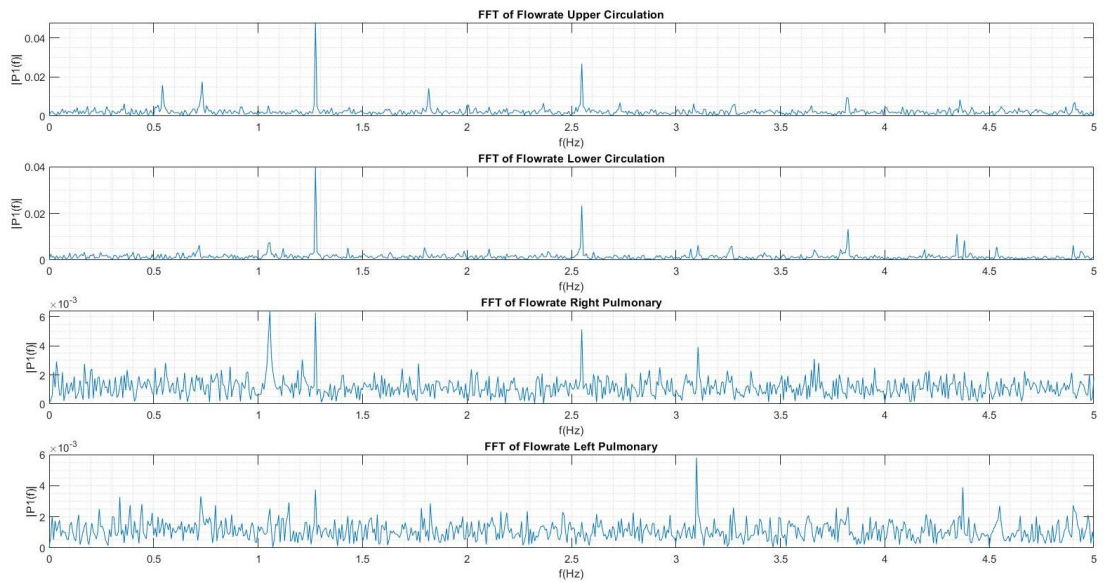


Figure 86 flowrate FFT PVR30

Figure 87- Figure 89 show the unfiltered flowrate waveforms for the qualified cases of each parametric group. These unfiltered waveforms are embedded with high-frequency noise.

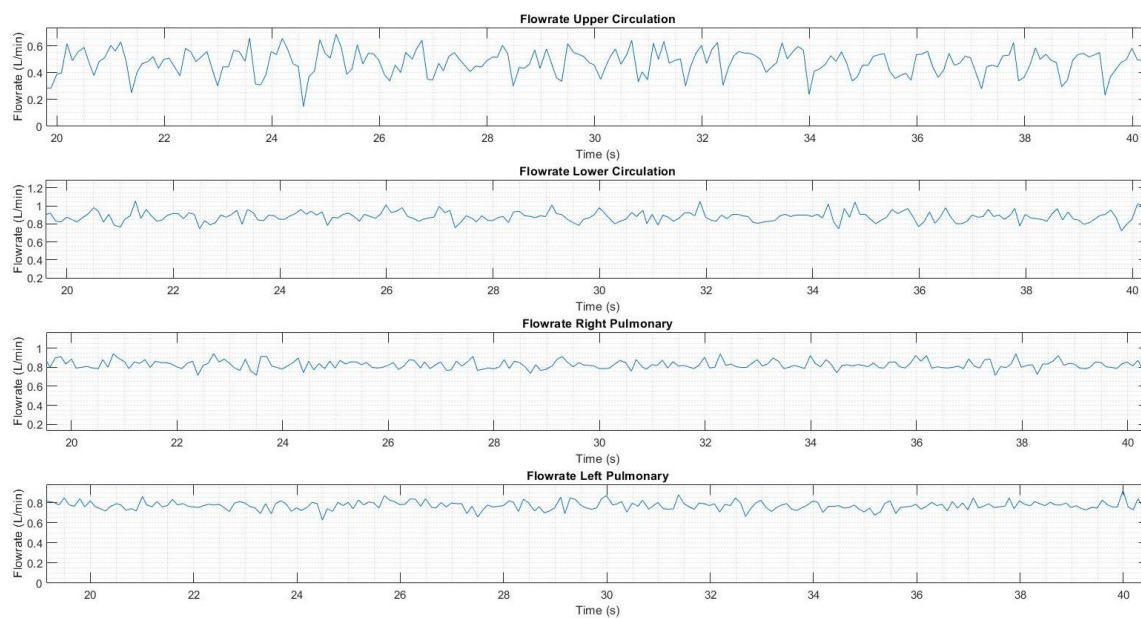


Figure 87 Unfiltered flowrate for 3mm IJS

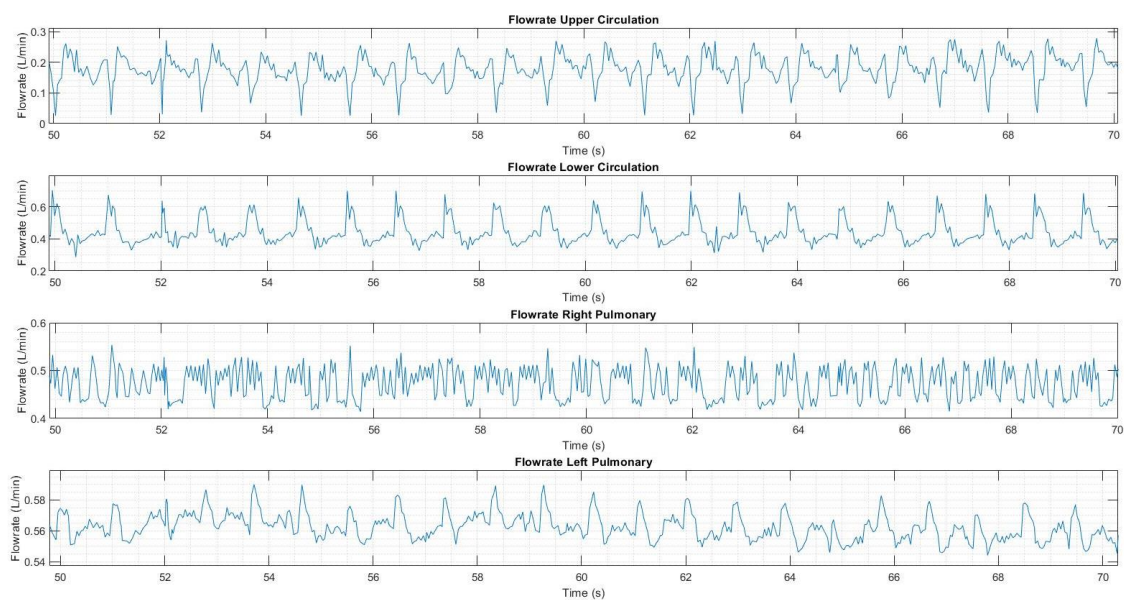


Figure 88 Unfiltered flowrate for 3mm IJS at 5 degree

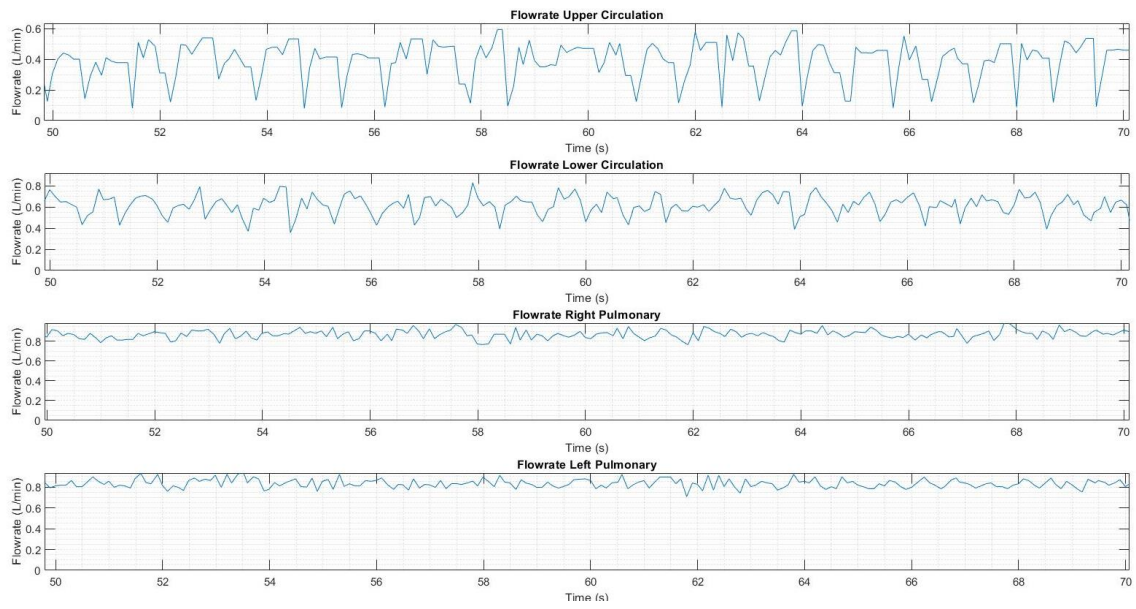


Figure 89 Unfiltered flowrate for PVR30

Figure 90 to Figure 92 show the comparison of the filtered and unfiltered flowrate waveforms after implement this filtering scheme. By comparing the systolic and diastolic features between filtered and unfiltered waves, it can be seen that embedded noise is filtered out.

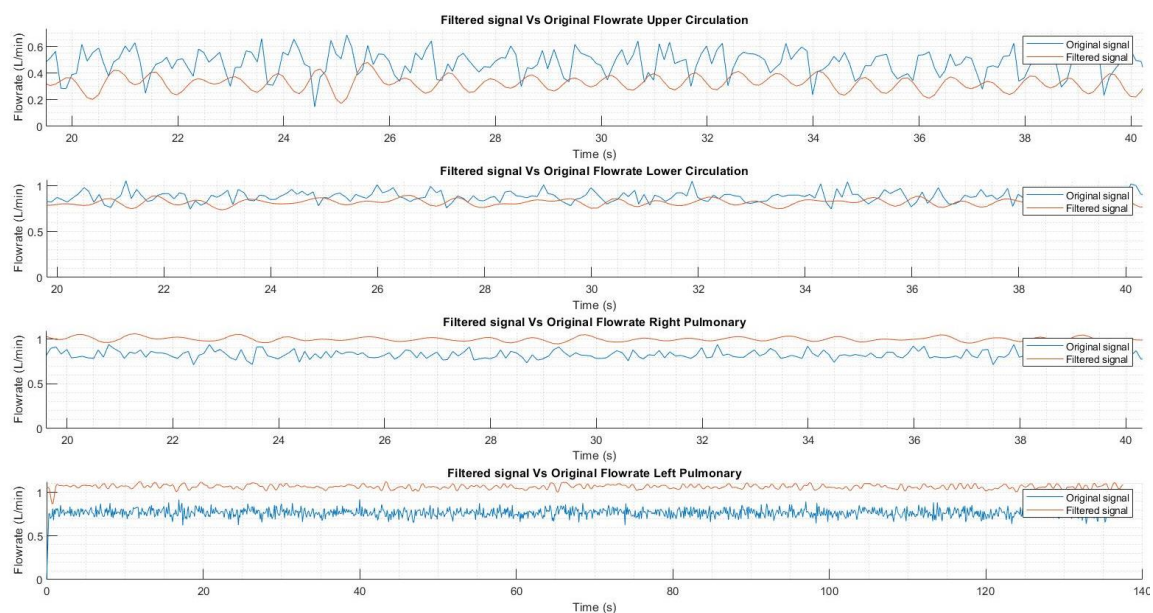


Figure 90 Filtered and Unfiltered flowrate for 3mm IJS

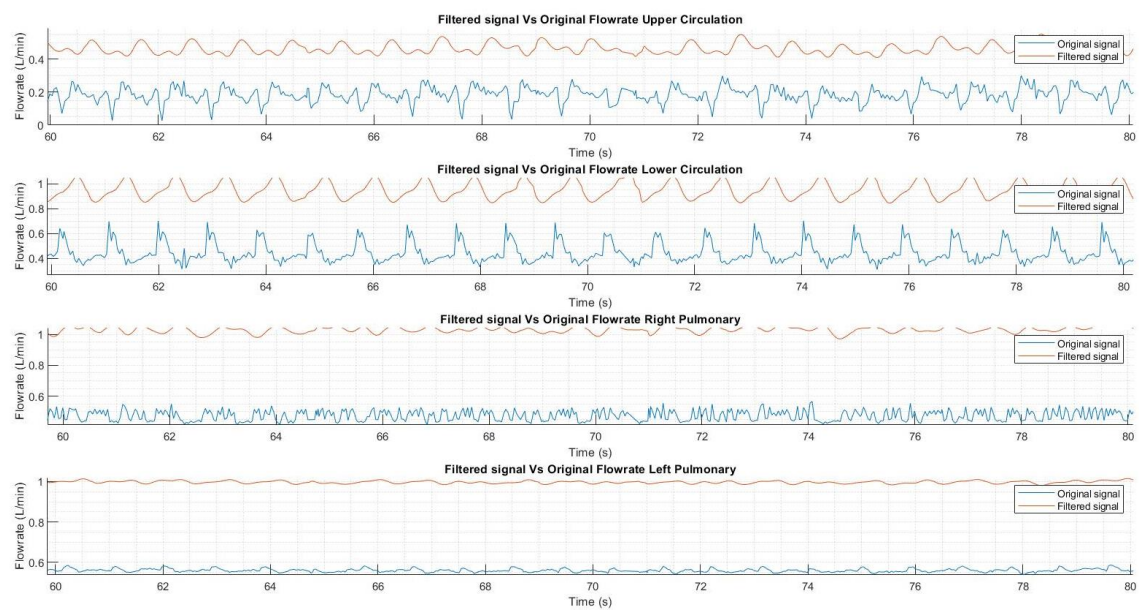


Figure 91 Filtered and unfiltered flowrate for 3mm IJS at 5 degree

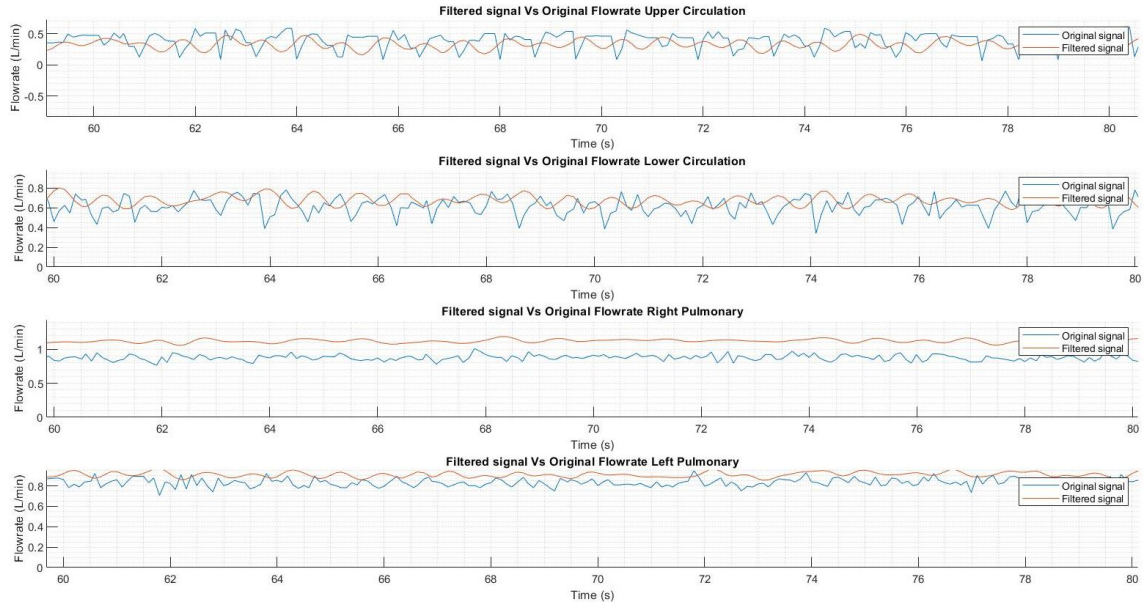


Figure 92 Filtered and unfiltered flowrate for PVR30

In the same fashion, the filtering scheme has been applied to the analog pressure sensors.

To successfully implement the filtering scheme, spectral analyses have been performed on each of the pressure sensors present in each compartment of the MFL, as shown in Figure 93 to Figure 95.

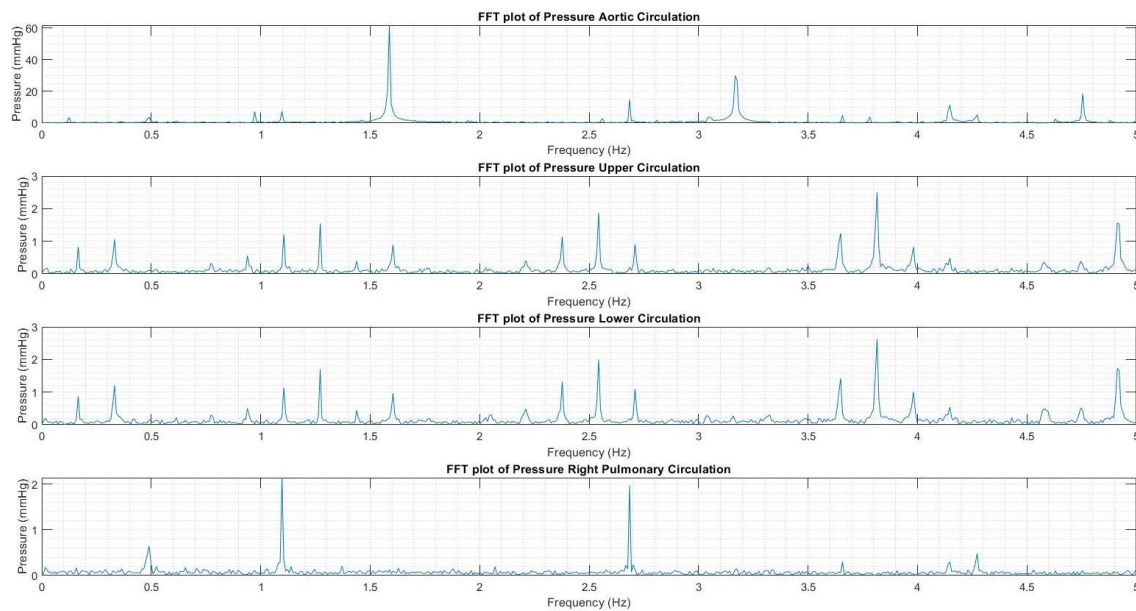


Figure 93 Pressure FFT 3mm IJS

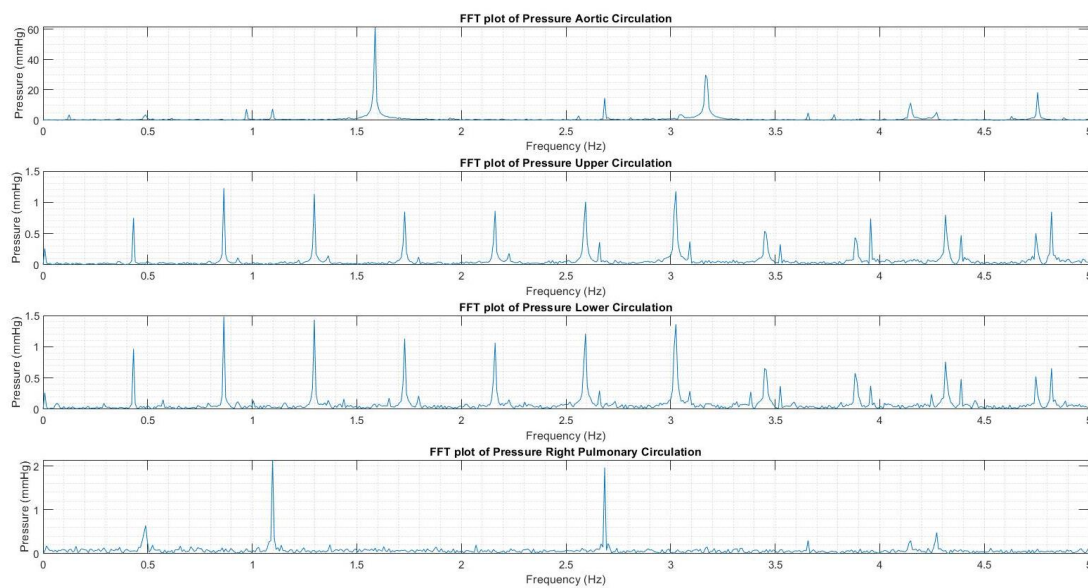


Figure 94 Pressure FFT of 3mm IJS at 5 degree

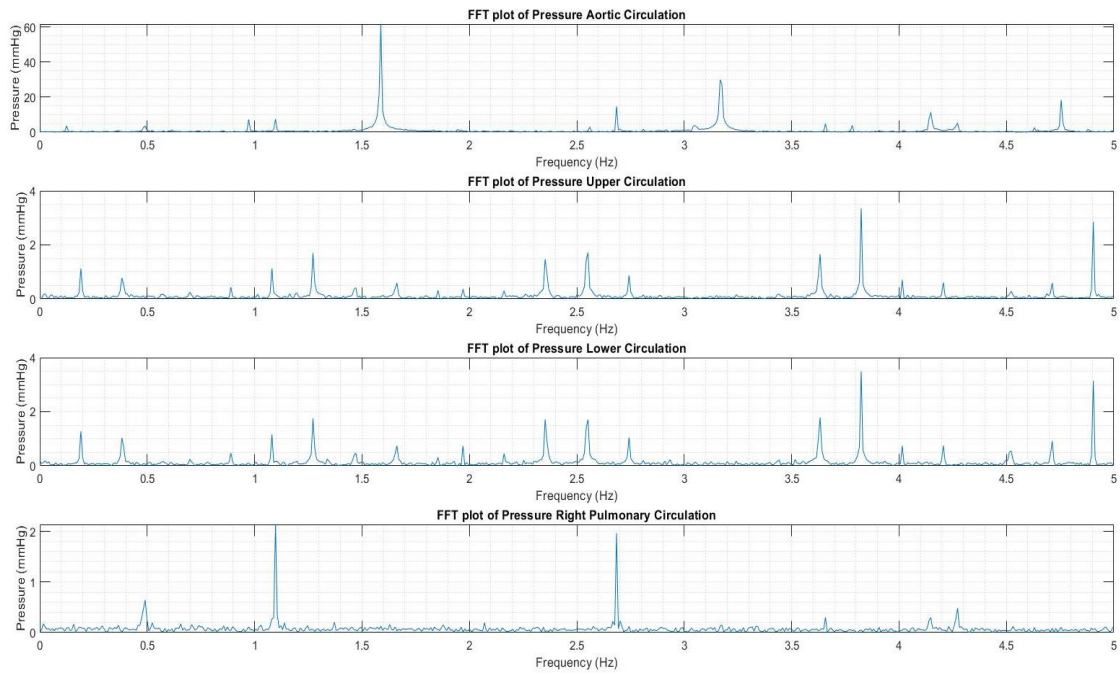


Figure 95 Pressure FFT PVR30

Figure 96 to Figure 98 show the unfiltered pressure waveforms for all the best cases of parametric studies.

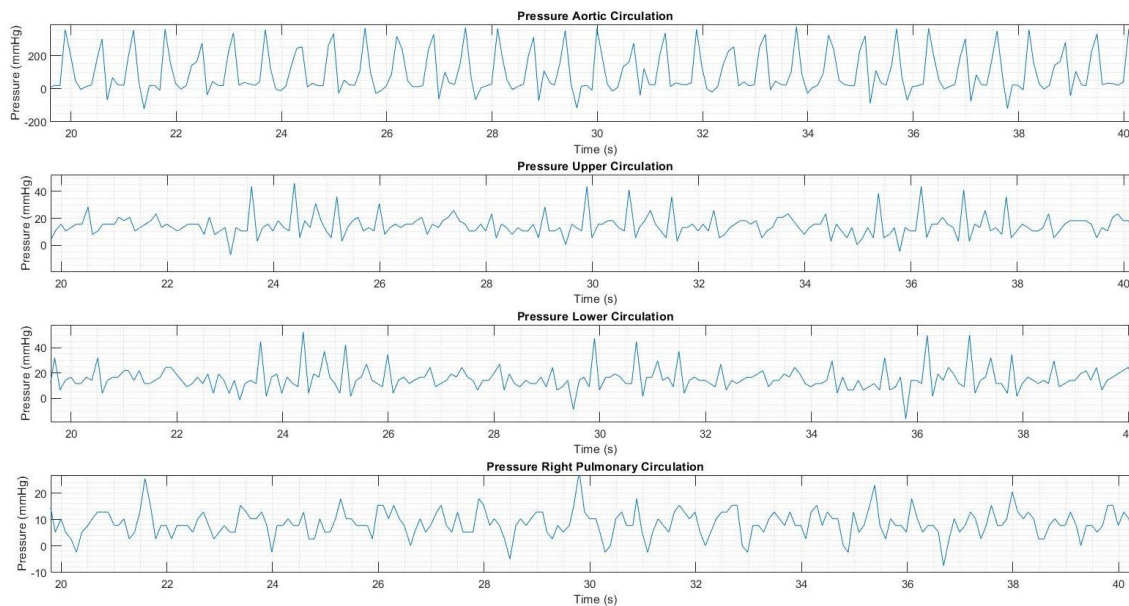


Figure 96 Unfiltered Pressure for 3mm IJS

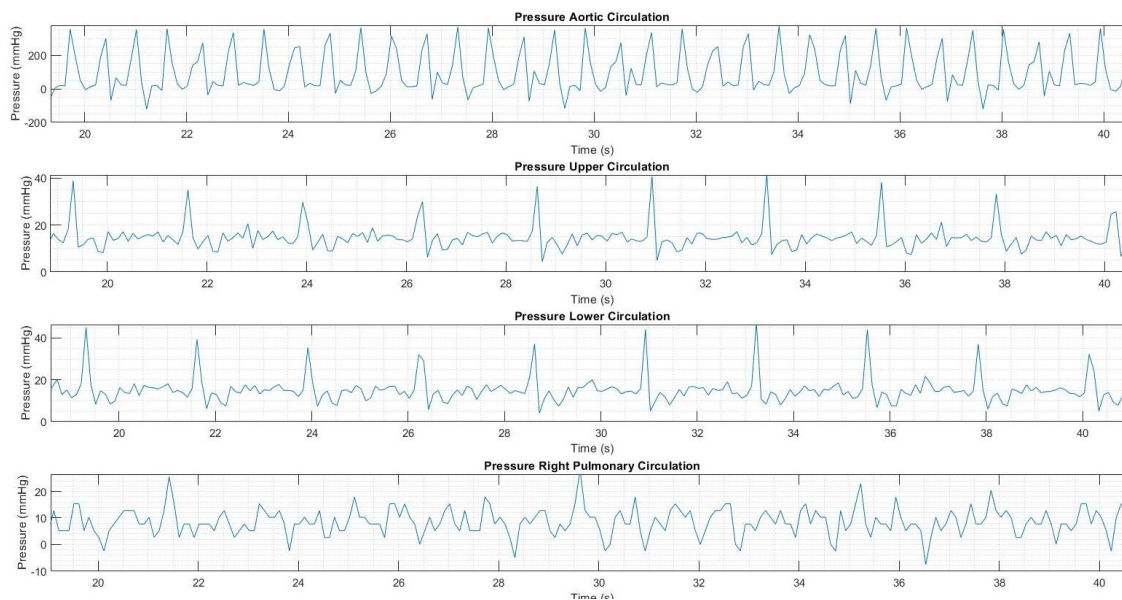


Figure 97 Unfiltered Pressure for 3mm IJS at 5 degree

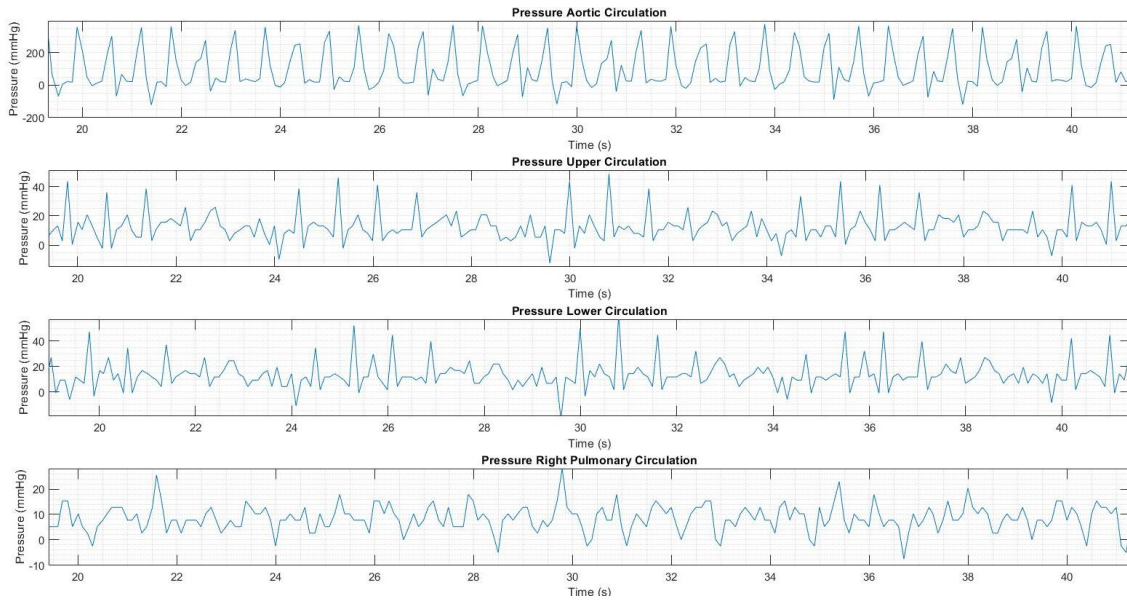


Figure 98 Unfiltered Pressure for PVR30

Figure 99 to Figure 101 compares the filtered and unfiltered pressure waveforms after implementing this filtering scheme. By comparing the systolic and diastolic features between filtered and unfiltered waves, it can be seen that embedded noise is filtered out.

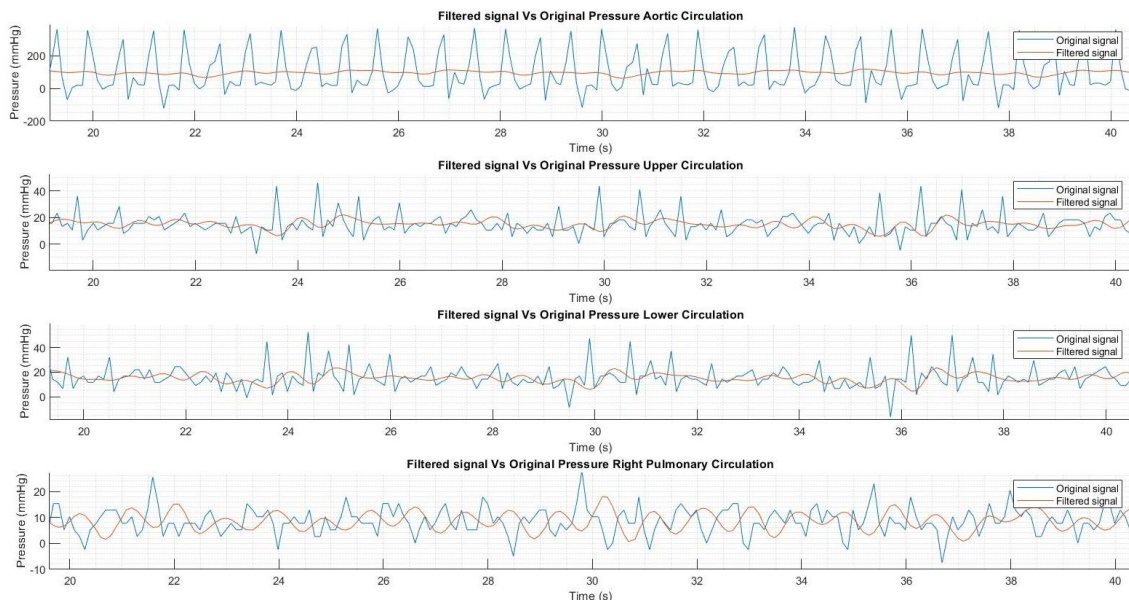


Figure 99 Filtered and unfiltered pressure for 3mm IJS

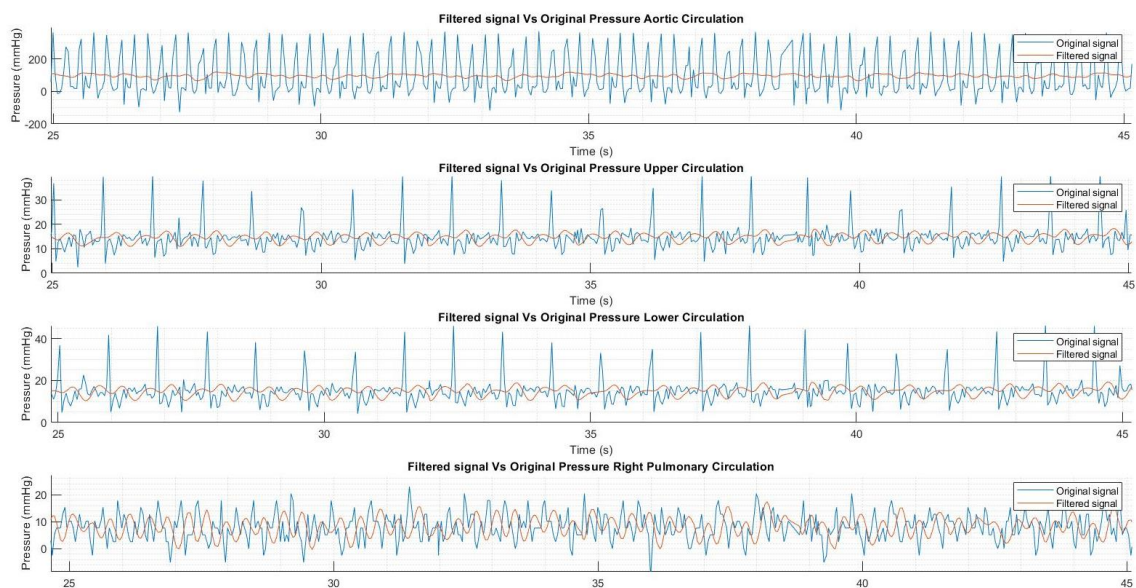


Figure 100 Filtered and unfiltered pressure for 3mm IJS at 5 degree

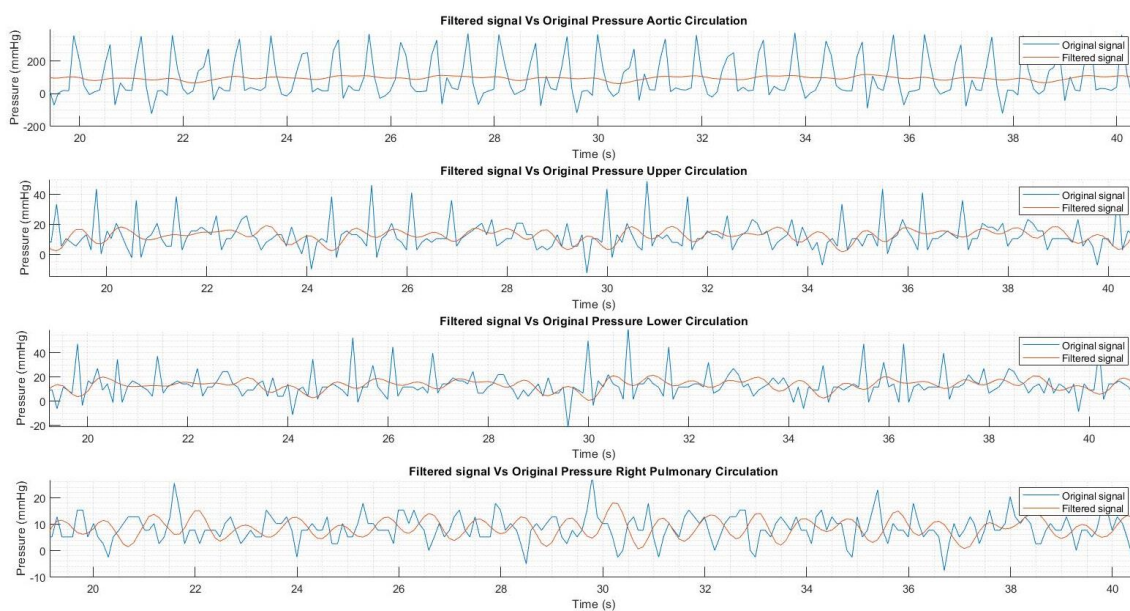


Figure 101 Filtered and unfiltered pressure for PVR30

4.1.3. PVR and entrainment study

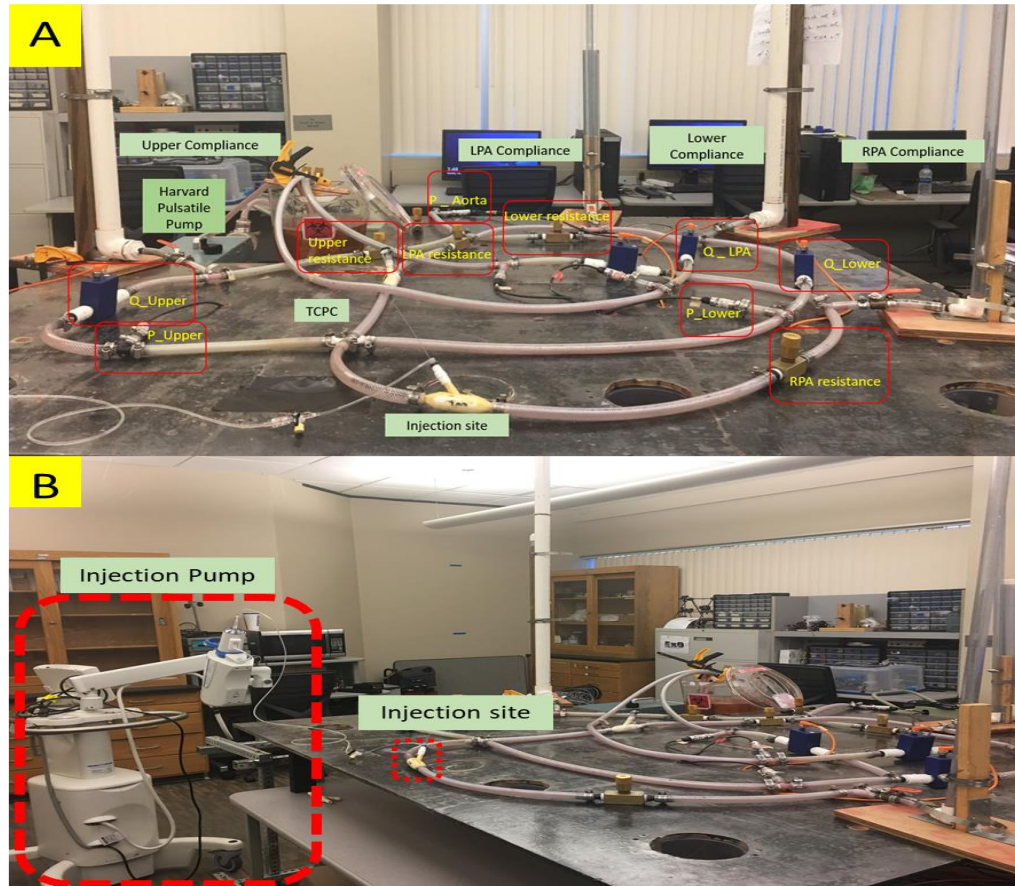


Figure 102 MFL setup for PVR study

Figure 46 represents the TCPC used for this experiment. The catheter is represented by the conduit placed on the RPA side. The site of the injection site is shown in Figure 102. A 7Fr catheter (outer diameter 2.3368 mm) was used with the injection pump during the experiment. The injection pump is user-controlled equipment that was used during the experiment. The controls on the pump allow the user to vary the flow rate, and the volume to inject during each burst. The pump is programmed manually prior to a given experimental condition. The MFL setup for this experiment includes the upper, lower,

right pulmonary and left pulmonary circulation. The loop is tuned by setting the Harvard pulsatile pump to 80 *bpm* and 30 *cc / s* as the stroke volume, thereby replicating a cardiac output of $2.4 \frac{L}{min}$. A single cardiac beat represents 30% systolic and 70% diastolic.

Resistors were tuned to achieve the required flow splits in the conduits. The upper circulation is having 30% flow and 70% flow towards the lower circulation. At the Fontan TCPC, the flow is equally split between the LPA and RPA. The baseline attained is of normal Fontan. The MFL operated with the baseline condition for one minute. After 60-70 seconds, the injections were pushed. Each protocol developed by the interventionist was conducted 3 times.

4.2. Experimental Results

4.2.1. HCSII

In this section, first, the hemodynamic quantifications are discussed and then followed by quantitative and qualitative analyses of other parameters like stented-baffle displacements and particle residence time are presented.

4.2.1.1. Hemodynamic

As mentioned in the previous section 4.1.1, experimental runs are made to match the catheter reports of two patients. Table 8 and Table 9 quantifies and compares the hemodynamics of both patients obtained by experimental runs and the catheter reports provided by our clinical partners. This table shows that results obtained by in-vitro experiments closely match with the in-vivo results. Results show that flow splits in the systemic and pulmonary circulations fall under the clinically acceptable range in the experimental runs. In Table 8, Q_{Upper} Q_{Lower} Q_{RPA} Q_{LPA} represents flow rate measured in

the upper systemic, lower systemic, left pulmonary, and right pulmonary circulations, respectively.

Table 8 Hemodynamic flowrate results obtained using Catheter data and MFL for patients 1 and 2

	P1		P2	
	Catheter data	MFL	Catheter data	MFL
$Q_{upper}[L/min]$	1.25	1.288	0.76	1.079
$Q_{lower}[L/min]$	1.74	1.865	0.99	0.747
$Q_{LPA}[L/min]$	0.50	0.646	0.31	0.527
$Q_{RPA}[L/min]$	0.75	0.642	0.45	0.552
$CO[L/min]$	2.99	3.153	1.75	1.826

Table 9 Hemodynamic pressure results obtained using Catheter data and MFL for patient 1 and 2

	P1		P2	
	Catheter data	MFL	Catheter data	MFL
$P_{mpa} [mmHg]$	65	57.303	52	40.712
$P_u [mmHg]$	9	19.407	15	19.811
$P_{ao} [mmHg]$	65	65.387	48	49.181
$P_{da} [mmHg]$	54	58.524	50	47.915
$P_{lpa} [mmHg]$	8	14.845	11	14.877

P_{rpa} [mmHg]	8	10.835	11	12.726
------------------	---	--------	----	--------

In Table 9, the P_{mpa} , P_u , P_{ao} , P_{da} , P_{lpa} , P_{rpa} represent pressure measured in MPA conduit, Upper systemic, ascending aorta, descending aorta, left pulmonary artery, and right pulmonary artery, respectively.

Our clinical collaborators provided the following catheter waveforms for two deidentified patients, as shown in Figure 103 to Figure 105.

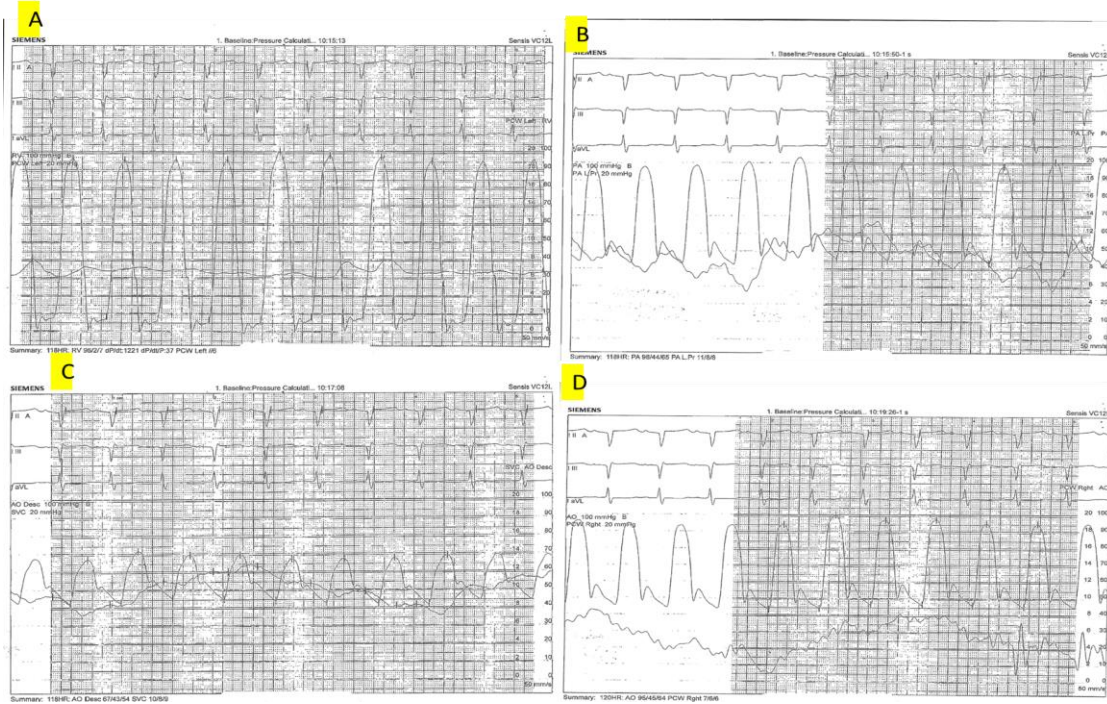


Figure 103 Pressure plots obtained from catheter data for patient 1

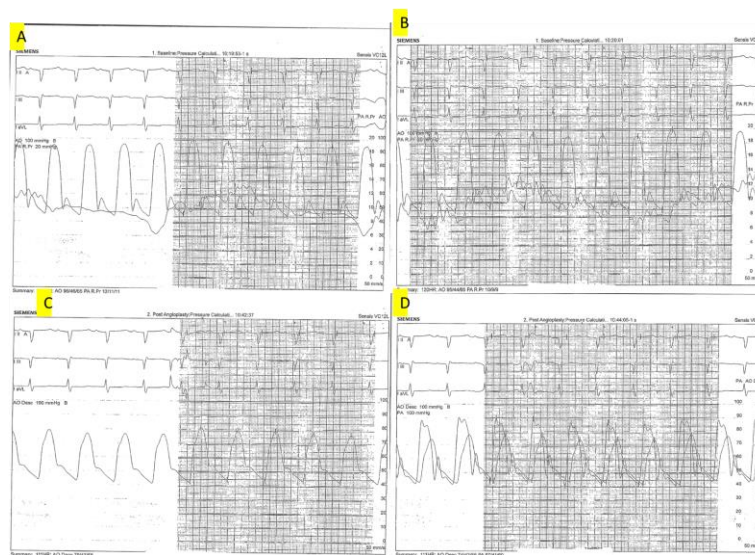


Figure 104 Pressure plots obtained from catheter data for patient 1

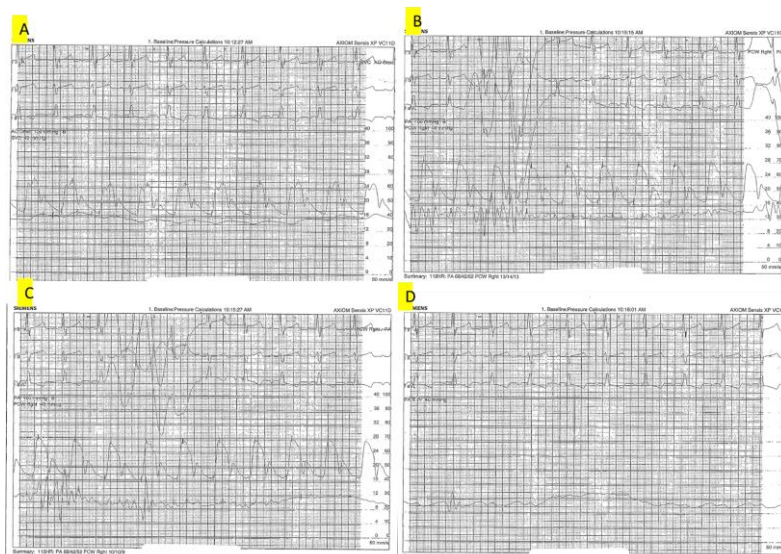


Figure 105 Pressure plots obtained from catheter data for patient 2

Flowrate:

Figure 106 and Figure 107 depict the features of the filtered flowrate waveforms obtained from the experimental runs.

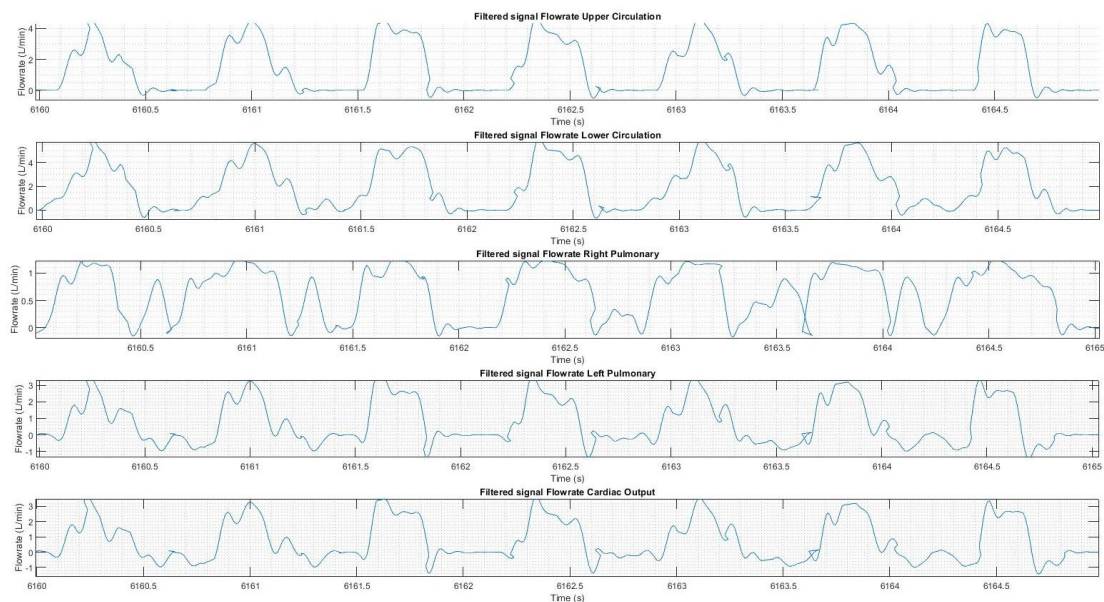


Figure 106 Filtered flowrate of patient 1

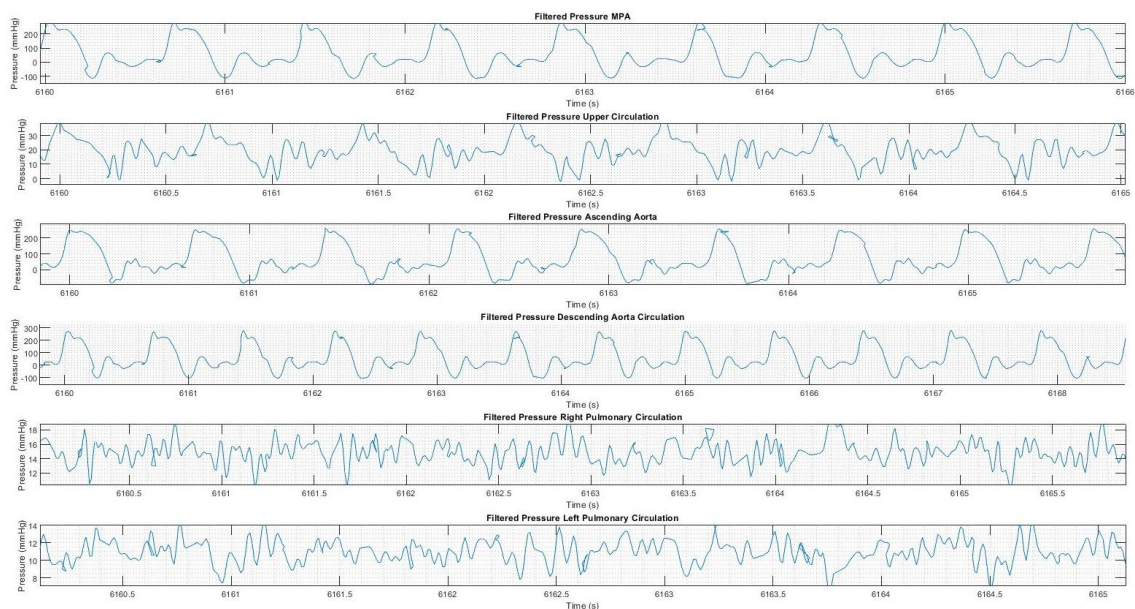


Figure 107 Filtered flowrate of patient 2

Pressure:

These are the pressure waveforms as shown in Figure 108, and Figure 109 are obtained from the MFL experimental runs. These waveforms closely match with features of the catheter waveforms.

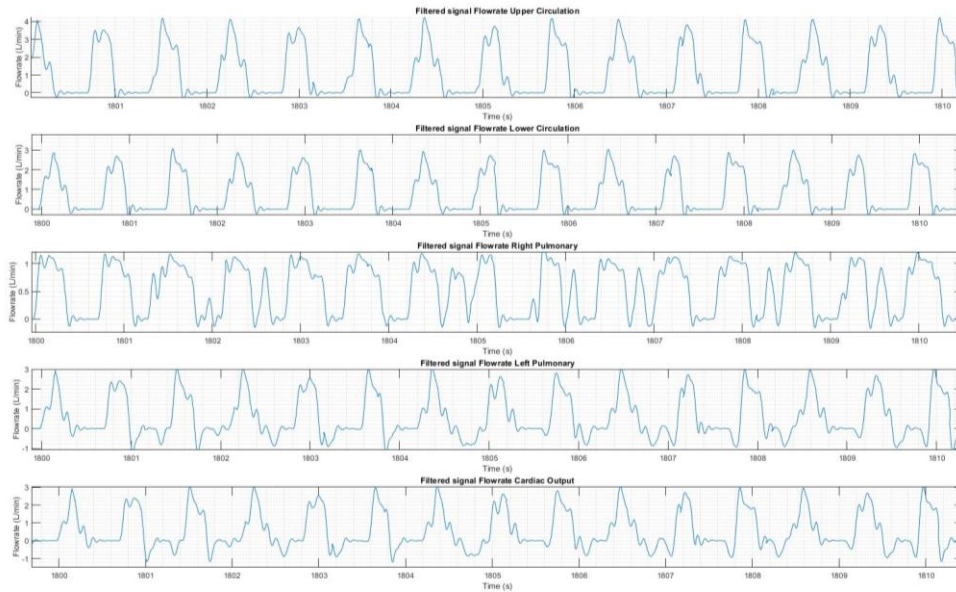


Figure 108 Filtered pressure of patient 1

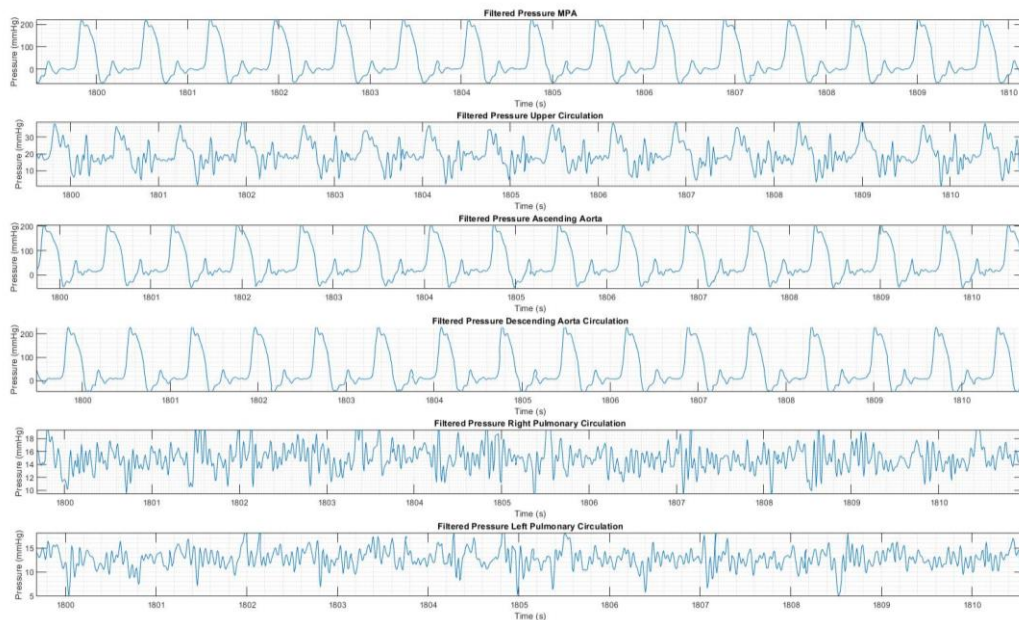


Figure 109 Filtered pressure of patient 2

4.2.1.2. Statistical analysis (z score)

The hemodynamic parameters obtained after conducting the experiment are compared against the catheter data. The null hypothesis for this testing states no difference in the hemodynamic parameters between the surgical and experimental procedures. The alternate hypothesis states that there is a difference in the parameter's values. The two tail z-score test was performed at a significance level of 0.1. The p-value for this test was 0.784. The p-value obtained during testing is greater than the significance level 0.1, thereby rejecting the alternating hypothesis and accepting the null hypothesis.

4.2.1.3. Oxygen transport

Oxygen transport is reported for both patient subsets. The oxygen delivery and saturation are reported with different pulmonary vein saturations values (100%, 95%, 90%, 85%) as shown in the Figure 110

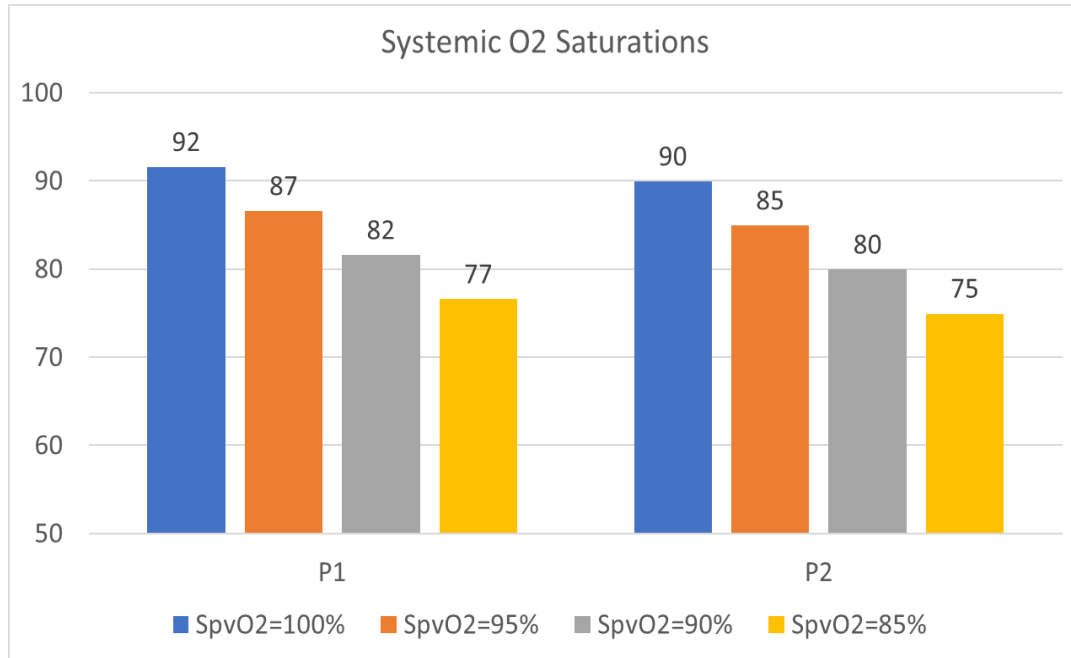


Figure 110 Systemic Oxygen saturation level between patient 1 and patient 2

In-vitro oxygen transport analyses for patient 1 closely matches with the in-silico findings conducted by Hameed et al. [224].

4.2.1.4. Stented-Baffle tracking

The tracking algorithm has successfully tracked the displacement of the stented baffle geometry under the pulsatile loading condition for eight cases, as shown in Figure 111.

The marked minimum displacement 0.17 mm and maximum displacement 1.88 mm. The average displacement is 0.65 mm. It is also observed from Table 10 that stented- baffle displacement is a function of CO. As the CO decreases the stented- baffle displacement also gradually decreases.

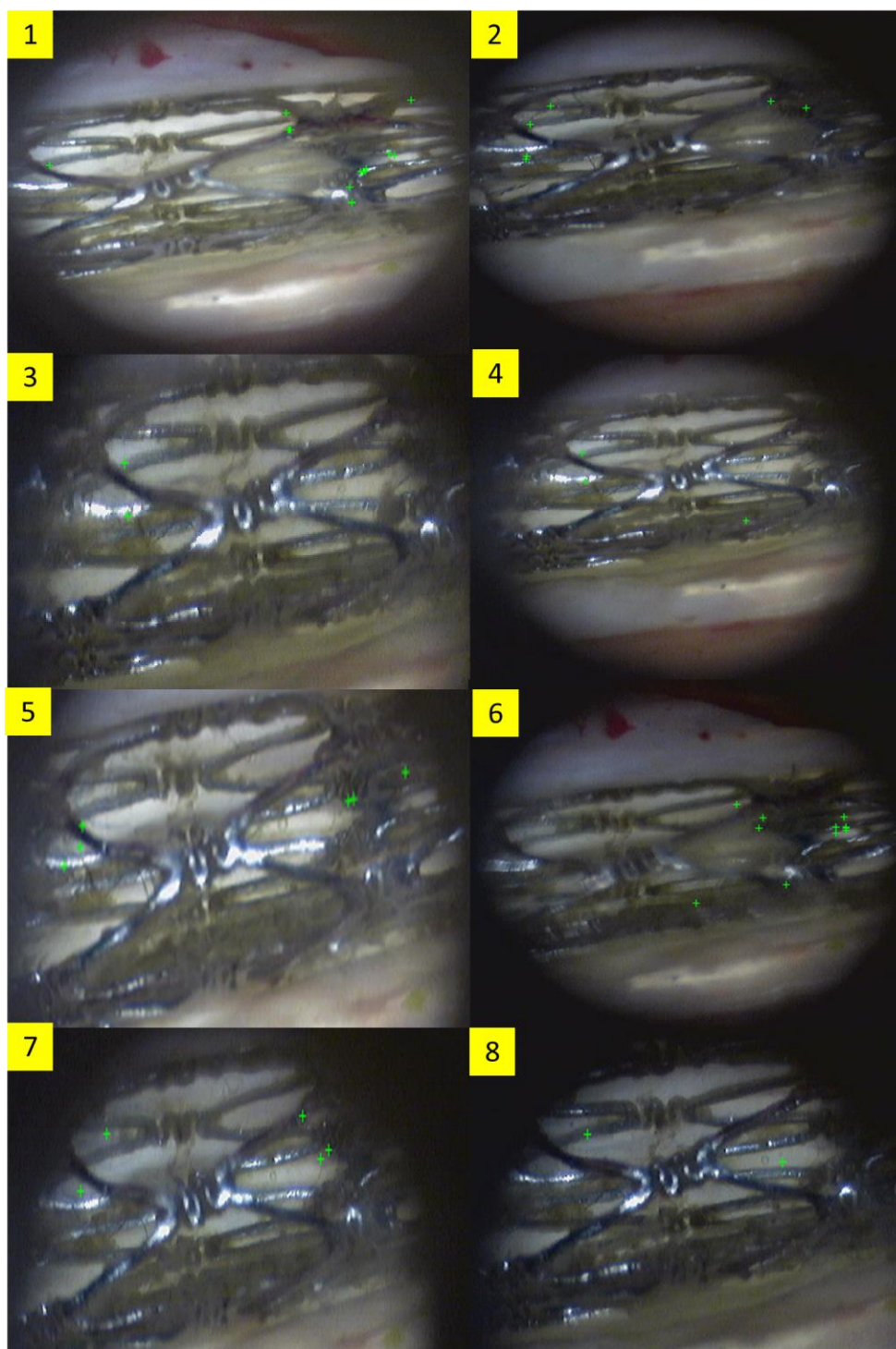


Figure 111 Final stent and baffle tracked in different location for Patient 1

Table 10 Displacement of stent at various sites for patient 1 and patient 2

Location #	Patient 1 (<i>mm</i>)	Patient 2 (<i>mm</i>)
Case 1	0.2406	0.2382
Case 2	0.4176	0.8643
Case 3	1.4352	0.219
Case 4	0.3116	0.3717
Case 5	0.3973	0.3493
Case 6	1.886437	0.4345
Case 7	0.1324	0.4712
Case 8	0.1701	0.0258
Average	0.6554	0.3717

4.2.1.5. Fatigue Study

The crushing of the baffle is due to the stress from the outside system flow. The pressure value of MPA is obtained for each heart cycle, and the pressure acts on the baffle, thereby causing the stent to displace from its original location. For each pulsatile loading, the stent is being displaced. The following paragraphs explain the numerical computation carried out to obtain the stress acting on the stent.

As the stent is placed horizontally and parallelly to the PA conduits, the pressure between the LPA and RPA sides is used to compute the hoop stress acting on the cylinder. The maximum hoop stress is computed, and the minimum hoop stress is zero. For the given loading condition, the principal stress is computed and compared with von-misses stress with a factor of safety 2. Using the modified Paris law equation, the number of cycles was obtained.

Patient 1 had an average LPA-RPA pressure of 12.840234 *mmHg* that corresponds to 1711.89 *Pa*

$$\sigma_{hoop} = \frac{Pr}{t}$$

$$\sigma_{hoop} = 0.067 \text{ MPa}$$

As the stent does not have any loading in other directions and there is no torsion loading, σ_x and τ_{xy} is equated to zero. Therefore, there exists one principal stress. For the given loading conditions, the principal stress obtained through

$$\sigma_{1,2} = \frac{\sigma_x + \sigma_y}{2} \pm \sqrt{\left(\frac{\sigma_x - \sigma_y}{2}\right)^2 + \tau_{xy}^2}$$

$$\sigma_1 = \sigma_y$$

$$\sigma_1 = 0.067 \text{ MPa}$$

The above value represents the σ_1 , i.e., the principal stress acting normal to the plane in which the shear stress is zero. The first principal stress is the maximum value seen on the stent material during the loading conditions. Von-mises stress criterion with Factor of Safety 2 identifies if the stent will be crushed due to the pulsatile loading during a given instance. The yield strength of Nitinol is 195 *MPa*.

$$\sigma_v = \sigma_1^2 - \sigma_1\sigma_2 + \sigma_2^2 = \frac{\sigma_{yp}^2}{2}$$

As $\sigma_2 = 0$, σ_v becomes

$$\sigma_v = \sigma_1^2 - \sigma_1\sigma_2 + \sigma_2^2 = \frac{\sigma_{yp}^2}{2}$$

$$\sigma_v = \sigma_1^2 = \frac{\sigma_{yp}^2}{2}$$

$$\sigma_1^2 = \frac{\sigma_{yp}^2}{2}$$

$$(0.067)^2 < \frac{(195)^2}{2}$$

From the above equations, it can be established that the maximum stress acting on the stent and minimum stress is zero. The stent reaches the maximum and minimum stresses in a repetitive pattern (cyclic). The cyclic pattern occurring for 'N' cycles makes the stent undergo a fatigue failure at the Nth cycle. The principal stress obtained above provides an insight that the stent will undergo high cycle fatigue failure as the stress applied falls well within the elastic region.

For calculation purposes, critical crack length was identified at two specific locations, as shown in Figure 112. Figure 112A represents location one, and Figure 112 B represents location two to compute the number of cycles to failure if a crack occurs at the crack tip., The exact number of cycles to failure can be computed by knowing the change in the crack length after each cycle.

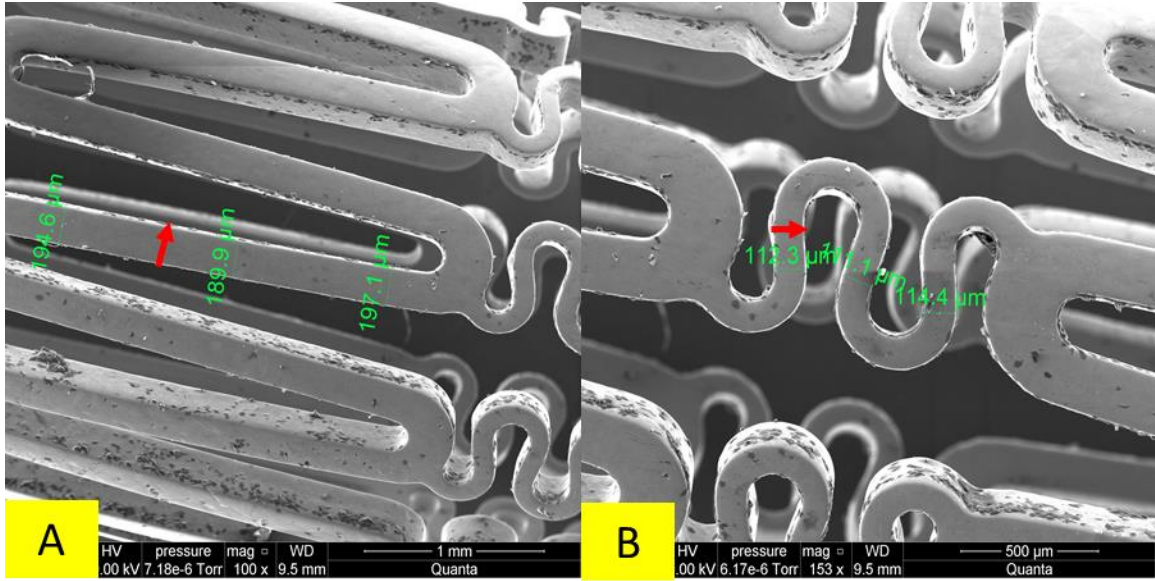


Figure 112 Critical locations for crack propagation

For calculation purposes, few assumptions are taken into consideration. The initial critical crack length is assumed to be zero, and a steady crack growth rate is assumed at the location of failure. The Paris law equation is used to provide the number of cycles to failure. The Paris law is based on the material properties and loading conditions. The equation is integrated using two different limits; the crack length is integrated from initial to final crack length, the number of cycles is integrated from zero to final. The modified Paris law equation is given by Equation (54).

$$N_f = \frac{2 \left(a_c^{\left(\frac{n-2}{2} \right)} - a_i^{\left(\frac{n-2}{2} \right)} \right)}{(n-2)C.y^n . \Delta \sigma^n . \pi^{n/2}} \quad (54)$$

Where N_f is a number of cycles to failure, a_c is critical crack growth, a_i initial crack growth, $\Delta \sigma$ the difference in maximum and minimum stress, n , C , and y are material constants.

Using the critical length at the exact location 1, the number of cycles to failure N_1 is computed

$$N_1 = \frac{2(197.10^{-6})^{0.6}}{(3.2-2).(1.62.10^{-12}).(1)^{3.2}.(0.067)^{3.2}.(\pi)^{3.2}}$$

$$N_1 = 9.0.10^{11} \text{ cycles}$$

For location 2, the number of cycles to failure N_2 is computed

$$N_2 = \frac{2(112.3.10^{-6})^{0.6}}{(3.2-2).(1.62.10^{-12}).(1)^{3.2}.(0.067)^{3.2}.(\pi)^{3.2}}$$

$$N_2 = 1.13.10^{12} \text{ cycles}$$

Patient 2 had an average LPA-RPA pressure of 13.8015035 *mmHg* that corresponds to 1840.05 *Pa*

$$\text{Stress acting on stent } \sigma_y = \frac{\text{Pr}}{t}$$

$$\sigma_y = 0.072 \text{ MPa}$$

$$\sigma_{1,2} = \frac{\sigma_x + \sigma_y}{2} \pm \sqrt{\left(\frac{\sigma_x - \sigma_y}{2}\right)^2 + \tau_{xy}^2}$$

$$\sigma_1 = \sigma_y$$

$$\sigma_1 = 0.072 \text{ MPa}$$

The above value represents the σ_1 , i.e., the principal stress acting normal to the plane in which the shear stress is zero. Using Von-mises criterion

$$\sigma_v = \sigma_1^2 - \sigma_1\sigma_2 + \sigma_2^2 = \frac{\sigma_{yp}^2}{2}$$

As $\sigma_2 = 0$, σ_v becomes

$$\sigma_v = \sigma_1^2 - \sigma_1\sigma_2 + \sigma_2^2 = \frac{\sigma_{yp}^2}{2}$$

$$\sigma_v = \sigma_1^2 = \frac{\sigma_{yp}^2}{2}$$

$$\sigma_1^2 = \frac{\sigma_{yp}^2}{2}$$

$$(0.072)^2 < \frac{(195)^2}{2}$$

From the above equations, it can be established that the maximum stress acting on the stent is lower than the yield stress of Nitinol. Using the Paris law given by Equation 51 to compute the number of cycles to failure at two different locations with two different critical crack lengths.

For location 1 the number of cycles to failure N_1 is computed

$$N_1 = \frac{2(197.10^{-6})^{0.6}}{(3.2-2).(1.62.10^{-12}).(1)^{3.2}.(0.072)^{3.2} .(\pi)^{3.2}}$$

$$N_1 = 7.15.10^{11} \text{ cycles}$$

For location 2 the number of cycles to failure N_2 is computed

$$N_2 = \frac{2(112.3 \cdot 10^{-6})^{0.6}}{(3.2 - 2) \cdot (1.62 \cdot 10^{-12}) \cdot (1)^{3.2} \cdot (0.072)^{3.2} \cdot (\pi)^{3.2}}$$

$$N_2 = 1.42 \cdot 10^{12} \text{ cycles}$$

The number of cycles to failure is computed for the critical locations and compared based on the LPA-RPA pressure values. It is seen that the stent goes through high cycle fatigue failure for the giving loading conditions. Table 11 provides the summary for the fatigue study conducted based on patient one and patient two data.

Table 11 Conclusion summary of fatigue study on the stent for patient 1 and patient 2 data

Type of study	Location	Number of cycles to failure
Circumferential Stress (patient 1)	1	$9 \cdot 10^{12}$ cycles
	2	$1.13 \cdot 10^{12}$ cycles
Circumferential Stress (patient 2)	1	$7.15 \cdot 10^{11}$ cycles
	2	$1.42 \cdot 10^{12}$ cycles

4.2.1.6. Particle Residence Time

Particle residence time is the amount of time taken by a particle in the flow stream to exit an outlet boundary. PRT study indicates any pathological flow present in the domain and the risk of thrombus formation. In Figure 113, the Kalman tracker has successfully tracked all the particles injected in the flow field. The particles have been tracked in the early systole, peak systole, early diastole, and late diastole stages.

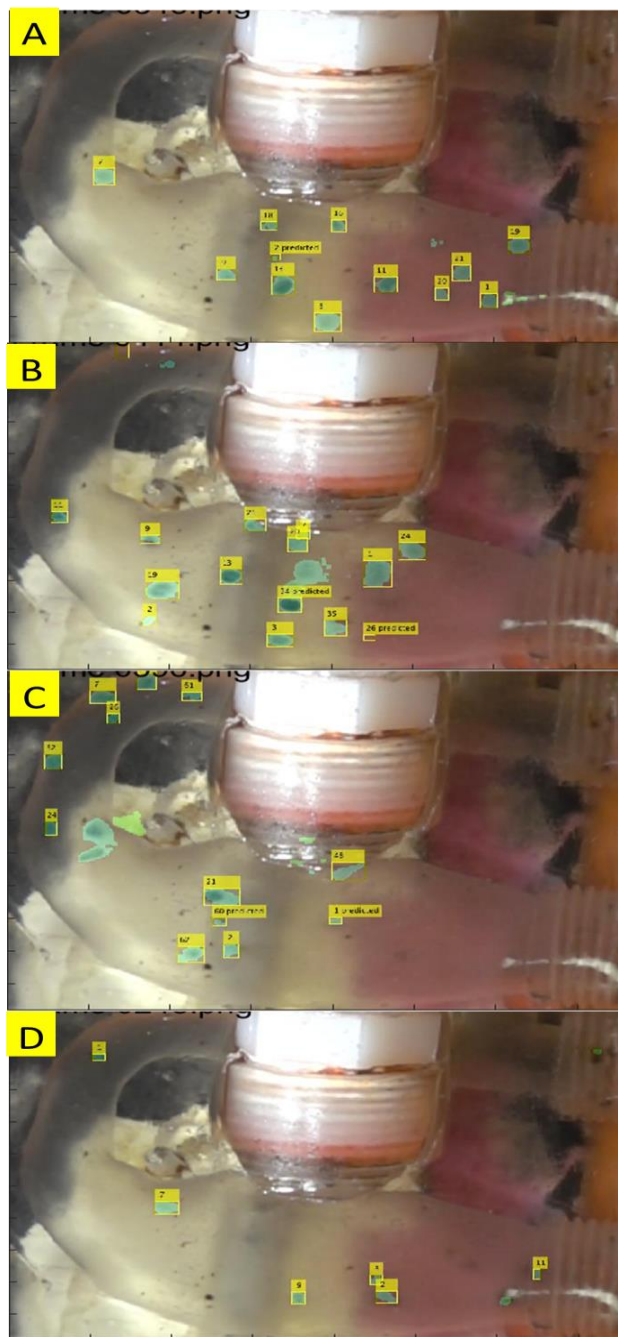


Figure 113 Tracked PRT: A: Early systole, B: Peak systole, C: Early Diastole, D: Late Diastole

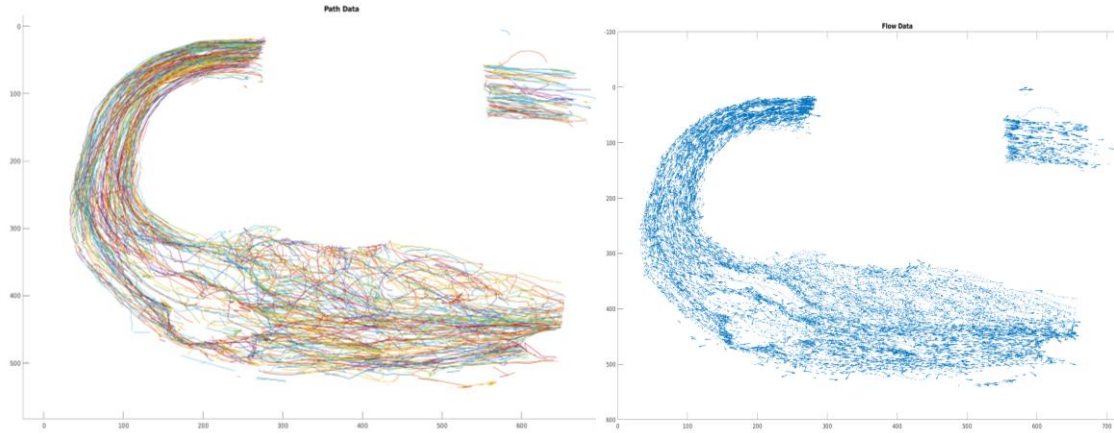


Figure 114 Particle path lines (left) Particle velocity (right)

After analyzing all the path lines generated from each tracked particle, as shown in Figure 114, the result showed that, on average, each particle exited the MPA conduit within 2.8 s to 3.2 s. This result proves that this reconstructed physiology does not have any pathological flow or any probability of flow recirculation.

4.2.2. Fontan with IJS

4.2.2.1. Comparative study of IJS nozzles: 2mm, 3mm, and 4mm

The purpose of this study is to determine whether the implementation of an IJS would prove beneficial for Fontan patients. To this goal, the MFL is first tuned to match the physiological conditions of a failing Fontan with elevated caval pressure around 20 *mmHg* and a systemic flow of $2.03 \frac{L}{min}$. Following tuning, the study assesses the IJS viability by altering two parameters. First, the IJS is sequentially activated to mimic various proximal aortic anastomosis angles, and then the PVR is reduced, as shown in Figure 115. Table 12-Table 14 provides an overview of the flow and pressure measurements obtained by conducting the parametric study on IJS nozzle diameter, change in anastomosis angle, and change in PVR drop.

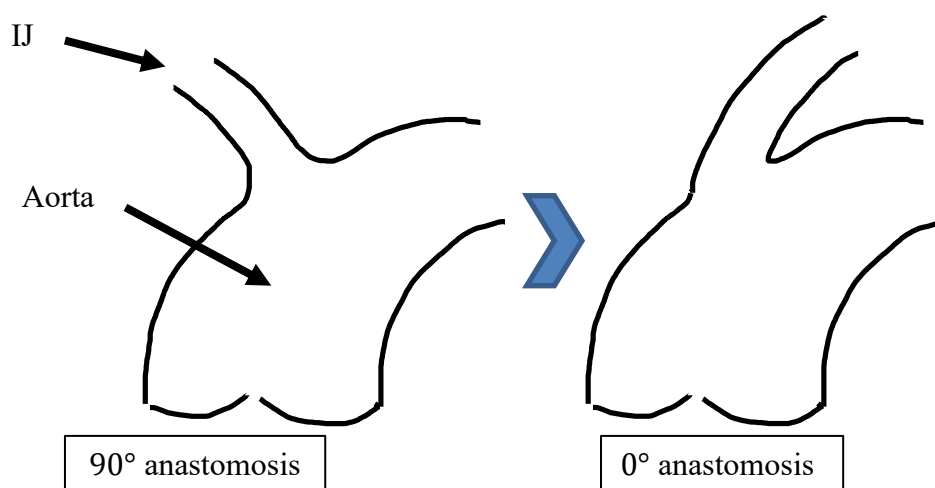


Figure 115 IJS proximal anastomosis angle.

As it can be seen from Table 12, the 3mm IJS nozzle has proved to be the best candidate in the parametric study on IJS nozzle size. By using the 3mm IJS nozzle, a caval pressure drop of 5mmHg is achieved. This caval pressure drop occurs at the expense of Q_p/Q_s 1.5.

Hemodynamic pressure and flowrate waveforms for all the cases of nozzle study are shown in Figure 116 to Figure 121. First, all the flowrate waveforms generate from all three nozzle sizes are discussed and then, followed by all the pressure waveforms are discussed.

Table 12 Pressure and flow measurement for baseline and various IJS diameters

IJS diameters				
No-IJS	2mm	3mm	4mm	

$Q_s \left[\frac{L}{\text{min}} \right]$	1.51	1.499	1.35	1.24
$Q_p \left[\frac{L}{\text{min}} \right]$	1.53	2.05	2.03	2.038
$\frac{Q_p}{Q_s}$	1.00	1.366	1.503	1.643
	20.75	15.4	15.245	16.2
$P_{IVC} [mmHg]$				
	54.38	97.015	97.017	97.017
$P_{AO} [mmHg]$				

Flowrate:

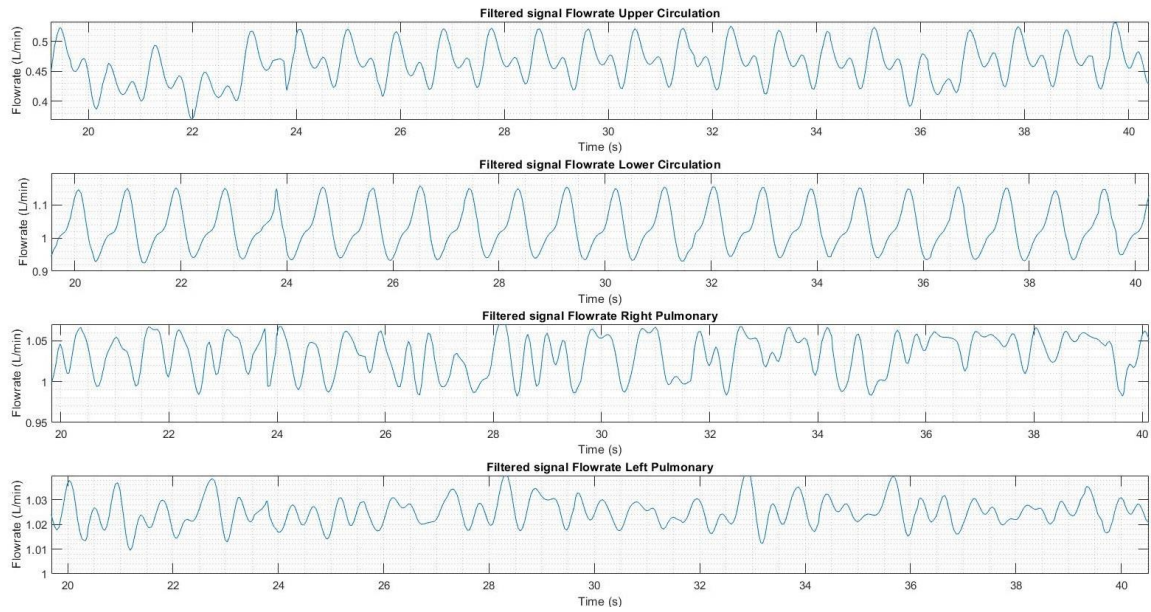


Figure 116 Filtered flowrate 2mm IJS

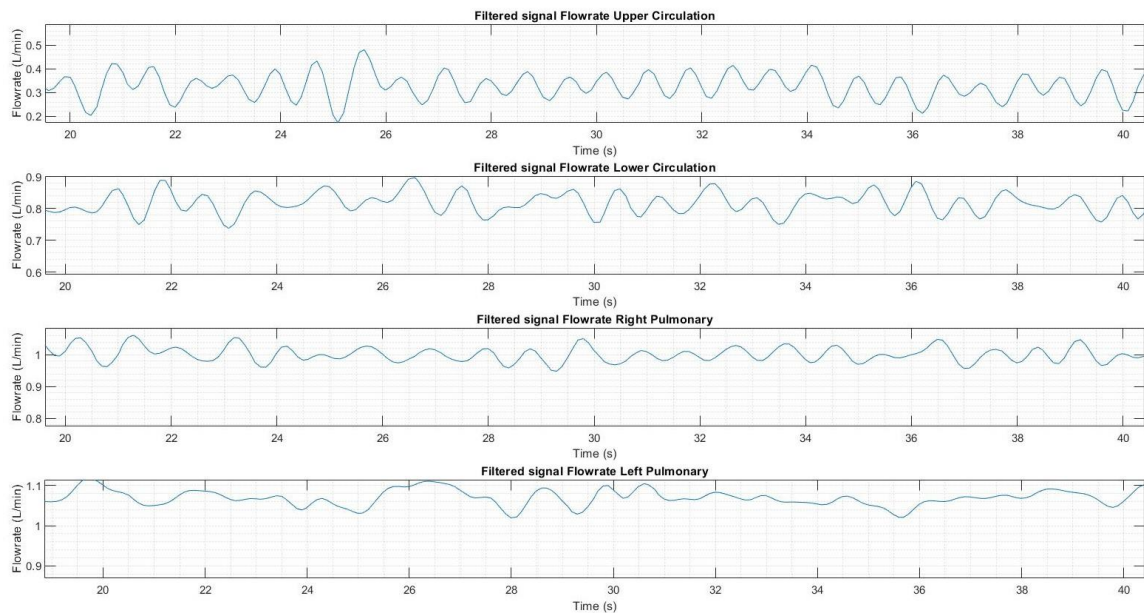


Figure 117 Filtered flowrate 3mm IJS

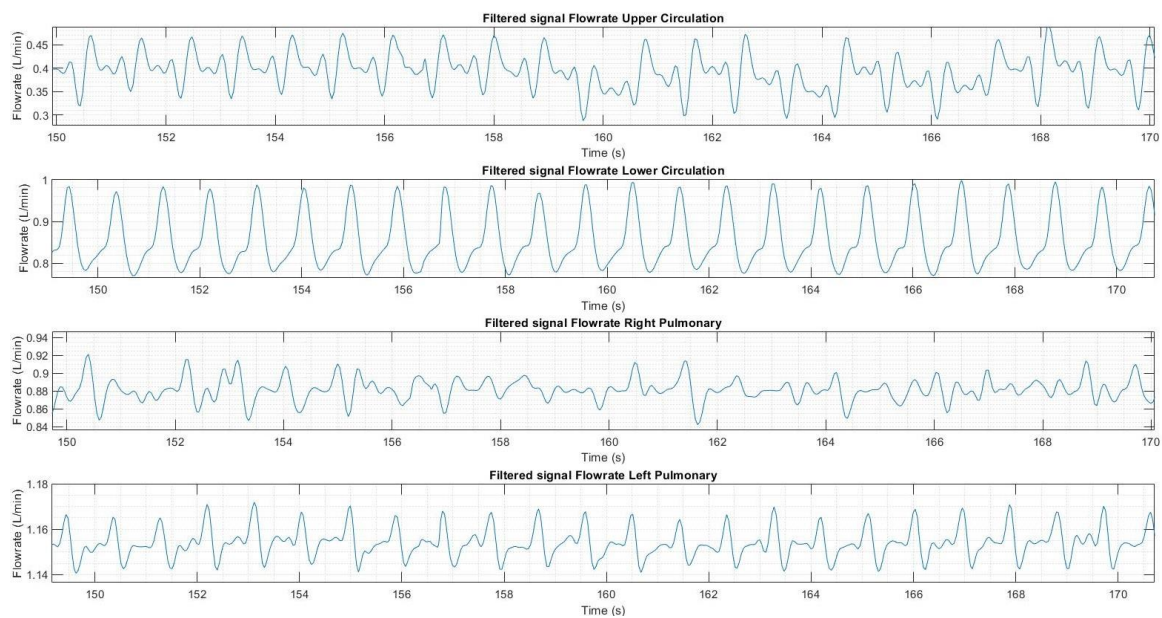


Figure 118 Filtered flowrate 4mm IJS

Pressure

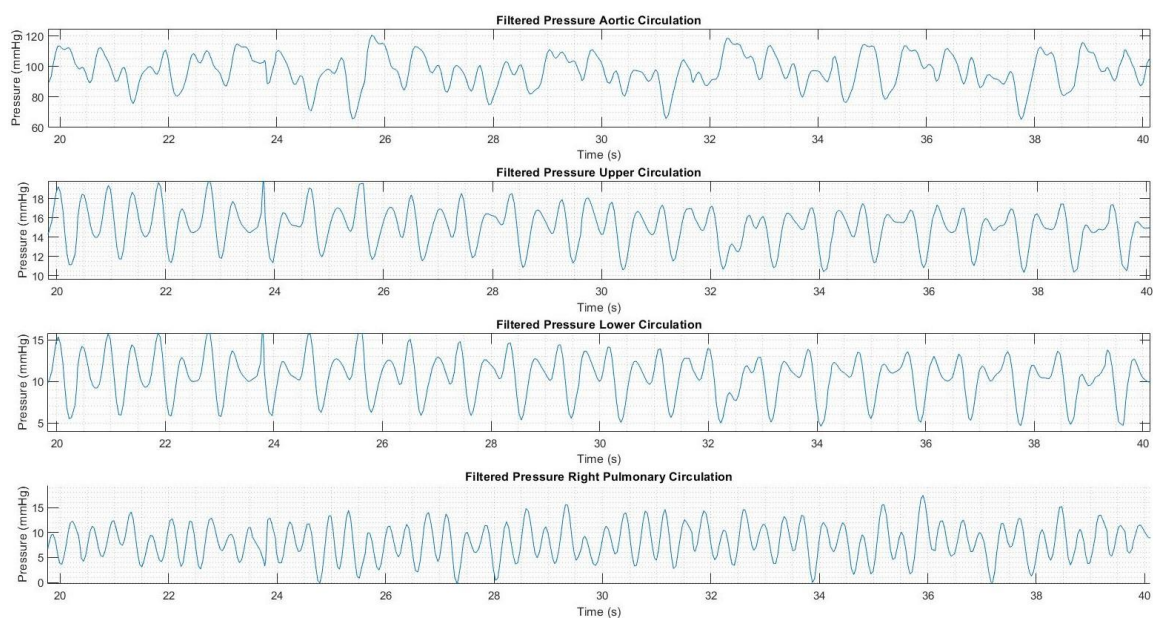


Figure 119 Filtered pressure 2mm IJS

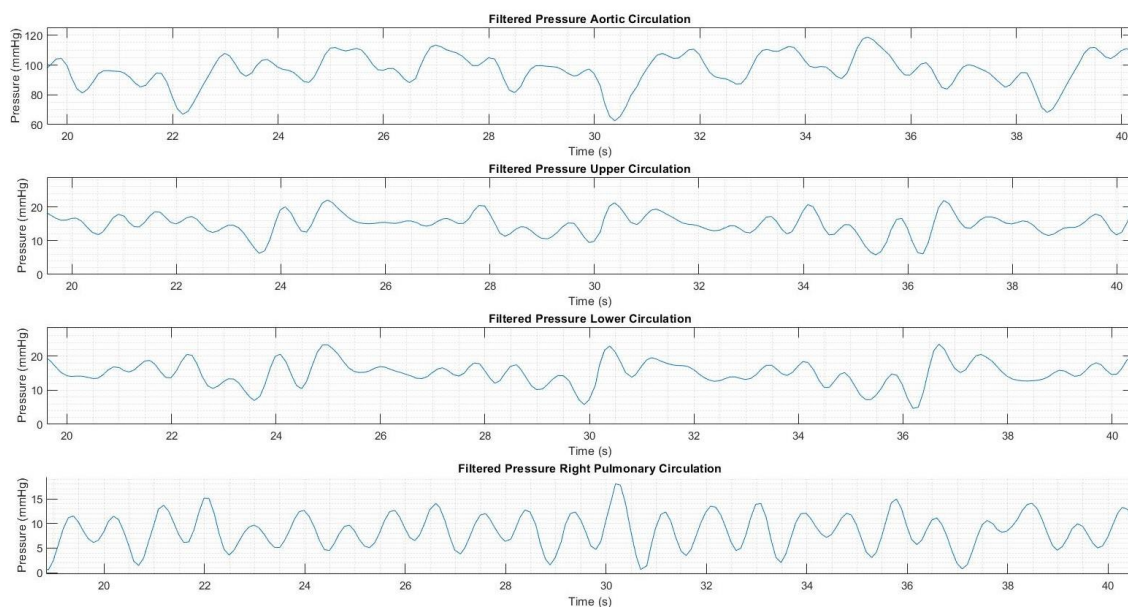


Figure 120 Filtered pressure 3mm IJS

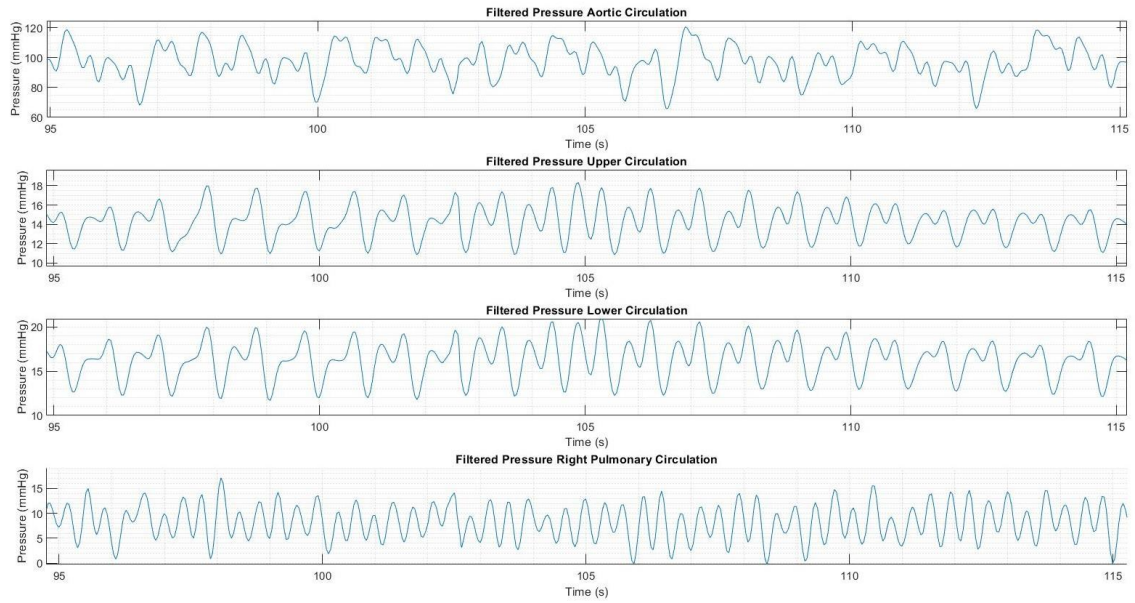


Figure 121 Filtered pressure 4mm IJS

4.2.2.2. Comparative study of angles : 5,45 and 90 degree

In Table 13 the implementation of the IJS clearly results in a significant pressure drop in IVC. Upon tuning the measured IVC pressure is of 20.75 mmHg with a systemic flow of 1.51 L/min , following the IJS implementation at a 90° angle the pressure drops to 17.58 mmHg and the systemic flow is 1.03 L/min . At an 45° angle the pressure further drops to 16.38 mmHg and at 0° angle the pressure is found to be 16.20 mmHg . Once the IJS is activated the Q_s remains mostly constant however the IVC pressure sees up to a 1.38 mmHg drop. This notable pressure drop is due to the kind of pressure the proximal IJS takeoff is subjected to. In the 90° case the flow across the IJS is driven solely by the static pressure in the aortic arch. On the other hand, in the 0° case the IJS flow is powered by the combination of the static pressure and in part to the dynamic pressure of the moving flow

in the arch. For each case the Q_p/Q_s constraint is met at about 1.65. Hemodynamic pressure and flowrate waveforms for all the cases of IJS anastomosis angles are shown in Figure 122 to Figure 127. This study does not include a feedback mechanism to maintain homeostatic systemic flow. This results in the observed drop in Q_s following the IJS activation.

Table 13 Pressure and flow measurement for active 3mm IJS with varying angle

	Active 3mm IJS			
	No-IJS	90°	45°	5°
$Q_s \left[\frac{L}{\text{min}} \right]$	1.51	1.32	1.38	1.41
$Q_p \left[\frac{L}{\text{min}} \right]$	1.53	2.03	2.03	2.03
Q_p/Q_s	1.00	1.537	1.471	1.439
$P_{IVC} [mmHg]$	20.75	17.58	16.38	16.20
$P_{AO} [mmHg]$	54.38	97.122	97.017	97.017

In Table 13 it can be observed that Q_p increases following IJS activation from the baseline value of $1.53 \frac{L}{\text{min}}$ to $1.69 \frac{L}{\text{min}}$.

Flowrate

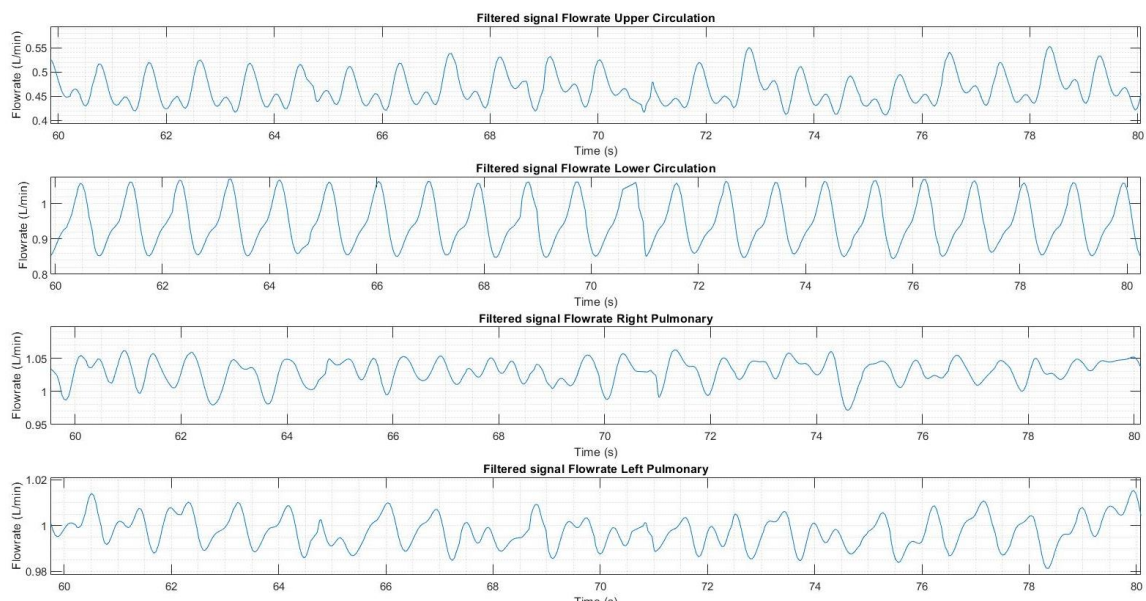


Figure 122 Filtered flowrate of 3mm IJS at 5 degree

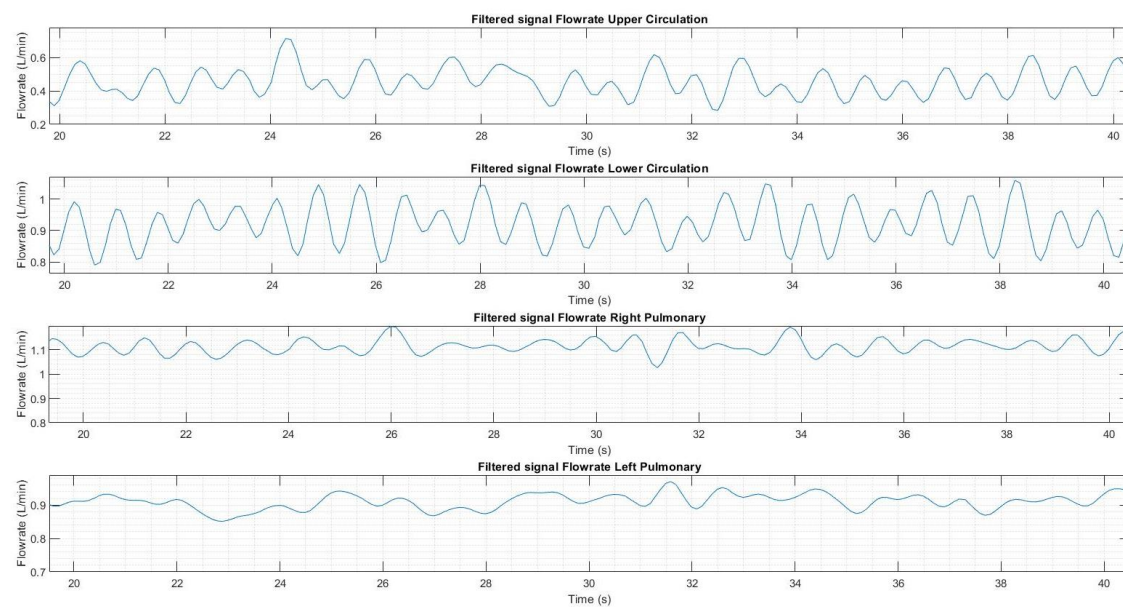


Figure 123 Filtered flowrate of 3mm IJS at 45 degree

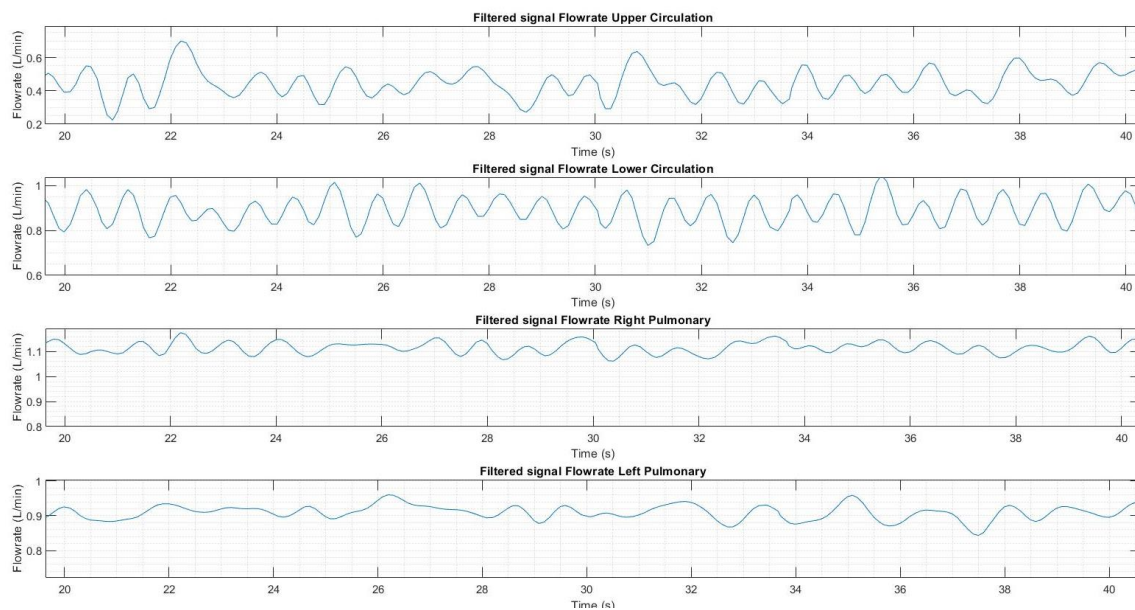


Figure 124 Filtered flowrate of 3mm IJS at 90 degree

Pressure:

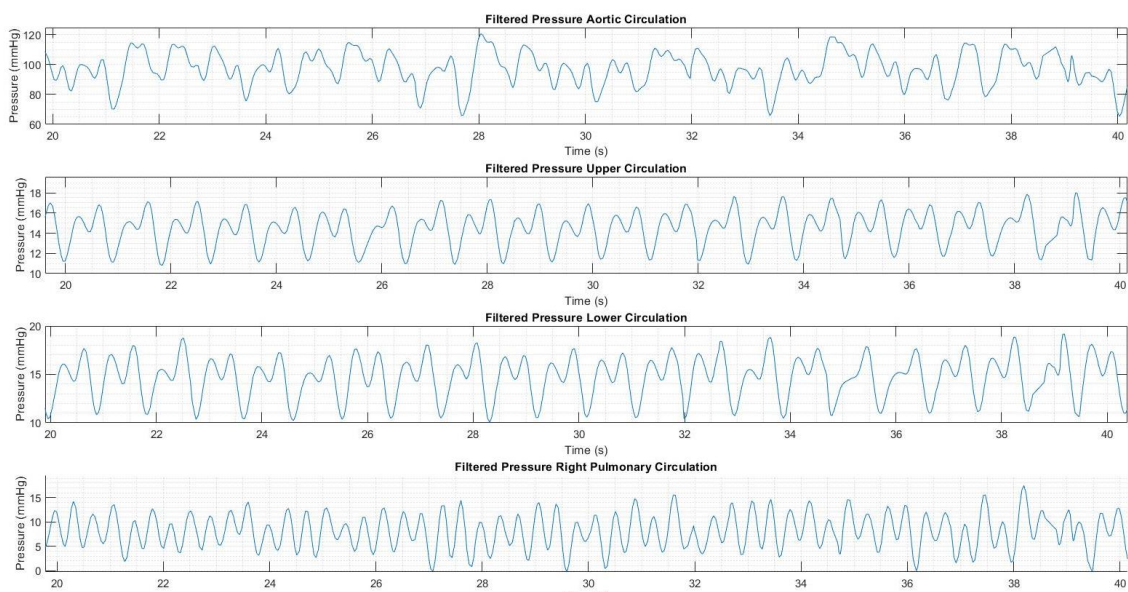


Figure 125 Filtered pressure of 3mm IJS at 5 degree

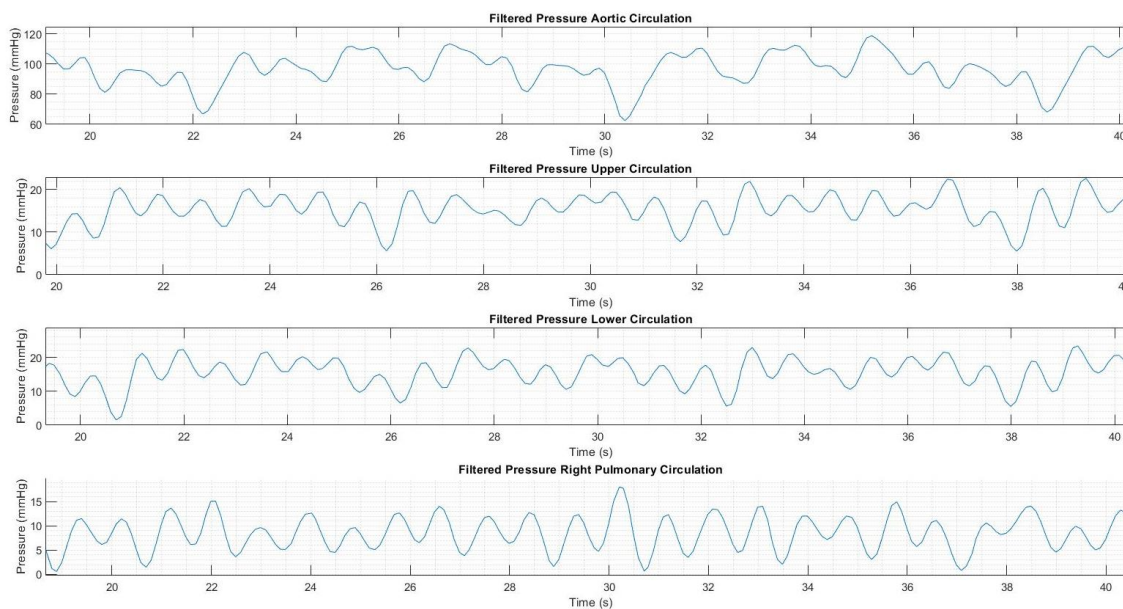


Figure 126 Filtered pressure of 3mm IJS at 45 degree

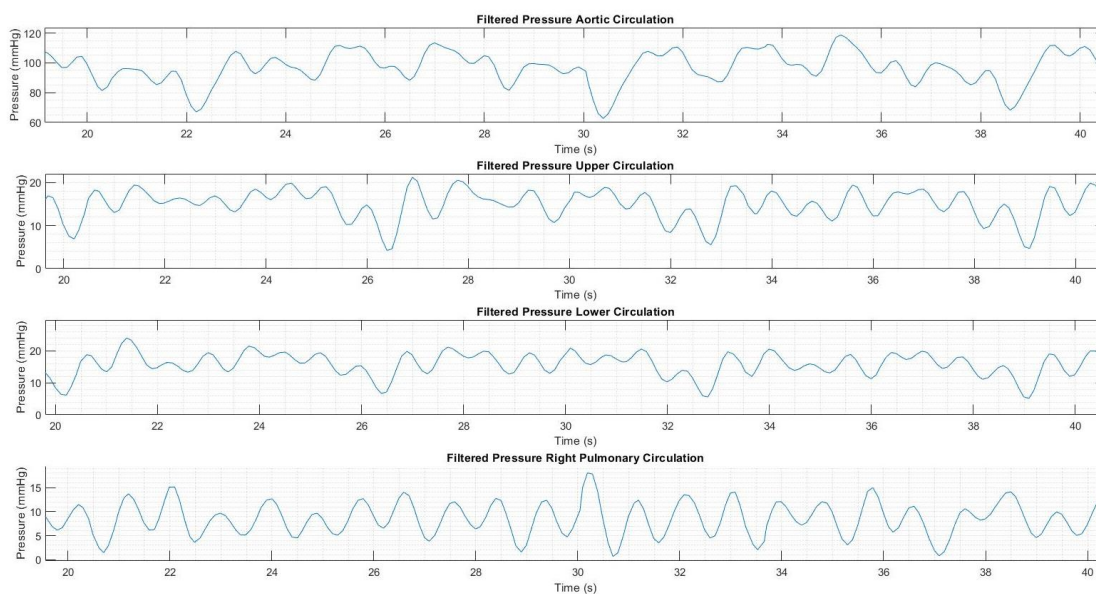


Figure 127 Filtered pressure of 3mm IJS at 90 degree

4.2.2.3. Comparative study of PVR drop by 10 and 30 percent

Per our hypothesis, as flow to the pulmonary system increases PVR drops. Table 14 summarizes results for varying PVR. As PVR decreases there is not a significant change in either Q_s or Q_p . IVC pressure however is significantly affected. Starting from the most optimal IJS implementation angle of 0° the PVR is first dropped by 10% resulting in a 14.41 *mmHg* IVC pressure. A further PVR drop to 20% of baseline decrease IVC pressure to 13.45 *mmHg*. While dropping PVR the constraint on Q_p/Q_s is maintained. Hemodynamic pressure and flowrate waveforms for all the cases of IJS anastomosis angles are shown in Figure 128. Figure 131.

Table 14 Pressure and flow measurements for active IJS and decreasing PVR

Active 3mm IJS 0°		
	10% PVR Drop	30% PVR Drop
$Q_s \left[\frac{L}{\min} \right]$	1.187	1.00
$Q_p \left[\frac{L}{\min} \right]$	2.03	2.03
$\frac{Q_p}{Q_s}$	1.710	2.03
$P_{IVC} [mmHg]$	14.41	13.75
$P_{AO} [mmHg]$	97.0177	97.0177

Before dropping PVR, the IVC pressure drop totals at 4.55 *mmHg*. Once PVR is reduced, the IVC pressure drop increases to 7.30 *mmHg*. These results suggest that the surgical

implementation of an IJS alone can be very beneficial to a Fontan patient. The further benefit arises from the hypothetical PVR drop.

Flowrate

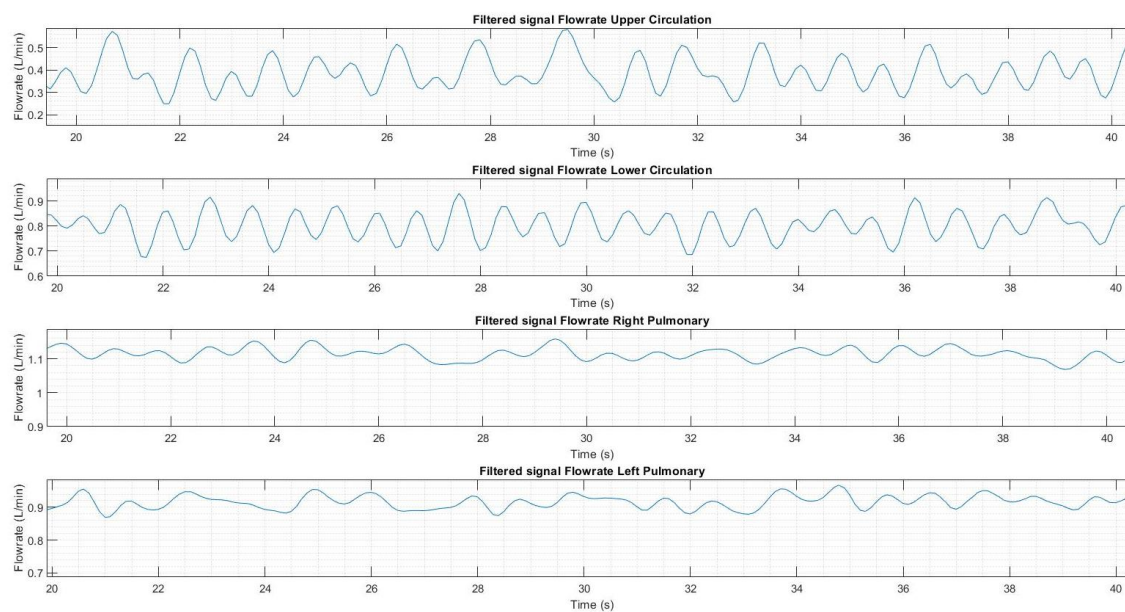


Figure 128 Filtered flowrate PVR10

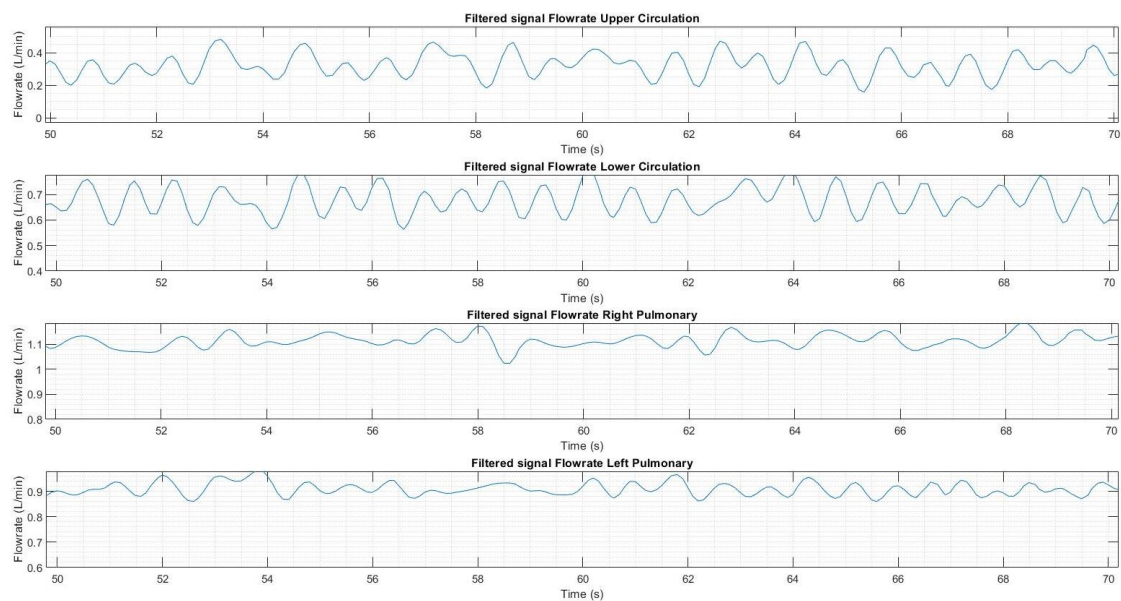


Figure 129 Filtered flowrate PVR30

Pressure

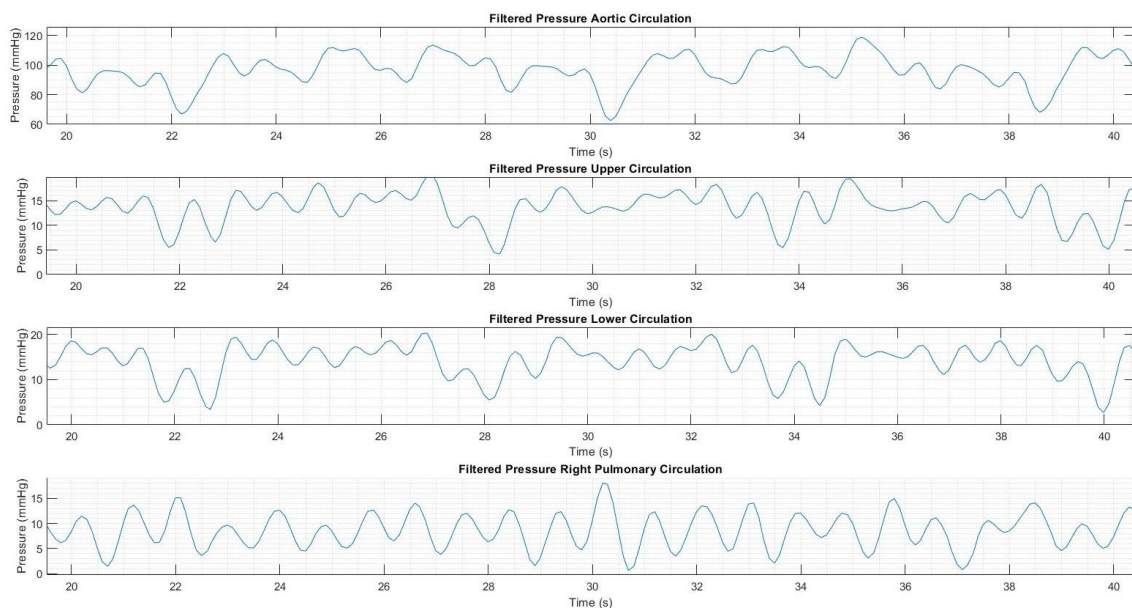


Figure 130 Filtered Pressure PVR10

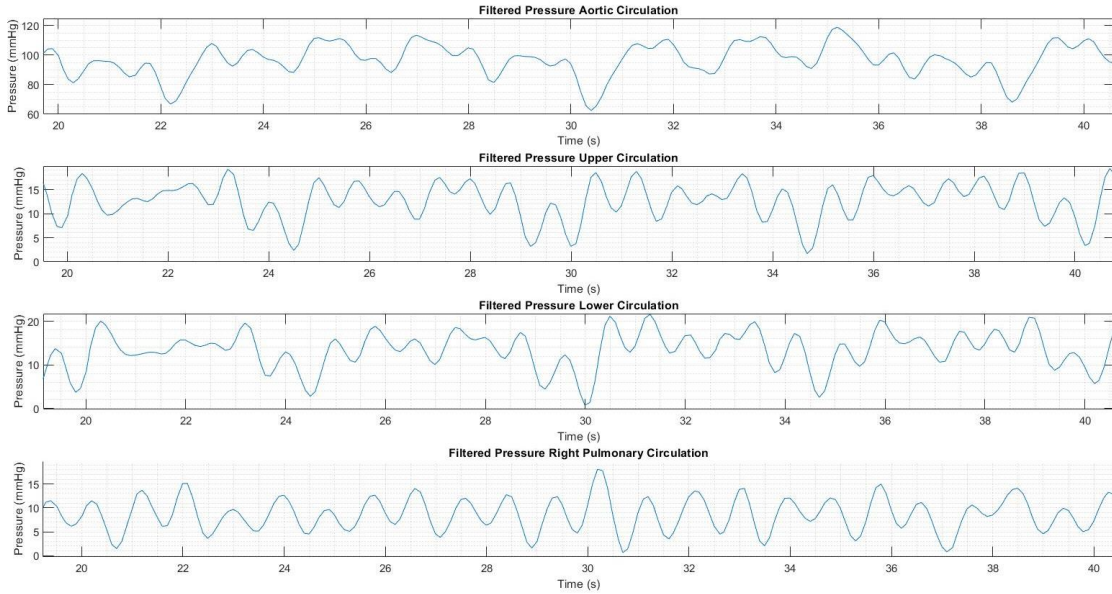


Figure 131 Filtered Pressure PVR30

4.2.2.4. Oxygen transport

Following the tabulated Table 13 and Table 14 flow measurements presented in the earlier section, the oxygen transport in the systemic arterial and venous sides can be evaluated.

Due to the lower CO used in these experiments, the oxygen consumption rate per unit weight had to adjust accordingly. As described in the literature, the oxygen consumption rate can have a linear relationship to the cardiac out, hence based on these results the consumption rate was linearly scaled down to 6.3 mL/s/kg . The results that follow present

oxygen saturations for the systemic arterial and venous circuits for different pulmonary venous saturation (representing various degrees of oxygen extraction by the lungs) for each Fontan model explored offers a complete overview of the oxygen saturation calculations. It can be readily observed that, as mentioned in the oxygen model description, the systemic saturation for a non-fenestrated Fontan geometry matches the pulmonary venous

saturation. The arterial saturations calculated fall within the acceptable range. Due to the oxygen transport model employed, the systemic venous saturations are highly dependent upon the correct implementation of the consumption rates. As mentioned earlier, the consumption rate found in the literature was scaled down accordingly to match the CO used in these experiments. The resulting systemic venous saturation falls within the expected range, particularly for the baseline case, which can be readily compared to clinical data. This indicates that the consumption rate scaling was performed correctly. Baseline and models implementing the IJS only differ for systemic venous saturations. This difference is due entirely to the strong drop-in Q_s that occurs when the IJS valve is opened. Once the IJS becomes active, proximal shunt anastomosis angle and PVR reduction do not strongly affect oxygen saturation. In general as the pulmonary venous saturation drops the systemic arterial and venous saturation follow the same trend.

Figure 132 takes a closer look at the arterial and venous saturation separately. The decreasing trend in oxygen saturation with dropping ventilation is clear. The strong drop in systemic venous saturation upon IJS activation has been highlighted as well as the lack

of noticeable change in saturations (especially on the venous side) due to model alterations (IJS takeoff angle and PVR).

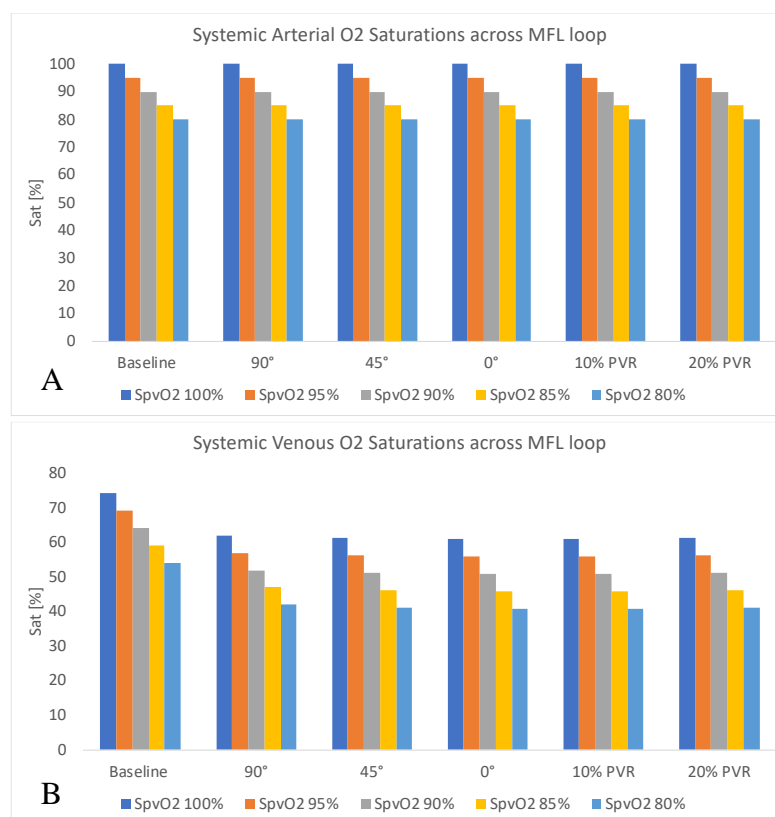


Figure 132 - Systemic arterial (A) and venous (B) oxygen saturations for various pulmonary venous saturations (SpvO2) in all the models explored.

The results presented in this section offer a good degree of validation for the oxygen transport model implemented. The computed quantities match expected trends and can be readily compared to clinical data.

4.2.3. PVR entrainment Study

4.2.3.1. Hemodynamics for PVR protocol

As per the described protocol in section 3.3, experimental runs for all short and long bursts of injections in the LPA conduit are conducted. The pressure levels in all four sections are observed along with the pressure in the aortic section. The tables below show the averaged

value of each protocol that was conducted for three times. From Table 15 to Table 22, it can be concluded that there is no appreciable change to the pressure in the PAs. In this result section, Figure 133 to Figure 148 plots the hemodynamic response of the MFL for all significant type of short and long bursts of injections.

Flow rate and pressure waveforms are captured during the experiment. Peaks of pressure waveform tend to be consistent during the experimentation, proving that the injection protocol does not increase the pressure at the injection site during in-vitro studies.

Table 15 Short multiple injections at 5cc/s A. Flowrate values B. Pressure values

A	Flow rates (L/min)					
	5cc/s	Q_{upper}	Q_{lower}	Q_{RPA}	Q_{LPA}	Q_p/Q_s
	5 x 20cc (100cc)	0.796	1.497	1.229	1.190	1.055
	5 x 15cc (75cc)	0.795	1.530	1.227	1.214	1.049
	10 x 10cc (100cc)	0.798	1.530	1.230	1.212	1.048
	10 x 5cc (50cc)	0.795	1.528	1.219	1.208	1.045
B	Pressure ($mmHg$)					
	5cc/s	P_{upper}	P_{lower}	P_{RPA}	P_{LPA}	P_{aortic}

5 x 20cc (100cc)	16.565	18.779	7.272	7.9	94.197
5 x 15cc (75cc)	16.579	18.763	7.311	7.546	98.132
10 x 10cc (100cc)	16.517	18.832	7.239	7.518	99.040
10 x 5cc (50cc)	16.561	18.749	7.299	7.537	97.825

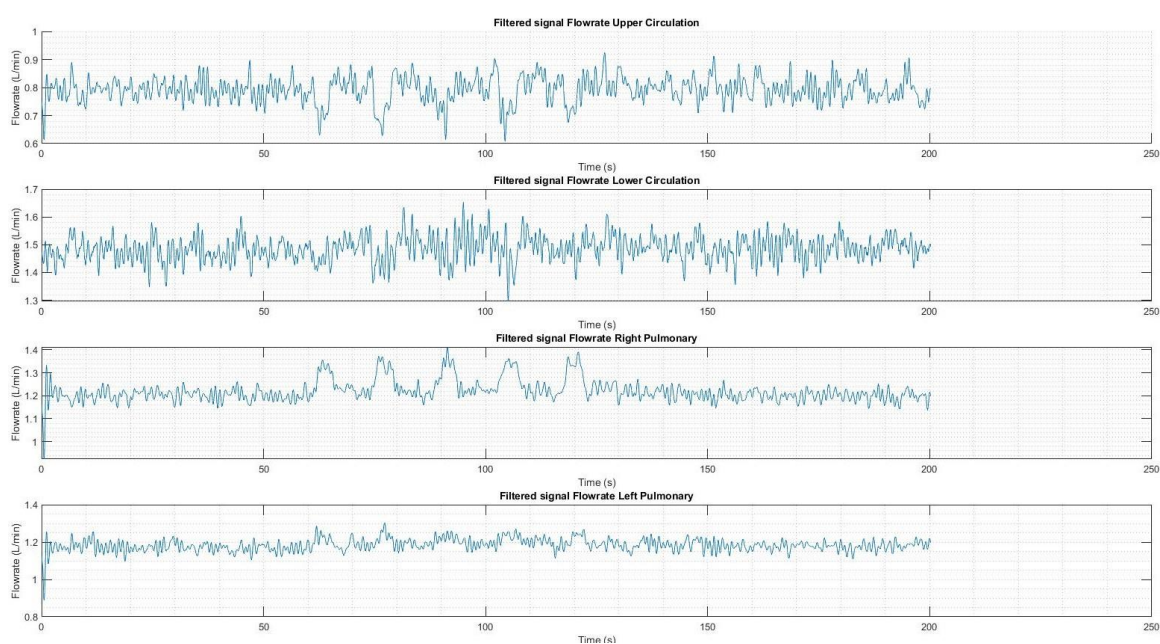


Figure 133 Filtered flowrate for 5cc/s with 20cc volume for five shots

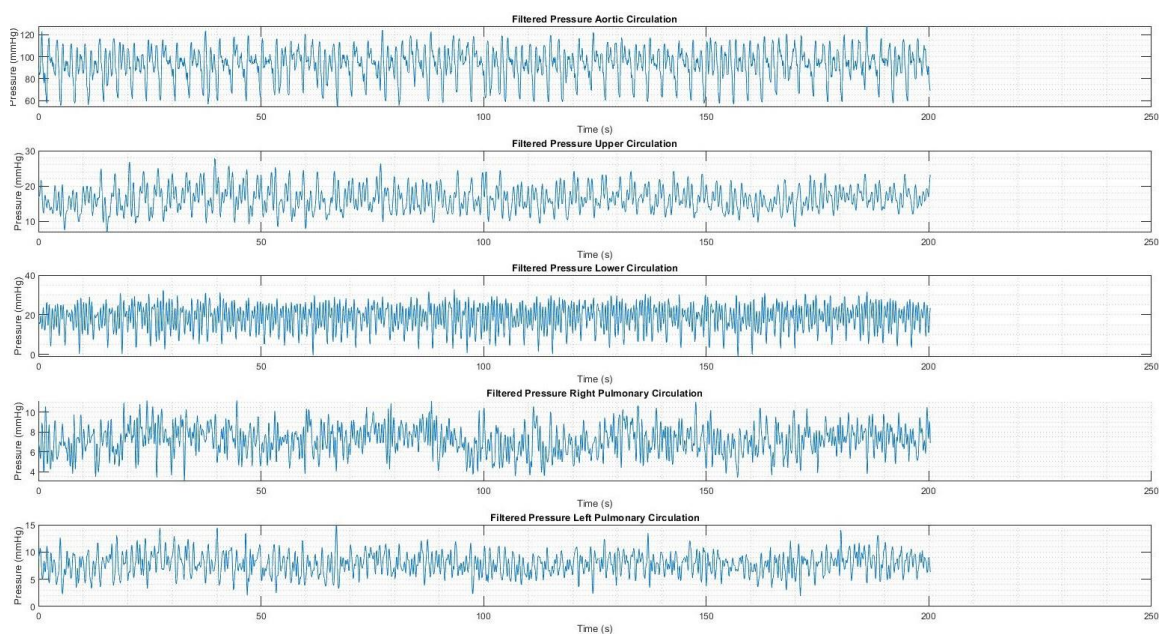


Figure 134 Filtered pressure for 5cc/s with 20cc volume for five shots

Table 16 Short multiple injection at 10cc/s A. Flowrate values B. Pressure values

A	Flow rates (L/min)				
10cc/s	Q_{upper}	Q_{lower}	Q_{RPA}	Q_{LPA}	Q_p/Q_s
5 x 20cc (100cc)	0.788	1.522	1.225	1.208	1.053
5 x 15cc (75cc)	0.796	1.524	1.225	1.208	1.048
10 x 10cc (100cc)	0.801	1.526	1.232	1.211	1.049
10 x 5cc (50cc)	0.798	1.537	1.226	1.211	1.049

B	Pressure (<i>mmHg</i>)				
	10cc/s	P_{upper}	P_{lower}	P_{RPA}	P_{LPA}
5 x 20cc (100cc)	16.569	18.816	7.266	7.590	97.954
5 x 15cc (75cc)	16.684	18.866	7.379	7.580	98.416
10 x 10cc (100cc)	16.626	18.889	7.321	7.610	98.856
10 x 5cc (50cc)	16.535	18.844	7.330	7.599	99.607

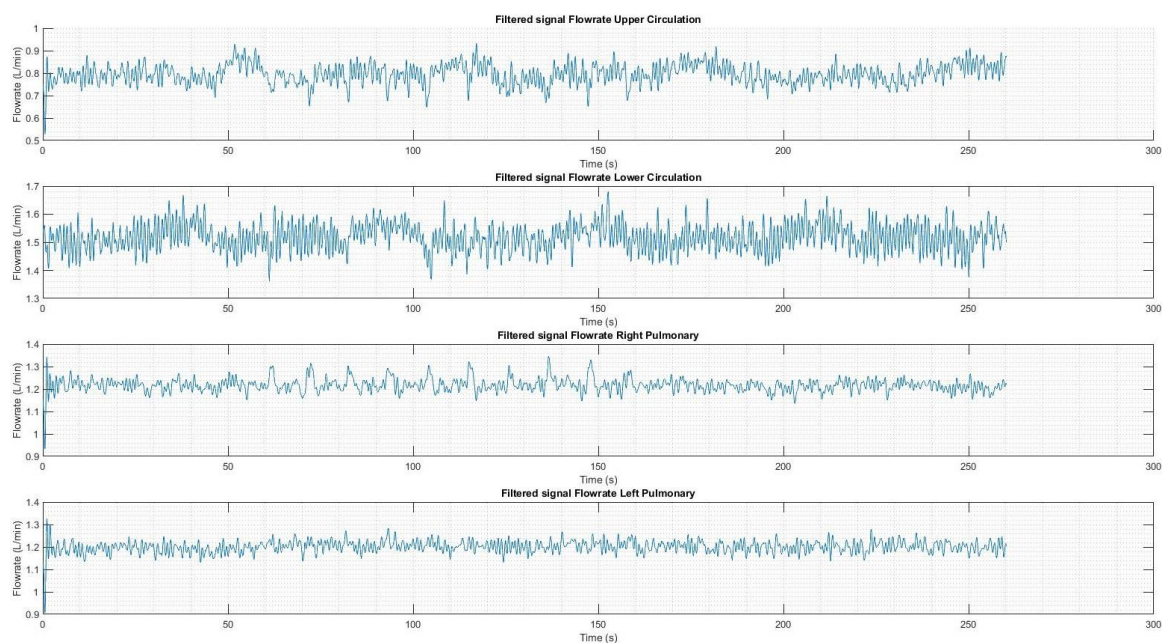


Figure 135 Filtered flowrate for 10cc/s with 20cc volume for ten shots

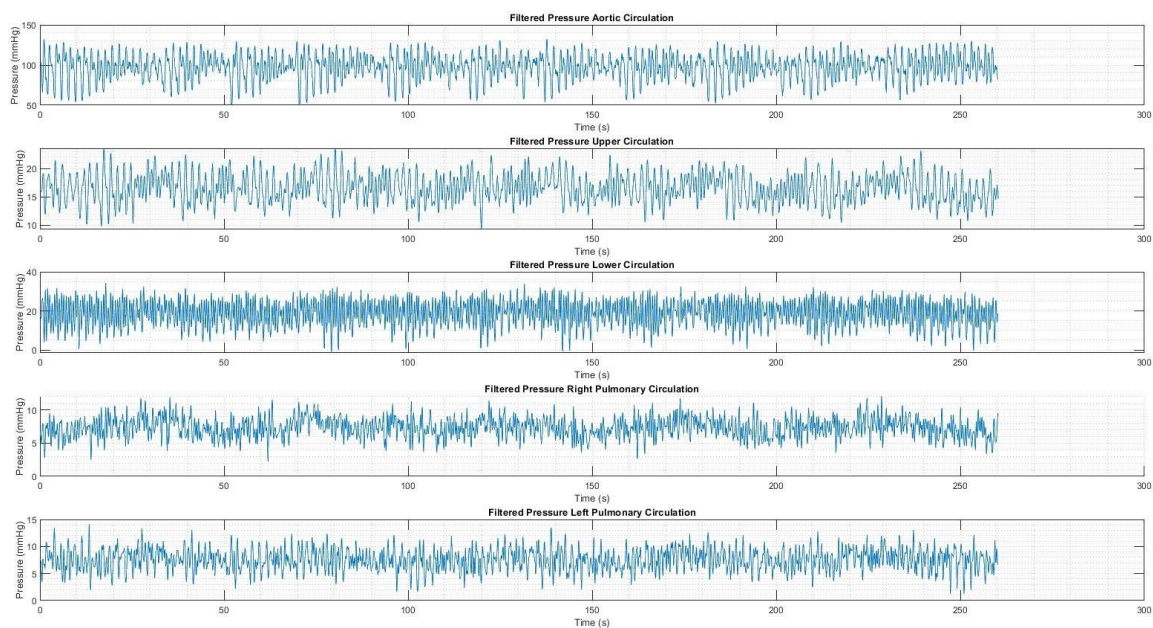


Figure 136 Filtered pressure for 10cc/s with 20cc volume for ten shots

Table 17 Short multiple injection at 15cc/s A. Flowrate values B. Pressure values

A	Flow rates (L/min)				
15cc/s	Q_{upper}	Q_{lower}	Q_{RPA}	Q_{LPA}	Q_p/Q_s
5 x 20cc (100cc)	0.804	1.508	1.255	1.178	1.051
5 x 15cc (75cc)	0.797	1.512	1.266	1.1582	1.049
10 x 10cc (100cc)	0.800	1.511	1.271	1.162	1.053
10 x 5cc (50cc)	0.798	1.506	1.258	1.156	1.047

B	Pressure (<i>mmHg</i>)				
	15cc/s	<i>P_{upper}</i>	<i>P_{lower}</i>	<i>P_{RPA}</i>	<i>P_{LPA}</i>
5 x 20cc (100cc)	16.990	19.217	7.526	8.437	96.882
5 x 15cc (75cc)	17.418	19.55	7.664	8.940	96.8
10 x 10cc (100cc)	17.338	19.544	7.615	8.912	96.808
10 x 5cc (50cc)	17.289	19.501	7.664	8.948	96.541

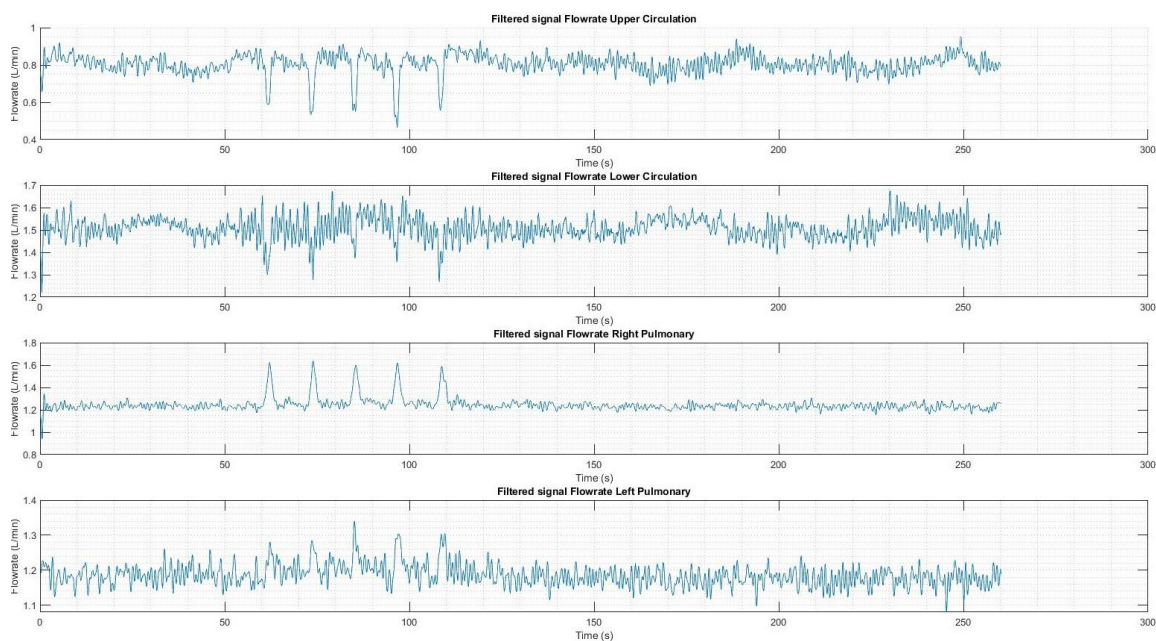


Figure 137 Filtered flowrate for 15cc/s with 20cc volume for five shots

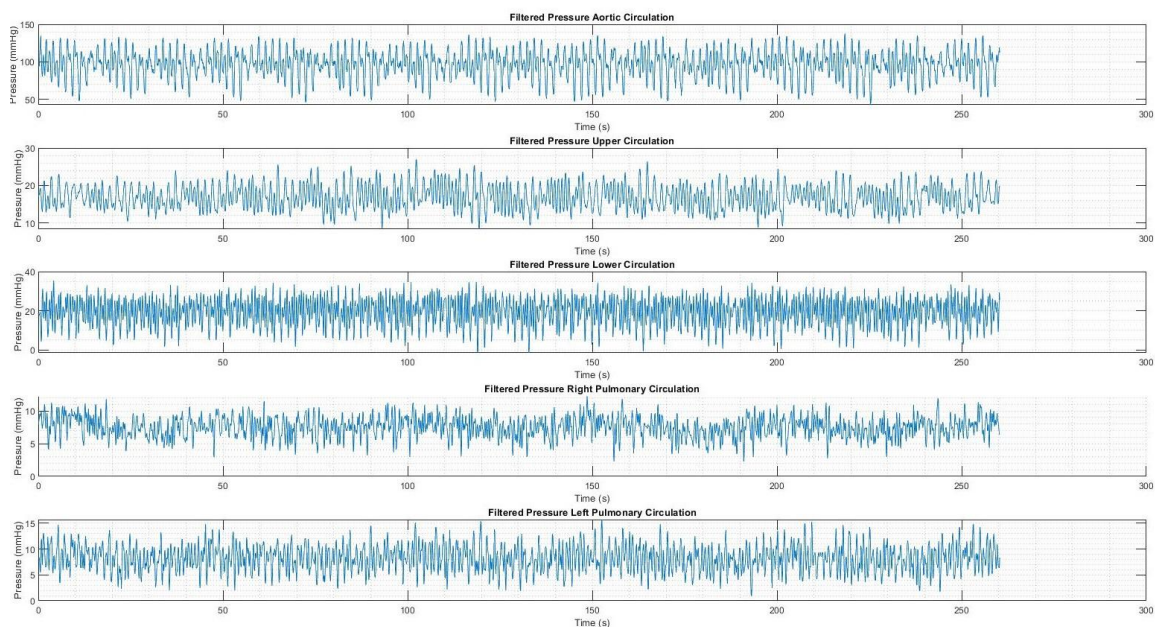


Figure 138 Filtered pressure for 15cc/s with 20cc volume for five shots

Table 18 Short multiple injection at 20cc/s A. Flowrate values B. Pressure values

A	Flow rates (L/min)				
20cc/s	Q_{upper}	Q_{lower}	Q_{RPA}	Q_{LPA}	Q_p/Q_s
5 x 20cc (100cc)	0.808	1.514	1.274	1.168	1.051
5 x 15cc (75cc)	0.804	1.517	1.269	1.164	1.048
10 x 10cc (100cc)	0.808	1.509	1.234	1.199	1.049
10 x 5cc (50cc)	0.808	1.512	1.265	1.163	1.047

B	Pressure (<i>mmHg</i>)				
	20cc/s	P_{upper}	P_{lower}	P_{RPA}	P_{LPA}
5 x 20cc (100cc)	17.603	19.751	7.704	8.940	1.051
5 x 15cc (75cc)	17.422	19.639	7.654	8.938	1.048
10 x 10cc (100cc)	17.542	19.726	7.737	9.001	1.049
10 x 5cc (50cc)	17.509	19.675	7.706	9.030	1.047

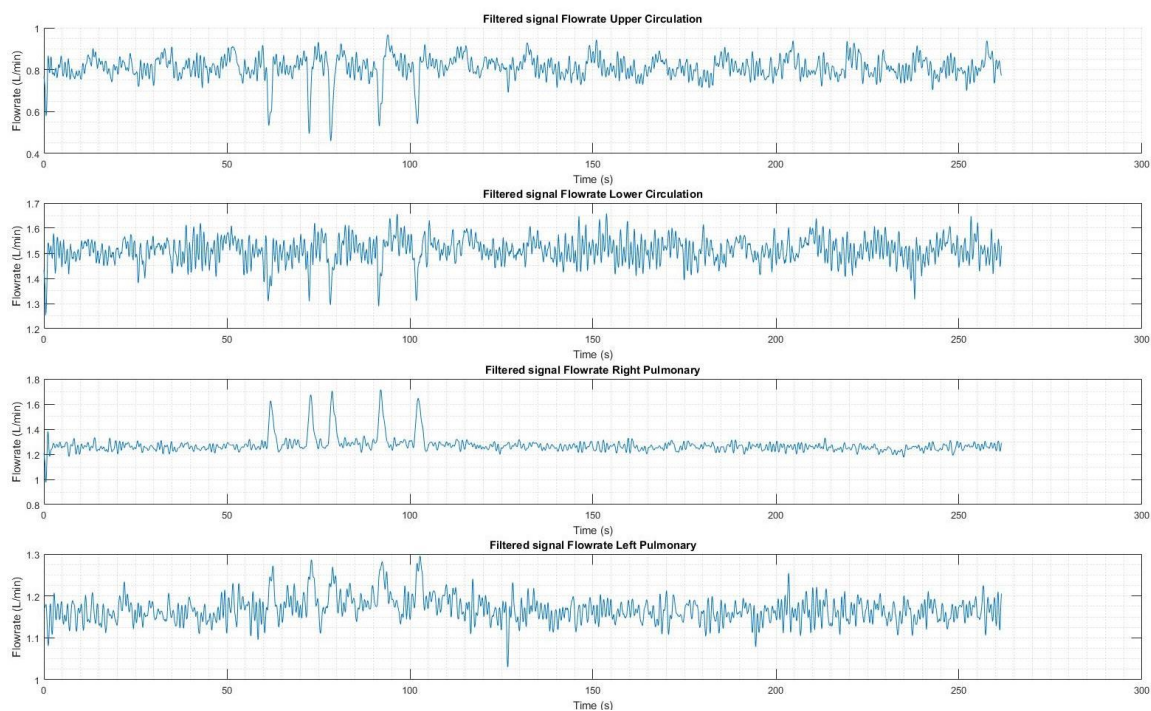


Figure 139 Filtered flowrate for 20cc/s with 20cc volume for five shots

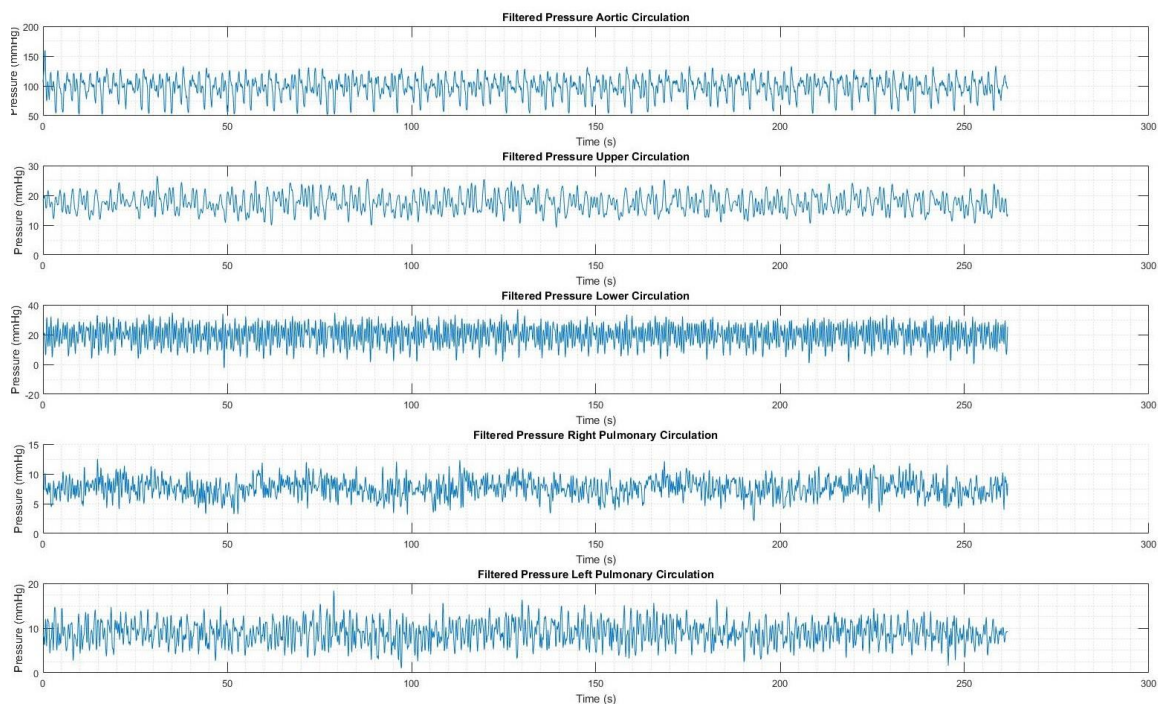


Figure 140 Filtered pressure for 20cc/s with 20cc volume for five shots

Table 19: Long single injection at 5cc/s A. Flowrate values B. Pressure values

A	Flow rates (L/min)				
5cc/s	Q_{upper}	Q_{lower}	Q_{RPA}	Q_{LPA}	Q_p/Q_s
1 x 50cc (50cc)	0.796	1.497	1.229	1.190	1.055
1 x 100cc (100cc)	0.795	1.530	1.227	1.214	1.049
1 x 150cc (10cc)	0.798	1.530	1.230	1.212	1.048

B	Pressure (<i>mmHg</i>)				
	5cc/s	P_{upper}	P_{lower}	P_{RPA}	P_{LPA}
1 x 50cc (50cc)	16.565	18.779	7.272	7.9	94.197
1 x 100cc (100cc)	16.579	18.763	7.311	7.546	98.312
1 x 150cc (10cc)	16.517	18.832	7.239	7.518	99.040

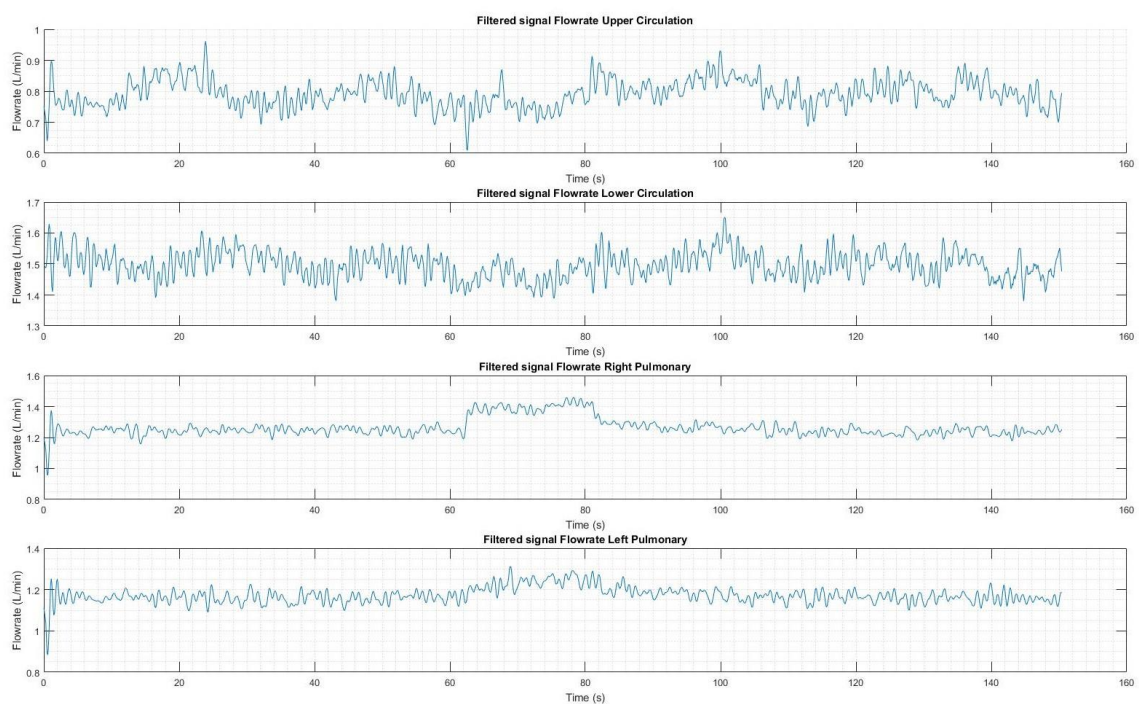


Figure 141 Filtered flow rate for 5cc/s with 100cc volume for one long shot

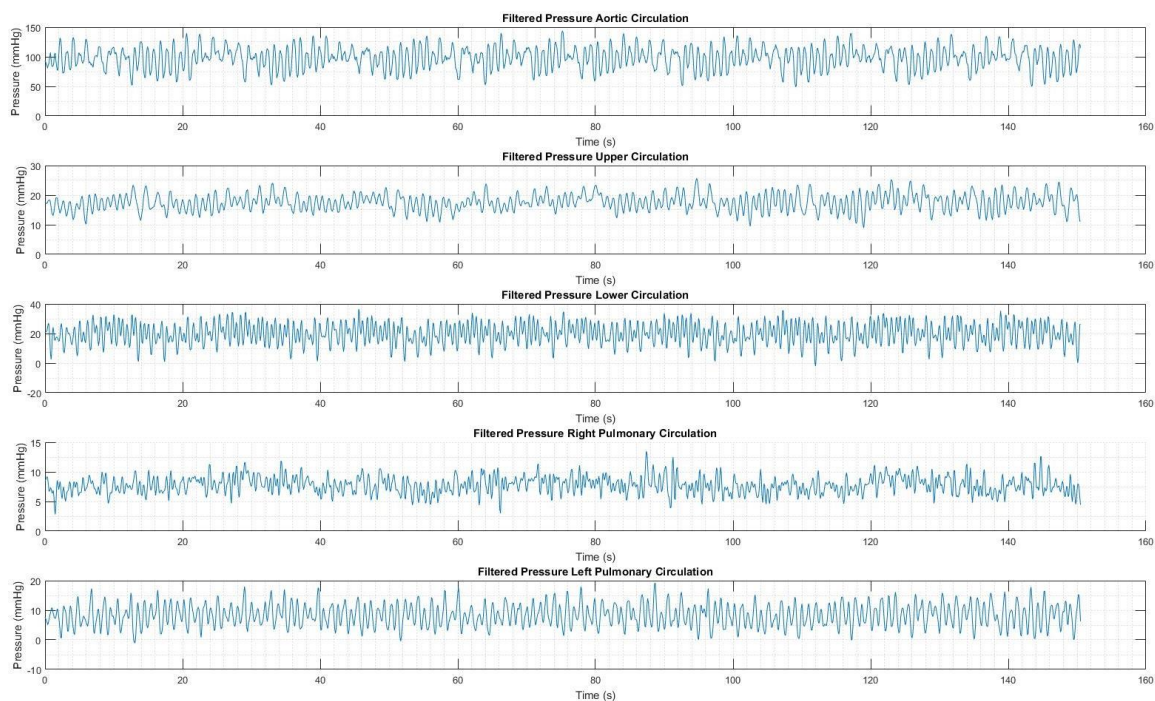


Figure 142 Filtered pressure for 5cc/s with 100cc volume for one long shot

Table 20 Long single injection at 10cc/s A. Flowrate values B. Pressure values

A	Flow rates (L/min)				
	Q_{upper}	Q_{lower}	Q_{RPA}	Q_{LPA}	Q_p/Q_s
10cc/s					
1 x 50cc (50cc)	0.798	1.501	1.260	1.170	1.056
1 x 100cc (100cc)	0.799	1.506	1.270	1.179	1.062
1 x 150cc (10cc)	0.791	1.509	1.285	1.183	1.072

B 10cc/s	Pressure (<i>mmHg</i>)				
	P_{upper}	P_{lower}	P_{RPA}	P_{LPA}	P_{aortic}
1 x 50cc (50cc)	17.417	19.612	7.694	8.266	98.384
1 x 100cc (100cc)	17.590	19.831	7.794	8.244	98.505
1 x 150cc (10cc)	17.785	20.011	7.731	8.295	99.259

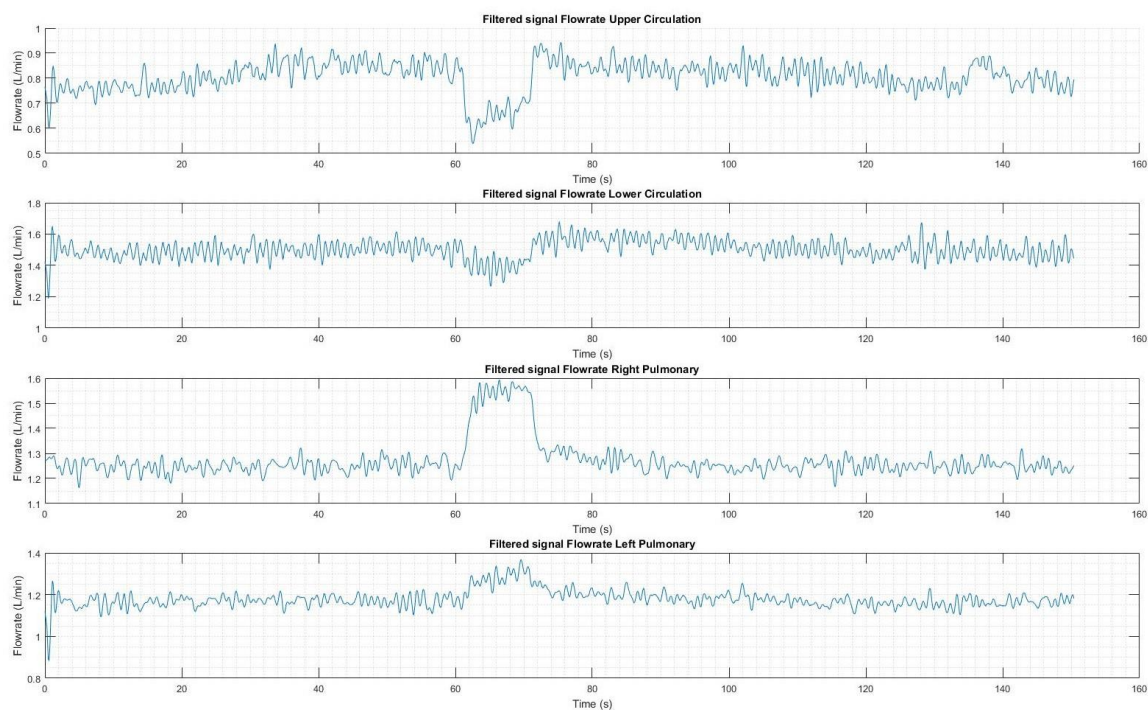


Figure 143 Filtered flow rate for 10cc/s with 100cc volume for one long shot

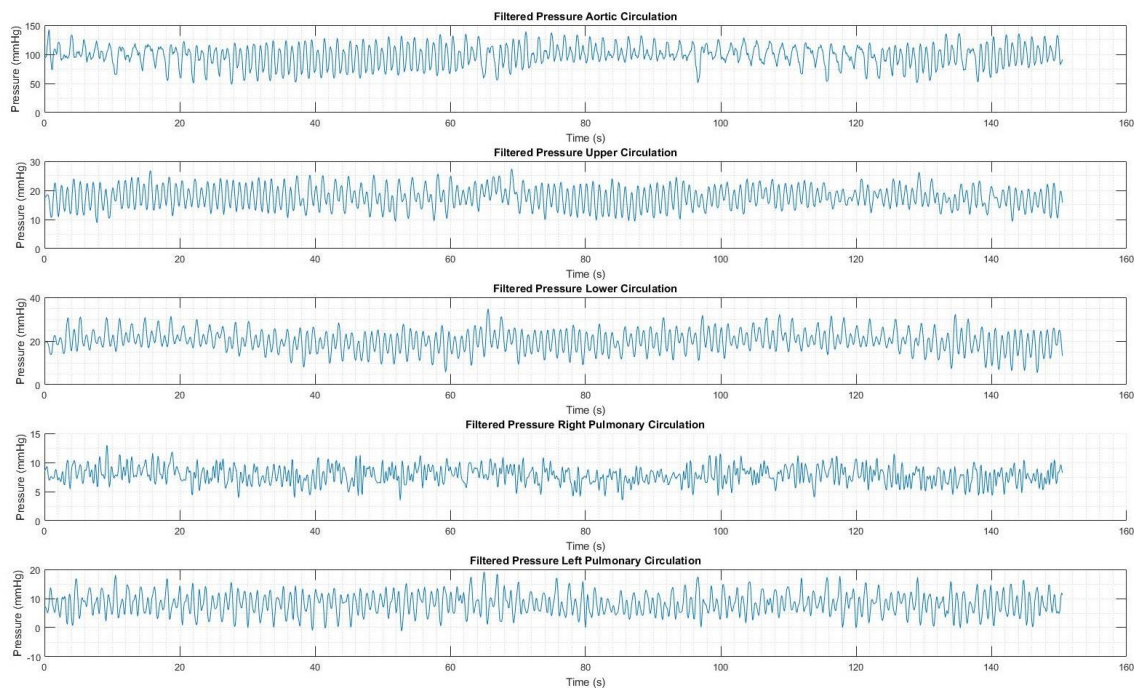


Figure 144 Filtered pressure for 10cc/s with 100cc volume for one long shot

Table 21 Long single injection at 15cc/s A. Flowrate values B. Pressure values

A	Flow rates (L/min)				
	Q_{upper}	Q_{lower}	Q_{RPA}	Q_{LPA}	Q_p/Q_s
15cc/s					
1 x 50cc (50cc)	0.775	1.513	1.251	1.164	1.055
1 x 100cc (100cc)	0.774	1.512	1.264	1.166	1.062
1 x 150cc (10cc)	0.766	1.510	1.272	1.169	1.072

B	Pressure (<i>mmHg</i>)				
	P_{upper}	P_{lower}	P_{RPA}	P_{LPA}	P_{aortic}
15cc/s					
1 x 50cc (50cc)	17.284	19.488	7.750	8.229	98.702
1 x 100cc (100cc)	17.273	19.511	7.633	8.177	98.792
1 x 150cc (10cc)	17.361	19.599	7.792	8.208	97.960

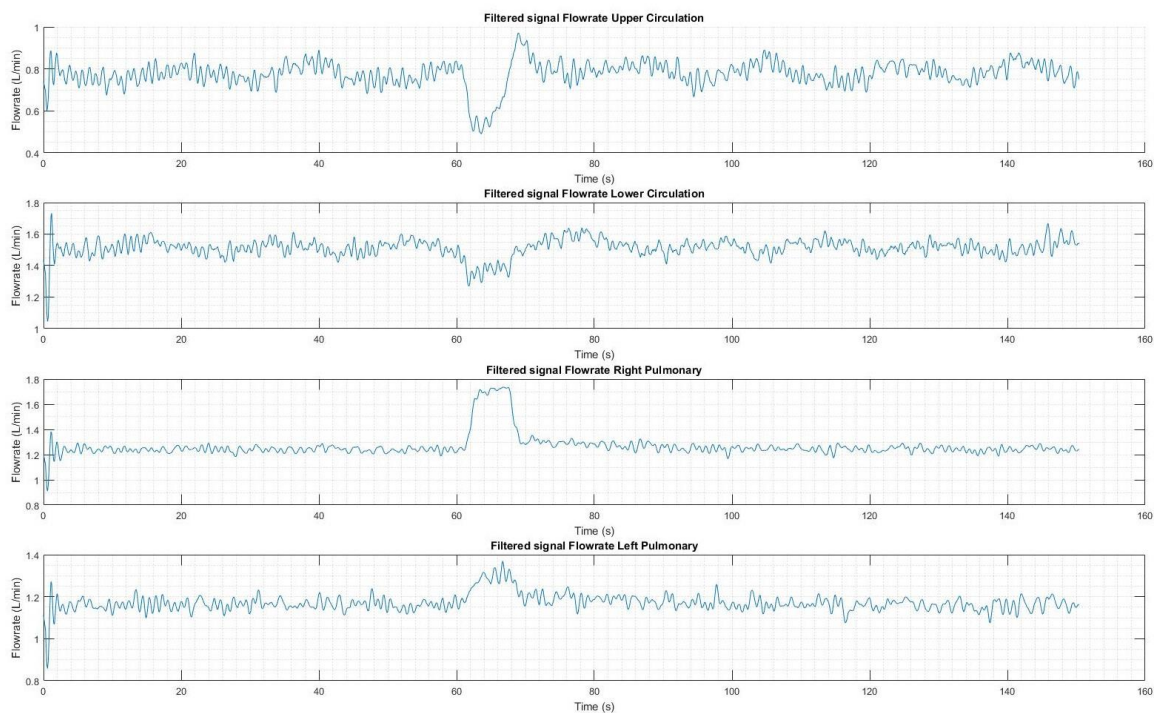


Figure 145 Filtered flow rate for 15cc/s with 100cc volume for one long shot

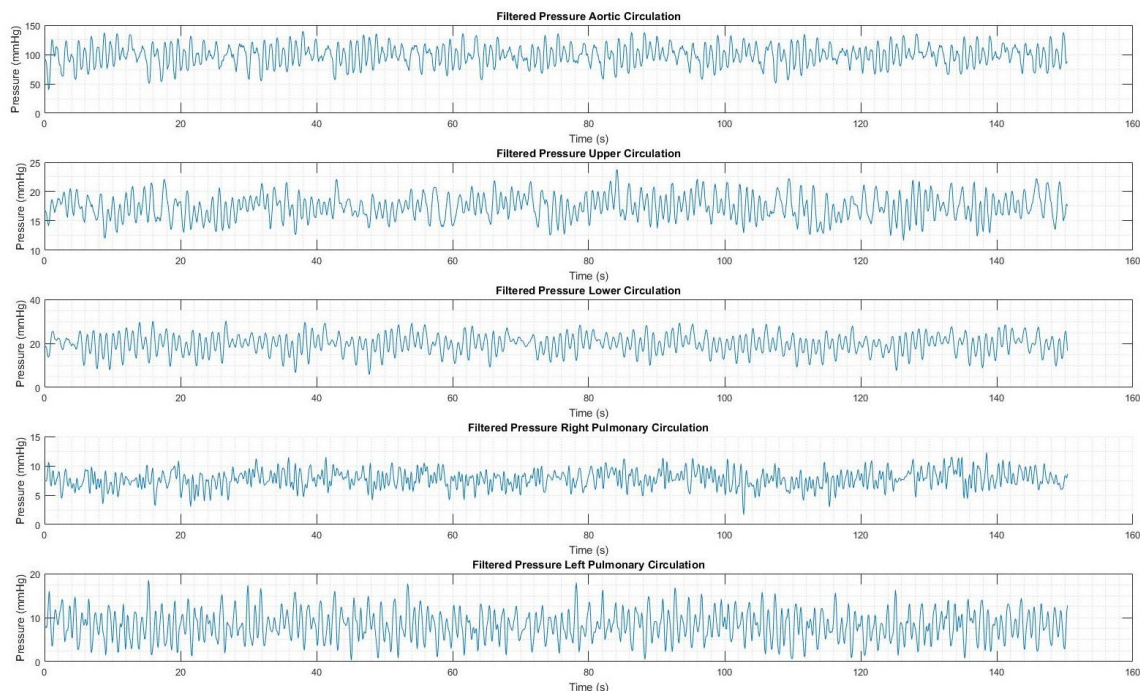


Figure 146 Filtered pressure for 15cc/s with 100cc volume for one long shot

Table 22 Long single injection at 20cc/s A. Flowrate values B. Pressure values

A	Flow rates (L/min)				
	Q_{upper}	Q_{lower}	Q_{RPA}	Q_{LPA}	Q_p/Q_s
20cc/s					
1 x 50cc (50cc)	0.806	1.509	1.262	1.160	1.048
1 x 100cc (100cc)	0.802	1.504	1.277	1.163	1.058
1 x 150cc (10cc)	0.798	1.499	1.287	1.166	1.067

B	Pressure (<i>mmHg</i>)					
	20cc/s	P_{upper}	P_{lower}	P_{RPA}	P_{LPA}	P_{aortic}
1 x 50cc (50cc)		17.390	19.453	7.643	8.994	97.361
1 x 100cc (100cc)		17.426	19.616	7.612	8.899	96.878
1 x 150cc (10cc)		17.462	19.615	7.662	8.988	96.772

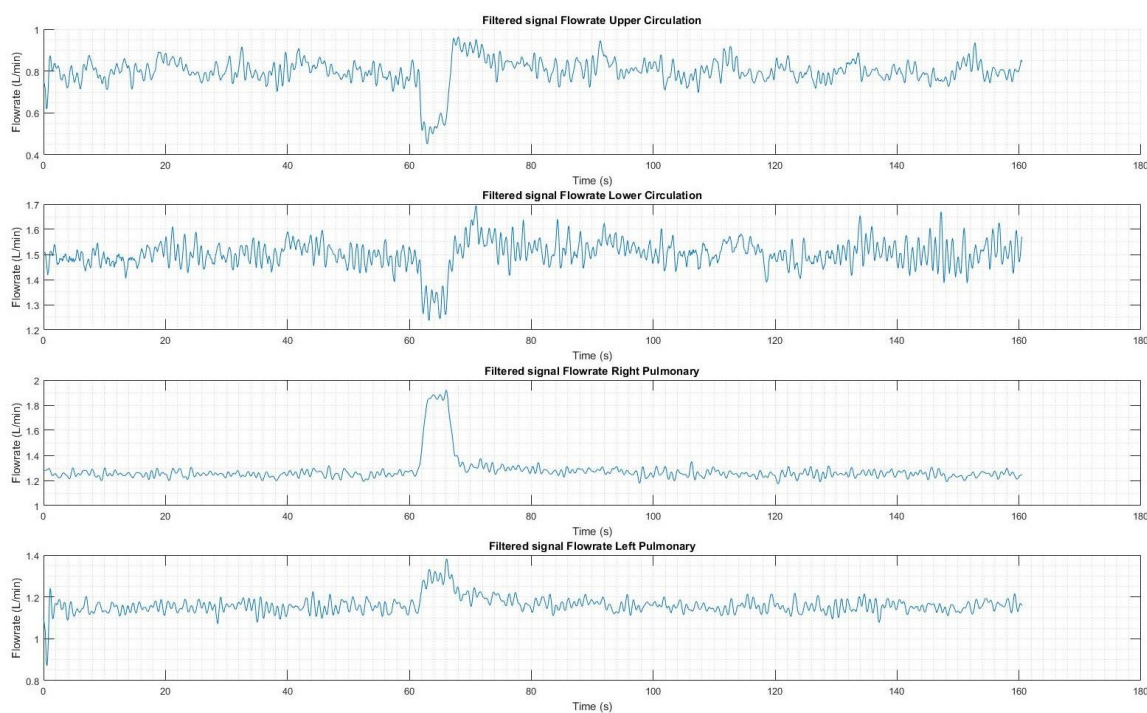


Figure 147 Filtered flowrate for 20cc/s with 100cc volume for one long shot

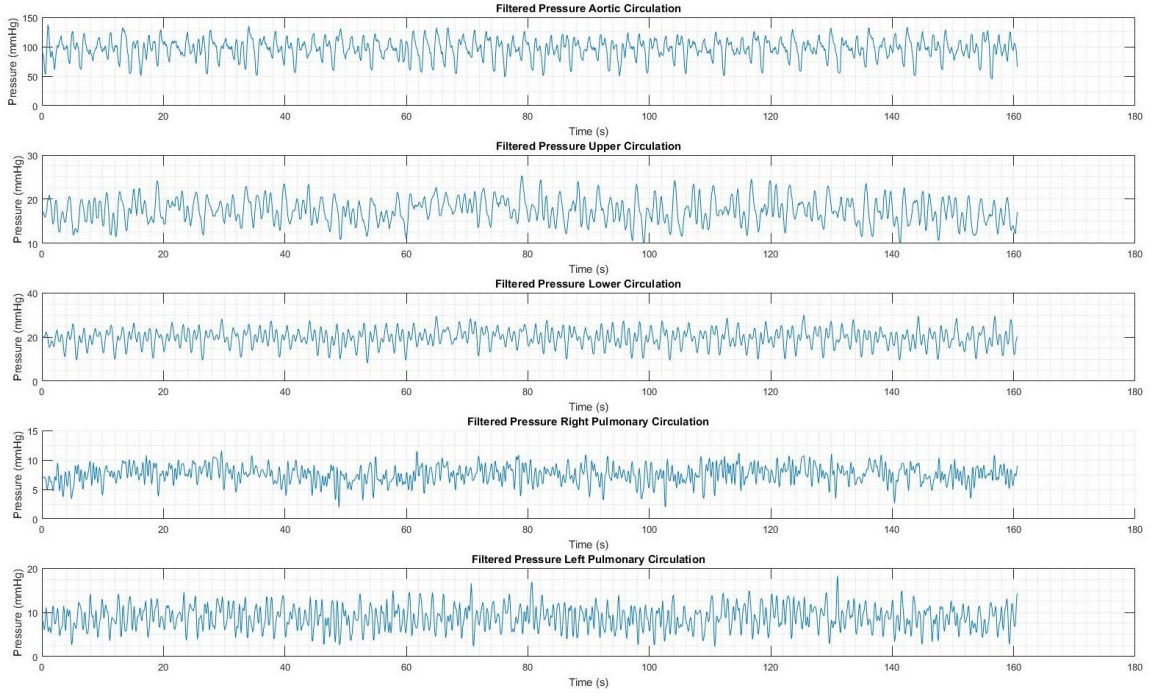


Figure 148 Filtered pressure for 20cc/s with 100cc volume for one long shot

4.2.3.2. Entrainment Quantification

Once the experimental protocol has been completed, flow rates sampled at described locations are time-averaged. Entrainment is calculated from Equation 21 and reported for the whole parameter space explored in Table 23. Green values $\dot{Q}_{ent} > 0$ represent cases for which entrainment was detected, and red values $\dot{Q}_{ent} < 0$ are cases where the blockage occurred.

One can observe how for either continuous or pulsed injections, varying the total volume injected has no significant influence on the entrainment rate across all injection rates. On the other hand, increasing injection rate results in a reduction in entrainment consistent across all injected volumes for both injection conditions. Given the constant diameter shunt

2.6 mm used in this experiment, this outcome suggests that entrainment is strongly correlated to the co-flow velocity ratio (and flow rate ratio) and weakly correlated to the total injected volume. In addition, Table 24 offers significant insight on the differences between injection conditions (continuous vs. pulsed). In Table 24-A, the entrainment cutoff appears to be $\dot{Q}_{inj} \sim 0.6 \text{ L/min}$, whereas in Table 23-B the cutoff occurs from a smaller flow rate $\dot{Q}_{inj} \sim 0.3 \text{ L/min}$. To better understand the degree of entrainment, the tabulated maximum values (for $\dot{Q}_{inj} = 0.3$) can be normalized by the \dot{Q}_{inj} . After averaging across the column, for a continuous injection $\frac{\dot{Q}_{ent}}{\dot{Q}_{inj}} = 0.63$ and $\frac{\dot{Q}_{ent}}{\dot{Q}_{inj}} = 0.16$ for a pulsed injection. This stark contrast highlights a clear difference between injection conditions which emphasize the importance of ensuring proper physiological modeling: pulsatility cannot be overlooked. Conversely this opens the door for a discussion involving pulsatility modulation to enhance entrainment. Since, the shunt diameter is kept constant, an increasing flow rate indicated an increased co-flow velocity ratio ($V_{jet}/V_{background}$), it would sound counterintuitive to have increasingly positive results for a decreasing velocity ratio. However, results presented in the following section for the jet relaxation time will provide further insight in the jet dynamics and clarify this puzzling outcome.

Table 23 Jet relaxation time [s] for various injection rates \dot{Q}_{inj} and injection volumes V_{inj} for (A) continuous and (B) pulsed injections. Green values $t_{rel} > 0$ and red values $t_{rel} < 0$.

(A)	$\dot{Q}_{inj} \text{ [L/min]}$			
	0.3	0.6	0.9	1.2

	0.05	0.1646	0.0015	-0.1084	-0.2263
$V_{inj}[L]$	0.1	0.2125	0.0389	-0.0860	-0.2265
	0.15	0.1985	0.0144	-0.0866	-0.2454

(B)	$\dot{Q}_{inj} [L/min]$				
		0.3	0.6	0.9	1.2
	0.015	0.0441	-0.1494	-0.4581	-0.7167
$V_{inj}[L]$	0.02	0.0496	-0.1353	-0.3395	-0.6096

Table 24 offers an overview of the calculated jet relaxation time t_{rel} for the same parameter space explored in the previous section. Green values ($t_{rel} > 0$) represent lack of potential fluid buildup and red values ($t_{rel} < 0$) would indicate a high likelihood of fluid buildup. Due to the choice of sampling rate in the experimental phase the following tabulated observations may show some inconsistency, nevertheless for most cases a trend can be perceived.

In Table 23-A, aside from the data reported for $V_{inj} = 0.1$ which displays an opposite tendency, for continuous injections it can be observed that varying the injected volume V_{inj} does not significantly alter t_{rel} . On the other hand, increasing \dot{Q}_{inj} appears to display decreasing trend with a maximum for $\dot{Q}_{inj} = 0.6$. This would indicate that for increasing injection flow rate, the fall-time tends towards the rise-time; suggesting that for increasing co-flow velocity ratio the flow field requires significantly more time to dissipate the jet effect. A similar trend can be seen for pulsed injections. Such an outcome is to be expected. This flow relaxation feature helps understand the counterintuitive observation made for the

entrainment quantifications where for lower co-flow velocity ratio enhanced entrainment is registered. This observations become even more relevant for the pulsed injection cases.

Table 24 Jet relaxation time [s] for various injection rates \dot{Q}_{inj} and injection volumes V_{inj} for (A) continuous and (B) pulsed injections . Green values $t_{rel} > 0$ and red values $t_{rel} < 0$.

(A)		$\dot{Q}_{inj} [L/min]$			
		0.3	0.6	0.9	1.2
$V_{inj} [L]$	0.05	0.497	0.891	0.398	0.198
	0.1	0.103	0.100	0.509	0.504
	0.15	0.495	0.607	0.399	0.107

(B)		$\dot{Q}_{inj} [L/min]$			
		0.3	0.6	0.9	1.2
$V_{inj} [L]$	0.015	0.715	0.341	0.118	0.151
	0.02	0.196	0.315	0.809	0.021

4.3. Uncertainty Analysis

Table 25 provides the types of errors specified by the manufacturers of the pressure sensor. The uncertainty due to the different types of error is computed using the Type B estimate.

Table 25 Error parameters for Pressure sensor

Parameter	Description	Mean Value	Error limits	Percentage confidence
-----------	-------------	------------	--------------	-----------------------

P_{app}	Calibration Pressure	7.5 psi		
E1	Accuracy (Combined linearity, hysteresis, repeatability)	0	$\pm 0.25\%$ FS (mv/V)	95
E2	Setting Zero Offset and Span	0	$\pm 2\%$ FS (mv/V)	95
E3	Total Error band	0	$\pm 2\%$ FS (mv/V)	95
S	Sensitivity	9.974 mV/V		
V_{ex}	Applied Excitation Voltage	10 V		95

Sensitivity - influence coefficient

Pressure(P) :m* Voltage(V) [calibration equation]

Equation from calibrated sensor P:150.37* V

$$P_v = \frac{\partial P}{\partial V} = 150.37$$

Uncertainty due to error is computed using Equation (49) discussed in section 3.10.1

$$\text{Uncertainty due to Accuracy (E1): } \frac{0.125}{1.9600} = 0.0638V$$

$$\text{Uncertainty due to Setting Zero Offset and Span (E2): } \frac{0.1}{1.9600} = 0.051V$$

$$\text{Uncertainty due to Total error band (E3): } \frac{0.1}{1.9600} = 0.051V$$

The total uncertainty model is given by Equation (55)

$$u = \sqrt{\text{var}(c_x \cdot \varepsilon_x + c_y \cdot \varepsilon_y + c_z \cdot \varepsilon_z)} \quad (55)$$

Where u is the total uncertainty, c_x, c_y, c_z are sensitivity coefficients and $\varepsilon_x, \varepsilon_y, \varepsilon_z$ are uncertainty due to a errors in the system. There exists no correlation between error sources within the pressure sensor. The uncertainty model is re-written

$$u = \sqrt{c_x^2 \cdot \varepsilon_x^2 + c_y^2 \cdot \varepsilon_y^2 + c_z^2 \cdot \varepsilon_z^2}$$

$$u = \sqrt{(0.0638)^2 + (0.051)^2 + (0.051)^2} = 0.0963 \text{ V}$$

The pressure sensor's combined error is converted *mmHg* to compute the error values at different sections, thereby establishing the true pressure value. Figure 149 shows the mean IVC pressure values for the various MFL parameters tested.

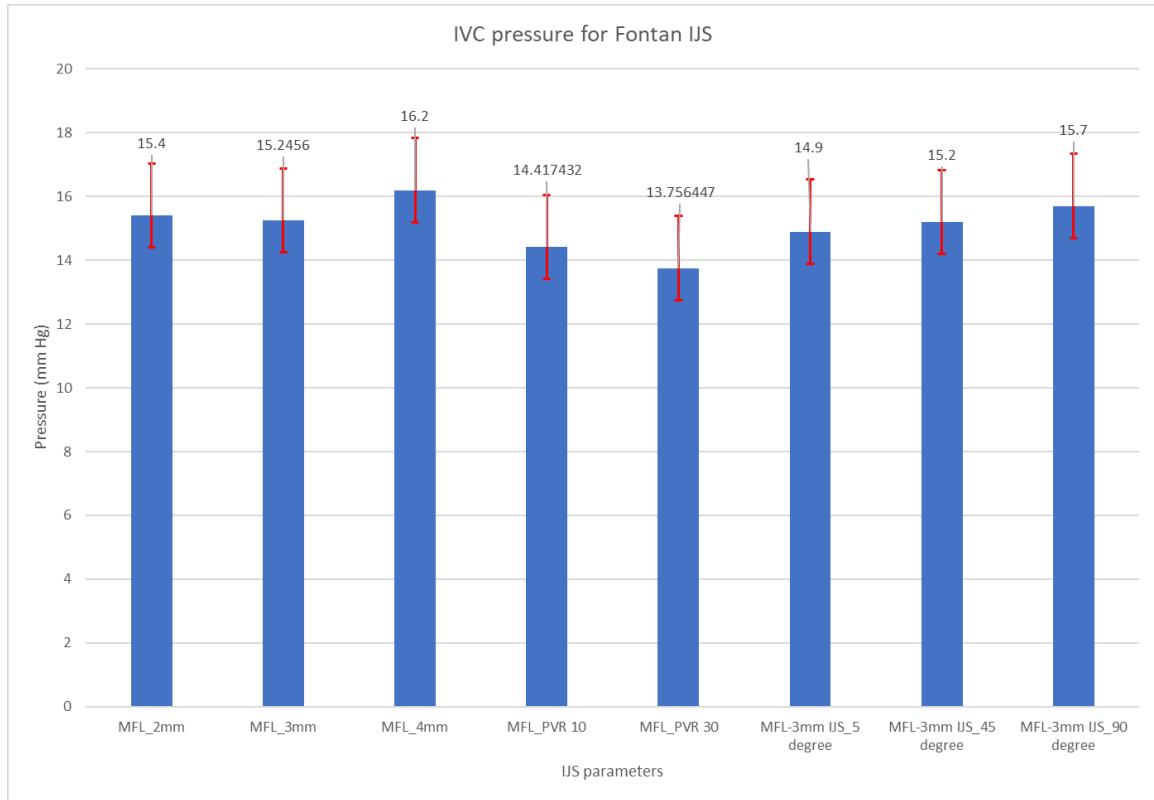


Figure 149 IVC mean pressure value with the error band

5. Conclusion

Overall, through this research work, the implementation of experimental methodologies has been demonstrated to quantify and qualify the detailed hemodynamics of two novel surgical techniques, i.e., HCSII and the self-powered Fontan circulation. These in-vitro investigations allowed us to determine the potential presence of any pathological flow fields and estimate the efficacy of tools implemented to improve patient care.

A multiscale model of the HCSII circulation is designed and developed. In this study, the MFL experimentally quantifies the stented baffle deformation over periodic cardiac cycles. The in-situ observation of the stented baffle deformation shows that the stent placed in the PA conduit goes for a minimal deformation for each heart cycle. Fatigue analysis on this stent deformation proves that the stent will not fail under the pulsatile loading condition produced due to the systemic circulation at the MPA site. Hence the pulmonary artery will remain unobstructed. Experimental particle residence time analyses elucidate that there is a minimal chance for the occurrence of any pathological flow and the probability of thrombus formation in this reconstructed physiology is very low.

Secondly, another multi-scale model of the Fontan circulation has been constructed. The MFL used in this study experimentally simulates the effect of the IJS implementation in the TCPC. The MFL setup is also calibrated to simulate the PVR effect. This in-vitro model

combines the 0-D scale of the patient's circulation in the LPM with a 3-D centerpiece physiological representative TCPC model. Various patient generic TCPC models and IJS prototypes have been developed using stereolithography technology. The outcome of these experimentations has successfully satisfied the hypothesis as established in the objective of the study. A parametric study on IJS nozzle diameter, IJS anastomosis angles, and PVR effect have been conducted in these experiments. The comparative study on the IJS nozzle shows that the 3mm nozzle is the most efficient for entraining the flow in the PAs. The IJS anastomosis angle study shows that the IJS nozzle can entrain better in the PAs as the angle becomes shallower. Finally, by incorporating the PVR effect along with the 3mm IJS nozzle, the desired pressure drop of 5mmHg is achieved. While conducting these experiments, as the IJS nozzles are introduced to the flow field, pulsatility in the PAs has been increased, and comparatively, high-frequency noise is introduced. This high-frequency noise is filtered by conducting spectral analysis. Few benefits of the IJS include:

- Increased Pulmonary flow Q_p
- Increased systemic oxygen
- Lesser pathological flow in TCPC

Thirdly, another in-vitro analysis is conducted to experimentally quantify the change in the hemodynamics of a sick Fontan while performing the PVR protocols as provided by our clinical collaborators from Arnold Palmer Hospital for Children. The outcome of the PVR injection study is twofold. The preliminary in-vitro analyses show that PVR injections do not elevate the PA pressure beyond any critical threshold. For all long and short bursts of injections, no pathological flows have been observed in the systemic, pulmonary, and TCPC sections. These analyses infer that in-vivo trials will be clinically safe to perform on

patient subsets. The entrainment study quantitatively shows that the degree of entrainment varies with the long and short burst of injections. Jet relaxation time provides a good insight into the IJS dynamics.

6. Recommendations and Future Work

This research has successfully demonstrated the capabilities of various types of in-vitro setups that can be used to investigate and validate in-silico and in-vivo results. However, there are certain limitations to this study. Few of these limitations can be overcome in future work. Both MFL setups do not have any feedback mechanism, which is especially important for conducting investigations like self-powered Fontan circulation. We aim to couple a fully automated Hardware in the Loop-based Harvard apparatus pump with the MFL loops in our future work. This modification will incorporate some amount of autoregulatory feedback mechanism in the MFL setups.

In HCSII circulation research project, currently, only a particle diameter of 2mm has been injected. In the future, different size particles should be injected into the MPA conduit to complete the PRT studies.

The proof of concept study on Fontan will help us to proceed to more complex models. The 3-D phantoms should be made of a compliant material to validate the fluid-structure interaction studies. Also, particle image velocimetry capabilities should be incorporated into MFL setups.

7. References

- [1] M. D. J. C. Mary Ann Clark, Biology 2e.
Available:<https://openstax.org/books/biology-2e/pages/1-introduction>, Houston, Texas: OpenStax, 2018.
- [2] D. Chang, "Wikimedia Commons," [Online].
- [3] D. Timms, M. Hayne, K. McNeil and A. Galbraith, "A complete mock circulation loop for the evaluation of left, right, and biventricular assist devices," *Artificial Organs*, vol. 29, no. 7, pp. 564-572, 2005.
- [4] R. Seeley, T. Stephens and P. Tate, Anatomy and Physiology 6th Edition, New York: McGraw-Hill Companies Inc., 2003.
- [5] R. E. Klabunde, Cardiovascular Physiology Concepts, Baltimore: Lippincott Williams & Wilkins, 2004.
- [6] W.G. MEMBERS, M. Blaha, S. Chiuve, S. Chiuve, M. Cushman, S. Das, R. Deo, S. de Ferranti, J. Floyd and M. Fornage, "Heart disease and stroke statistics-2017 update:135 (2017) e146.," a report from the American Heart Association, 2017.
- [7] M. Lev, "Pathologic anatomy and interrelationship of the hypoplasia of the aortic tract complex," *Lab Invest*, vol. 1, pp. 61-70, 1952.
- [8] J. A. Connor and R. Thiagarajan, "Hypoplastic left heart syndrome," *Orphanet journal of rare diseases*, vol. 2, no. 23, pp. 1-5, 2007.

- [9] . J. A. Quintessenza, . V. O. Morell and J. P. Jacobs, "Achieving a balance in the current approach to the surgical treatment of hypoplastic left heart syndrome," *Cardiology in the Young*, vol. 14, no. S1, pp. 127-130, 2004.
- [10] J. Atallah, I. Dinu, A. Joeffe, C. Robertson, R. Sauuve, J. Dyck and I. Rebeyka , "tWestern Canadian Complex Pediatric Therapies Follow-Up Group. Two-year survival and mental and psychomotor outcomes after the Norwood procedure: an analysis of the modified Blalock-Taussig shunt and right ventricle-to-pulmonary artery shunt surgical eras," *Circulation*, vol. 118, no. 14, pp. 1410-1418, 2008.
- [11] W. Norwood, P. Lang, A. Castaneda and D. Campbell, "Experience with operations for hypoplastic left heart syndrome," *The Journal of thoracic and cardiovascular surgery*, vol. 82, no. 4, pp. 511-519, 1981.
- [12] W. Glenn, N. Ordway, N. Talner and E. Call Jr., "Circulatory Bypass of the Right Side of the Heart: VI. Shunt between Superior Vena Cava and Distal Right Pulmonary Artery; Report of Clinical Application in Thirty-eight Cases," *Circulation*, vol. 31, pp. 172-189, 1965.
- [13] A. Blalock and H. Taussig, "The surgical treatment of malformations of the heart: in which there is pulmonary stenosis or pulmonary atresia. ," *Journal of the American Medical Association*, vol. 128, no. 3, pp. 189-202, 1945.
- [14] P. Karpawich, C. Bush, J. Antillon, J. Amato, M. Marbey and K. Agarwal, "Modified Blalock-Taussig shunt in infants and young children: Clinical and catheterization assessment.," *The Journal of thoracic and cardiovascular surgery*, vol. 89, no. 2, pp. 275-279, 1985.

- [15] A. Azakie, S. Merklinger , B. McCrindle, G. Van Arsdell, K. Lee, L. Benson and W. Williams , "Evolving strategies and improving outcomes of the modified Norwood procedure: a 10-year single-institution experience.," *The annals of thoracic surgery*, vol. 72, no. 4, pp. 1349-1353, 2001.
- [16] S. Sano, K. Ishino , M. Kawada, S. Arai, S. Kasahara, T. Asai and S. Ohtsuki, "Right ventricle–pulmonary artery shunt in first-stage palliation of hypoplastic left heart syndrome," *The journal of thoracic and cardiovascular surgery*, vol. 126, no. 2, pp. 504-509, 2003.
- [17] W. Norwood, P. Lang and D. Hansen, "Physiologic repair of aortic atresia–hypoplastic left heart syndrome," *New England Journal of Medicine*, vol. 308, no. 1, pp. 23-26, 1983.
- [18] W. Mahle, T. Spray , G. Wernovsky, J. Gaynor and B. Clark III, "Survival after reconstructive surgery for hypoplastic left heart syndrome: a 15-year experience from a single institution. ," *Circulation*, vol. 102, no. suppl_3, pp. 136-141, 2000.
- [19] N. De Oliveira, D. Ashburn, F. Khalid, H. Burkhardt, I. Adatia, H. Holtby and G. Van Arsdell, "Prevention of early sudden circulatory collapse after the Norwood operation.," *Circulation*, vol. 110, no. 11_suppl_1, pp. 133-138, 2004.
- [20] C. Stasik, C. Goldberg , E. Bove, E. Devaney and R. Ohye, "Current outcomes and risk factors for the Norwood procedure," *The Journal of thoracic and cardiovascular surgery*, vol. 131, no. 2, pp. 412-417, 2006.

- [21] C. Caldarone, L. Benson , H. Holtby, J. Li , A. Redington and G. Van Arsdell, "Initial experience with hybrid palliation for neonates with single-ventricle physiology," *The annals of thoracic surgery*, vol. 84, no. 4, pp. 1294-1300, 2007.
- [22] M. Galantowicz and J. Cheatham, "Lessons learned from the development of a new hybrid strategy for the management of hypoplastic left heart syndrome," *Pediatric cardiology*, vol. 26, no. 2, pp. 190-199, 2005.
- [23] H. Akintuerk, I. Michel-Behnke , K. Valeske, M. Mueller, J. Thul , J. Bauer and D. Schranz, "Stenting of the arterial duct and banding of the pulmonary arteries: basis for combined Norwood stage I and II repair in hypoplastic left heart.," *Circulation*, vol. 105, no. 9, pp. 1099-1103, 2002.
- [24] E. Bacha, S. Daves, J. Hardin, R. Abdulla, J. Anderson, M. Kahana and Z. Hijaz, "Single-ventricle palliation for high-risk neonates: the emergence of an alternative hybrid stage I strategy," *The Journal of thoracic and cardiovascular surgery*, vol. 131, no. 1, pp. 163-171, 2006.
- [25] M. Galantowicz and A. Yates, "Improved outcomes with the comprehensive stage 2 procedure after an initial hybrid stage 1,," *The Journal of thoracic and cardiovascular surgery*, vol. 151, pp. 424-429, 2016.
- [26] J. Gibbs, C. Wren, K. Watterson, S. Hunter and J. Hamilton, "Stenting of the arterial duct combined with banding of the pulmonary arteries and atrial septectomy or septostomy: a new approach to palliation for the hypoplastic left heart syndrome," *Heart*, vol. 69, no. 6, pp. 551-555, 1993.

- [27] C. Ruiz, H. Gamra, H. Zhang, E. Garcia and M. Boucek, "Stenting of the ductus arteriosus as a bridge to cardiac transplantation in infants with the hypoplastic left-heart syndrome," *New England Journal of Medicine*, vol. 328, no. 22, pp. 1605-1608, 1993.
- [28] M. Mitchell , D. Campbell, M. Boucek, H. Sondheimer, K. Chan , D. Ivy and T. Mackenzie , "Mechanical limitation of pulmonary blood flow facilitates heart transplantation in older infants with hypoplastic left heart syndrome," *European journal of cardio-thoracic surgery*, vol. 23, no. 5, pp. 735-742, 2003.
- [29] M. Galantowicz, J. Cheatham, A. Phillips, C. Cua, T. Hoffman, S. Hill and R. Rodeman, "Hybrid approach for hypoplastic left heart syndrome: intermediate results after the learning curve," *The annals of thoracic surgery*, vol. 85, no. 6, pp. 2063-2071, 2008.
- [30] C. Caldarone, O. Honjo, L. Benson and G. Van Arsdell, "Modification of stage II procedure after hybrid palliation (bilateral pulmonary artery banding and ductal stenting) for hypoplastic left-sided heart syndrome: modified arch reconstruction with retained stented ductus patch," *Journal of thoracic and cardiovascular surgery*, vol. 134, no. 6, pp. 1588-1589, 2007.
- [31] O. Honjo and C. Caldarone, "Hybrid palliation for neonates with hypoplastic left heart syndrome: current strategies and outcomes," *Korean circulation journal*, vol. 40, no. 3, pp. 103-111, 2010.
- [32] O. Honjo, L. Benson, H. Mewhort, D. Predescu, H. Holtby, G. Van Arsdell and C. Caldarone, "Clinical outcomes, program evolution, and pulmonary artery growth

- in single ventricle palliation using hybrid and Norwood palliative strategies," *The annals of thoracic surgery*, vol. 87, no. 6, pp. 1885-1893, 2009.
- [33] H. Van de WAl, R. Ouknine, D. Tamisier , M. Levy, P. Vouhe and F. Leca, "Bi-directional cavopulmonary shunt: is accessory pulsatile flow, good or bad?," *European journal of cardio-thoracic surgery*, vol. 16, no. 2, pp. 104-110, 1999.
- [34] D. McElhinney, S. Marianeschi and V. Reddy, "Additional pulmonary blood flow with the bidirectional Glenn anastomosis: does it make a difference? ," *The annals of thoracic surgery*, vol. 66, no. 2, pp. 668-672, 1998.
- [35] R. Mainwaring, J. Lamberti, K. Uzark, R. Spicer, M. Cocalis and J. Moore, "Effect of accessory pulmonary blood flow on survival after the bidirectional Glenn procedure. ," *Circulation*, vol. 100, no. suppl_2, pp. 151-156, 1999.
- [36] F. Gervaso, S. Kull, G. Pennati, F. Migliavacca, G. Dubini and V. Luisi , "The effect of the position of an additional systemic-to-pulmonary shunt on the fluid dynamics of the bidirectional cavo-pulmonary anastomosis ," *Cardiology in the Young*, vol. 14, no. S3, pp. 38-43, 2004.
- [37] L. Ma, Y. Liu , X. Zhao, X. Ren, F. Bai, J. Ding and H. Han, "Hemodynamic influence of different pulmonary stenosis degree in Glenn procedure: a numerical study, 6, 472370.," *Advances in Mechanical Engineering*, vol. 6, pp. 1-10, 2014.
- [38] M. Esmaily Moghadam, F. Migliavacca, I. Vignon-Clementel, T. Hsia, A. Marsden and MOCHA Investigators, "Optimization of shunt placement for the Norwood surgery using multi-domain modeling," *Journal of biomechanical engineering*, vol. 134, no. 5, pp. 051002-0510014, 2012.

- [39] F. Migliavacca, R. Balossino, G. Pennati, G. Dubini, T. Hsia, M. de Leval and E. Bove, "Multiscale modelling in biofluidynamics: application to reconstructive paediatric cardiac surgery," *Journal of biomechanics*, vol. 39, no. 6, pp. 1010-1020, 2006.
- [40] K. Sunagawa, W. Maughan, D. Burkhoff and K. I. I. C. H. I. Sagawa, "Left ventricular interaction with arterial load studied in isolated canine ventricle ," *American Journal of Physiology-Heart and Circulatory Physiology*, vol. 245, no. 5, pp. H773-H780, 1983.
- [41] K. Sunagawa, W. Maughan and K. Sagawa, "Optimal arterial resistance for the maximal stroke work studied in isolated canine left ventricle," *Circulation research*, vol. 56, no. 4, pp. 586-595, 1985.
- [42] R. Kelly, C. Ting, T. Yang, C. Liu, W. Maughan, M. Chang and D. Kass, "Effective arterial elastance as index of arterial vascular load in humans," *Circulation*, vol. 86, no. 2, pp. 513-521, 1992.
- [43] R. Torii, N. Wood, A. Hughes, S. Thom , J. Aguado-Sierra, J. Davies and X. Xu, "A computational study on the influence of catheter-delivered intravascular probes on blood flow in a coronary artery model," *Journal of biomechanics*, vol. 40, no. 11, pp. 2501-2509, 2007.
- [44] J. Li, Dynamics of the vascular system , Singapore : World Scientific, 2004.
- [45] R. Nerem, W. Seed and N. Wood, "An experimental study of the velocity distribution and transition to turbulence in the aorta," *Journal of Fluid Mechanics*, vol. 52, no. 1, pp. 137-160, 1972.

- [46] D. de Zélicourt, K. Pekkan, J. Parks, K. Kanter, M. Fogel and A. Yoganathan, "Flow study of an extracardiac connection with persistent left superior vena cava," *The Journal of Thoracic and Cardiovascular Surgery*, vol. 131, no. 4, pp. 785-791, 2006.
- [47] C. Corsini, C. Baker, A. Baretta, G. Biglino, A. Hlavacek, T. Hsia and G. Pennati, "Integration of clinical data collected at different times for virtual surgery in single ventricle patients: a case study," *Annals of biomedical engineering*, vol. 43, no. 6, pp. 1310-1320, 2015.
- [48] A. Magee, B. McCrindle, J. Mawson, L. Benson, W. Williams and R. Freedom, "Systemic venous collateral development after the bidirectional cavopulmonary anastomosis: prevalence and predictors," *Journal of the American College of Cardiology*, vol. 32, no. 2, pp. 502-508, 1998.
- [49] D. McElhinney, V. Reddy, F. Hanley and P. Moore, "Systemic venous collateral channels causing desaturation after bidirectional cavopulmonary anastomosis: evaluation and management," *Journal of the American College of Cardiology*, vol. 30, no. 3, pp. 817-824, 1997.
- [50] E. Kung, B. A., C. Baker, G. Arbia, G. Biglino, C. Corsini and M. O. C. H. A. (. Investigators, "Predictive modeling of the virtual Hemi-Fontan operation for second stage single ventricle palliation: two patient-specific cases," *Journal of biomechanics*, vol. 46, no. 2, pp. 423-429, 2013.
- [51] C. Corsini, C. Baker, E. Kung, S. Schievano, G. Arbia, A. Baretta and A. Dorfman, "An integrated approach to patient-specific predictive modeling for

- single ventricle heart palliation," *Computer methods in biomechanics and biomedical engineering*, vol. 17, no. 14, pp. 1572-1589, 2014.
- [52] A. Baretta, C. Corsini, W. Yang, I. Vignon-Clementel, A. Marsden, J. Feinstein and M. o. C. H. A. (. Investigators, "Virtual surgeries in patients with congenital heart disease: a multi-scale modelling test case," *Philosophical Transactions of the Royal Society A: Mathematical, Physical and Engineering Sciences*, vol. 369, no. 1954, pp. 4316-4330, 2011.
- [53] J. Coppoletta and S. B. Wolbach, "Body length and organ weights of infants and children: a study of the body length and normal weights of the more important vital organs of the body between birth and twelve years of age," *The American journal of pathology*, vol. 9, no. 1, pp. 55-70, 1933.
- [54] G. Pennati and R. Fumero, "Scaling approach to study the changes through the gestation of human fetal cardiac and circulatory behaviors," *Annals of biomedical engineering*, vol. 28, no. 4, pp. 442-452, 2000.
- [55] M. Li, D. Scott, R. Shandas, K. Stenmark and W. Tan, "High pulsatility flow induces adhesion molecule and cytokine mRNA expression in distal pulmonary artery endothelial cells," *Annals of biomedical engineering*, vol. 37, no. 6, pp. 1082-1092, 2009.
- [56] J. Zhou, M. Esmaily-Moghadam, T. Conover, T. Hsia, A. Marsden and R. Figliola, "In vitro assessment of the assisted bidirectional Glenn procedure for stage one single ventricle repair," *Cardiovascular engineering and technology*, vol. 6, no. 3, pp. 256-267, 2015.

- [57] M. Esmaily-Moghadam, T. Hsia, A. Marsden and MOCHA Investigators , "The assisted bidirectional Glenn: a novel surgical approach for first-stage single-ventricle heart palliation," *The Journal of thoracic and cardiovascular surgery*,, vol. 149, no. 3, pp. 699-705, 2015.
- [58] K. Lagana, R. Balossino, F. Migliavacca, G. Pennati, E. Bove, M. de Leval and G. Dubini, "Multiscale modeling of the cardiovascular system: application to the study of pulmonary and coronary perfusions in the univentricular circulation.," *Journal of biomechanics*, vol. 38, no. 5, pp. 1129-1141, 2005.
- [59] G. Biglino, A. Giardini, C. Baker, R. Figliola, T. Hsia, A. Taylor and S. Schievano, "In vitro study of the Norwood palliation: a patient-specific mock circulatory system.," *ASAIO journal*, vol. 58, no. 1, pp. 25-31, 2012.
- [60] M. Moghadam, I. Vignon-Clementel, R. Figliola, A. Marsden and a. M. investigators, "A modular numerical method for implicit 0D/3D coupling in cardiovascular finite element simulations," *Journal of Computational Physics*, vol. 244, pp. 63-79, 2013.
- [61] T. Hsia, D. Cosentino, C. Corsini, G. Pennati, G. Dubini, F. Migliavacca and a. M. investigators, "Use of mathematical modeling to compare and predict hemodynamic effects between hybrid and surgical Norwood palliations for hypoplastic left heart syndrome," *Circulation*, vol. 124, no. 11_suppl_1, pp. 204-210, 2011.
- [62] M. Vukicevic, J. Chiulli, T. Conover, G. Pennati, T. Hsia, R. Figliola and a. M. investigators, "Mock circulatory system of the Fontan circulation to study

- respiration effects on venous flow behavior," *ASAIO Journal (American Society for Artificial Internal Organs)*, vol. 59, p. 253, 2013.
- [63] R. Naeije, "Pulmonary vascular resistance," *Intensive care medical*, vol. 29, no. 4, pp. 526-529, 2003.
- [64] I. Schulze-Neick, J. Li, D. Penny and A. Redington, "Pulmonary vascular resistance after cardiopulmonary bypass in infants: effect on postoperative recovery," *The Journal of Thoracic and Cardiovascular surgery*, vol. 121, no. 6, pp. 1033-1039, 2001.
- [65] E. Kung and C. Taylor , "Development of a physical Windkessel module to recreate in vivo vascular flow impedance for in vitro experiments," *Cardiovascular engineering and technology*, vol. 2, no. 1, pp. 2-14, 2011.
- [66] M. Frommelt, P. Frommelt, S. Berger, A. Pelech, D. Lewis, J. Tweddell and S. Litwin, "Does an additional source of pulmonary blood flow alter outcome after a bidirectional cavopulmonary shunt?," *Circulation*, vol. 92, no. 9, pp. 240-244, 1995.
- [67] M. Yoshida, M. Yamaguchi, Yoshimura and Murakami, "Appropriate additional pulmonary blood flow at the bidirectional Glenn procedure is useful for completion of total cavopulmonary connection," *The annals of thoracic surgery*, vol. 80, no. 3, pp. 976-981, 2005.
- [68] Migliavacca, Pennati, Dubini, Fumero and Pietrabissa, "Modeling of the Norwood circulation: effects of shunt size, vascular resistances, and heart rate," *American Journal of Physiology Heart and Cicrulatory Physiology*, vol. 280, no. 5, 2001.

- [69] Spilker , Feinstein, Parker and Reddy, "Morphometry-based impedance boundary conditions for patient-specific modeling of blood flow in pulmonary arteries," *Annals of Biomedical Engineering*, pp. 546-559, 2007.
- [70] Troianowski, Taylor, Feinstein and Vignon-Clementel, "Three-dimensional simulations in Glenn patients:clinically based boundary conditions,hemodynamic results and sensitivity to input data," *Journal of Biomedical Engineering* , vol. 133, pp. 111006-111022, 2011.
- [71] Noordergraaf and Verdouw, "The use of analog computer in a circulation model," *Progress in Cardiovascular diseases*, vol. 5, no. 5, pp. 419-439, 1963.
- [72] Snyder, Rideout and Hillestad, "Computer modeling of the human systemic arterial tree," *Journals of Biomechanics*, vol. 1, no. 4, pp. 341-353, 1968.
- [73] Snyder and RIdout, "Computer simulation studies of the venous circulation," *IEEE transaction on Biomedical Engineering* q, pp. 325-334, 1969.
- [74] K. Berg, W. Berg and Graham, "CFD in the evaluation of hemodyanmic performance of cavopulmonary connections after the Norwood," *Psychophysiology*, vol. 8, no. 1, pp. 30-44.
- [75] Bove, de Leval, Migliavacca and Guadagni, "Computational fluid dynamics in the evaluation of hemodynamic performance of cavopulmonary connections after the norwood procedure for hypoplastic left heart syndrome," *The Journal of Thoracic and Cardiovascular*, vol. 126, no. 4, p. 2003.

- [76] Pekkan, Dasi and Sundareswaran, "Hemodynamic Performance of Stage-2 Univentricular Reconstruction," *Annals of Biomedical Engineering* , vol. 37, pp. 50-63.
- [77] Brown, Leverett, Lewis and Alfrey, "Morphological, biochemical, and functional changes in human platelets subjected to shear stress,," *The Journal of lab and clinical medicine*.
- [78] Whitehead, Pekkan, Kitajima and Paridon, "Nonlinear power loss during exercise in single-ventricle patients after the Fontan: insights from computational fluid dynamics," *Circulation*, pp. 165-171, 2007.
- [79] Marsden, Vignon-Clementel and Chan, "Effects of exercise and respiration on hemodynamic efficiency in CFD simulations of the total cavopulmonary connection," *Annals of biomedical engineering*, vol. 35, 2007.
- [80] D. E. Schiavazzi, E. O. Kung, A. L. Marsden, C. Baker, G. Pennati, T.-Y. Hsia, A. Hlavacek, A. L. Dorfman, M. of Congenital Hearts Alliance (MOCHA) Investigators and others, "Hemodynamic effects of left pulmonary artery stenosis after superior cavopulmonary connection: a patient-specific multiscale modeling study," *The Journal of thoracic and cardiovascular surgery*, vol. 149, p. 689–696, 2015.
- [81] J. M. Forbess, N. Cook, A. Serraf, R. P. Burke, J. E. Mayer and R. A. Jonas, "An institutional experience with second-and third-stage palliative procedures for hypoplastic left heart syndrome: the impact of the bidirectional cavopulmonary shunt," *Journal of the American College of Cardiology*, vol. 29, p. 665–670, 1997.

- [82] E. L. Bove, "Surgical treatment for hypoplastic left heart syndrome," *The Japanese Journal of Thoracic and Cardiovascular Surgery*, vol. 47, p. 47–56, 1999.
- [83] D. P. Bichell, J. J. Lamberti, G. J. Pelletier, C. Hoecker, M. W. Cocalis, F. F. Ing and R. A. Jensen, "Late left pulmonary artery stenosis after the Norwood procedure is prevented by a modification in shunt construction," *The Annals of thoracic surgery*, vol. 79, p. 1656–1660, 2005.
- [84] A. Azakie, B. W. McCrindle, L. N. Benson, G. S. Van Arsdell, J. L. Russell, J. G. Coles, D. Nykanen, R. M. Freedom and W. G. Williams, "Total cavopulmonary connections in children with a previous Norwood procedure," *The Annals of thoracic surgery*, vol. 71, p. 1541–1546, 2001.
- [85] J. W. Moore, R. L. Spicer, J. C. Perry, J. W. Mathewson, S. E. Kirkpatrick, L. George, K. Uzark, R. L. Mainwaring and J. J. Lamberti, "Percutaneous use of stents to correct pulmonary artery stenosis in young children after cavopulmonary anastomosis," *American heart journal*, vol. 130, p. 1245–1249, 1995.
- [86] R. H. Franch and B. B. Gay Jr, "Congenital stenosis of the pulmonary artery branches: a classification, with postmortem findings in two cases," *The American journal of medicine*, vol. 35, p. 512–529, 1963.
- [87] H. S. Weber and J. L. Myers, "Association of asymmetric pulmonary artery growth following palliative surgery for hypoplastic left heart syndrome with ductal coarctation, neo-aortic arch compression, and shunt-induced pulmonary artery stenosis," *American Journal of Cardiology*, vol. 91, p. 1503–1506, 2003.

- [88] G. Biglino, A. Giardini, H. N. Ntsinjana, S. Schievano, T.-Y. Hsia, A. M. Taylor, M. of Congenital Hearts Alliance Collaborative Group and others, "Ventriculoarterial coupling in palliated hypoplastic left heart syndrome: noninvasive assessment of the effects of surgical arch reconstruction and shunt type," *The Journal of thoracic and cardiovascular surgery*, vol. 148, p. 1526–1533, 2014.
- [89] M. Szopos, N. Poussineau, Y. Maday, C. Canniffe, D. S. Celermajer, D. Bonnet and P. Ou, "Computational modeling of blood flow in the aorta—insights into eccentric dilatation of the ascending aorta after surgery for coarctation," *The Journal of thoracic and cardiovascular surgery*, vol. 148, p. 1572–1582, 2014.
- [90] S. Schievano, F. Migliavacca, L. Coats, S. Khambadkone, M. Carminati, N. Wilson, J. E. Deanfield, P. Bonhoeffer and A. M. Taylor, "Percutaneous pulmonary valve implantation based on rapid prototyping of right ventricular outflow tract and pulmonary trunk from MR data," *Radiology*, vol. 242, p. 490–497, 2007.
- [91] C. E. Baker, C. Corsini, D. Cosentino, G. Dubini, G. Pennati, F. Migliavacca, T.-Y. Hsia, M. of Congenital Hearts Alliance (MOCHA) Investigators and others, "Effects of pulmonary artery banding and retrograde aortic arch obstruction on the hybrid palliation of hypoplastic left heart syndrome," *The Journal of thoracic and cardiovascular surgery*, vol. 146, p. 1341–1348, 2013.

- [92] C. A. Taylor, T. J. R. Hughes and C. K. Zarins, "Finite element modeling of blood flow in arteries," *Computer methods in applied mechanics and engineering*, vol. 158, p. 155–196, 1998.
- [93] L. A. Taber, "Biomechanics of growth, remodeling, and morphogenesis," *Applied Mechanics Reviews*, 1995.
- [94] G. Agnoletti, Y. Boudjemline, D. Bonnet, D. Sidi and P. Vouhe, "Surgical reconstruction of occluded pulmonary arteries in patients with congenital heart disease: effects on pulmonary artery growth," *Circulation*, vol. 109, p. 2314–2318, 2004.
- [95] W. Glenn, M. Browne and Whittemore, R, "Circulatory bypass of the right side of the heart: cava-pulmonary artery shunt—indications and results (report of a collected series of 537 cases)," *The heart and circulation in the newborn and infant*, pp. 345-357, 1966.
- [96] W. Glen, "Circulatory bypass of the right side of the heart. IV. Shunt between superior vena cava and distal right pulmonary artery; report of clinical application," *The New England Journal of Medicine*, vol. 259, no. 3, pp. 117-120, 1958.
- [97] W. Glenn and J. Patino, "Circulatory by-pass of the right heart. I. Preliminary observations on the direct delivery of vena caval blood into the pulmonary arterial circulation. Azygos vein-pulmonary artery shunt," *The Yale journal of biology and medicine*, vol. 27, no. 3, pp. 147-151, 1954.

- [98] S. Nuland, W. Glenn and P. Guilfoil, "Circulatory bypass of the right heart. III. Some observations on long-term survivors," *Surgery*, vol. 43, no. 2, pp. 184-201, 1958.
- [99] E. Bove, F. Migliavacca, M. de Leval, R. Balossino, G. Pennati, T. Lloyd and G. Dubini, "Use of mathematic modeling to compare and predict hemodynamic effects of the modified Blalock–Taussig and right ventricle–pulmonary artery shunts for hypoplastic left heart syndrome.," *The Journal of thoracic and cardiovascular surgery*, vol. 136, no. 2, pp. 312-320, 2008.
- [100] M. Esmaily-Moghadam, B. Murtuza, T. Hsia and A. Marsden, "Simulations reveal adverse hemodynamics in patients with multiple systemic to pulmonary shunts," *Journal of biomechanical engineering*, vol. 137, no. 3, pp. 031001-031012, 2015.
- [101] G. Arbia, C. Corsini, M. E. Moghadam, A. L. Marsden, F. Migliavacca, G. Pennati, T.-Y. Hsia, I. E. Vignon-Clementel, M. O. C. H. A. (. Investigators and others, "Numerical blood flow simulation in surgical corrections: what do we need for an accurate analysis?," *journal of surgical research*, vol. 186, p. 44–55, 2014.
- [102] J. J. Yeung, H. J. Kim, T. A. Abbruzzese, I. E. Vignon-Clementel, M. T. Draney-Blomme, K. K. Yeung, I. Perakash, R. J. Herfkens, C. A. Taylor and R. L. Dalman, "Aortoiliac hemodynamic and morphologic adaptation to chronic spinal cord injury," *Journal of vascular surgery*, vol. 44, p. 1254–1265, 2006.
- [103] J. F. Jr. LaDisa, R. J. Dholakia, C. A. Figueroa, I. E. Vignon-Clementel, F. P. Chan, M. M. Samyn, J. R. Cava, C. A. Taylor and J. A. Feinstein, "Computational simulations demonstrate altered wall shear stress in aortic coarctation patients

- treated by resection with end-to-end anastomosis," *Congenital heart disease*, vol. 6, p. 432–443, 2011.
- [104] R. Torii and M. Oshima, "An integrated geometric modelling framework for patient-specific computational haemodynamic study on wide-ranged vascular network," *Computer methods in biomechanics and biomedical engineering*, vol. 15, p. 615–625, 2012.
- [105] I. E. Vignon-Clementel, A. L. Marsden and J. A. Feinstein, "A primer on computational simulation in congenital heart disease for the clinician," *Progress in Pediatric Cardiology*, vol. 30, p. 3–13, 2010.
- [106] W. Yang, I. E. Vignon-Clementel, G. Troianowski, V. M. Reddy, J. A. Feinstein and A. L. Marsden, "Hepatic blood flow distribution and performance in conventional and novel Y-graft Fontan geometries: a case series computational fluid dynamics study," *The Journal of thoracic and cardiovascular surgery*, vol. 143, p. 1086–1097, 2012.
- [107] H. G. Morales, M. Kim, E. E. Vivas, M.-C. Villa-Uriol, I. Larrabide, T. Sola, L. Guimaraens and A. F. Frangi, "How do coil configuration and packing density influence intra-aneurysmal hemodynamics?," *American Journal of Neuroradiology*, vol. 32, p. 1935–1941, 2011.
- [108] A. Prasad, L. K. To, M. L. Gorrepati, C. K. Zarins and C. A. Figueroa, "Computational analysis of stresses acting on intermodular junctions in thoracic aortic endografts," *Journal of Endovascular Therapy*, vol. 18, p. 559–568, 2011.

- [109] S. Pant, G. Limbert, N. P. Curzen and N. W. Bressloff, "Multiobjective design optimisation of coronary stents," *Biomaterials*, vol. 32, p. 7755–7773, 2011.
- [110] W. Yang, J. A. Feinstein, S. C. Shadden, I. E. Vignon-Clementel and A. L. Marsden, "Optimization of a Y-graft design for improved hepatic flow distribution in the Fontan circulation," *Journal of biomechanical engineering*, vol. 135, 2013.
- [111] P. Gresho and R. Sani, *Incompressible flow and the finite element method*, New York: Wiley & Sons, 2000.
- [112] R. Eymard, T. Gallouët and R. Herbin, "Finite volume methods," *Handbook of numerical analysis*, vol. 7, p. 713–1018, 2000.
- [113] W. M. DeCampi, C. E. Fleishman and D. G. Nykanen, "Hybrid approach to the comprehensive stage II operation in a subset of single-ventricle variants," *The Journal of thoracic and cardiovascular surgery*, vol. 149, p. 1095–1100, 2015.
- [114] A. A. Brescia, S. Jureidini, S. Danon, E. Armbrecht, A. C. Fiore and C. B. Huddleston, "Hybrid versus Norwood procedure for hypoplastic left heart syndrome: contemporary series from a single center," *The Journal of thoracic and cardiovascular surgery*, vol. 147, p. 1777–1782, 2014.
- [115] W. Knirsch, S. Bertholdt, G. Stoffel, B. Stiasny, R. Weber, H. Dave, R. Prêtre, M. von Rhein and O. Kretschmar, "Clinical course and interstage monitoring after the Norwood and hybrid procedures for hypoplastic left heart syndrome," *Pediatric cardiology*, vol. 35, p. 851–856, 2014.

- [116] D. F. A. Lloyd, L. Cutler, S. M. Tibby, S. Vimalasvaran, S. A. Qureshi, E. Rosenthal, D. Anderson, C. Austin, H. Bellsham-Revell and T. Krasemann, "Analysis of preoperative condition and interstage mortality in Norwood and hybrid procedures for hypoplastic left heart syndrome using the Aristotle scoring system," *Heart*, vol. 100, p. 775–780, 2014.
- [117] J. Photiadis, N. Sinzobahamvya, V. Hraška and B. Asfour, "Does bilateral pulmonary banding in comparison to Norwood procedure improve outcome in neonates with hypoplastic left heart syndrome beyond second-stage palliation? A review of the current literature," *The Thoracic and cardiovascular surgeon*, vol. 60, p. 181–188, 2012.
- [118] H. Dave, B. Rosser, W. Knirsch, M. Hübler, R. Prêtre and O. Kretschmar, "Hybrid approach for hypoplastic left heart syndrome and its variants: the fate of the pulmonary arteries," *European Journal of Cardio-Thoracic Surgery*, vol. 46, p. 14–19, 2014.
- [119] Z. Reinhardt, J. De Giovanni, J. Stickley, V. K. Bhole, B. Anderson, B. Murtuza, C. Mehta, P. Miller, R. Dhillon and O. Stumper, "Catheter interventions in the staged management of hypoplastic left heart syndrome," *Cardiology in the Young*, vol. 24, p. 212, 2014.
- [120] S. Kutty, R. P. Burke, R. L. Hannan and E. M. Zahn, "Hybrid aortic reconstruction for treatment of recurrent aortic obstruction after stage 1 single ventricle palliation: medium term outcomes and results of redilation," *Catheterization and Cardiovascular Interventions*, vol. 78, p. 93–100, 2011.

- [121] R. Stanfill, D. G. Nykanen, S. Osorio, R. Whalen, R. P. Burke and E. M. Zahn, "Stent implantation is effective treatment of vascular stenosis in young infants with congenital heart disease: Acute implantation and long-term follow-up results," *Catheterization and Cardiovascular Interventions*, vol. 71, p. 831–841, 2008.
- [122] C. Duke, E. Rosenthal and S. A. Qureshi, "The efficacy and safety of stent redilatation in congenital heart disease," *Heart*, vol. 89, p. 905–912, 2003.
- [123] F. Fontan and E. Baudet, "Surgical repair of tricuspid atresia," *Thorax*, vol. 26, p. 240–248, 1971.
- [124] M. Gewillig, "The fontan circulation," *Heart*, vol. 91, p. 839–846, 2005.
- [125] M. de Leval, "The Fontan circulation: a challenge to William Harvey?," *Nature clinical practice Cardiovascular medicine*, vol. 2, no. 4, pp. 202–208, 2005.
- [126] M. R. de Leval, P. Kilner, M. Gewillig, C. Bull and D. C. McGoon, "Total cavopulmonary connection: a logical alternative to atriopulmonary connection for complex Fontan operations: experimental studies and early clinical experience," *The Journal of thoracic and cardiovascular surgery*, vol. 96, p. 682–695, 1988.
- [127] C. Marcelletti, A. Como, S. Giannico and B. Marino, "Inferior vena cava-pulmonary artery extracardiac conduit: a new form of right heart bypass," *The Journal of thoracic and cardiovascular surgery*, vol. 100, p. 228–232, 1990.
- [128] T.-J. Yun, Y.-M. Im, S.-H. Jung, W.-K. Jhang, J.-J. Park, D.-M. Seo, Y.-H. Kim, I.-S. Park, J.-K. Ko and M.-S. Lee, "Pulmonary vascular compliance and pleural

- effusion duration after the Fontan procedure," *International journal of cardiology*, vol. 133, p. 55–61, 2009.
- [129] V. Alexi-Meskishvili, S. Ovroutski, P. Ewert, I. Dähnert, F. Berger, P. Lange and R. Hetzer, "Optimal conduit size for extracardiac Fontan operation," *European journal of cardio-thoracic surgery*, vol. 18, no. 6, pp. 690-695, 2000.
- [130] K. Itatani, K. Miyaji, T. Tomoyasu, Y. Nakahata, O. Kuniyoshi, S. Takamoto and M. Ishii, "Optimal Conduit Size of the Extracardiac Fontan Operation Based on Energy Loss and Flow Stagnation," *The Society of Thoracic Surgeons*, vol. 88, no. 2, pp. 565-573, 2009.
- [131] D. J. Penny and A. N. Redington, "Doppler echocardiographic evaluation of pulmonary blood flow after the Fontan operation: the role of the lungs.," *Heart*, vol. 66, p. 372–374, 1991.
- [132] T.-Y. Hsia, S. Khambadkone, A. N. Redington, F. Migliavacca, J. E. Deanfield and M. R. de Leval, "Effects of respiration and gravity on infradiaphragmatic venous flow in normal and Fontan patients," *Circulation*, vol. 102, p. Iii–148, 2000.
- [133] A. N. Redington, D. Penny and E. A. Shinebourne, "Pulmonary blood flow after total cavopulmonary shunt.," *Heart*, vol. 65, p. 213–217, 1991.
- [134] V. E. Hjortdal, K. Emmertsen, E. Stenbøg, T. Frund, M. R. Schmidt, O. Kromann, K. Sørensen and E. M. Pedersen, "Effects of exercise and respiration on blood flow in total cavopulmonary connection: a real-time magnetic resonance flow study," *Circulation*, vol. 108, p. 1227–1231, 2003.

- [135] A. Marsden, A. Bernstein , V. Reddy, S. Shadden , R. Spilker, F. Chan, C. Taylor and J. Feinstein, "Evaluation of a novel Y-shaped extracardiac Fontan baffle using computational fluid dynamics," *J Thorac Cardiovasc Surg*, vol. 137, pp. 394-403, 2009.
- [136] T.-Y. Hsia, S. Khambadkone, S. M. Bradley and M. R. de Leval, "Subdiaphragmatic venous hemodynamics in patients with biventricular and Fontan circulation after diaphragm plication," *The Journal of thoracic and cardiovascular surgery*, vol. 134, p. 1397–1405, 2007.
- [137] T. Hsia, F. Migliavacca , S. Pittaccio , A. Radaelli, G. Dubini, G. Pennati and M. de Leval, "Computational Fluid Dynamic Study of Flow Optimization in Realistic Models of the Total Cavopulmonary Connections," *Journal of Surgical Research*, vol. 116, pp. 305-313, 2004.
- [138] M. de Leval, G. Dubini, F. Migliavacca, H. Jalali, G. Camporini, A. Redington and R. Pietrabissa, "Use of Computational Fluid Dynamics in the Design of Surgical Procedures: Application to the Study of Competitive Flows in Cavopulmonary Connections," *Thoracic and Cardiovascular Surgery*, vol. 111, pp. 502-513, 1996.
- [139] E. Bove, M. De Leval, F. Migliavacca, R. Balossino and G. Dubini, "Toward optimal hemodynamics: computer modeling of the Fontan circuit," *Pediatric cardiology*, vol. 28, no. 6, pp. 477-481, 2007.
- [140] S. Ovroutski, P. Ewert, O. Miera, V. Alexi-Meskishvili, B. Peters, R. Hetzer and F. Berger, "Long-term cardiopulmonary exercise capacity after modified Fontan

- operation," *European journal of cardio-thoracic surgery*, vol. 37, p. 204–209, 2010.
- [141] M. Gewillig, S. Brown, B. Eyskens, R. Heying, J. Ganame, W. Budts, A. Gerche and M. Gorenflo, "State-of-the-art congenital the Fontan circulation: who controls the cardiac output?," *Interactive CardioVascular and Thoracic Surgery*, vol. 10, pp. 428-433, 2010.
- [142] M. Gewillig and S. Brown, "The Fontan circulation after 45 years: update in physiology," *Heart*, vol. 102, pp. 1081-1086, 2016.
- [143] M. Gewillig and D. Goldberg, "Failure of the Fontan circulation," *Heart failure clinics*, vol. 10, no. 1, pp. 105-116, 2014.
- [144] R. Henaine , M. Vergnat, E. Bacha, B. Baudet, V. Lambert, E. Belli and A. Serraf, "Effects of lack of pulsatility on pulmonary endothelial function in the Fontan circulation," *J Thorac Cardiovasc Surg.*, vol. 146, pp. 522-529, 2013.
- [145] B. H. Goldstein, C. E. Connor, L. Gooding and A. P. Rocchini, "Relation of systemic venous return, pulmonary vascular resistance, and diastolic dysfunction to exercise capacity in patients with single ventricle receiving fontan palliation," *The American journal of cardiology*, vol. 105, p. 1169–1175, 2010.
- [146] G. B. Shachar, B. P. Fuhrman, Y. A. N. G. Wang, R. V. Lucas Jr and J. E. Lock, "Rest and exercise hemodynamics after the Fontan procedure.," *Circulation*, vol. 65, p. 1043–1048, 1982.

- [147] J. T. Reeves, J. H. Linehan and K. R. Stenmark, "Distensibility of the normal human lung circulation during exercise," *American Journal of Physiology-Lung Cellular and Molecular Physiology*, vol. 288, p. L419–L425, 2005.
- [148] K. Forton, Y. Motoji, G. Deboeck, V. Faoro and R. Naeije, "Effects of body position on exercise capacity and pulmonary vascular pressure-flow relationships," *Journal of Applied Physiology*, vol. 121, p. 1145–1150, 2016.
- [149] R. Naeije and N. Chesler, "Pulmonary circulation at exercise," *Comprehensive Physiology*, vol. 2, p. 711–741, 2011.
- [150] B. Schmitt, P. Steendijk, S. Ovroutski, K. Lunze, P. Rahmzadeh, N. Maarouf, P. Ewert, F. Berger and T. Kuehne, "Pulmonary vascular resistance, collateral flow, and ventricular function in patients with a Fontan circulation at rest and during dobutamine stress," *Circulation: Cardiovascular Imaging*, vol. 3, p. 623–631, 2010.
- [151] I. R. Rivera, M. A. Mendonça, J. L. Andrade, V. Moises, O. Campos, C. C. Silva and A. C. Carvalho, "Pulmonary venous flow index as a predictor of pulmonary vascular resistance variability in congenital heart disease with increased pulmonary flow: a comparative study before and after oxygen inhalation," *Echocardiography*, vol. 30, p. 952–960, 2013.
- [152] J. A. Petrofski, C. W. Hoopes, T. M. Bashore, S. D. Russell and C. A. Milano, "Mechanical ventricular support lowers pulmonary vascular resistance in a patient with congenital heart disease," *The Annals of thoracic surgery*, vol. 75, p. 1005–1007, 2003.

- [153] S. Cavalcanti, G. Gnudi, P. Masetti, G. Ussia and C. Marcelletti, "Analysis by mathematical model of haemodynamic data in the failing Fontan circulation," *Physiological measurement*, vol. 22, no. 1, p. 209, 2001.
- [154] M. D. Rodefeld, S. H. Frankel and G. A. Giridharan, "Cavopulmonary assist:(em) powering the univentricular fontan circulation," in *Seminars in Thoracic and Cardiovascular Surgery: Pediatric Cardiac Surgery Annual*, 2011.
- [155] A. F. Corno, C. Vergara, C. Subramanian, R. A. Johnson, T. Passerini, A. Veneziani, L. Formaggia, N. Alphonso, A. Quarteroni and J. C. Jarvis, "Assisted Fontan procedure: animal and in vitro models and computational fluid dynamics study," *Interactive cardiovascular and thoracic surgery*, vol. 10, p. 679–684, 2010.
- [156] Y. Delorme, K. Anupindi, A. E. Kerlo, D. Shetty, M. Rodefeld, J. Chen and S. Frankel, "Large eddy simulation of powered Fontan hemodynamics," *Journal of biomechanics*, vol. 46, p. 408–422, 2013.
- [157] J. Valdovinos, E. Shkolyar, G. P. Carman and D. S. Levi, "In Vitro Evaluation of an External Compression Device for Fontan Mechanical Assistance," *Artificial organs*, vol. 38, p. 199–207, 2014.
- [158] K. Pekkan, D. Frakes, D. De Zelicourt, C. W. Lucas, W. J. Parks and A. P. Yoganathan, "Coupling pediatric ventricle assist devices to the Fontan circulation: simulations with a lumped-parameter model," *ASAIO journal*, vol. 51, p. 618–628, 2005.

- [159] E. Kung, G. Pennati, F. Migliavacca, T.-Y. Hsia, R. Figliola, A. Marsden, A. Giardini, M. O. C. H. A. Investigators and others, "A simulation protocol for exercise physiology in Fontan patients using a closed loop lumped-parameter model," *Journal of biomechanical engineering*, vol. 136, 2014.
- [160] H. Marshall, H. Swan, H. Burchell and E. Wood, "Effect of breathing oxygen on pulmonary artery pressure and pulmonary vascular resistance in patients with ventricular septal defect," *Circulation*, vol. 23, p. 241–252, 1961.
- [161] L. Socci, F. Gervaso, F. Migliavacca, G. Pennati, G. Dubini, L. Ait-Ali, P. Festa, F. Amoretti, L. Scebba and V. S. Luisi, "Computational fluid dynamics in a model of the total cavopulmonary connection reconstructed using magnetic resonance images," *Cardiology in the Young*, vol. 15, p. 61, 2005.
- [162] A. B. Brahim, M. Prevost and R. Bugarel, "Momentum transfer in a vertical down flow liquid jet ejector: case of self gas aspiration and emulsion flow," *International journal of multiphase flow*, vol. 10, p. 79–94, 1983.
- [163] M. T. Kandakure, V. G. Gaikar and A. W. Patwardhan, "Hydrodynamic aspects of ejectors," *Chemical Engineering Science*, vol. 60, p. 6391–6402, 2005.
- [164] R. L. Yadav and A. W. Patwardhan, "Design aspects of ejectors: Effects of suction chamber geometry," *Chemical Engineering Science*, vol. 63, p. 3886–3897, 2008.
- [165] D. Mukherjee, M. N. Biswas and A. K. Mitra, "Hydrodynamics of liquid-liquid dispersion in ejectors and vertical two phase flow," *The Canadian Journal of Chemical Engineering*, vol. 66, p. 896–907, 1988.

- [166] F. M. Donovan, "Design of a hydraulic analog of the circulatory system for evaluating artificial hearts," *Biomaterials, medical devices, and artificial organs*, vol. 3, p. 439–449, 1975.
- [167] P. R. Verdonck, K. Dumont, P. Segers, S. Vandenberghe and G. Van Nooten, "Mock loop testing of On-x prosthetic mitral valve with Doppler echocardiography," *Artificial organs*, vol. 26, p. 872–878, 2002.
- [168] K. Naemura, M. Umezu and T. Dohi, "Preliminary Study on the New Self-Closing Mechanical Mitral Valve," *Artificial organs*, vol. 23, p. 869–875, 1999.
- [169] Z. Feng, M. Umezu, T. Fujimoto, T. Tsukahara, M. Nurishi and D. Kawaguchi, "In vitro hydrodynamic characteristics among three bileaflet valves in the mitral position," *Artificial organs*, vol. 24, p. 346–354, 2000.
- [170] M. Grigioni, C. Daniele, G. D'avenio and V. Barbaro, "Hemodynamic Performance of Small-Size Bileaflet Valves: Pressure Drop and Laser Doppler Anemometry Study Comparison of Three Prostheses," *Artificial organs*, vol. 24, p. 959–965, 2000.
- [171] Y. S. Morsi and A. A. Sakhaeimanesh, "Flow characteristics past jellyfish and St. Vincent valves in the aortic position under physiological pulsatile flow conditions," *Artificial organs*, vol. 24, p. 564–574, 2000.
- [172] T. Walther, S. Lehmann, V. Falk, J. Köhler, N. Doll, J. Bucerius, J. Gummert and F. W. Mohr, "Experimental Evaluation and Early Clinical Results of a New Low-Profile Bileaflet Aortic Valve," *Artificial organs*, vol. 26, p. 416–419, 2002.

- [173] J. F. Cornhill, "An aortic-left ventricular pulse duplicator used in testing prosthetic aortic heart valves," *The Journal of thoracic and cardiovascular surgery*, vol. 73, p. 550–558, 1977.
- [174] W. J. Kolff, "Mock circulation to test pumps designed for permanent replacement of damaged hearts," *Cleveland Clinic Quarterly*, vol. 26, p. 223–226, 1959.
- [175] H. Reul, B. Tesch, J. Schoenmackers and S. Effert, "Hydromechanical simulation of systemic circulation," *Medical and biological engineering*, vol. 12, no. 4, pp. 431-436, 1974.
- [176] L. N. Scotten, D. K. Walker and R. T. Brownlee, "Construction and evaluation of a hydromechanical simulation facility for the assessment of mitral valve prostheses," *Journal of medical engineering & technology*, vol. 3, p. 11–18, 1979.
- [177] G. Rosenberg, W. M. PHILLIPS, D. L. LANDIS, W. S. PIERCE and others, "Design and evaluation of the Pennsylvania State University mock circulatory system," 1981.
- [178] P. Verdonck, A. Kleven, R. Verhoeven, B. Angelsen and J. Vandenbogaerde, "Computer-controlled in vitro model of the human left heart.," *Medical & biological engineering & computing*, vol. 30, p. 656–659, 1992.
- [179] S. Vandenberghe, J. Van Loon, P. Segers, G. Rakhorst and P. Verdonck, "In vitro evaluation of the PUCA II intra-arterial LVAD," *The International journal of artificial organs*, vol. 26, no. 8, pp. 743-752, 2003.

- [180] G. Trittenwein, A. Zamberger, H. Trittenwein, G. Burda, J. Golej, M. Hermon and A. Pollak, "A Simple Neonatal Mock Circulation Enabling Pulsatility and Different Hemodynamical States for Neonatal ECMO Research: Application to Assess the Effect of a Centrifugal Pump Operated Neonatal ECMO System on the Circulation," *Artificial organs*, vol. 22, p. 414–418, 1998.
- [181] M. K. Sharp and R. K. Dharmalingham, "Development of a hydraulic model of the human systemic circulation.," *ASAIO Journal (American Society for Artificial Internal Organs: 1992)*, vol. 45, p. 535–540, 1999.
- [182] L. A. Baloa, J. R. Boston and J. F. Antaki, "Elastance-based control of a mock circulatory system," *Annals of biomedical engineering*, vol. 29, p. 244–251, 2001.
- [183] G. Fiore, A. Redaelli, M. Rasponi and R. Fumero, "Development of a model left ventricle with physiologic-like diastolic behaviour for studying mitral valve surgical correction," in *Summer Bioengineering Conference, Sonesta Beach Resort in Key Biscayne, Florida June*, 2003.
- [184] J. A. Goodwin, W. L. van Meurs, C. D. S. Couto, J. E. W. Beneken and S. A. Graves, "A model for educational simulation of infant cardiovascular physiology," *Anesthesia & Analgesia*, vol. 99, p. 1655–1664, 2004.
- [185] G. M. Pantalos, S. C. Koenig, K. J. Gillars, G. A. Giridharan and D. L. Ewert, "Characterization of an adult mock circulation for testing cardiac support devices," *ASAIO journal*, vol. 50, p. 37–46, 2004.
- [186] S. C. Koenig, G. M. Pantalos, K. J. Gillars, D. L. Ewert, K. N. Litwak and S. W. Etoch, "Hemodynamic and pressure–volume responses to continuous and pulsatile

- ventricular assist in an adult mock circulation," *ASAIO journal*, vol. 50, p. 15–24, 2004.
- [187] K. N. Litwak, S. C. Koenig, R. C. Cheng, G. A. Giridharan, K. J. Gillars and G. M. Pantalos, "Ascending aorta outflow graft location and pulsatile ventricular assist provide optimal hemodynamic support in an adult mock circulation," *Artificial organs*, vol. 29, p. 629–635, 2005.
- [188] Y. Liu, P. Allaire, H. Wood and D. Olsen, "Design and initial testing of a mock human circulatory loop for left ventricular assist device performance testing," *Artificial organs*, vol. 29, p. 341–345, 2005.
- [189] M. Kozarski, G. Ferrari, F. Clemente, K. Górczyńska, C. De Lazzari, M. Darowski, R. Mimmo, G. Tosti and M. Guaragno, "A hybrid mock circulatory system: development and testing of an electro-hydraulic impedance simulator," *The International Journal of artificial organs*, vol. 26, p. 53–63, 2003.
- [190] K. Dumont, J. Yperman, E. Verbeken, P. Segers, B. Meuris, S. Vandenberghe, W. Flameng and P. R. Verdonck, "Design of a new pulsatile bioreactor for tissue engineered aortic heart valve formation," *Artificial organs*, vol. 26, p. 710–714, 2002.
- [191] J. Bustamante, J. F. Barros, A. Roldán, S. García and A. F. Salazar, "Physical model of the cardiovascular system, dynasim," in *Memorias 3er congreso Virtual de Cardiología TTVC Buenos Aires, Argentina*, 2003.
- [192] J. L. Williams, J. F. Antaki, J. R. Boston, S. L. Williams, J. C. Woodard, P. J. Miller and R. L. Kormos, "Load sensitive mock circulatory system for left

- ventricular assist device controller evaluation and development," in *Proceedings of 16th Annual International Conference of the IEEE Engineering in Medicine and Biology Society*, 1994.
- [193] B. S. Conklin, S. M. Surowiec, P. H. Lin and C. Chen, "A simple physiologic pulsatile perfusion system for the study of intact vascular tissue," *Medical engineering & physics*, vol. 22, p. 441–449, 2000.
- [194] S. Patel, P. E. Allaire, H. G. Wood, J. M. Adams and D. Olsen, "Design and construction of a mock human circulatory system," in *Summer Bioengineering Conference, Sonesta Beach Resort, Florida*, 2003.
- [195] N. Stergiopoulos, B. E. Westerhof and N. Westerhof, "Total arterial inertance as the fourth element of the windkessel model," *American Journal of Physiology-Heart and Circulatory Physiology*, vol. 276, p. H81–H88, 1999.
- [196] M. I. M. Noble, "The contribution of blood momentum to left ventricular ejection in the dog," *Circulation research*, vol. 23, p. 663–670, 1968.
- [197] A. S. Ferreira, M. N. Souza and others, "Comparison of segmental arterial compliance determined with three and four element windkessel models," in *Proceedings of the 25th Annual International Conference of the IEEE Engineering in Medicine and Biology Society (IEEE Cat. No. 03CH37439)*, 2003.
- [198] L. A. Garrison, J. A. Frangos, D. B. Geselowitz, T. C. Lamson and J. M. Tarbell, "A new mock circulatory loop and its application to the study of chemical additive and aortic pressure effects on hemolysis in the Penn State electric ventricular assist device," *Artificial organs*, vol. 18, p. 397–407, 1994.

- [199] R. H. Marcus, C. Korcarz, G. McCray, A. Neumann, M. Murphy, K. Borow, L. Weinert, J. Bednarz, D. D. Gretler and K. T. Spencer, "Noninvasive method for determination of arterial compliance using Doppler echocardiography and subclavian pulse tracings. Validation and clinical application of a physiological model of the circulation.," *Circulation*, vol. 89, p. 2688–2699, 1994.
- [200] S. J. Woodruff, M. K. Sharp and G. M. Pantalos, "Compact compliance chamber design for the study of cardiac performance in microgravity.," *ASAIO Journal (American Society for Artificial Internal Organs: 1992)*, vol. 43, p. 316–320, 1997.
- [201] M. Arabia and T. Akutsu, "A new test circulatory system for research in cardiovascular engineering," *Annals of biomedical engineering*, vol. 12, p. 29–48, 1984.
- [202] G. Ferrari, C. De Lazzari, R. Mimmo, G. Tosti, D. Ambrosi and K. Gorczynska, "A computer controlled mock circulatory system for mono-and biventricular assist device testing.," *The International journal of artificial organs*, vol. 21, p. 26–36, 1998.
- [203] P. Kolh, V. D'Orio, B. Lambermont, P. Gerard, C. Gommès and R. Limet, "Increased aortic compliance maintains left ventricular performance at lower energetic cost," *European journal of cardio-thoracic surgery*, vol. 17, p. 272–278, 2000.
- [204] S. D. Lick, J. B. Zwischenberger, D. Wang, D. J. Deyo, S. K. Alpard and S. D. Chambers, "Improved right heart function with a compliant inflow artificial lung

- in series with the pulmonary circulation," *The Annals of thoracic surgery*, vol. 72, p. 899–904, 2001.
- [205] T. G. Papaioannou, D. S. Mathioulakis, J. N. Nanas, S. G. Tsangaris, S. F. Stamatelopoulos and S. D. Moulopoulos, "Arterial compliance is a main variable determining the effectiveness of intra-aortic balloon counterpulsation: quantitative data from an in vitro study," *Medical engineering & physics*, vol. 24, p. 279–284, 2002.
- [206] J. Haft, J. Bull, R. Rose, J. Katsra, J. Grotberg, R. Bartlett and R. Hirschl, "Design of an artificial lung compliance chamber for pulmonary replacement," *ASAIO*, vol. 49, no. 1, pp. 35–40, 2003.
- [207] T. A. McMahon, C. Clark, V. S. Murthy and A. H. Shapiro, "Intra-aortic balloon experiments in a lumped-element hydraulic model of the circulation," *Journal of biomechanics*, vol. 4, p. 335–350, 1971.
- [208] W. M. Swanson and R. E. Clark, "A simple cardiovascular system simulator: design and performance.," *Journal of bioengineering*, vol. 1, p. 135–145, 1977.
- [209] S. H. L. O. M. O. Gabbay, D. M. McQueen, E. L. Yellin and R. W. Frater, "In vitro hydrodynamic comparison of mitral valve bioprostheses.," *Circulation*, vol. 60, p. 62–70, 1979.
- [210] F. Cassot, D. Morvan, P. Issartier and R. Pelissier, "New versatile physical model fitting the systemic circulation accurately," *Medical and Biological Engineering and Computing*, vol. 23, p. 511–516, 1985.

- [211] C. T. Bowles, S. S. Shah, K. Nishimura, C. Clark, D. V. E. Cumming, C. W. Pattison, J. R. Pepper and M. H. Yacoub, "Development of mock circulation models for the assessment of counterpulsation systems," *Cardiovascular research*, vol. 25, p. 901–908, 1991.
- [212] B. Knierbein, H. Reul, R. Eilers, M. Lange, R. Kaufmann and G. Rau, "Compact mock loops of the systemic and pulmonary circulation for blood pump testing," *The International journal of artificial organs*, vol. 15, p. 40–48, 1992.
- [213] H. Schima, H. Baumgartner, F. Spitaler, P. Kühn and E. Wolner, "A modular mock circulation for hydromechanical studies on valves, stenoses, vascular grafts and cardiac assist devices," *The International journal of artificial organs*, vol. 15, p. 417–421, 1992.
- [214] Y. Orime, S. Takatani, K. Tasai, Y. Ohara, K. Naito, K. Mizuguchi, K. Makinouchi, Y. Matsuda, T. Shimono, J. Glueck and others, "In vitro and in vivo validation tests for total artificial heart," *Artificial organs*, vol. 18, p. 54–72, 1994.
- [215] A. Andrade, D. Nicolosi, J. Lucchi, J. Biscegli, A. C. F. Arruda, Y. Ohashi, J. Mueller, E. Tayama, J. Glueck and Y. Nosé, "Auxiliary total artificial heart: a compact electromechanical artificial heart working simultaneously with the natural heart," *Artificial organs*, vol. 23, p. 876–880, 1999.
- [216] P. J. Ayre, N. H. Lovell and J. C. Woodard, "Non-invasive flow estimation in an implantable rotary blood pump: a study considering non-pulsatile and pulsatile flows," *Physiological measurement*, vol. 24, p. 179, 2003.

- [217] L. Athanassiou, S. M. Hancock and R. P. Mahajan, "Doppler estimation of zero flow pressure during changes in downstream pressure in a bench model of a circulation using pulsatile flow," *Anaesthesia*, vol. 60, p. 133–138, 2005.
- [218] I. Avrahami, M. Rosenfeld, S. Raz and S. Einav, "Numerical model of flow in a sac-type ventricular assist device," *Artificial organs*, vol. 30, p. 529–538, 2006.
- [219] K. Hassani, M. Navidbakhsh and M. Rostami, "Modeling of the aorta artery aneurysms and renal artery stenosis using cardiovascular electronic system," *Biomedical engineering online*, vol. 6, no. 1, pp. 1-10, 2007.
- [220] N. Stergiopoulos, J. Meister and N. Westerhof, "Simple and accurate way for estimating total and segmental arterial compliance: the pulse pressure method," *Annals of biomedical engineering*, vol. 22, no. 4, pp. 392-397, 1994.
- [221] P. Segers, P. Verdonck, Y. Deryck, S. Brimioulle, R. Naeije, S. Carlier and N. Stergiopoulos, "Pulse pressure method and the area method for the estimation of total arterial compliance in dogs: sensitivity to wave reflection intensity.," *Annals of biomedical engineering*, vol. 27, no. 4, pp. 480-485, 1999.
- [222] M. Ni, "Computational Fluid Dynamics Proof of Concept and Analysis of a Self-Powered Fontan Circulation".
- [223] F. White, Fluid Mechanics, New York: McGraw-Hill higher .
- [224] Hameed, "Computational Fluid Dynamics Investigation of A Novel Hybrid Comprehensive Stage II Operation For Single Ventricle Palliation".

- [225] Scherer and Figueiredo, "Ferrofluids: properties and application," *Brazilian journal of physics*.
- [226] Santamore and Banea, "Theoretical optimization of pulmonary-to-systemic flow ratio after a bidirectional cavopulmonary anastomosis," *American Journal of physiology*.
- [227] Alfonso and Cymberknop, "Elastic mismatch between ePTFE and PLLA vascular grafts in relation to femoral and carotid arteries in humans," *Health and Technology*, 2016.
- [228] McGarry, O'donnell and McHugh, "Analysis of the mechanical performance of a cardiovascular stent design based on micromechanical modelling," *Computational Materials Science* .
- [229] Wei and Chen, "Structural and hemodynamic analyses of different stent structures in curved and stenotic coronary artery," *Frontiers in bioengineering and biotechnology*, vol. 7, p. 366, 2019.
- [230] Gray, Random Process, and ergodic properties, Springer-Verlag.

Appendix A

1.1 Instrumentation wiring schematic

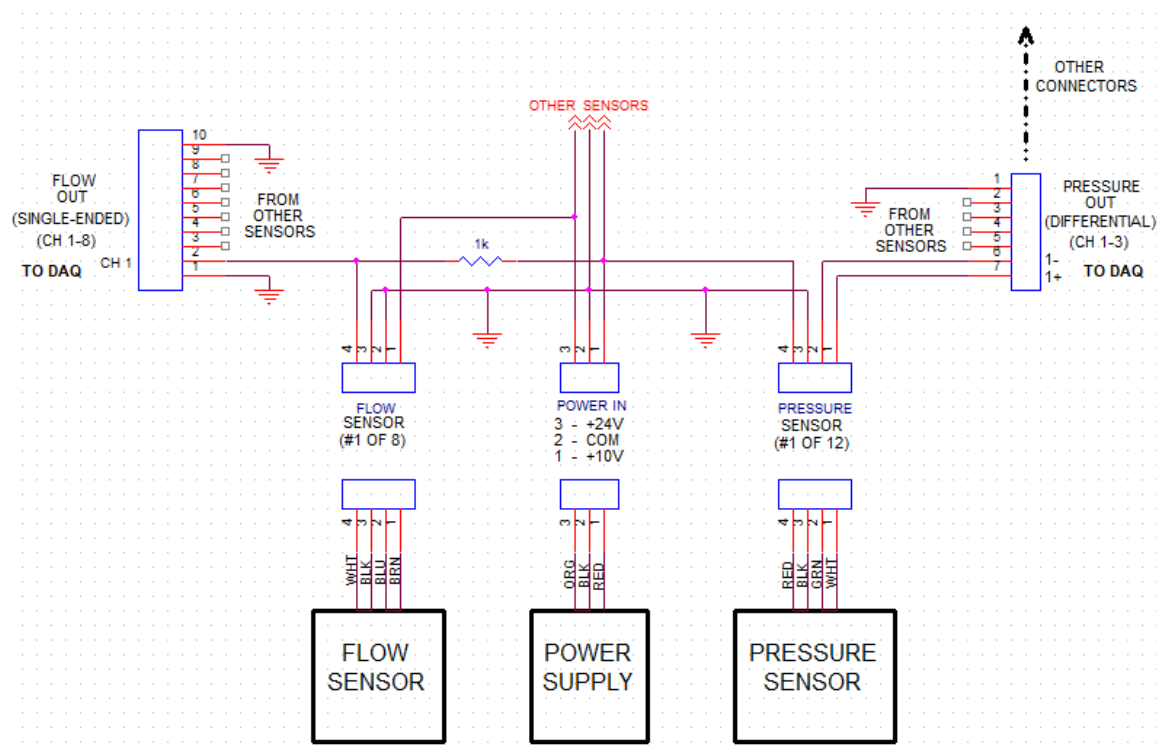


Figure 150 DAQ instrumentation schematic

1.2 Fontan hemodynamics

1.2.1 2mm IJS

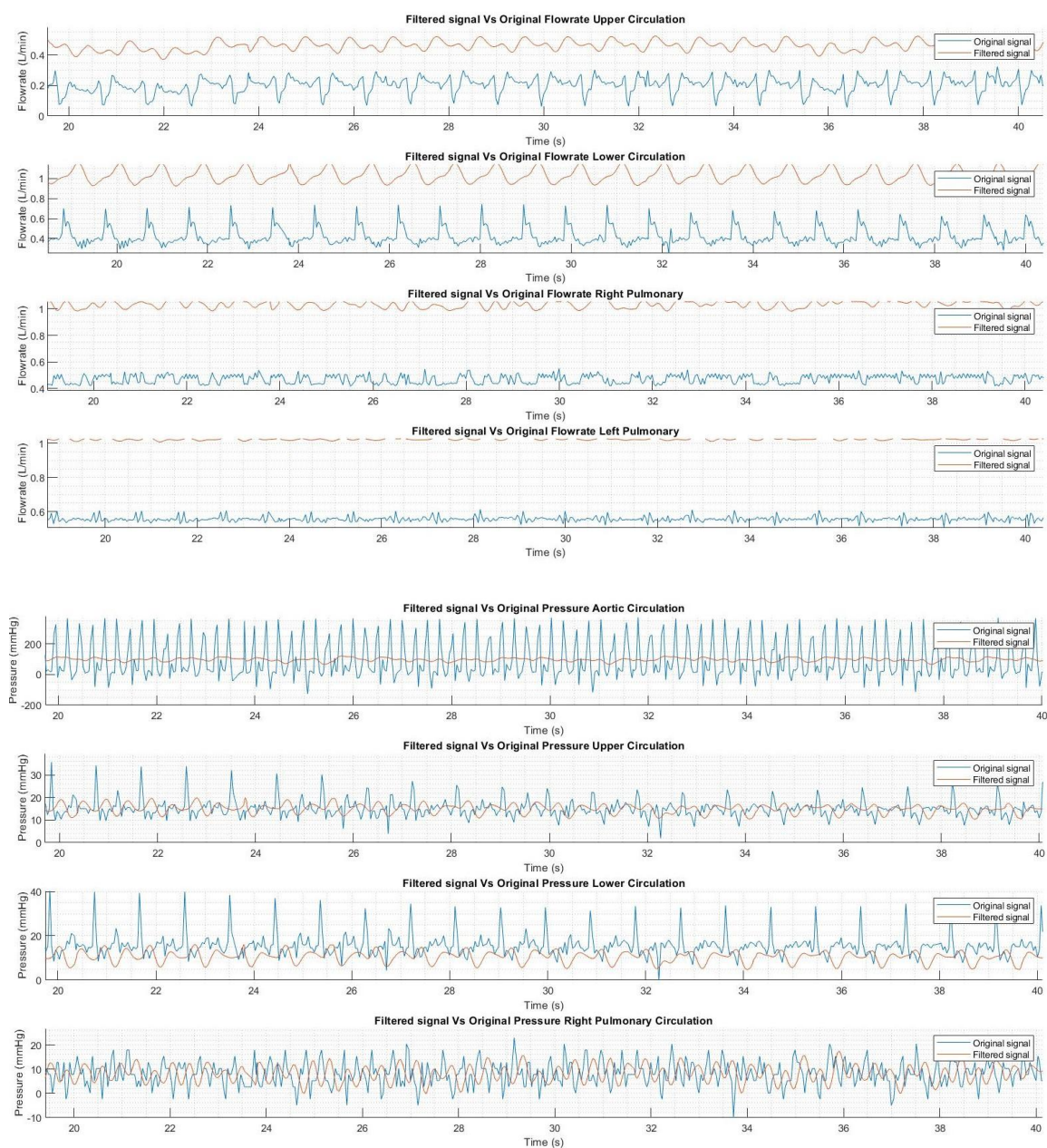


Figure 151 Filtered and unfiltered flowrate (U) and pressure (L) for IJS with 2mm diameter

1.2.2 4mm IJS

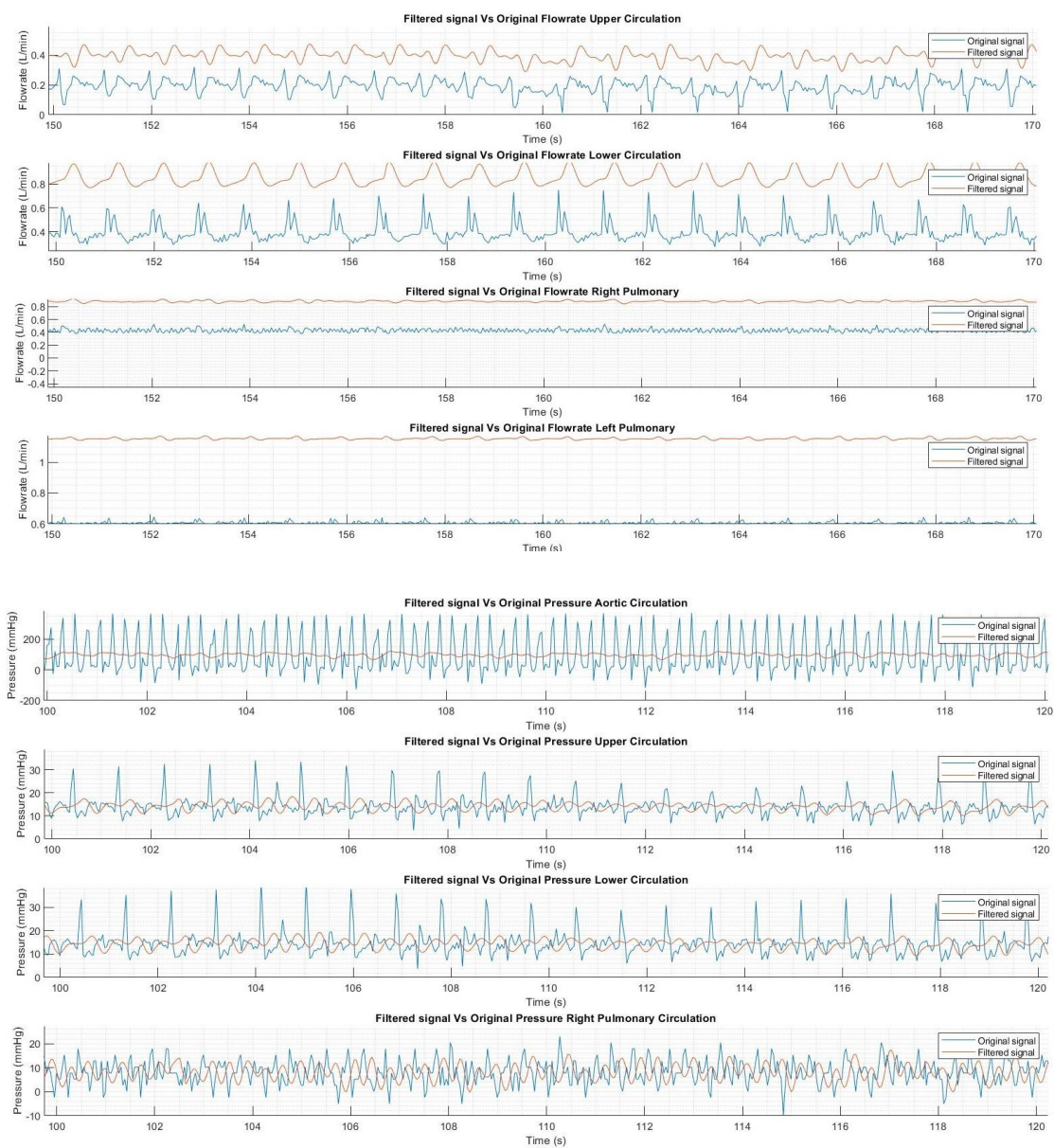


Figure 152 Filtered and unfiltered flowrate (U) and pressure (L) for IJS with 4mm diameter

1.2.3 3mm IJS at 45 degree

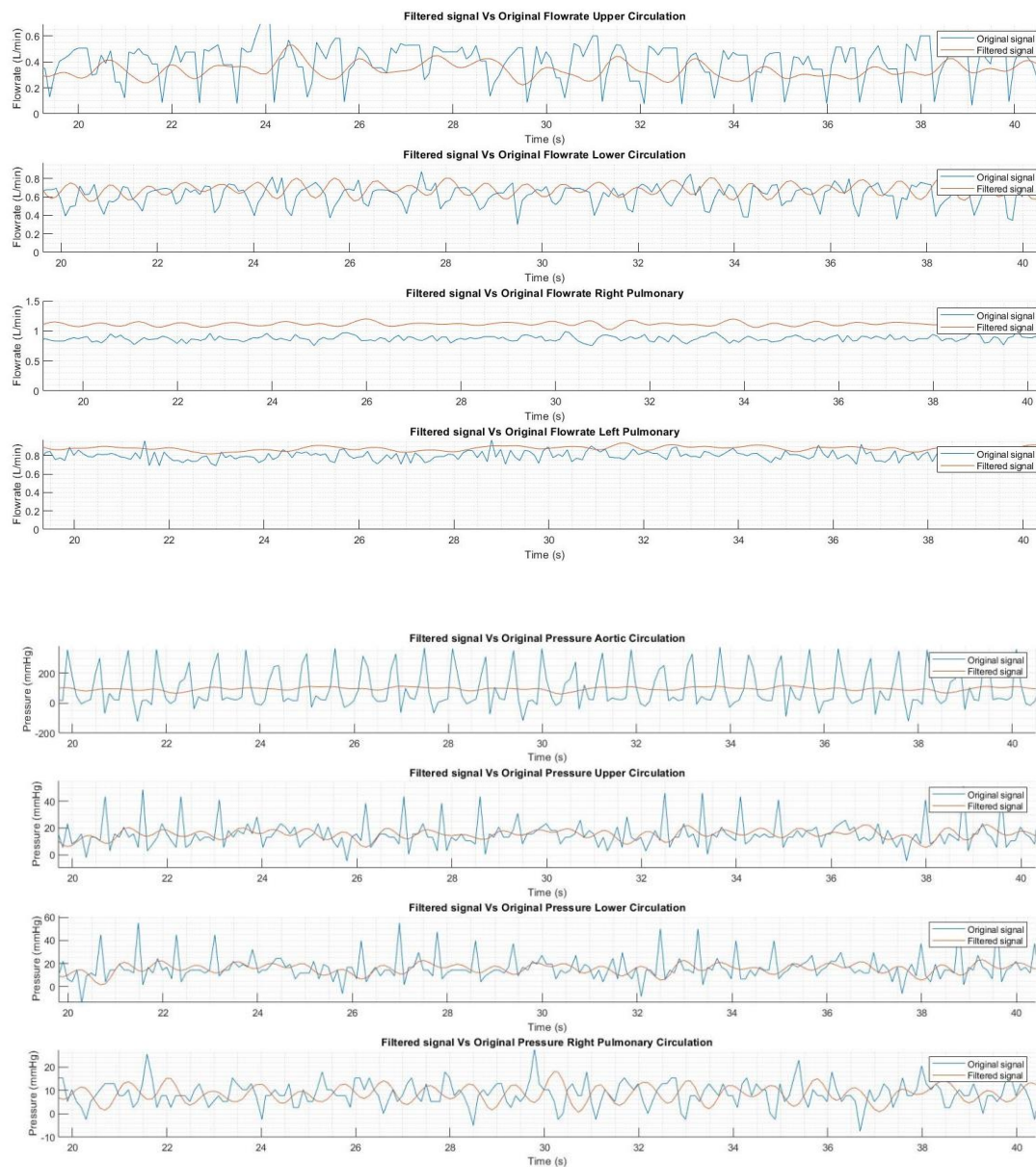


Figure 153 Filtered and unfiltered flowrate (U) and pressure (L) for 3mm IJS at 45 degree

1.2.4 3mm IJS at 90 degree

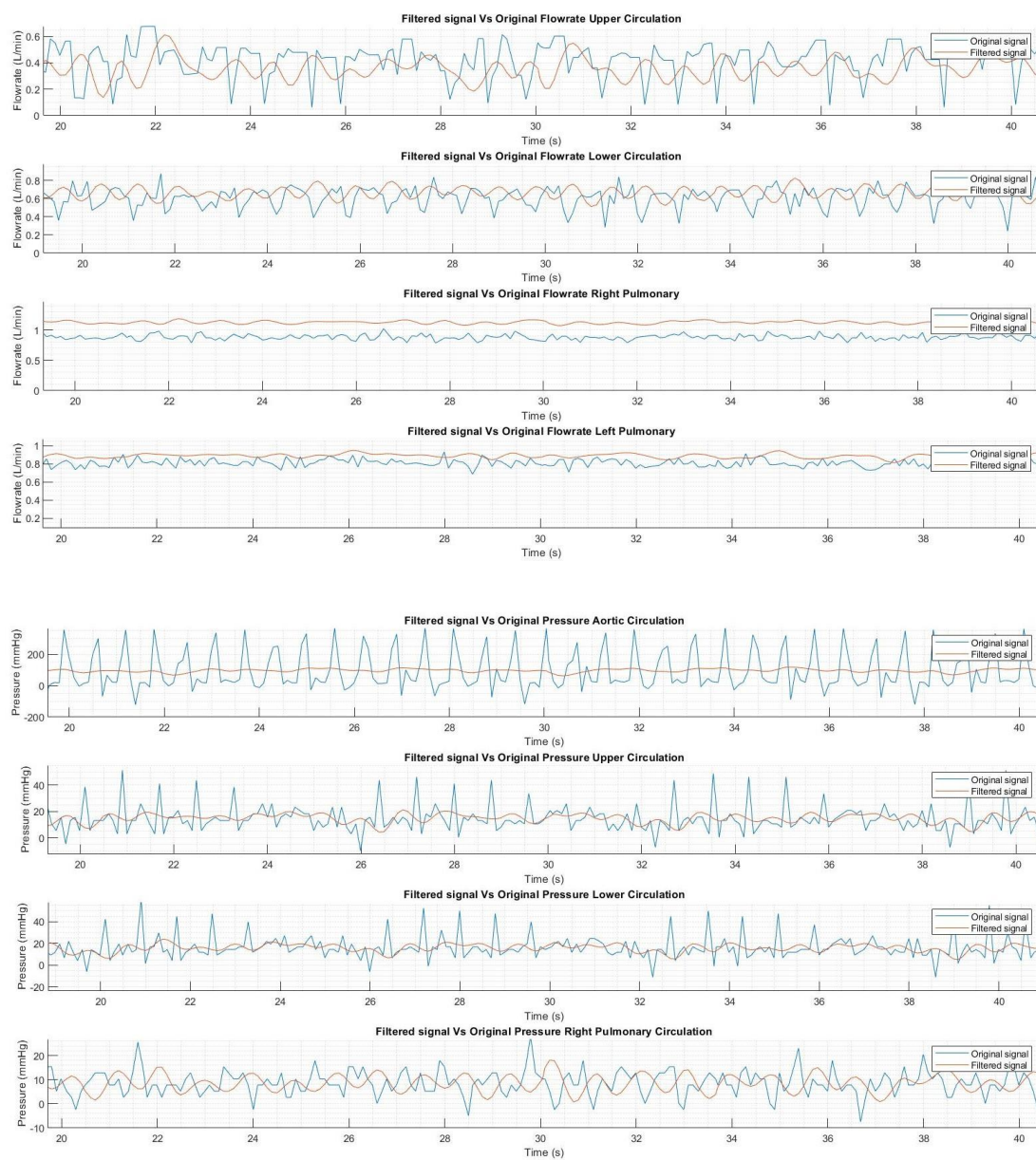


Figure 154 Filtered and unfiltered flowrate (U) and pressure (L) for 3mm IJS at 90 degree

1.2.5 PVR10

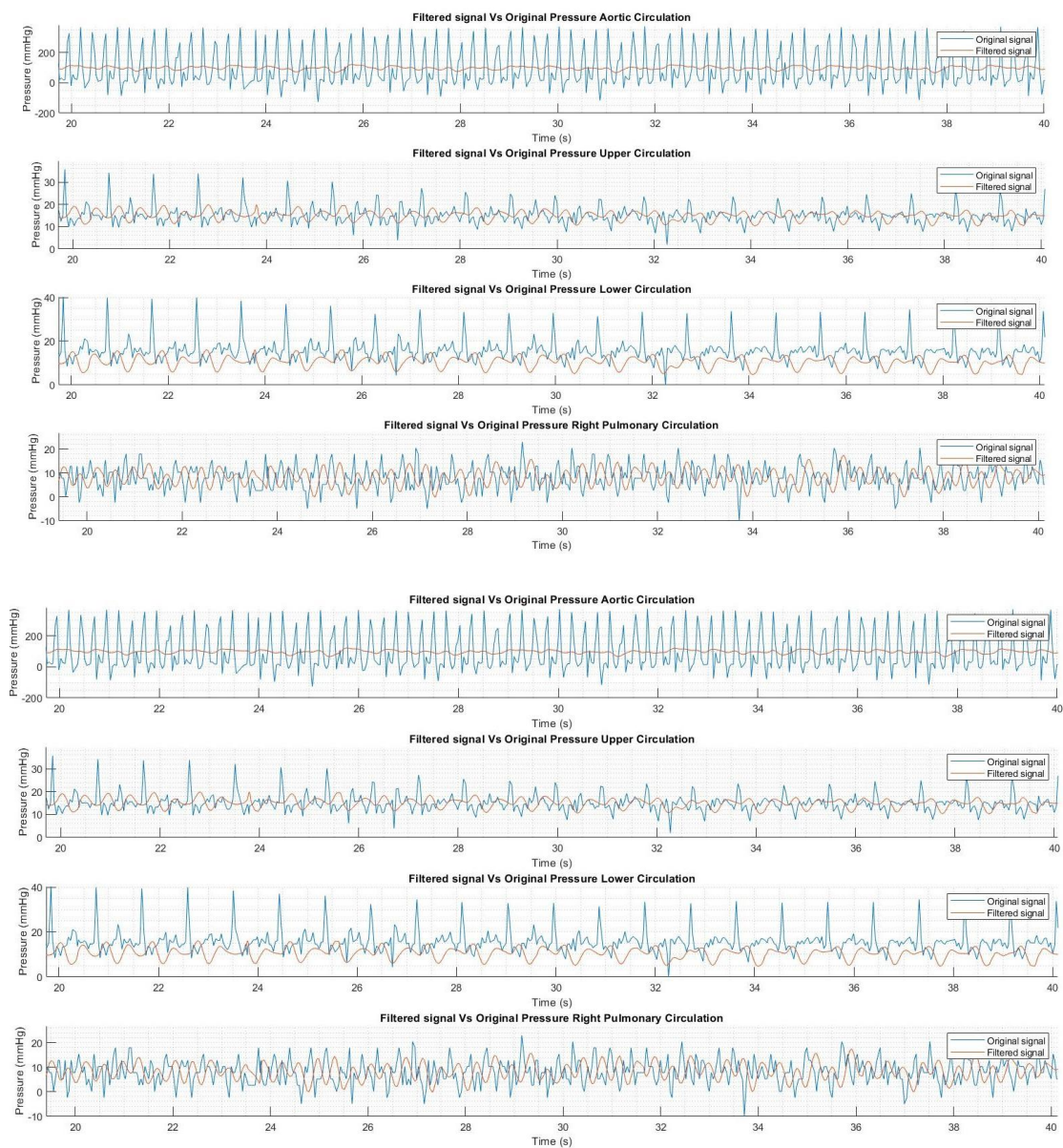


Figure 155 Filtered and unfiltered flowrate (U) and pressure (L) for PVR10

1.3 PVR injection experiment

1.3.1 Case 1: 5 cc/s short injection

1.3.1.1 5 x 15cc injections (75cc total volume)

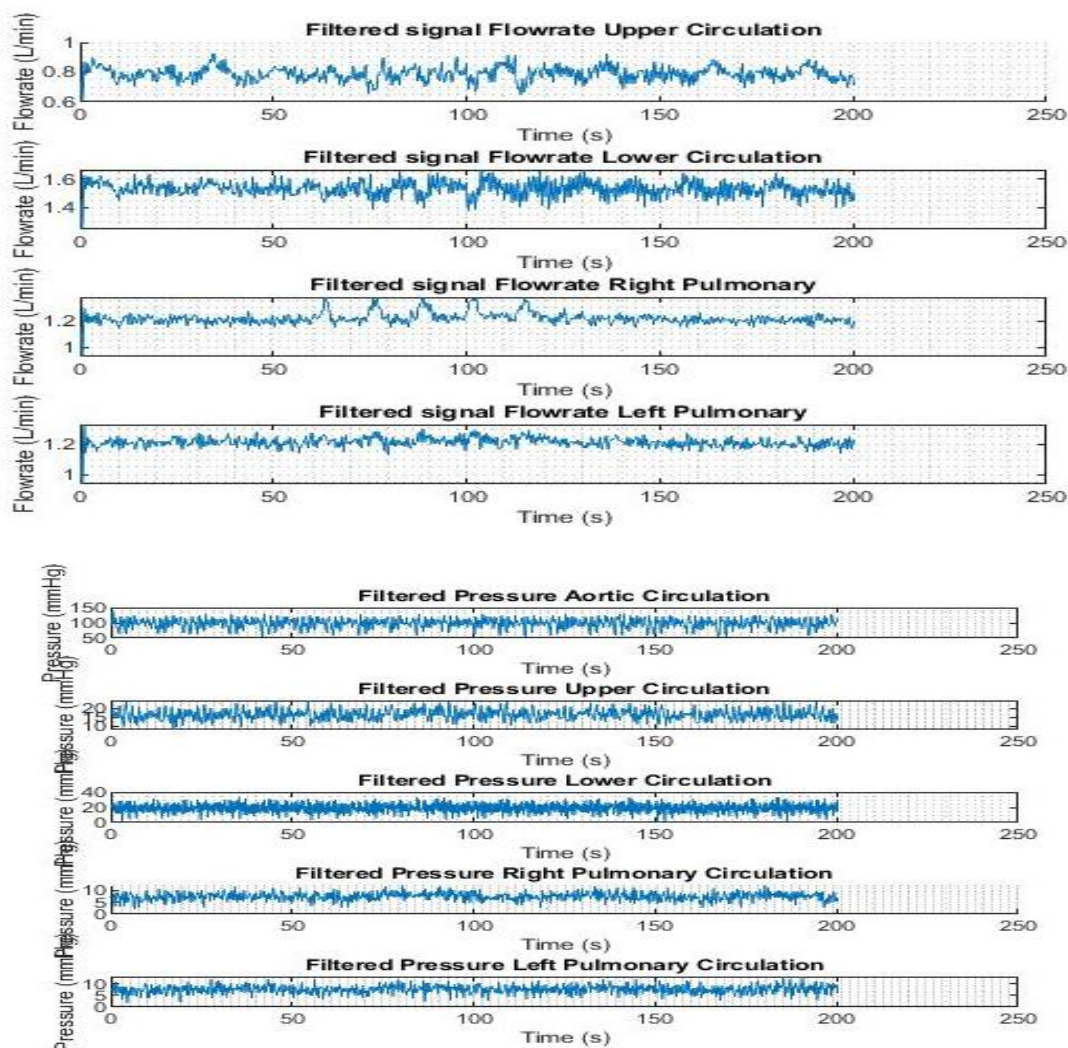


Figure 156 Filtered flowrate (U) and pressure (L) for 5cc/s with 15cc volume for one short shot

1.3.1.2 10 x 10cc injections (100cc total volume)

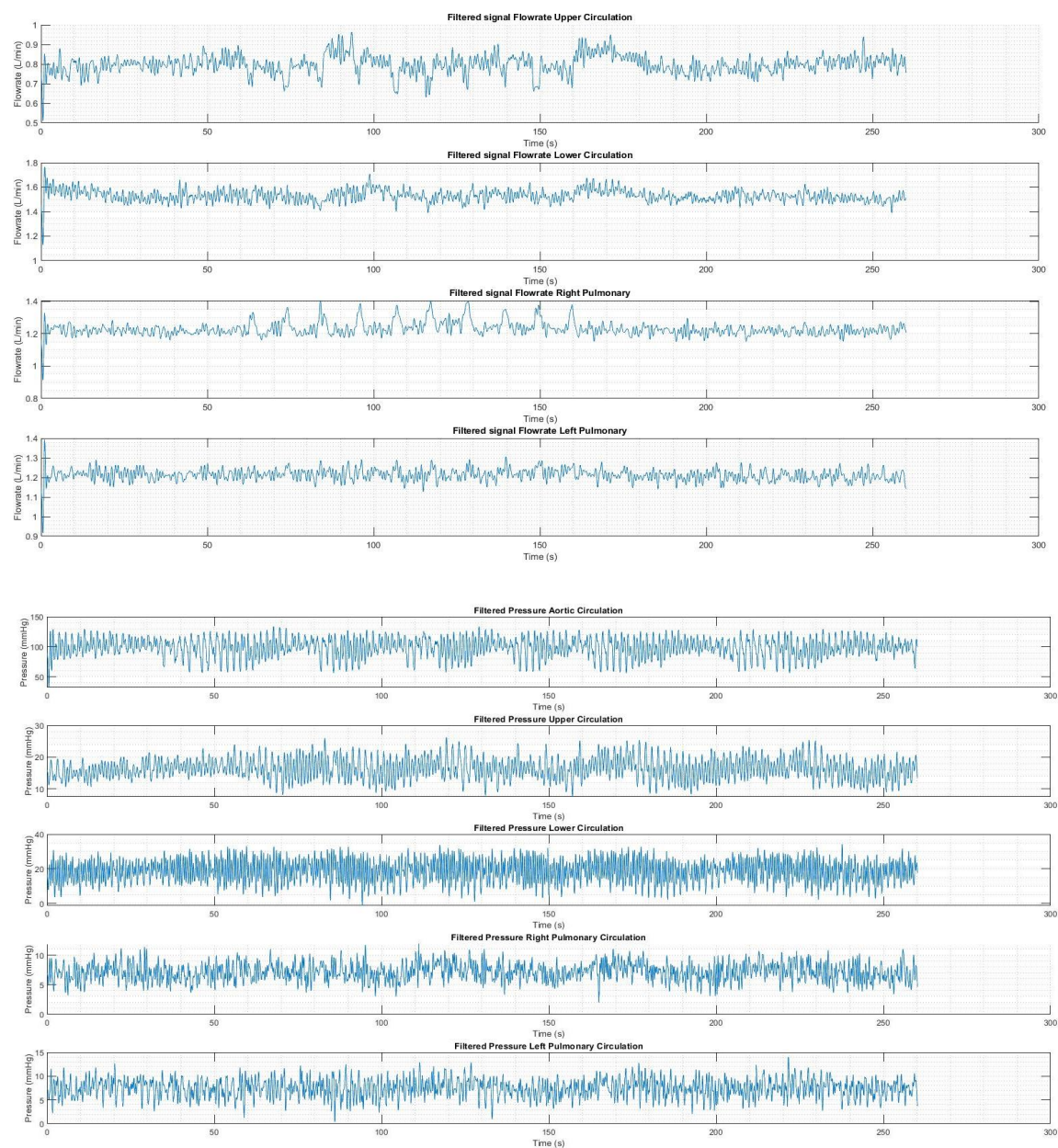


Figure 157 Filtered flowrate (U) and pressure (L) for 5cc/s with 10cc volume for one short shot

1.3.1.3 10 x 5cc injections (50cc total volume)

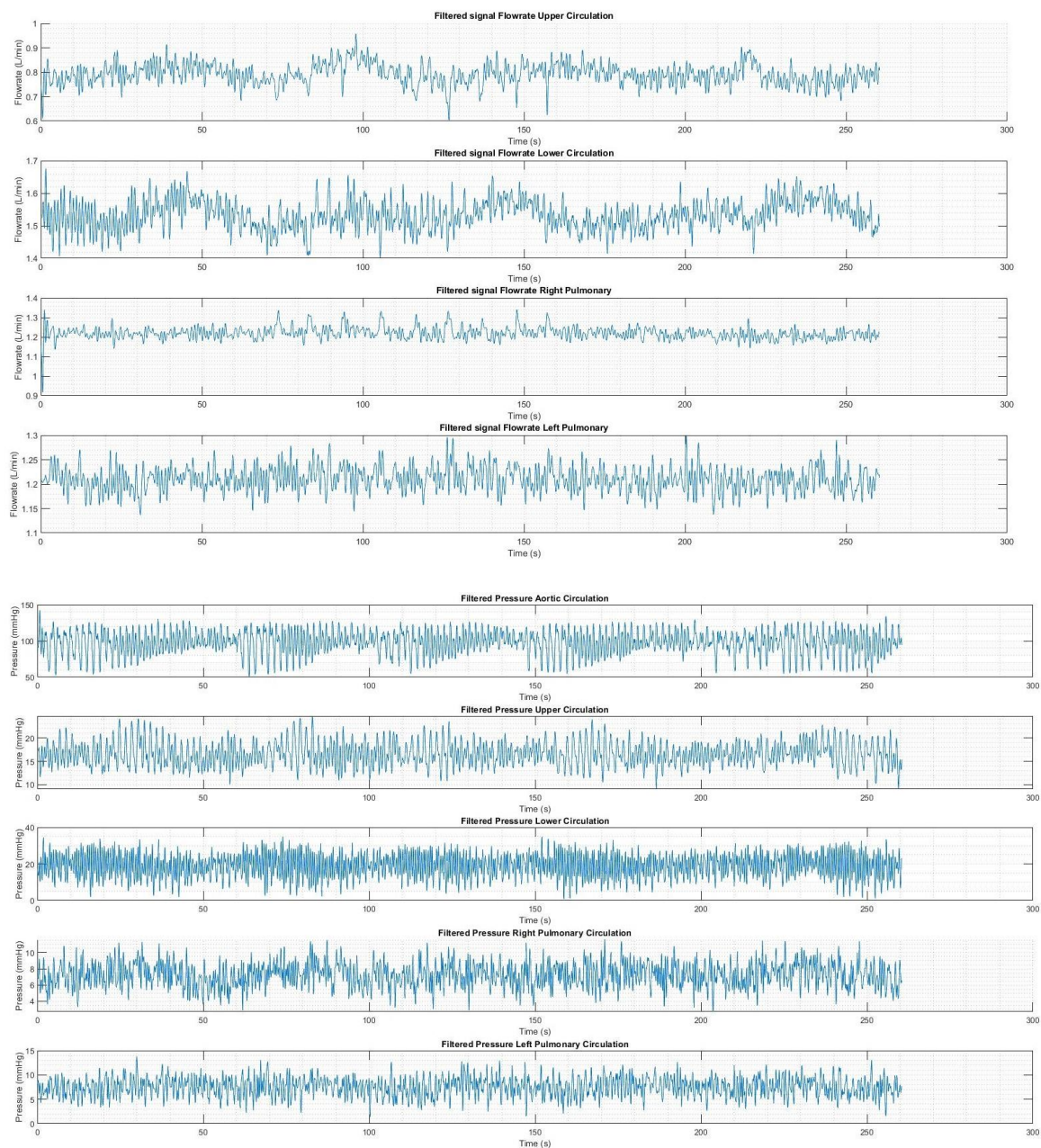


Figure 158 Filtered flowrate (U) and pressure (L) for 5cc/s with 5cc volume for one short shot

1.3.2 Case 2: 10 cc/s short injection

1.3.2.1 5 x 15cc injections (75cc total volume)

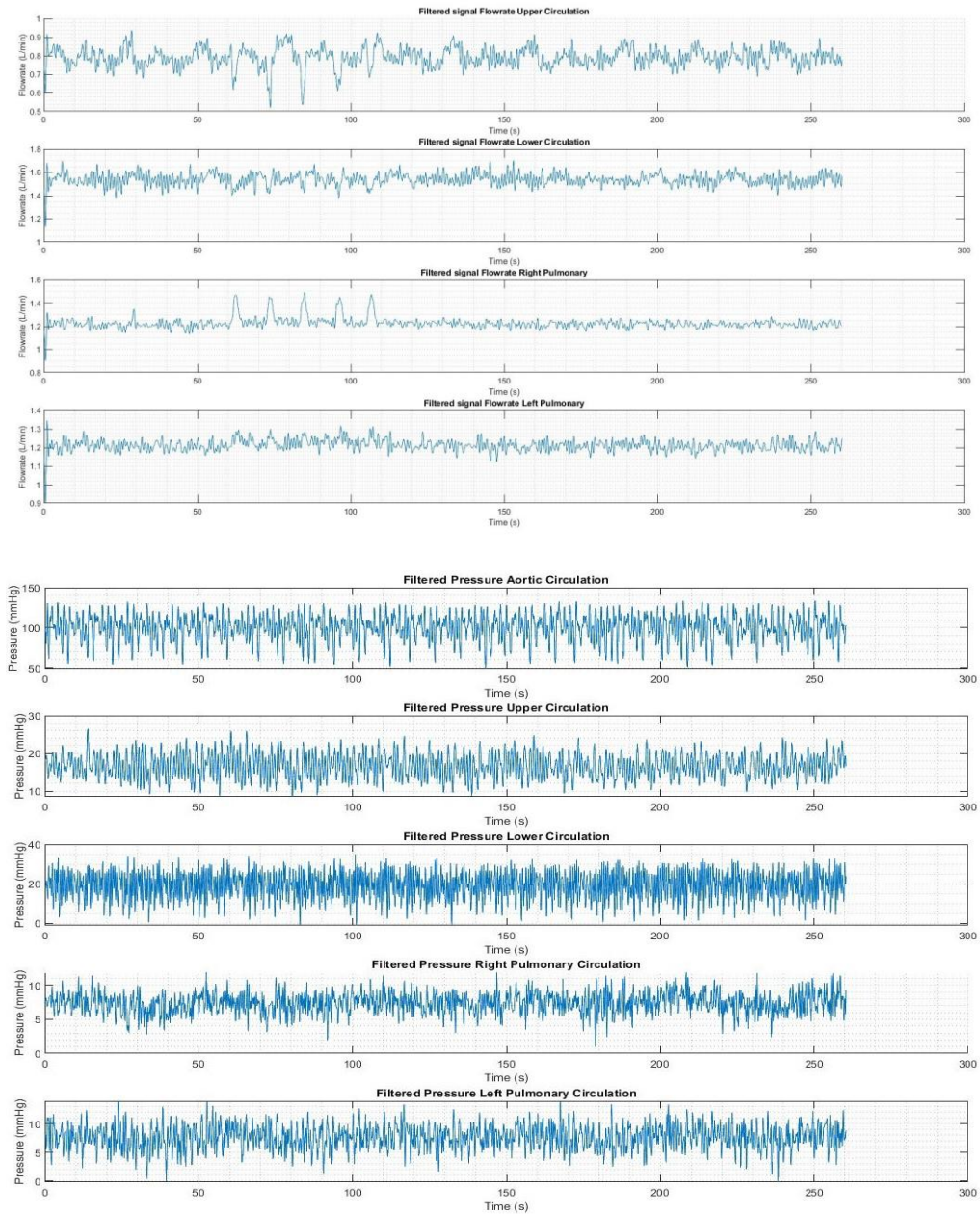


Figure 159 Filtered flowrate (U) and pressure (L) for 10cc/s with 15cc volume for one short shot

1.3.2.2 10 x 10cc injections (100cc total volume)

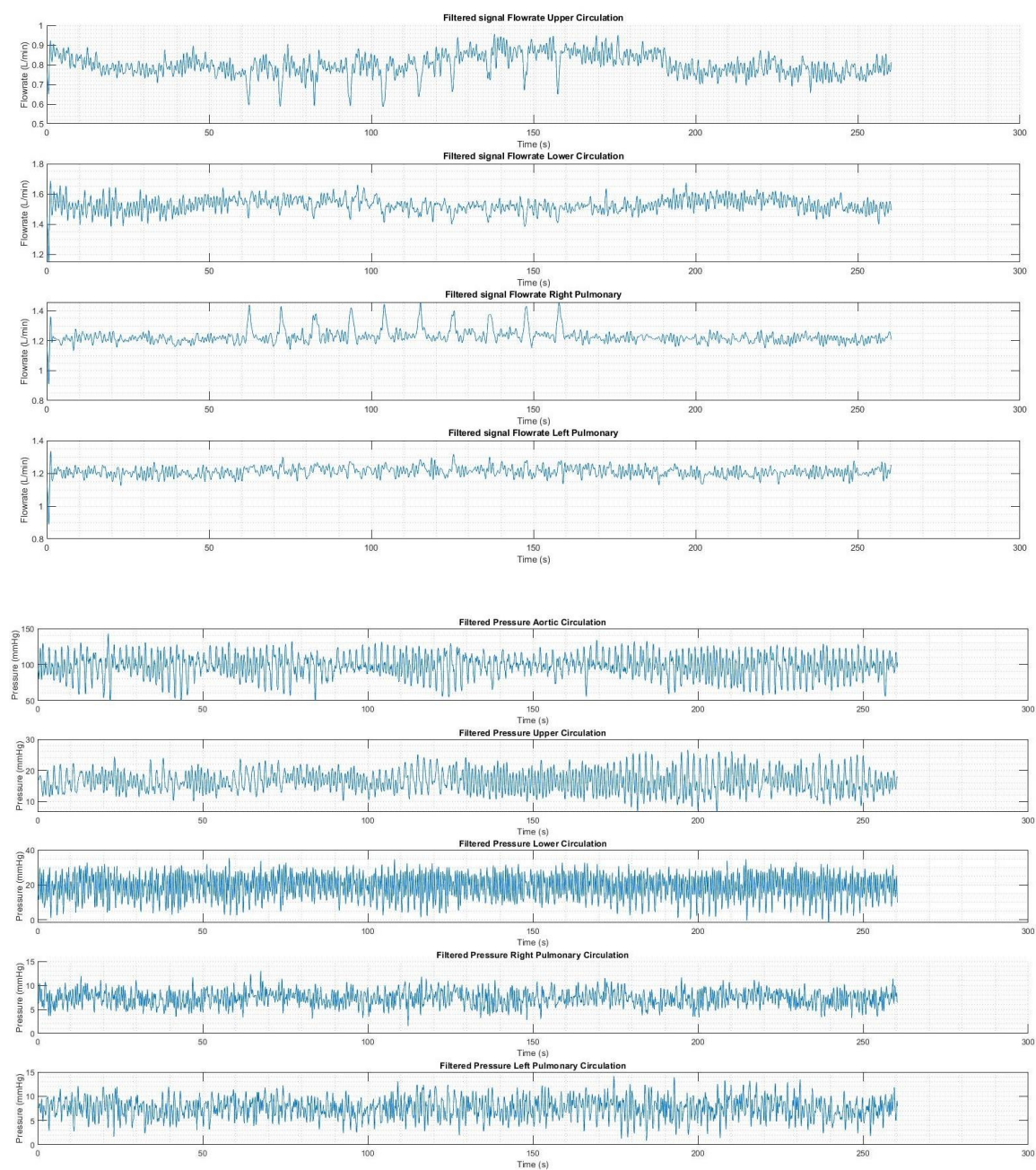


Figure 160 Filtered flowrate (U) and pressure (L) for 10cc/s with 10cc volume for one short shot

1.3.2.3 10 x 5cc injections (50cc total volume)

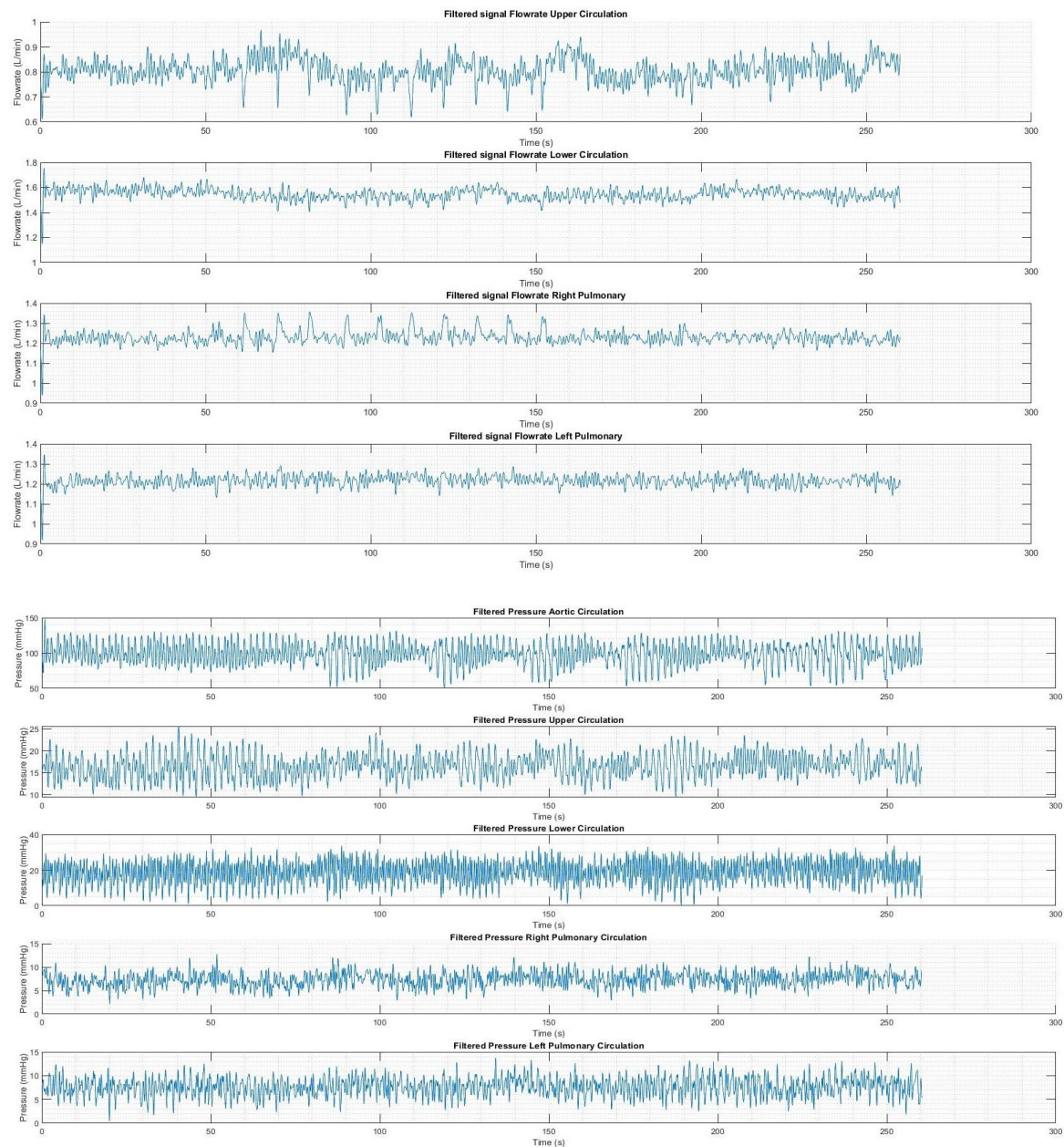


Figure 161 Filtered flowrate (U) and pressure (L) for 10cc/s with 5cc volume for one short shot

1.3.3 Case 3: 15 cc/s short injection

1.3.3.1 5 x 15cc injections (75cc total volume)

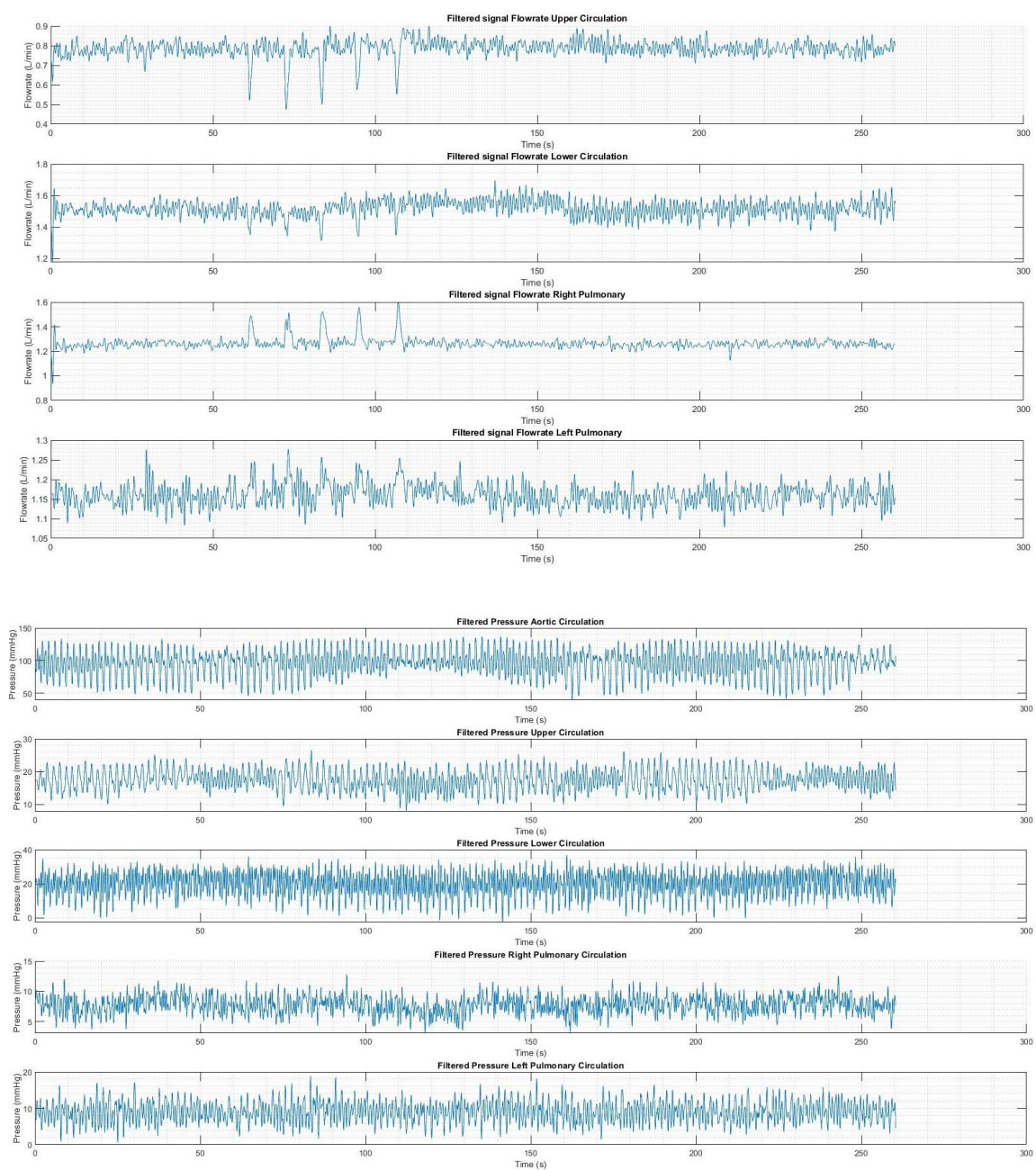


Figure 162 Filtered flowrate (U) and pressure (L) for 15cc/s with 15cc volume for one short shot

1.3.3.2 10 x 10cc injections (100cc total volume)

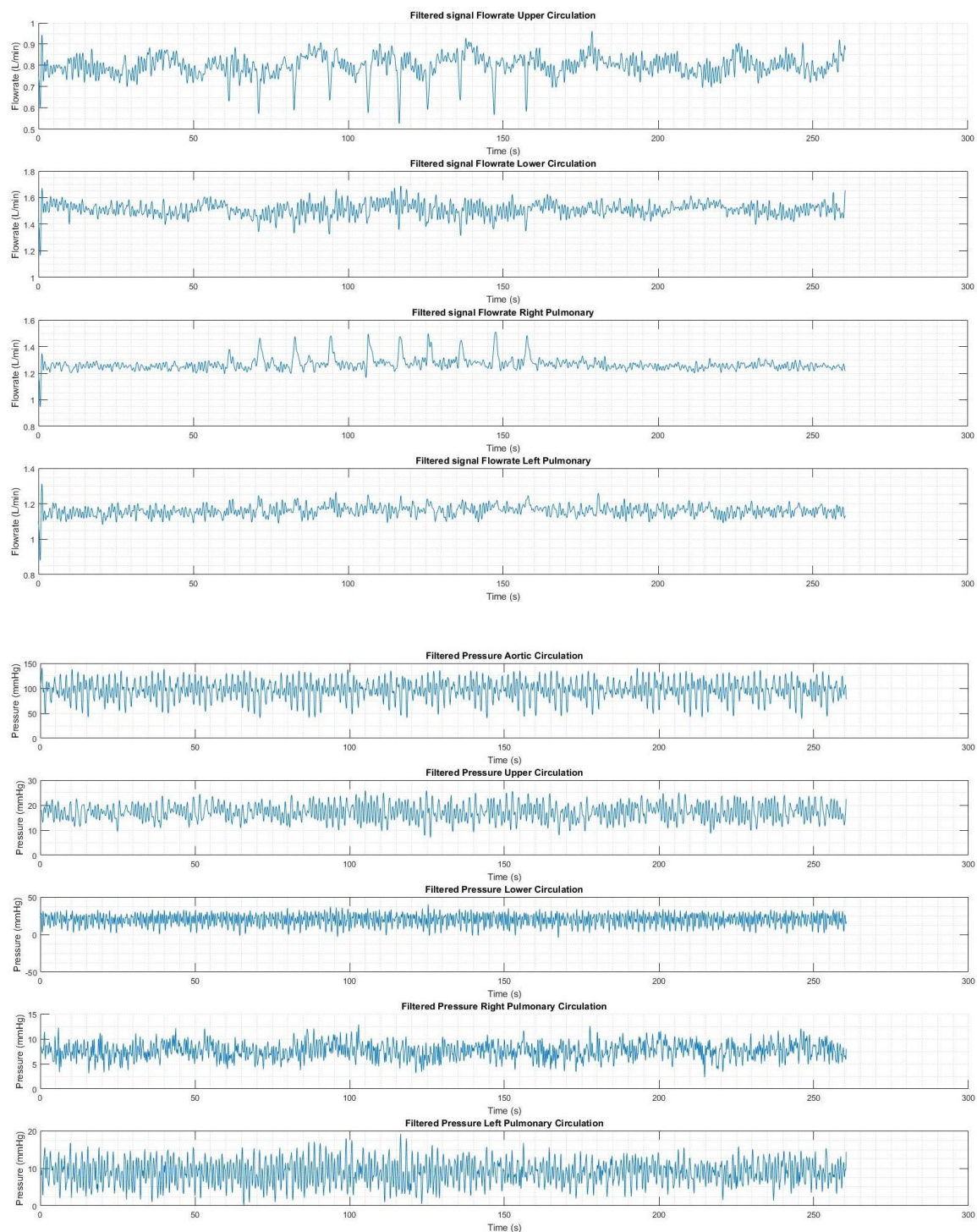


Figure 163 Filtered flowrate (U) and pressure (L) for 15cc/s with 10cc volume for one short shot

1.3.3.3 10 x 5cc injections (50cc total volume)

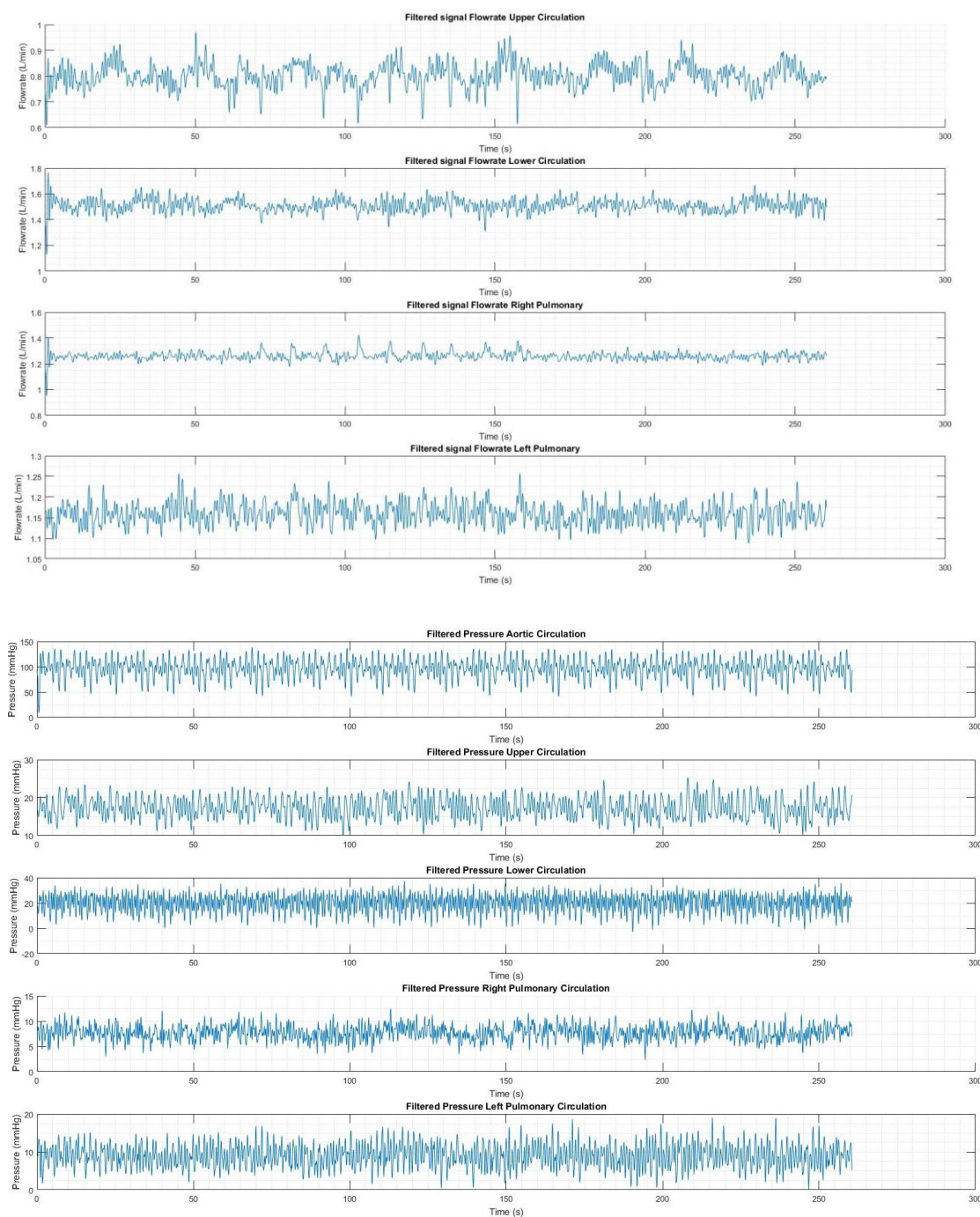


Figure 164 Filtered flowrate (U) and pressure (L) for 15cc/s with 5cc volume for one short shot

1.3.4 Case 4: 20 cc/s short injection

1.3.4.1 5 x 15cc injections (75cc total volume)

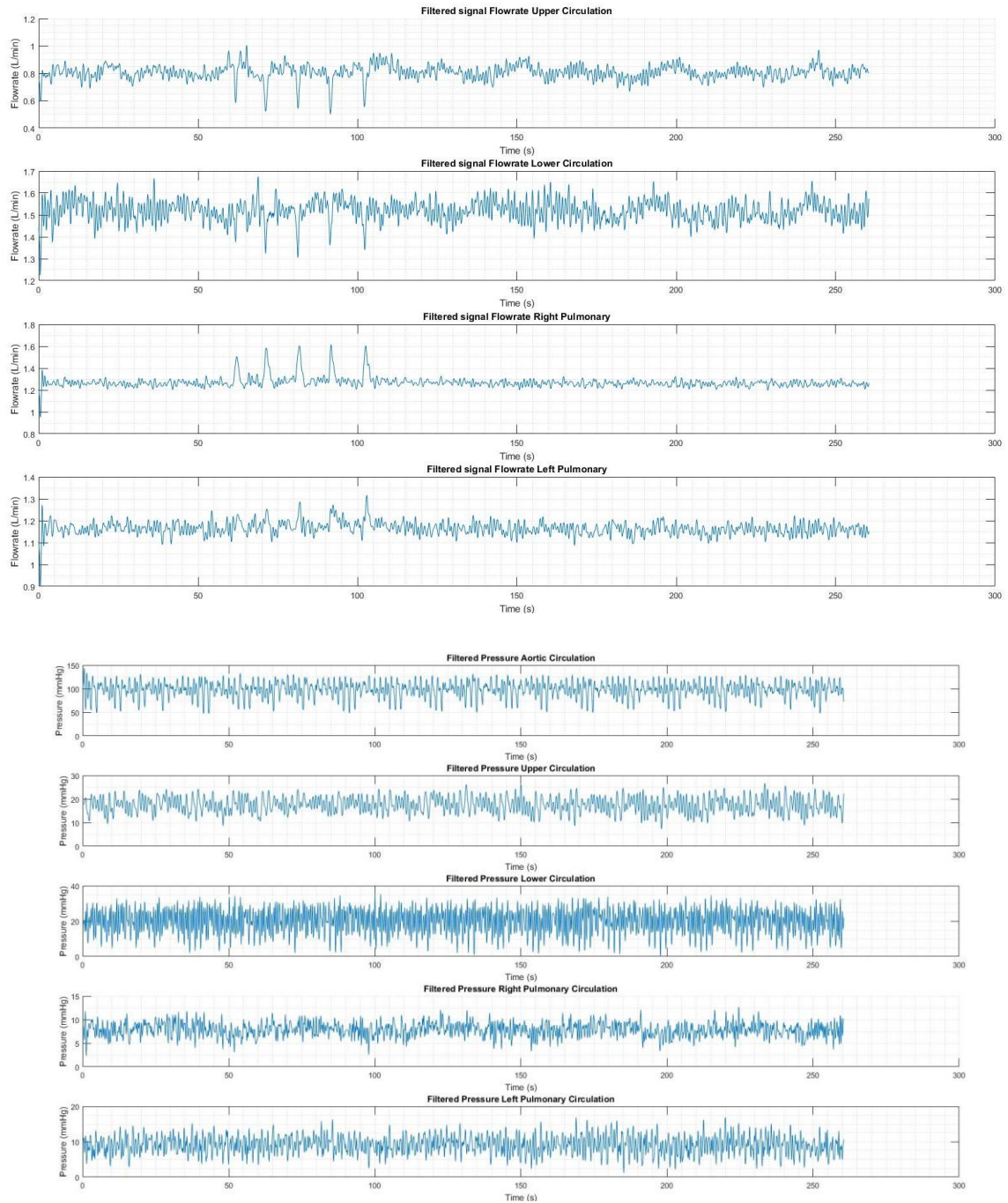


Figure 165 Filtered flowrate (U) and pressure (L) for 20cc/s with 15cc volume for one short shot

1.3.4.2 10 x 10cc injections (100cc total volume)

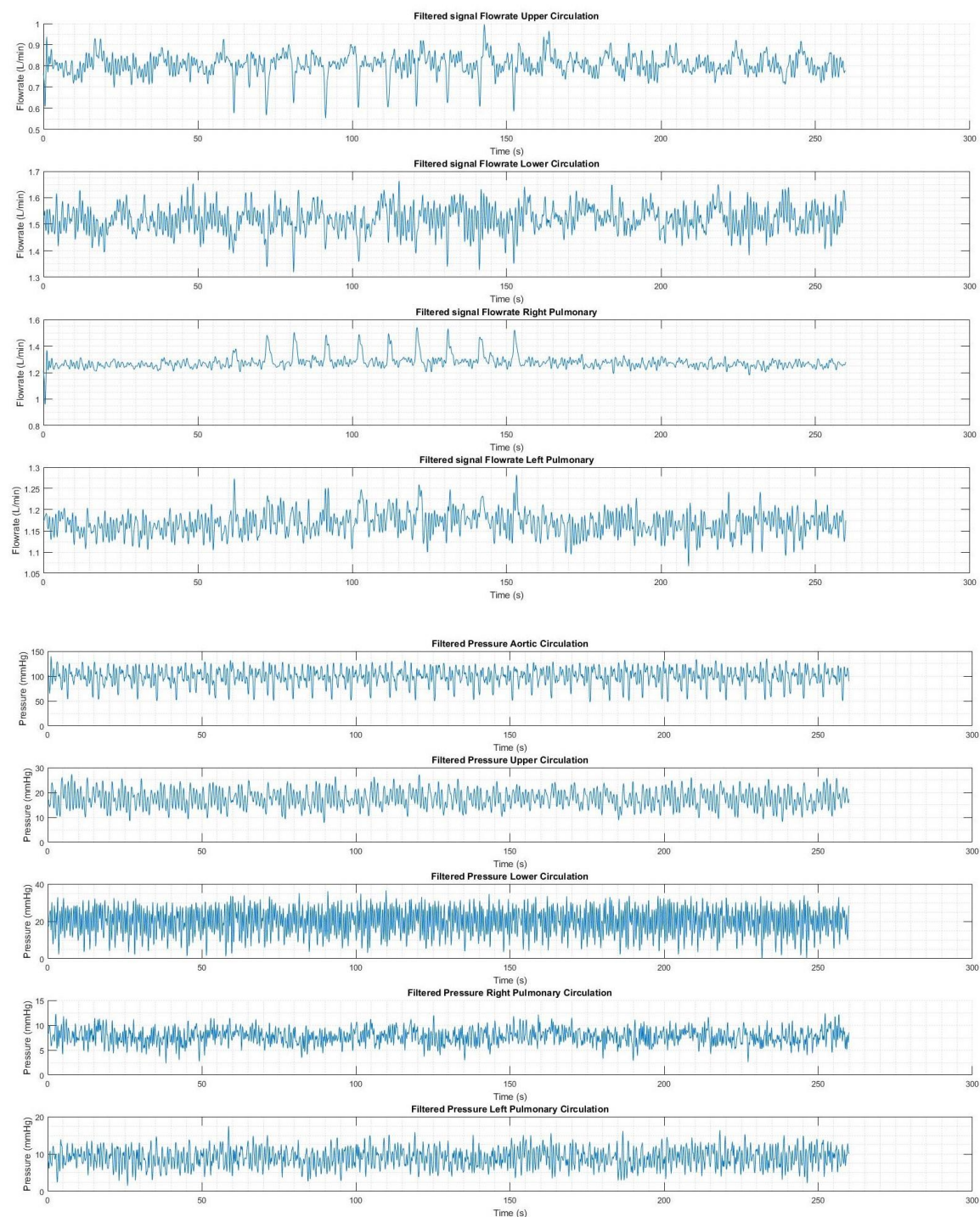


Figure 166 Filtered flowrate (U) and pressure (L) for 20cc/s with 10cc volume for one short shot

1.3.4.3 10 x 5cc injections (50cc total volume)

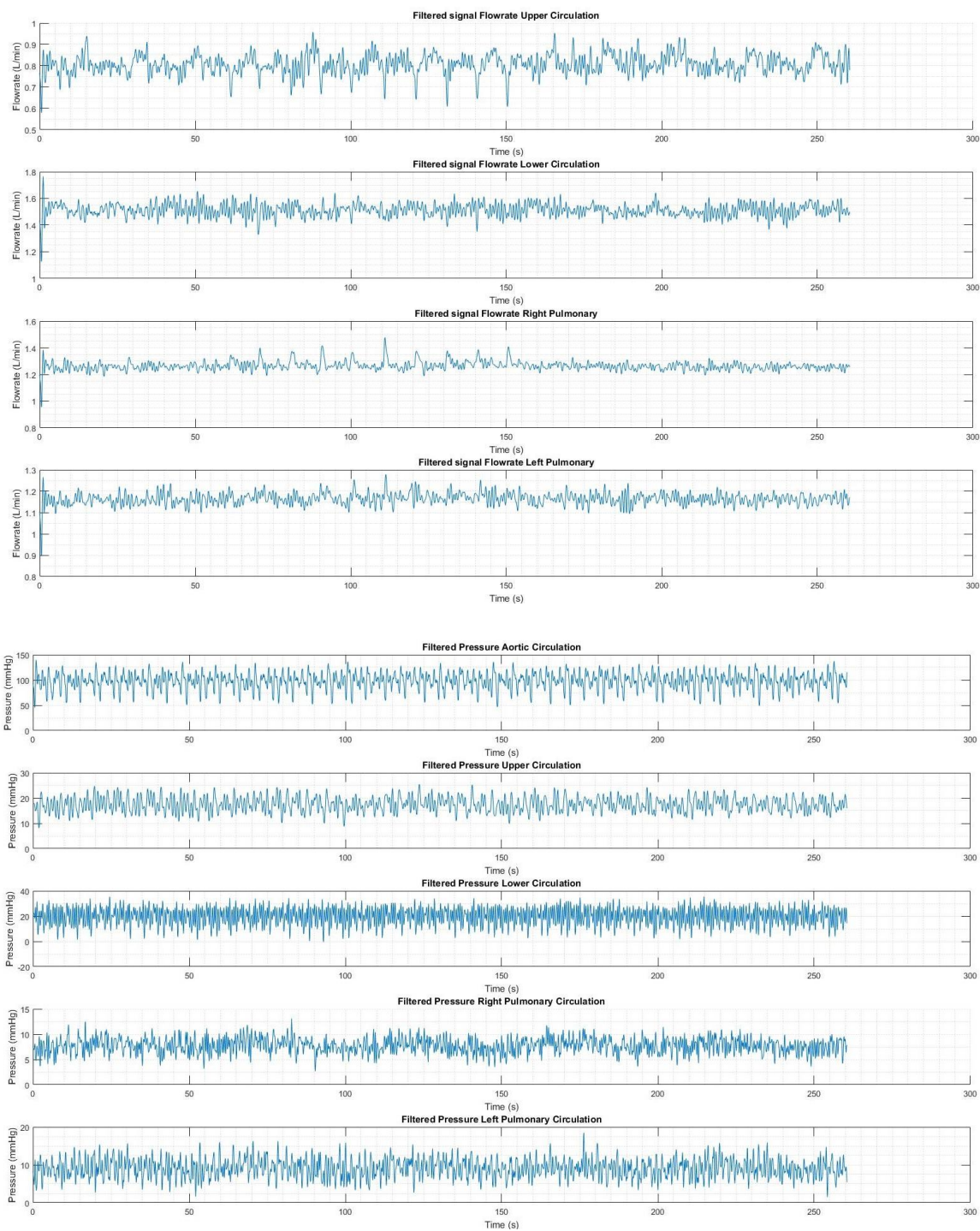


Figure 167 Filtered flowrate (U) and pressure (L) for 20cc/s with 5cc volume for one short shot

1.3.5 Case 5: 5 cc/s long injection

1.3.5.1 1 x 50cc injections (50cc total volume)

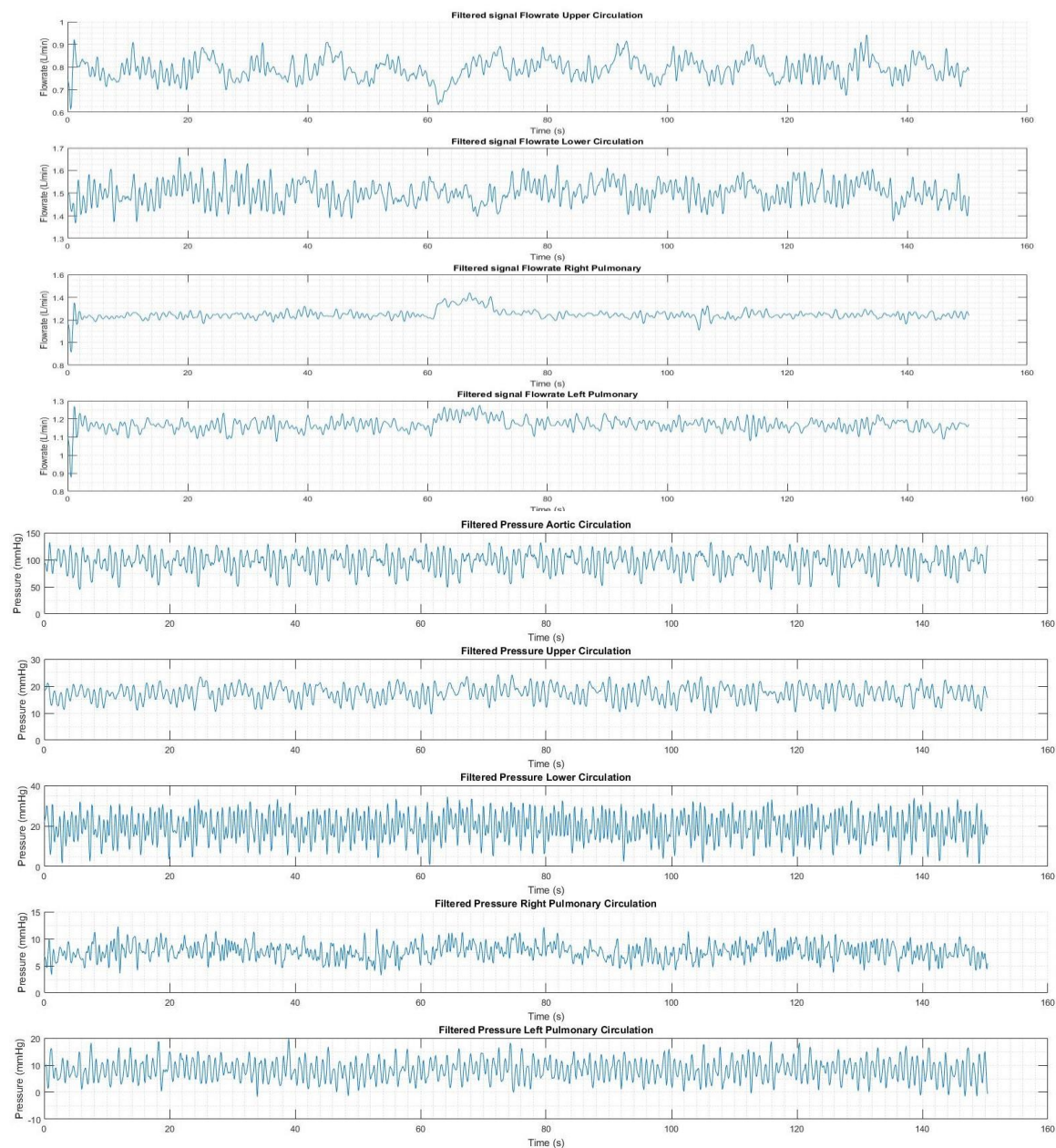


Figure 168 Filtered flowrate (U) and pressure (L) for 5cc/s with 50cc volume for one long shot

1.3.5.2 1 x 150cc injections (150cc total volume)

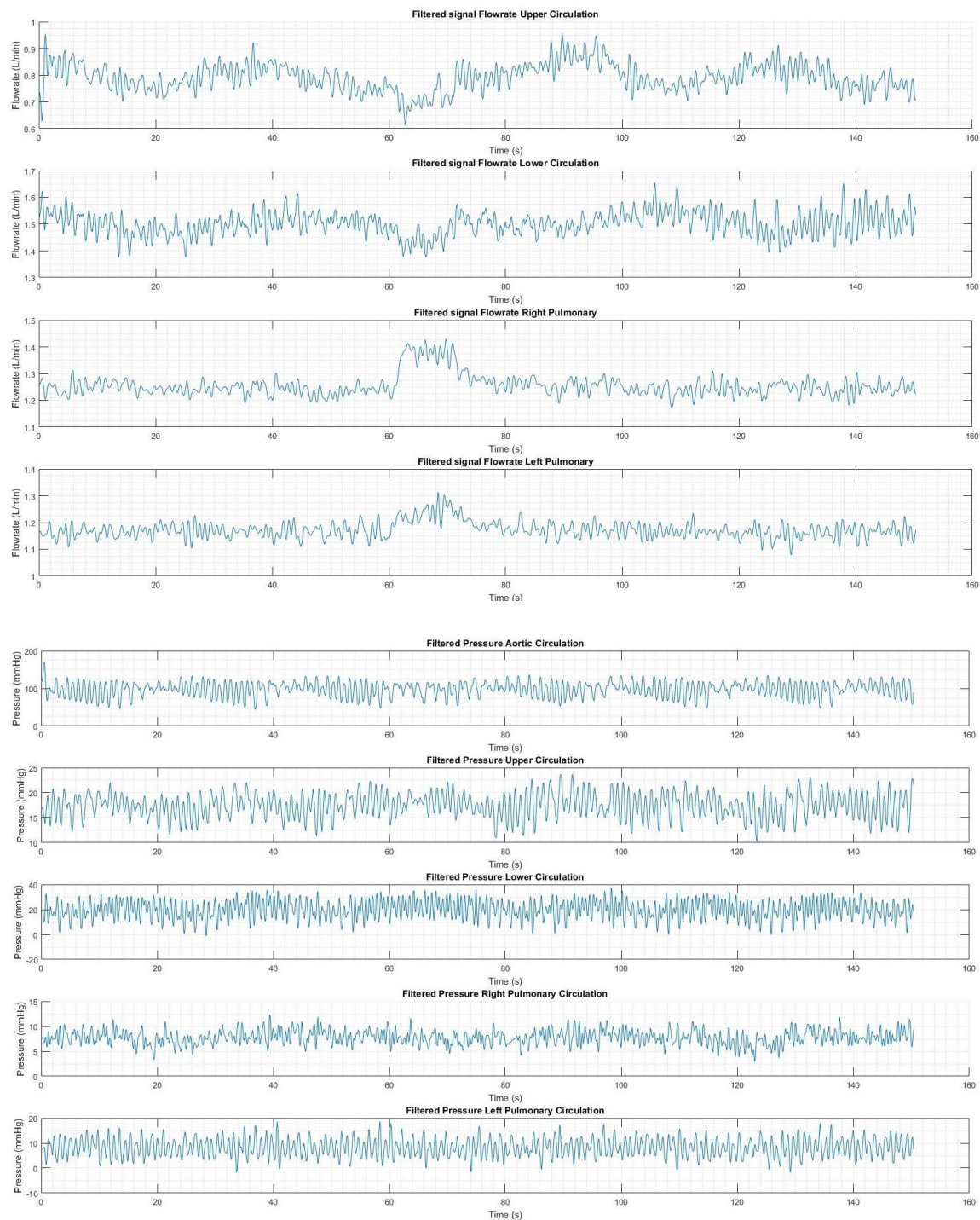


Figure 169 Filtered flowrate (U) and pressure (L) for 5cc/s with 150cc volume for one long shot

1.3.6 Case 6: 10 cc/s long injection

1.3.6.1 1 x 50cc injections (50cc total volume)

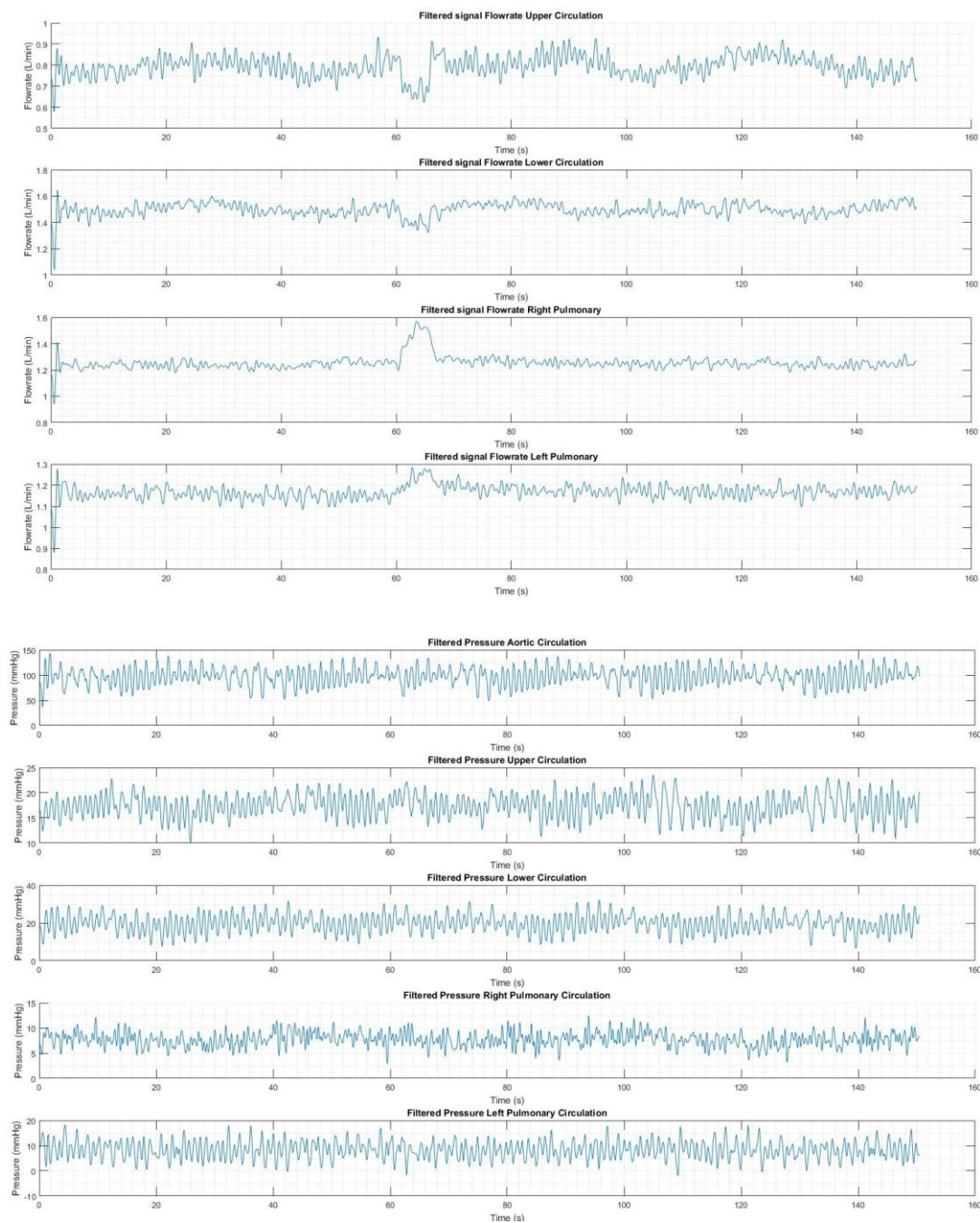


Figure 170 Filtered flowrate (U) and pressure (L) for 10cc/s with 50cc volume for one long shot

1.3.6.2 1 x 150cc injections (150cc total volume)

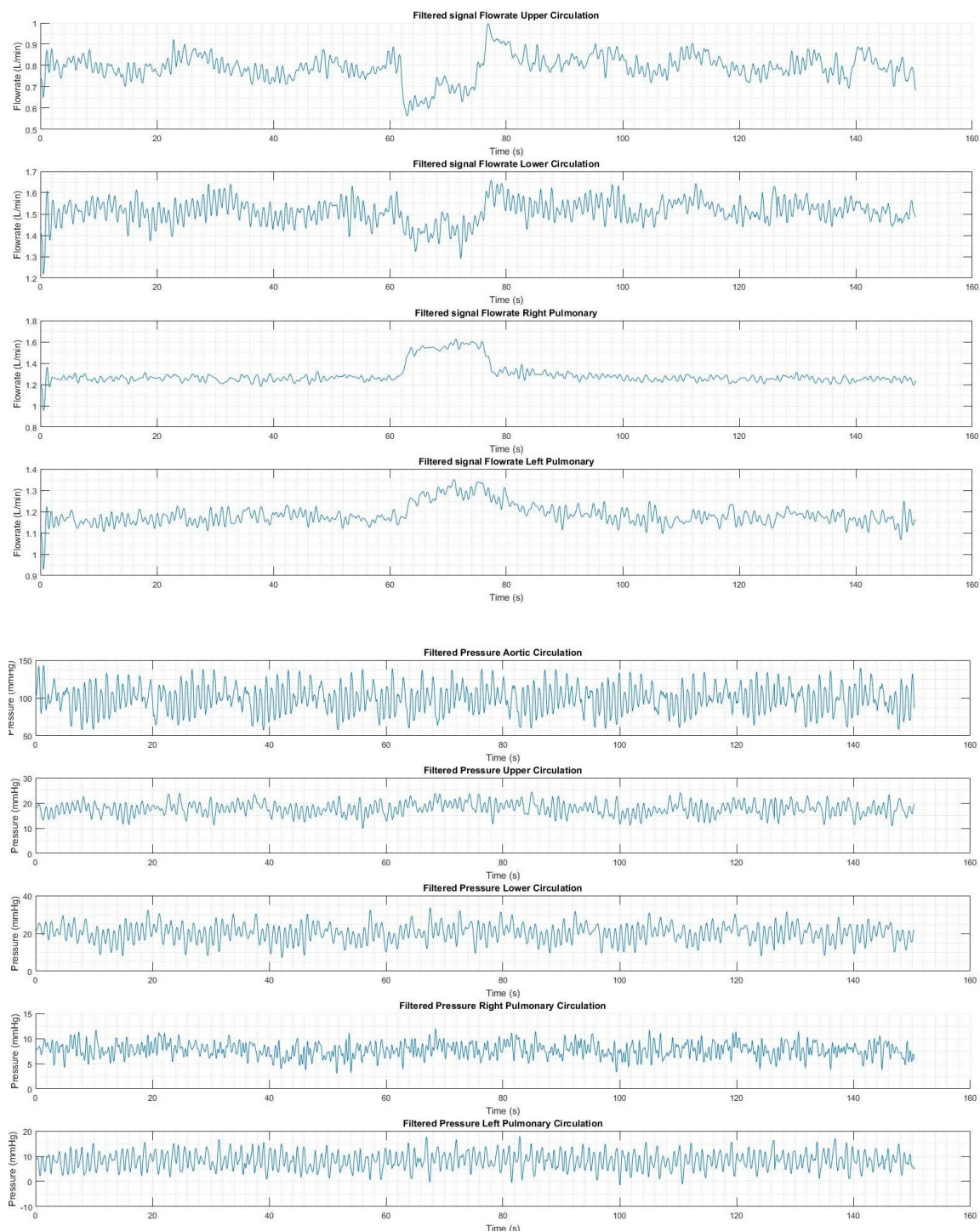


Figure 171 Filtered flowrate (U) and pressure (L) for 10cc/s with 150cc volume for one long shot

1.3.7 Case 7: 15 cc/s long injection

1.3.7.1 1 x 50cc injections (50cc total volume)

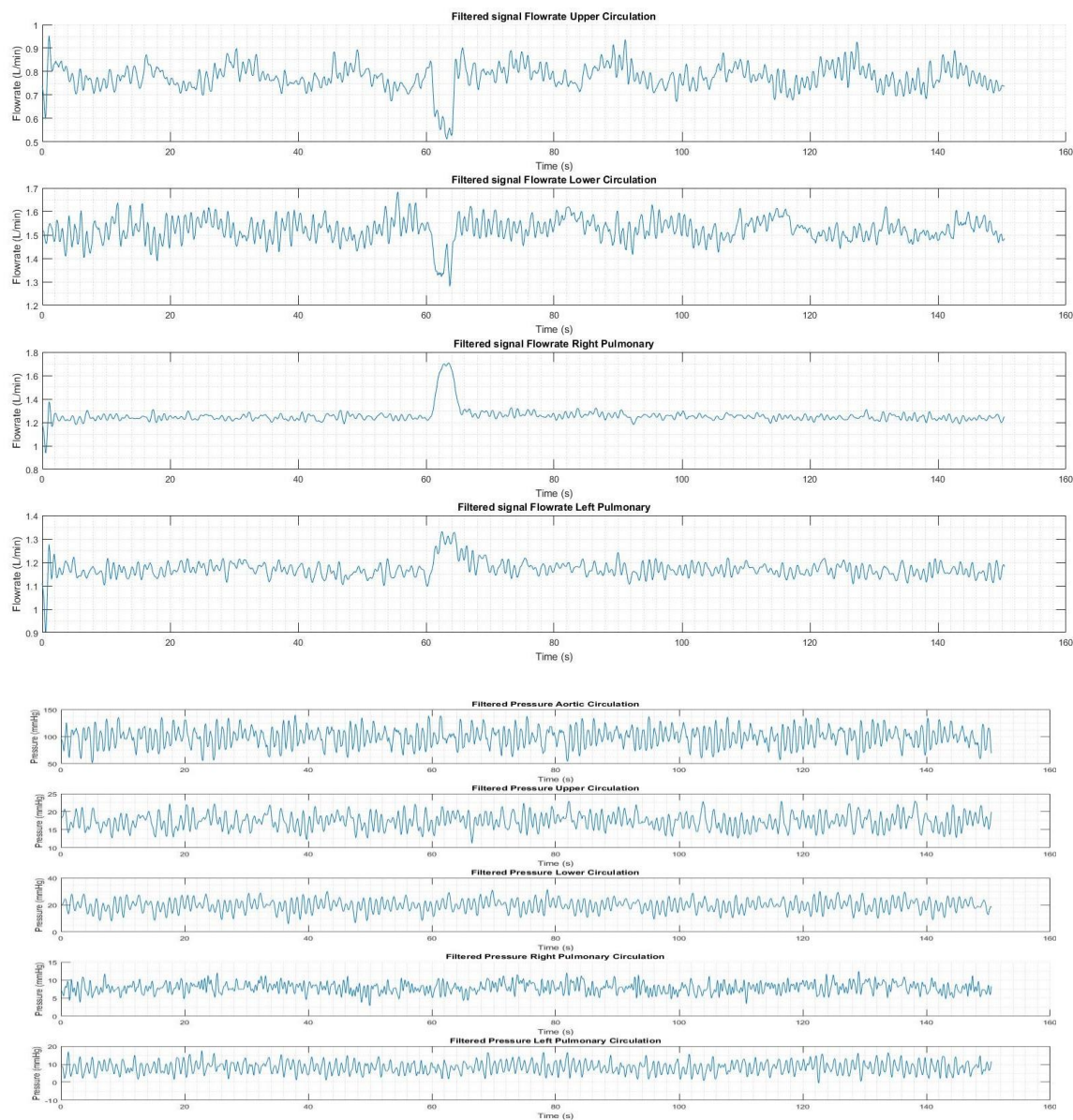


Figure 172 Filtered flowrate (U) and pressure (L) for 15cc/s with 50cc volume for one long shot

1.3.7.2 1x 150cc injections (150cc total volume)

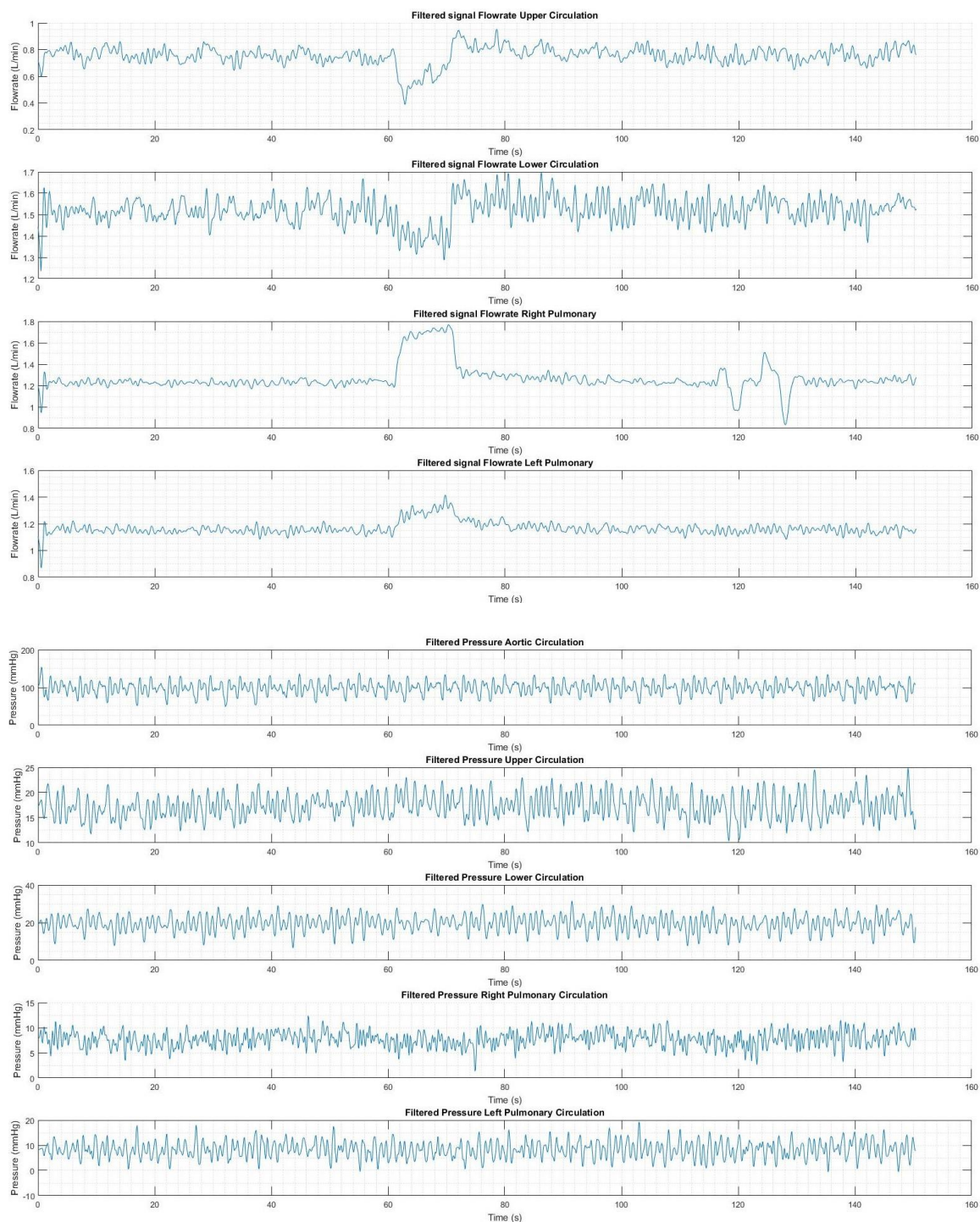


Figure 173 Filtered flowrate (U) and pressure (L) for 15cc/s with 150cc volume for one long shot

1.3.8 Case 8: 20 cc/s long injection

1.3.8.1 1 x 50cc injections (50cc total volume)

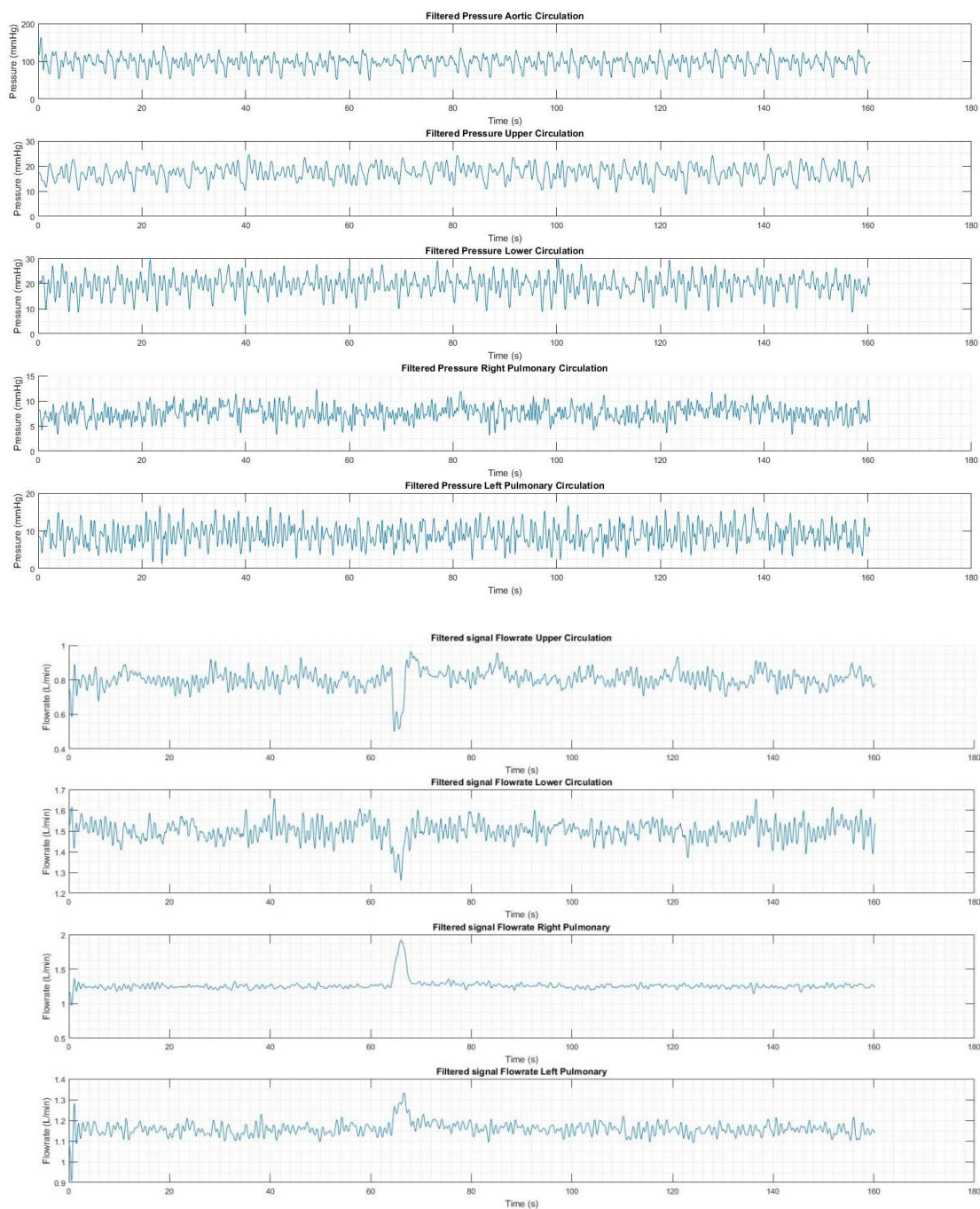


Figure 174 Filtered flowrate (U) and pressure (L) for 20cc/s with 50cc volume for one long shot

1.3.8.2 1 x 150cc injections (150cc total volume)

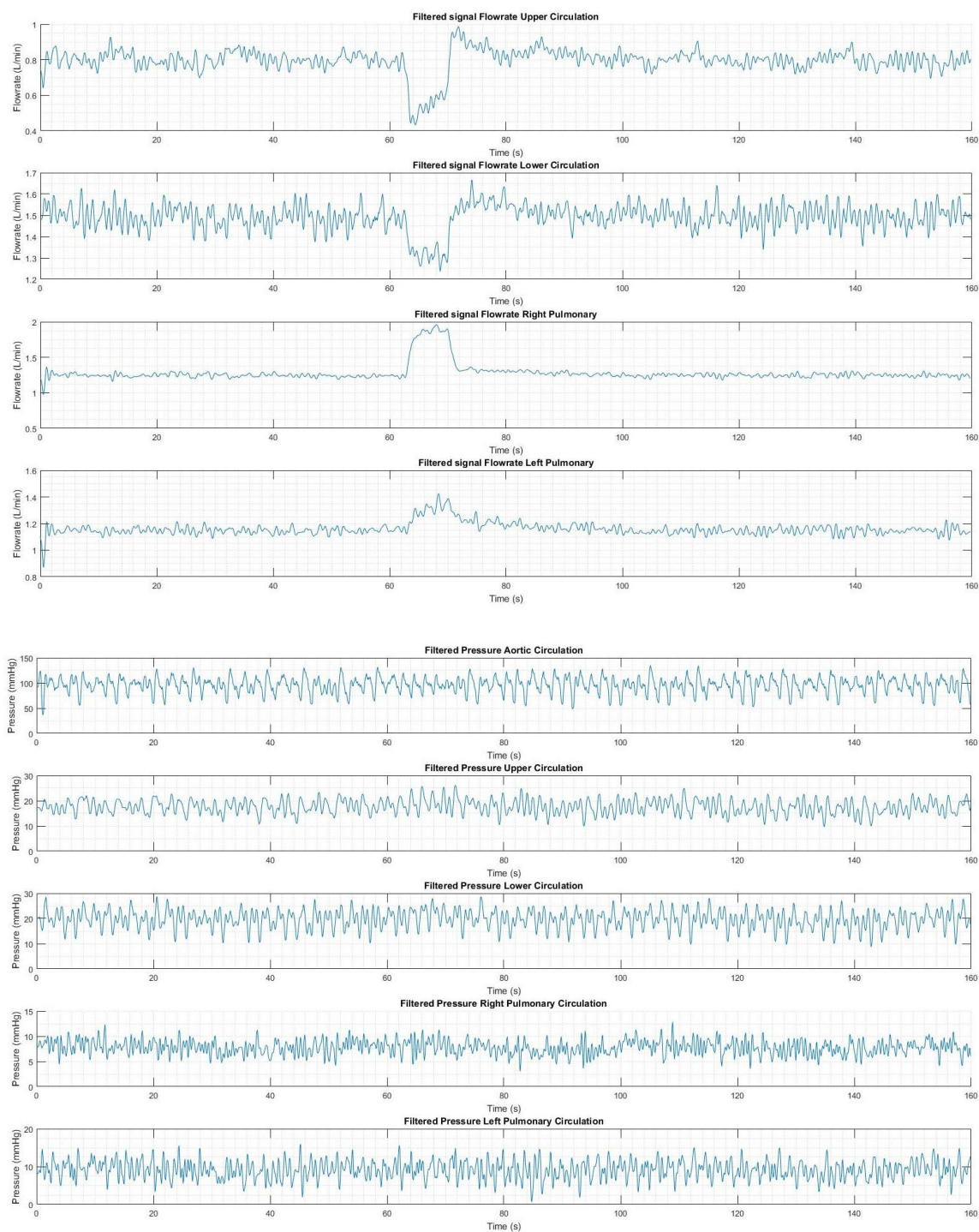


Figure 175 Filtered flowrate (U) and pressure (L) for 20cc/s with 150cc volume for one long shot